

STRUCTURE PREDICTION OF PEROVSKITE
SURFACES AND NANOCCLUSERS

Daniel Deacon-Smith

A thesis submitted for the degree of
Doctor of Philosophy

University College London

2015

Declaration

I, Daniel Deacon-Smith, confirm that the work presented in this thesis is my own. Where information has been derived from other sources, I confirm that this has been indicated in the thesis.

Signed:

Abstract

Perovskite materials possess a broad range of novel and useful properties. This has led to perovskites being used in a broad range of applications, with considerable ongoing research being invested into them. While the bulk structure of these materials have been thoroughly investigated and documented, the polar surface and nanocluster structures of these compounds are relatively unknown. This is largely due to conventional structural determination techniques, such as X-ray and neutron scattering, proving ineffective on these non-bulk phases.

In this thesis computational methods have been used to model the ABZ_3 type perovskite materials $KTaO_3$, $KMgF_3$, and $KZnF_3$. Global optimisation techniques have been employed to predict the structure of the compounds in non-bulk phases. The global optimisations were performed using interatomic potentials, with the lowest energy candidates being refined through density functional theory.

Reconstructions of the (001) polar $KTaO_3$ surface were investigated. It was found that the lowest energy reconstructions involved the migration of the Ta ions from the surface, towards the bulk, where they were able to achieve a fuller coordination. The K ions moved in the opposite direction, migrating towards the surface. Defects in the form of neutral K and O vacancies were introduced to the surface. It was found that both types of vacancy resulted in an upward band bending towards the surface. This indicated an accumulation of holes at the surface for K vacancies, and an accumulation of electrons in the bulk for O vacancies.

The structures of small nanoclusters, containing 5 - 100 atoms, were predicted for the compounds $KMgF_3$ and $KZnF_3$. The low energy structures revealed that it was energetically favourable for the B cations, Mg or Zn, to adopt positions close to the cluster centre, while the K cations resided at the edges of the clusters. The optical gap of the clusters was found to vary with the size of the cluster. This indicates the properties may be tuned by controlling cluster size.

Acknowledgements

First and foremost, I would like to thank my supervisor Scott Woodley for giving me the opportunity to do my PhD. Scott provided the support and advice which have made completion of this PhD possible. He has also given me the opportunity to attend various conferences to present my work.

I would also like to thank: Alexey Sokol for his insight on many of the theoretical aspects of the thesis, and his continuous supply of doughnuts; Matt Farrow for fixing all my software issues; Christian Schoen for his collaboration and inviting me to Germany; David Scanlon for his VASP skills; and Richard Catlow for his advice on many aspects of the project.

I also thank the rest of the KLB crew for sharing the journey with me. Shout outs to Andy, David (Fonz), Tom, Giota, Stephen, John.

Lastly, I would like to thank my family (Paul, Chinyere, Rachael, Emues) for their love and support, which has put me into the position where I could attempt a PhD, and carried me through.

Contents

Declaration	2
Abstract	3
Acknowledgements	4
Contents	5
List of Figures	8
List of Tables	16
Preamble	19
1 Perovskites	20
1.1 Introduction	20
1.2 Structure	20
1.2.1 Structural Distortions	21
1.3 Properties and Applications	23
1.4 Perovskite Surface Types	25
2 Methods	27
2.1 Introduction	27
2.2 Crystalline Systems	27
2.2.1 Reciprocal lattice, k-points and the first Brillouin zone	28
2.3 Atomistic Calculations	31
2.3.1 Introduction	31
2.3.2 Calculating the Energy	31
2.3.3 Periodic calculations	34
2.3.4 Fitting	34
2.4 Electronic Structure Calculations	35
2.5 Local Optimisation	37
2.6 Global Optimisation	37

2.7	Defects	39
2.7.1	The Super Cell Method	40
2.7.2	Defect formation energy	41
2.8	Surface Calculations	44
2.8.1	Calculating the Surface Energy	45
2.9	Implementation	47
2.9.1	Knowledge Led Master Controller (KLMC)	47
3	Bulk	49
3.1	Introduction	49
3.1.1	KTaO ₃	50
3.1.2	KMgF ₃	52
3.1.3	KZnF ₃	53
3.2	Electronic Calculations	54
3.2.1	VASP Settings	54
3.2.2	FHI-aims Settings	57
3.2.3	Formation Energy	58
3.2.4	Atomistic Calculations	60
3.3	Bulk Defects	70
3.3.1	Atomistic Defects	70
3.3.2	DFT defects	71
3.4	Summary	75
4	The (001) KTaO₃ Surface	77
4.1	Introduction	77
4.1.1	The KTaO ₃ (001) Surface	77
4.2	Interatomic Potentials (IP)	78
4.3	A Polar Surface	79
4.3.1	Reconstructed Surface	80
4.4	Global Optimisation and KLMC	82
4.5	Stable Atomistic Reconstructions	84
4.5.1	IP KO Terminated Reconstructions	85
4.5.2	IP TaO ₂ Terminated Reconstructions	89
4.5.3	Summary of Atomistic Surfaces	92
4.5.4	The 4 x 4 Surface	94
4.6	DFT Refined Surfaces	95
4.6.1	DFT KO Terminated Reconstructions	96
4.6.2	DFT TaO ₂ Terminated Reconstructions	101
4.6.3	Summary of DFT Surfaces	105
4.7	Electronic Structure	108
4.8	Defects	112

4.8.1	Atomistic Defect Models	112
4.8.2	DFT Defects	113
4.9	Data Mining Surfaces	119
4.10	Conclusion	122
5	KMgF₃ and KZnF₃ Clusters	124
5.1	Introduction	124
5.1.1	Nanocluster Structure Prediction	124
5.2	Global Optimisation: Performance	125
5.2.1	Efficiency Locating Global Minimum	125
5.2.2	Efficiency Locating Top Ten Local Minima	127
5.2.3	Cluster Geometry Optimisation Cost	129
5.2.4	Summary	131
5.3	The Global Optimisation Cluster Results	132
5.3.1	Cluster Energies	132
5.3.2	Atomic Structure of IP Clusters	134
5.4	IP vs DFT Energies	142
5.5	DFT Data Mining	149
5.6	Structures of the Clusters Optimised by DFT	152
5.7	Electronic Structure and Optical Properties	163
5.8	Bulk-like Clusters	168
5.9	Conclusion	171
6	Conclusion	173
	Bibliography	178

List of Figures

1.1	(a) ABZ_3 Cubic perovskite unit cell, where A are the purple cations on the corners, B the grey cations at the centre of the octahedra and unit cell, and Z the red anions on the unit cell face centres forming the octahedra vertices. (b) Extended view the perovskite lattice; $4 \times 4 \times 4$ supercell. . . .	21
1.2	The ABZ_3 ilmenite structure. The purple spheres are the A cations, the grey spheres B cations, and the red spheres the Z anions.	22
1.3	Example of a d^9 degeneracy in the d-orbitals before and after a Jahn–Teller distortion of an octahedral complex.	23
1.4	Example of a ferroelectric distortion in the perovskite $PbVO_3$. The purple spheres are Pb ions, the grey V ions, and the red O ions.	23
1.5	The planes in the: (a) (001); (b) (011); and (c) (001) direction of a cubic ABZ_3 perovskite. The A cations are the purple spheres, the B cations the grey, and the Z anions the red.	25
2.1	Atom vibrations in one dimension. Each unit cell contains one atom . .	30
2.2	The interactions experienced by each particle in the Shell Model. The circles labelled “s” represents a shell and the circles labelled “c” are cores. The core and shell of and individual ion are coupled solely by a spring. Both the core and shell experience Coulomb potentials from both cores and shells of other ions. Only the shell of an ion experiences the short range potentials.	33
2.3	Flow chart of a typical GA routine	38
2.4	The two regions as used in the Mott-Littleton method for defects	40
2.5	A 2-D representation of a defect in a super cell. The image on the left is a simple 1×1 cell, the image on the right is a 2×2 . The size of the super cell controls the concentration of the defects and the defect-defect interaction	41
2.6	Ternary phase diagram for hypothetical material ABO_3	42
3.1	(a) ABZ_3 Cubic perovskite unit cell, where A are the purple cations on the corners, B the grey cations at the centre of the octahedra, and Z the red anions on the octahedra corners. (b) Periodic lattice of the ABZ_3 unit cell.	50

3.2	Phonon dispersion of low energy modes in KTaO_3 at a range of temperatures from inelastic neutron scattering taken from Ref. [71]. Dashed lines and solid circles are modes at 20 K, the solid lines and empty circles 296 K, and the dotted line and crosses 1220 K. TO_1 is the ferro-electric soft mode.	51
3.3	KTaO_3 dielectric constant as a function of temperature; adapted from Ref. [77].	52
3.4	Lattice energy convergence of KTaO_3 , KMgF_3 , and KZnF_3 as a function of plane wave energy cut-off; calculated using VASP. The lattice energy shown is relative to the energy obtained using a 600 eV cut-off.	54
3.5	Lattice energy convergence of KTaO_3 , KMgF_3 , and KZnF_3 with respect to the number of $n \times n \times n$ k-points sampled; calculated using VASP. The lattice energies are set relative to the energy at $n = 9$	55
3.6	Lattice energy as a function of cell volume for KTaO_3 , KMgF_3 , and KMgF_3 ; calculated using VASP. The energy shown is relative to the energy at a volume of 60.24 \AA^3	56
3.7	Lattice energy convergence of KTaO_3 , KMgF_3 , and KZnF_3 with respect to the number of $n \times n \times n$ k-points sampled; calculated using FHI-aims. The lattice energies are set relative to the energy at $n = 8$	57
3.8	Lattice energy as a function of cell volume for KTaO_3 , KMgF_3 , and KMgF_3 ; calculated using FHI-aims. The energy shown is relative to the energy at a volume of 60.24 \AA^3	58
3.9	Phonon data taken from Ref. [71]. Dots are experimental results and solid lines are calculated from fitted force constants for KTaO_3 . Dashed lines are calculated from force constants for SrTiO_3	64
3.10	Electronic band structure for bulk KTaO_3 , as calculated using VASP. The valence band maximum is set to 0 (red line). The DOS is shown, in line, on the right.	66
3.11	Species decomposed DOS for KTaO_3 , and orbital decomposed DOS for each species in KTaO_3 ; calculated using VASP.	67
3.12	Electronic band structure for bulk KMgF_3 , as calculated using VASP. The valence band maximum is set to 0 (red line). The DOS is shown, in line, on the right.	68
3.13	Species decomposed DOS for KMgF_3 , and orbital decomposed DOS for each species in KMgF_3 ; calculated using VASP.	68
3.14	Electronic band structure for bulk KZnF_3 , as calculated using VASP. The valence band maximum is set to 0 (red line). The DOS is shown, in line, on the right.	69
3.15	Species decomposed DOS for KZnF_3 , and orbital decomposed DOS for each species in KZnF_3 ; calculated using VASP.	69

3.16	Phase diagrams for KTaO_3 (left) and KXF_3 (right), where $X = \text{Mg}$ or Zn .	72
4.1	Interatomic pair potentials used in GULP calculations. a) is the K–O interaction, b) the Ta–O interaction.	79
4.2	Surface energies of bulk terminated surfaces. (c) indicates core only calculations. (s) indicates shells were included in the calculations.	80
4.3	Initial reconstruction of the 2 x 2 slab	81
4.4	(a) Surface energies of the 2 x 2 reconstructed slab. (b) Surface energy convergence of the 2 x 2 reconstructed slab. The surface energy convergence is calculated as $ S_n - S_{n+1} $ where S_n is the surface energy for n layers thickness	81
4.5	An interlayer reconstruction process that occurs during the geometry relaxation of the KTaO_3 (001) half TaO_2 terminated surface. Goes from left to right.	82
4.6	A KLMC reconstruction process of the half TaO_2 terminated surface. (a) represents the initial configuration in a typical KLMC solid solution surface run. The faded atoms represent unoccupied lattice sites which are available for occupation during the KLMC reordering. Atoms positioned within the blue region will not be involved in the KLMC reordering process. (b) shows an example structure created by the KLMC re-ordering process	83
4.7	The seven different initial KLMC set ups showing only the lattice sites involved in the KLMC Monte-Carlo process of the half TaO_2 terminated surface. Below each of the images shown would exist the rest of the slab	84
4.8	KO terminated reconstruction: K-cornered zig-zag surface arrangement. a) top view. b) side view.	85
4.9	KO terminated reconstruction: KO island surface arrangement. a) top view. b) side view.	87
4.10	KO terminated reconstruction: O-cornered zig-zag surface arrangement. a) top view. b) side view.	88
4.11	KO terminated reconstruction: KO diagonal chain surface arrangement. a) top view. b) side view.	89
4.12	The stable mixed sub-layer produced during reconstructions of the half TaO_2 terminated surface.	90
4.13	KO terminated reconstruction: K-cornered zig-zag surface arrangement. a) top view. b) side view.	91
4.14	KO terminated reconstruction: KO island surface arrangement. a) top view. b) side view.	92
4.15	A 4x4 TaO_2 terminated reconstruction possessing a mixed sub-layer.	94
4.16	KO terminated reconstruction: KO diagonal chain surface arrangement.	96

4.17	KO terminated reconstruction: O-cornered zig-zag surface arrangement.	97
4.18	KO terminated reconstruction: K-cornered zig-zag surface arrangement.	98
4.19	KO terminated reconstruction: KO terraced surface arrangement.	100
4.20	KO terminated reconstruction: KO island surface arrangement.	100
4.21	TaO ₂ terminated reconstruction: K-cornered zig-zag surface arrangement.	102
4.22	TaO ₂ terminated reconstruction: KO terraced surface arrangement.	103
4.23	TaO ₂ terminated reconstruction: KO island surface arrangement.	104
4.24	TaO ₂ terminated reconstruction: TaO ₂ terraced surface arrangement.	105
4.25	Band structure for the TaO ₂ terminated K-cornered zig-zag structure. The top of the valence band is shifted to 0 eV.	108
4.26	The DOS projected onto the different layers in the slab. The DOS is further decomposed into its different species. The left shows the DOS over the range -30 – 10 eV. The right magnifies the -5 – 5 eV range in which the valence band and conduction band reside.	109
4.27	Two-dimensional charge density plot of the KTaO ₃ ground state surface (TaO ₂ terminated K-cornered). The image taken is of a plane in the (010) direction. The blue at the bottom of the spectrum represents low charge density while the red end is high charge density. The image on the right highlights the atom positions. The surface lies at the top of images.	110
4.28	Simulated STM images of the KTaO ₃ reconstructions. a) the TaO ₂ termi- nated K-cornered zig-zag surface. b) the TaO ₂ terminated KO terraced surface. c) the KO terminated KO terraced surface. The images were created by looking at constant charge density levels of bands near the top of the valence band. The brightness indicates the distance from the top of the surface.	111
4.29	Labelling of the unique ions at the surface of the KTaO ₃ (001) recon- structed ground state.	112
4.30	Plots of the atomistic defect energy for neutral O vacancies on the KTaO ₃ (001) reconstructed ground state surface. On the left the charge associ- ated with the O vacancy has been evenly distributed over all Ta ions. On the right the charge has been evenly distributed to the two Ta ions closest to the O vacancy.	113
4.31	Phase diagram for KTaO ₃	114
4.32	The DOS, close to the Fermi level, projected onto layers for a KTaO ₃ slab containing a neutral O vacancy (black line) and a stoichiometric slab without vacancies (red line). The Fermi energy is shifted to 0 eV (green line) and sits at the bottom of the conduction band. Even numbered layers are KO, and odd numbers layers are TaO ₂	117

4.33	Charge density distribution for a KTaO_3 slab containing an oxygen vacancy. a) shows an isosurface of the conduction band charge density. b) shows a contour plot of the conduction band charge density for a plane that bisects the Ta ions. a) and b) are aligned so that the layers are in line with each other, the surface is at the top. The purple, grey, and red spheres are K, Ta, and O, respectively.	118
5.1	Comparison of the efficiency at finding the $(\text{KMgF}_3)_n$ GM cluster for three different global optimisation techniques: Stochastic Quenching (SQ), Basin Hopping (BH), and Genetic Algorithms (GA). The computational cost is measured as the number of cluster optimisations performed before the GM structure is found, as a function of cluster size (formula units). The first graph reports the average obtained across four different runs; the second reports the standard deviation associated with this average; and the third reports the best (lowest cost) of the four runs.	126
5.2	Comparison of the efficiency at finding the $(\text{KZnF}_3)_n$ GM cluster for three different global optimisation techniques: Stochastic Quenching (SQ), Basin Hopping (BH), and Genetic Algorithms (GA). The computational cost is measured as the number of cluster optimisations performed before the GM structure is found, as a function of cluster size (formula units). The first graph reports the average obtained across four different runs; the second reports the standard deviation associated with this average; and the third reports the best (lowest cost) of the four runs.	127
5.3	Comparison of the efficiency at which the three different GLOp techniques, SQ, BH, and GA found the ten most stable clusters for different sized $(\text{KMgF}_3)_n$ clusters.	128
5.4	Comparison of the efficiency at which the three different GLOp techniques, SQ, BH, and GA found the ten most stable clusters for different sized $(\text{KZnF}_3)_n$ clusters.	129
5.5	Average number of calculations performed for each $(\text{KMgF}_3)_n$ cluster optimisation during the three GLOp techniques: Stochastic Quenching (SQ), Basin Hopping (BH), Genetic Algorithms (GA).	130
5.6	Average number of calculations performed for each $(\text{KZnF}_3)_n$ cluster optimisation during the three GLOp techniques: Stochastic Quenching (SQ), Basin Hopping (BH), Genetic Algorithms (GA).	131
5.7	IP energies for top ten structures for each cluster size relative to the bulk.	135
5.8	The three stable LM IP clusters found for $n = 1$. The table shows the energy for each cluster relative to the GM in eV/atom	135
5.9	Ten most thermodynamically stable LM IP clusters for $n = 2$. The table shows the energy for each cluster relative to the GM in eV/atom	136

5.10	Ten most thermodynamically stable LM IP clusters for $n = 3$. The table shows the energy for each cluster relative to the GM in eV/atom	139
5.11	Ten most thermodynamically stable LM IP clusters for $n = 4$. The table shows the energy for each cluster relative to the GM in eV/atom	140
5.12	Ten most thermodynamically stable LM IP clusters for $n = 5$. The table shows the energy for each cluster relative to the GM in eV/atom	141
5.13	The IP GM structures for $n = 6 - 9$	142
5.14	Plots comparing the energy of LM clusters calculated using different theoretical models for $(\text{KMgF}_3)_n$, $n = 2$. The axis are labelled $\langle \text{structure method} \rangle - \langle \text{energy method} \rangle$, where the structure method is the theoretical model used to relax the LM structure, and energy method is the model by which the energy was calculated (no additional relaxation). For Example, IP - PBEsol is the energy of a structure which has been relaxed using the IP model, but had the energy of that structure calculated using DFT with the PBEsol functional. All energies are relative to the GM and given in eV/atom.	143
5.15	The structural changes that occur for the two points circled in red in Figure 5.14. On the left the IP rank 11 cluster when refined through DFT collapses to the IP rank 2 structure. On the right the IP rank 37 when refined through DFT collapses to the IP rank 13 structure. . . .	144
5.16	Plots comparing the energy of LM clusters calculated using different theoretical models for $(\text{KMgF}_3)_n$, $n = 3$. All energies are relative to the GM and given in eV/atom. Refer to Figure 5.14 for details about axis labels.	145
5.17	Plots comparing the energy of LM clusters calculated using different theoretical models for $(\text{KMgF}_3)_n$, $n = 4$. All energies are relative to the GM and given in eV/atom. Refer to Figure 5.14 for details about axis labels.	146
5.18	Plots comparing the energy of LM clusters calculated using different theoretical models for $(\text{KZnF}_3)_n$, $n = 2$. All energies are relative to the GM and given in eV/atom. Refer to Figure 5.14 for details about axis labels.	146
5.19	Plots comparing the energy of LM clusters calculated using different theoretical models for $(\text{KZnF}_3)_n$, $n = 3$. All energies are relative to the GM and given in eV/atom. Refer to Figure 5.14 for details about axis labels.	147
5.20	Plots comparing the energy of LM clusters calculated using different theoretical models for a 100 random cluster sample created using the SQ technique for $(\text{KMgF}_3)_n$, $n = 4$ and 5. All energies are relative to the GM and given in eV/atom. Refer to Figure 5.14 for details about axis labels.	149

5.21	Plots showing the relative energy of $(\text{KMgF}_3)_n$ and $(\text{KZnF}_3)_n$ clusters when cross data mined for $n = 2$. * indicates the structure was created by performing a Mg-Zn swap on a previously found cluster, but the structure was not relaxed before calculating the energy. ** indicates the structure was created by performing a Mg-Zn swap on a previously found cluster, and the energy was calculated after performing a relaxation.	150
5.22	Plots showing the relative energy of $(\text{KMgF}_3)_n$ and $(\text{KZnF}_3)_n$ clusters when cross data mined for $n = 4$. * indicates the structure was created by performing a Mg-Zn swap on a previously found cluster, but the structure was not relaxed before calculating the energy. ** indicates the structure was created by performing a Mg-Zn swap on a previously found cluster, and the energy was calculated after performing a relaxation.	151
5.23	Plots showing the relative energy of $(\text{KMgF}_3)_n$ and $(\text{KZnF}_3)_n$ clusters when cross data mined for $n = 8$. * indicates the structure was created by performing a Mg-Zn swap on a previously found cluster, but the structure was not relaxed before calculating the energy. ** indicates the structure was created by performing a Mg-Zn swap on a previously found cluster, and the energy was calculated after performing a relaxation.	152
5.24	DFT energies relative to the bulk for top ten LM structures for each cluster size.	153
5.25	The three stable $(\text{KMgF}_3)_n$ and $(\text{KZnF}_3)_n$ DFT clusters for $n = 1$. The table shows the energy for each cluster relative to the GM in eV/atom.	154
5.26	The five lowest energy $(\text{KMgF}_3)_n$ and $(\text{KZnF}_3)_n$ LM DFT clusters for $n = 2$. The table shows the energy for the top ten clusters relative to the GM in eV/atom. In the table a superscript “1” indicates the structure was only found by IP to DFT refinement. A lack of superscript means the structure was found from both methods.	156
5.27	The five lowest energy $(\text{KMgF}_3)_n$ and $(\text{KZnF}_3)_n$ DFT clusters for $n = 3$. The table shows the energy for the top ten clusters relative to the GM in eV/atom. In the table a superscript “1” indicates the structure was only found by IP to DFT refinement, a “2” means the structure was only found through cross data mining. A lack of superscript means the structure was found from both methods.	158
5.28	The five lowest energy $(\text{KMgF}_3)_n$ and $(\text{KZnF}_3)_n$ DFT clusters for $n = 4$. The table shows the energy for the top ten clusters relative to the GM in eV/atom. In the table a superscript “1” indicates the structure was only found by IP to DFT refinement, a “2” means the structure was only found through cross data mining. A lack of superscript means the structure was found from both methods.	159

5.29	The five lowest energy DFT clusters for $n = 5$. The table shows the energy for the top ten clusters relative to the GM in eV/atom. In the table a superscript “1” indicates the structure was only found by IP to DFT refinement, a “2” means the structure was only found through cross data mining. A lack of superscript means the structure was found from both methods.	160
5.30	The three lowest energy $(\text{KMgF}_3)_n$ and $(\text{KZnF}_3)_n$ DFT clusters for $n = 6 - 9$. The tables shows the energy for the top ten clusters relative to the GM in eV/atom. In the table a superscript “1” indicates the structure was only found by IP to DFT refinement, a “2” means the structure was only found through cross data mining. A lack of superscript means the structure was found from both methods.	161
5.31	163
5.32	DOS for KMgF_3 (left) and KZnF_3 (right), clusters and bulk. The clusters sizes showns are for $n = 1, 4$, and 9 , where n is the number of formula units.	164
5.33	The HOMO-LUMO gap for the top ten structures at each size for KMgF_3 and KZnF_3 clusters. The red line tracks the gap for the GM structure at each size. The calculated values for the bulk band gap of KMgF_3 and KZnF_3 , are 7.02 eV and 3.72 eV, respectively.	165
5.34	166
5.35	Calculated infrared spectra for $(\text{KMgF}_3)_n$ and $(\text{KZnF}_3)_n$ clusters, where $n = 2, 4$ and 9	167
5.36	The central section of clusters created using Type 2. K, Mg, and F ions are purple, orange, and grey spheres, respectively.	169
5.37	The central section of clusters created using Type 2. K, Mg, and F ions are purple, orange, and grey spheres, respectively.	169

List of Tables

3.1	VASP vs FHI-aims. The lattice constant (a), percentage deviation from experimental value, formation energy (E_f), and the time taken to complete one SCF cycle using VASP and FHI-aims with the PBEsol functional. Room temperature experimental lattice parameters for KTaO_3 , KMgF_3 , and KZnF_3 are 3.989 Å [67], 3.988 Å [108], and 4.055 Å [115], respectively.	60
3.2	Potential parameters for KMgF_3. A radial cut-off of 25 Å and 10 Å was used for the Buckingham potentials and Lennard-Jones potentials, respectively.	61
3.3	Potential parameters for KZnF_3. A radial cut-off of 10 Å was used for all potentials.	61
3.4	Potential parameters for KTaO_3. A radial cut-off of 15 Å was used for all potentials.	62
3.5	Observables. The lattice parameter (a), bulk modulus (B_0), elastic constants (C_{xx}), dielectric constants (ϵ) and lowest energy transverse optical phonon mode (TO_1) as calculated in GULP and VASP, and experimental values, at room temperature when available, from the literature.	63
3.6	Atomistic defect energies. The values presented are the difference in energy between the defected and bulk systems in eV. Mott. indicates the Mott-Littleson method of defect calculation described in chapter 2. The correction used for the super cells is also described in chapter 2.	70
3.7	Chemical potentials. The chemical potentials for each species in KTaO_3 , KMgF_3 , and KZnF_3 , calculated at the points shown in the relevant phase diagrams (Figure 3.16).	73
3.8	DFT neutral vacancy energies. ΔE is the difference in energy between the perfect bulk system and the system containing one vacancy. The defect energies are calculated using chemical potentials at the points shown in the relevant phase diagrams (Figure 3.16).	74

4.1	Surface energy and key inter-atomic distances for the most stable GULP reconstructions. γ is the surface energy. K–O the bond length between surface K and O ions. O–O and K–K the smallest separation between like-species at the surface. Ta–O the bond length between the surface O and sub-layer Ta ions. O–K–O and K–O–K are the angles between surface ions. Δz K–O is the vertical separation between K and O ions on the surface. Δz L_1 – L_2 the separation between the surface and sub-layer planes. Δz L_2 – L_3 is the separation between the sub-layer and 3rd layer planes. The height of the plane is calculated as the average height of all atoms considered to be in that plane. The surface arrangements are abbreviated as K-c (K-cornered zig-zag), Island (KO island), O-c (O cornered zig-zag), Diagonal (KO diagonal chain).	93
4.2	Surface energy and key inter-atomic distances for DFT relaxed KTaO_3 surfaces. The properties listed are the same as in Table 4.1. Bracketed values indicate the difference between the DFT and atomistically optimised surfaces.	107
4.3	KTaO_3 surface band gaps. All the gaps are found to be direct at the Γ point. The bulk band gap for KTaO_3 was calculated to be 2.03 eV.	108
4.4	Defect energies. The defect energy of vacancies in a KTaO_3 slab calculated at the points shown in Figure 4.31.	115
4.5	Data mining of KTaO_3 surface reconstructions. The surface energies of the KTaO_3 reconstructions applied to the ABZ_3 cubic perovskite phases of KMgF_3 , KZnF_3 , and BaSnO_3	119
4.6	Perovskite 1 x 1 surface energies. The surface energies (001) 1 x 1 surfaces of KMgF_3 , KZnF_3 , and BaSnO_3	121
5.1	Calculation ratios. The relative cost of first (E') and second (E'') derivative calculations as a ratio against the cost of an energy calculation ($E'/E, E''/E$). Bear in mind the calculation of a derivative requires the calculation of the energy, the cost of these energy calculations are not included in the derivative cost.	131
5.2	KMgF_3 IP Cluster Energies $n = 1 - 5$. The IP energies of the ten lowest energy $(\text{KMgF}_3)_n$ LM clusters for $n = 1 - 5$. The clusters were found using the global optimisation routines and match those found by our collaborators.	132
5.3	KZnF_3 IP Cluster Energies $n = 1 - 5$. The IP energies of the ten lowest energy $(\text{KZnF}_3)_n$ LM clusters for $n = 1 - 5$. The clusters were found using the global optimisation routines and match those found by our collaborators.	133

5.4	KMgF₃ IP Cluster Energies $n = 6 - 9$. The IP energies of the ten lowest energy (KMgF ₃) _{<i>n</i>} LM clusters for $n = 6 - 9$. The clusters were found using the global optimisation routines and match those found by our collaborators.	133
5.5	KZnF₃ IP Cluster Energies $n = 6 - 9$. The IP energies of the ten lowest energy (KZnF ₃) _{<i>n</i>} LM clusters for $n = 6 - 9$. The clusters were found using the global optimisation routines and match those found by our collaborators.	134
5.6	Correlation between IP and DFT energies. The Pearson product-moment correlation coefficient between energies calculated from various computational methods. IP – represents interatomic potentials; PS – DFT calculation in FHI-AIMS using PBEsol functional; and P – DFT calculation in FHI-AIMS using PBE functional. The superscript denotes which computational method was used to obtain the LM structure. For example, PS ^{IP} describes the PBEsol energy of the LM found by relaxing with IP.	148
5.7	Data mining correlation. The Pearson product-moment correlation coefficient between relative energies of data mined structures. The three columns correspond to the respective columns of plots in Figures 5.21 – 5.23.	153

Preamble

This thesis is focused on the structure determination of perovskite materials outside of their bulk phase, i.e. surfaces and nanoclusters. The work is entirely computational and simulation based, and makes use of global optimisation techniques. Chapter 1 introduces the perovskite structure, and highlights its many useful properties and applications. Chapter 2 discusses the methods and techniques used to perform the computational simulations. Chapter 3 introduces the compounds modelled in this thesis, and looks at their bulk properties. Chapter 4 focuses on reconstructions of the polar (001) KTaO_3 surface. Chapter 5 investigates nanoclusters of the compounds KMgF_3 and KZnF_3 . Chapter 6 presents the conclusions of the thesis. The references are given after chapter 6.

Chapter 1

Perovskites

1.1 Introduction

This chapter introduces the perovskite class of materials on which this thesis is focused. The first section begins with a description of the cubic phase, typically seen at high temperatures, and then summarises the different lower symmetry variants caused by steric, magnetic, and electronic effects. The next section reports a number of key properties and applications of perovskite materials. Finally different surface types of perovskites are briefly described.

1.2 Structure

Perovskites are a class of material that adopt the same crystal structure as CaTiO_3 , the mineral from which the structure is named after. The ideal cubic perovskite has the chemical formula ABZ_3 , where A and B are cations, and Z anions. In many cases the anion is oxygen, and the B cation a transition metal. The structure adopted by these compounds is visualised as a lattice of corner sharing BZ_6 octahedra, with the A cations residing in the 12-coordinated holes between octahedra (c.f. Figure 1.1). The space group of the cubic perovskite cell is $\text{P}\bar{3}\text{m}3$, resulting in a cubic cell with the A cations on the corners of the cell, B cations at the centre of the cell, and Z anions on the face centres.

The perovskite structure is highly flexible in that it is capable of forming from a large array of element combinations [1–3]. Moreover, the flexibility of this structure enables it to accommodate a wide range of defects, while maintaining structural stability [4–9]. Perovskites can also form layered heterostructures, in which a perovskite is interlayered with different compounds or structures [10]. One such example is the Ruddlesden-Popper phase, [11–13], where layers of ABZ_3 perovskite and AZ rock salt are found to alternate through the material.

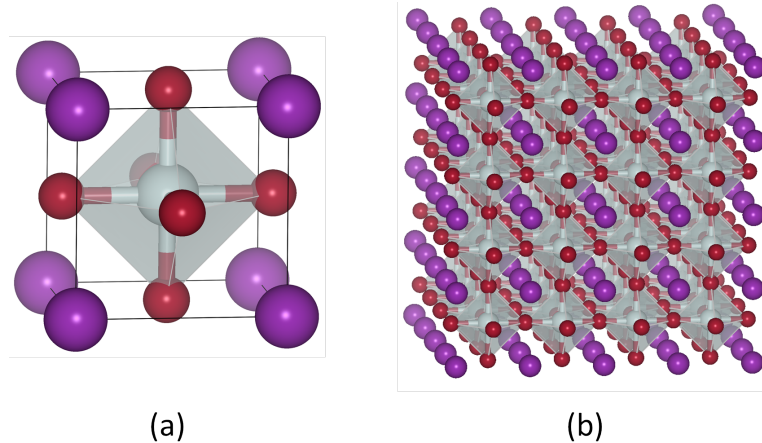


Figure 1.1: (a) ABZ_3 Cubic perovskite unit cell, where A are the purple cations on the corners, B the grey cations at the centre of the octahedra and unit cell, and Z the red anions on the unit cell face centres forming the octahedra vertices. (b) Extended view of the perovskite lattice; $4 \times 4 \times 4$ supercell.

1.2.1 Structural Distortions

The versatility of the perovskite structure is a result of its ability to distort. Deviation from the ideal cubic structure may occur due to non-ideal atomic radii ratios, or electronic and magnetic effects. The structural changes are often characterised by rotations or distortions of the BZ_6 octahedra [14].

Atom Size

Goldschmidt, a pioneer in crystal chemistry during the 1920s, devised a “tolerance factor” to determine the formability of perovskites based on the atomic radii of the constituents [15]. The Goldschmidt tolerance factor is expressed as:

$$t = \frac{r_A + r_Z}{\sqrt{2}(r_B + r_Z)} \quad (1.1)$$

where r_i is the ionic radius of atom species i . It was found, experimentally, that the perovskite structure is formed when $1.13 > t > 0.75$ [16]. Within this range the ideal cubic structure is formed when $0.89 < t < 1.00$. When t is below 0.89, the octahedra rotates to form an orthorhombic or rhombohedral structure, whereas above 1.00 a hexagonal arrangement is adopted. When t is less than 0.75 the ilmenite structure is typically formed [16]; see Figure 1.2.

The restraint on the Goldschmidt tolerance factor is a necessary, but not sufficient, condition in the formability of perovskites. Another restraint on the formability of perovskites is the octahedral factor [2], with the requirement:

$$t_{oct} = \frac{r_B}{r_Z} > 0.425 \quad (1.2)$$

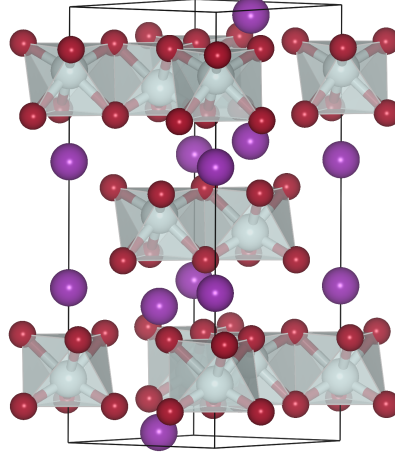


Figure 1.2: The ABZ_3 ilmenite structure. The purple spheres are the A cations, the grey spheres B cations, and the red spheres the Z anions.

This restraint imposes a minimum B to Z size ratio. If the B cation is too small the octahedra will be unstable due to the Z anions approaching too closely to each other.

Jahn-Teller Distortions

A Jahn–Teller distortion [17, 18] can occur in perovskites if the B cation is an open shell transition metal. Such distortions are associated with an increased separation in the energy between an occupied and an unoccupied d-orbital. For the ideal cubic perovskite, the regular BZ_6 octahedra results in the d-orbitals splitting into three degenerate lower energy t_{2g} orbitals and two degenerate higher energy e_g orbitals. Distorting the octahedra results in either the t_{2g} or e_g orbitals splitting. If either are partially occupied, the splitting would result in a stabilisation of the system. Typically, two of the B–Z bonds in the octahedral complex elongate and the other four shorten or two of the B–Z bonds contract and the other four elongate. An example of a d^9 degeneracy, which may be seen in a cuprate perovskite such as $KCuF_3$, is shown in Figure 1.3. The distortion is much more prominent when the degeneracy occurs in the e_g orbital, as these orbitals point towards the ligands.

Ferroelectric Distortion

A material is said to be ferroelectric if it possesses a spontaneous electric polarisation, which can be reversed by the application of an electric field. The ferroelectric behaviour of a material occurs at temperatures below the Curie point, T_c . Above this temperature, the lattice vibrations are large enough to disrupt the spontaneous electronic polarisation and the material is said to be in a paraelectric phase. In perovskites, the polarisation often causes the crystal to distort from a cubic to a tetragonal phase by stretching the octahedra and unit cell asymmetrically in one direction. In $PbVO_3$, the effect is

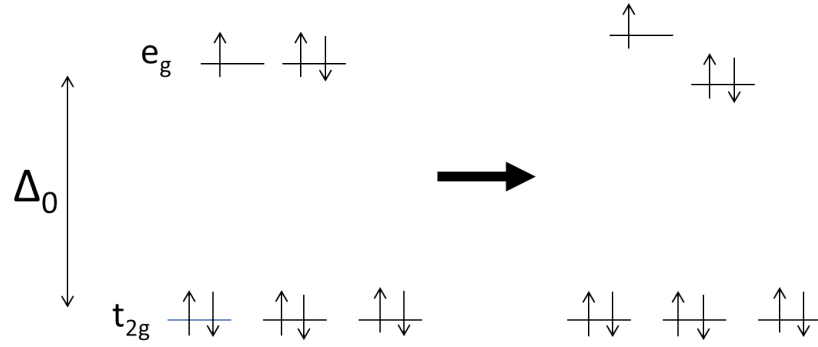


Figure 1.3: Example of a d^9 degeneracy in the d-orbitals before and after a Jahn–Teller distortion of an octahedral complex.

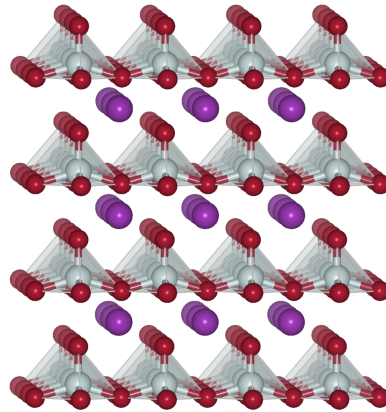


Figure 1.4: Example of a ferroelectric distortion in the perovskite PbVO_3 . The purple spheres are Pb ions, the grey V ions, and the red O ions.

so pronounced that the corner sharing octahedra become base corner sharing, square pyramids [19]; see Figure 1.4.

1.3 Properties and Applications

Perovskites possess a number of interesting and useful properties, which has lead to them being used in a wide range of applications. Discussed below are some of the properties that make certain perovskites useful for specific applications.

High Dielectric and Ferroelectricity

Many ferroelectric perovskites, such as BaTiO_3 , possess a large dielectric constant making them useful as capacitors. The effectiveness of a capacitor is determined by its ability to store charge, known as capacitance, which is calculated as:

$$C = \frac{\epsilon_\omega A}{d} \quad (1.3)$$

where ϵ_ω is the frequency dependant permittivity (dielectric constant), A the area

of the plates, and d the distance between the plates. Thus, using a material with a higher dielectric constant allows a capacitor of the same size to hold more charge.

Ferroelectric capacitors are used in Ferroelectric RAM [20]. They are read by applying an electric field to the memory cell and measuring the charge required to change the state of the cell. The measured charge contains information about what was previously stored on the cell. The downside to this is once the state of the cell has been changed the information is lost, and so the data must be used or written somewhere else.

Piezoelectricity and Pyroelectricity

If a perovskite is a ferroelectric, it will also be pyroelectric and piezoelectric. Thus, changes in temperature and applied stress will induce a voltage. This makes perovskites such as PZT useful in sensory applications such as: pressure pads, microphones and infrared sensors [3].

Superconductivity

A material is said to be in a superconducting state when its electrical resistance falls to exactly zero. This happens when the temperature falls below its superconducting critical temperature T_c . Another property of superconducting materials is that they repel magnetic fields due to the Meissner effect [21]. Cuprates with the perovskite structure such as YBaCuO make up the majority of High Temperature Superconductors (HTS) [22]. HTS are materials with $T_c > 77$ K, and so can be cooled with liquid nitrogen instead of the more expensive liquid helium.

The main application of superconductors is in electromagnets, where they are much more efficient than conventional electromagnets. These superconducting magnets increase the performance of MRI machines, mass spectrometers, and particle accelerators. Superconductors are also used in Superconducting Quantum Interference Devices (SQUID) [23] to measure very small magnetic fields.

Future applications for superconductors include: power transmission and storage, as the absence of resistance prevent power dissipation; and magnetic levitation, which has so far been used in maglev trains.

Colossal Magnetoresistance

This is the phenomenon seen in some manganese based perovskites, i.e. LnCaMnO_3 , where the resistance of the material is changed by orders of magnitude in the presence of a magnetic field. The main potential application for this property is in hard drives, where the read heads currently make use of Tunnel Magnetoresistance [24].

Electro-chemical Properties

The perovskite structure can incorporate a wide range of impurities and defects

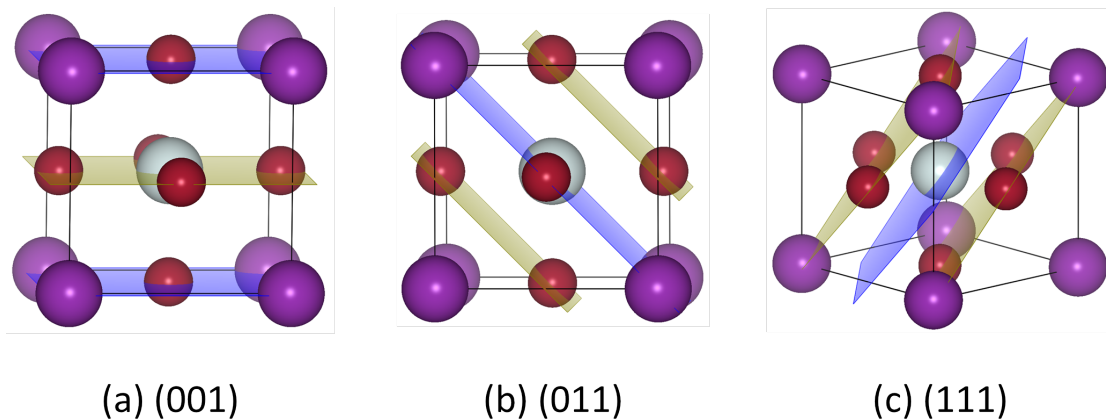


Figure 1.5: The planes in the: (a) (001); (b) (011); and (c) (001) direction of a cubic ABZ_3 perovskite. The A cations are the purple spheres, the B cations the grey, and the Z anions the red.

and remain structurally stable. Due to this, perovskites such as LaMO_3 are promising candidates in electro-chemical applications such as fuel cells [25, 26], where the flexibility of the structure may aid ion transport.

Each year more and more novel applications are being discovered for perovskites, particularly at their surfaces and interfaces. Thus, it is suggested that perovskite oxides may take over from silicon in the next generation of electronic devices [27–29].

1.4 Perovskite Surface Types

Many of the novel properties attributed to perovskites are associated with their surfaces and interfaces. When investigating perovskites, there are generally three directions for which surfaces planes are considered: the (001), the (011), and the (111). The planes in these directions are shown in Figure 1.5. The (001) surface is generally the most widely studied, and often the most stable. This direction contains alternating planes of AZ and BZ_2 . Thus, a perovskite can be cleaved to produce a (001) surface of either AZ, or BZ_2 . The distance separating two planes is half that of the lattice parameter, i.e. $0.5a$. The (011) direction contains alternating planes of ABZ and Z_2 , with a plane separation of $0.35a$. The (111) direction contains alternating planes of AZ_3 and B, with a plane separation of $0.29a$.

Results for the (001) surface will be presented in this thesis. Charge neutral layers are formed in the (001) direction when the charge on the A cation is equal and opposite to that of the Z anion and the charge on the B cation is double that of the Z anion. In the case of charge neutral layers, relaxed bulk terminated planes are generally the most stable. When the layers are not charge neutral the (001) surface becomes polar and must be reconstructed to remove the dipole perpendicular to the surface [30]. Predicting the structure of polar surfaces is often a challenge. This is especially so in ternary compounds

such as perovskites, as the variety of elements adds an additional level of complexity compared to the surfaces of single element and binary compounds. This thesis presents a method that enabled the problem of predicting the structure for polar perovskite surfaces to be resolved.

Chapter 2

Methods

2.1 Introduction

The work presented in this thesis revolves around the structure determination of perovskite materials. In this chapter the methods and theory required to perform the work of this thesis are discussed. Topics included are: crystalline materials and reciprocal space, atomic and electronic level computational simulation methods, global and local optimisation techniques, defect calculations, and surface modelling methods. A brief discussion on the implementation of the software packages used in this thesis is given at the end.

2.2 Crystalline Systems

Many solid materials possess crystalline structures. These structures, or crystal lattices, can be thought of as an individual atom or a series of atoms repeated periodically throughout the system. The crystal lattice can be separated into two components: (a) the Bravais lattice [31], an infinite array of discrete points with an arrangement and orientation that appear exactly the same regardless of the point chosen. (b) the local arrangement of atoms around each lattice point commonly referred to as the unit cell.

The position vector of all the Bravais lattice points from a given point are defined as:

$$\mathbf{R} = n_1\mathbf{a}_1 + n_2\mathbf{a}_2 + n_3\mathbf{a}_3 \quad (2.1)$$

where \mathbf{a}_1 , \mathbf{a}_2 , and \mathbf{a}_3 are the three vectors describing the lattice and n_1 , n_2 , and n_3 are integers. A translation by any integer value of one of the lattice vectors finds another lattice point, and results in the same crystal structure. In the case of cubic perovskites, the crystal structure of interest in this thesis, the Bravais lattice is cubic with a unit cell containing 5 atoms (ABX_3). Any vector \mathbf{r}' within the crystal lattice can be separated into two components such that:

$$\mathbf{r}' = \mathbf{R} + \mathbf{r} \quad (2.2)$$

where \mathbf{R} is the vector to the nearest lattice site, and \mathbf{r} the vector from that lattice site (i.e contained within a unit cell).

2.2.1 Reciprocal lattice, k-points and the first Brillouin zone

The reciprocal lattice plays a fundamental role in the study of periodic structures. Reciprocal space, often termed k-space, is widely used in the analysis of X-ray diffraction, phonon dispersion, and electronic bands; the latter two are used within this thesis.

The reciprocal lattice vectors are defined as:

$$\begin{aligned}\mathbf{b}_1 &= 2\pi \frac{\mathbf{a}_2 \times \mathbf{a}_3}{\mathbf{a}_1 \cdot (\mathbf{a}_2 \times \mathbf{a}_3)}, \\ \mathbf{b}_2 &= 2\pi \frac{\mathbf{a}_3 \times \mathbf{a}_1}{\mathbf{a}_1 \cdot (\mathbf{a}_2 \times \mathbf{a}_3)}, \\ \mathbf{b}_3 &= 2\pi \frac{\mathbf{a}_1 \times \mathbf{a}_2}{\mathbf{a}_1 \cdot (\mathbf{a}_2 \times \mathbf{a}_3)}.\end{aligned}\tag{2.3}$$

In the case of a cubic system, where all real space lattice vectors are orthogonal and of equal length, the reciprocal lattice vectors can be seen to align parallel to the real space lattice vectors from equation (2.1). A set of reciprocal lattice points can be defined as:

$$\mathbf{K} = n_1 \mathbf{b}_1 + n_2 \mathbf{b}_2 + n_3 \mathbf{b}_3\tag{2.4}$$

which relate to plane waves with the periodicity of the real space Bravais lattice such that:

$$e^{\pm i \mathbf{K} \cdot \mathbf{r}} = \cos(\mathbf{K} \cdot \mathbf{r}') \pm i \sin(\mathbf{K} \cdot \mathbf{r}')\tag{2.5}$$

where \mathbf{r}' is a vector in real space. Using equation 2.2 gives:

$$e^{\pm i \mathbf{K} \cdot \mathbf{r}'} = e^{\pm i \mathbf{K} \cdot (\mathbf{r} + \mathbf{R})} = e^{\pm i \mathbf{K} \cdot \mathbf{R}} e^{\pm i \mathbf{K} \cdot \mathbf{r}} = e^{\pm i \mathbf{K} \cdot \mathbf{r}}\tag{2.6}$$

as

$$e^{i \mathbf{K} \cdot \mathbf{R}} = 1\tag{2.7}$$

i.e. at two points a distance \mathbf{R} apart the amplitude of the wave is the same.

Just as real space can be represented by a unit cell, so can reciprocal space. The most commonly used cell in reciprocal space is the first Brillouin zone. This cell is formed by joining the bisectors of all the nearest reciprocal lattice sites. Just as any real space vector \mathbf{r}' can be broken down as in equation 2.2 so that \mathbf{r} determines the position in a unit cell, \mathbf{k}' , an arbitrary vector in reciprocal space, can be decomposed such that:

$$\mathbf{k}' = \mathbf{K} + \mathbf{k}\tag{2.8}$$

The significance of the Brillouin zone is that it contains all the unique wave vectors \mathbf{k} required to model interactions outside of the real space unit cell. At a real space lattice

site \mathbf{R} and using equation 2.7:

$$e^{i\mathbf{k}'\cdot\mathbf{R}} = e^{i(\mathbf{k}+\mathbf{K})\cdot\mathbf{R}} = e^{i\mathbf{K}\cdot\mathbf{R}}e^{i\mathbf{k}\cdot\mathbf{R}} = e^{i\mathbf{k}\cdot\mathbf{R}} \quad (2.9)$$

Thus, a wave vector not in the Brillouin zone can be translated into it by the addition or subtraction of some reciprocal lattice vector \mathbf{K} .

The usefulness of these wave vectors, or k-points as they are often called, within the Brillouin zone can be seen in the modelling of periodic systems. Take, for example, the vibration of atoms, and for simplicity consider a one-dimensional case, where each unit cell contains just one atom (Figure 2.1 (a)). Note that as an atom within the unit cell moves, so do all its images, with the same displacement. As the unit cell contains only one atom, each atom vibrates in phase. To model the system where each adjacent atom moves in the opposite direction (anti-phase) a cell containing two atoms would be required (Figure 2.1 (b)). An alternative way to model this is to use the one atom cell but apply a plane wave across the system with a wavelength equal to the length of two unit cells, i.e. a wave vector $\frac{1}{2}\mathbf{K}$. Figure 2.1 (c) shows how the application of this wave would affect the vibrations. From this it can be seen that the use of k-points allow the modelling of lattice interactions that would have otherwise required a much larger periodic cell.

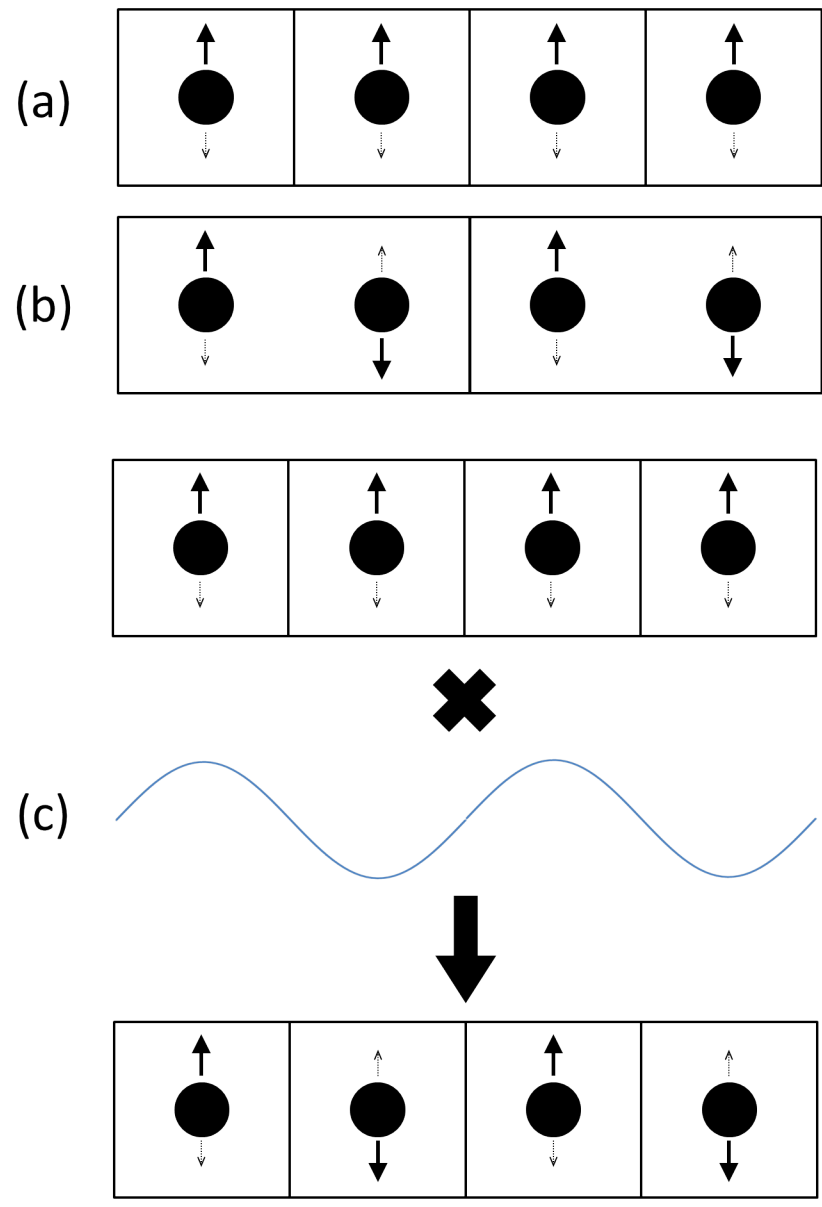


Figure 2.1: Atom vibrations in one dimension. Each unit cell contains one atom

2.3 Atomistic Calculations

2.3.1 Introduction

The work of this thesis is heavily based on the atomic structure of perovskite materials. Atomistic or force field based techniques are an efficient approach to determining the atomic structure of materials. Atomistic models typically simulate a system based upon atomic positions, however, they can also be used to model based upon molecular positions. Generally, atoms are treated as point like particles with a variety of interatomic potentials used to model the interactions between each particle. As these techniques do not model at the electronic level they are unable to calculate many of the electronic properties associated with a material. Force field methods have, however, been shown to reproduce atomic structure accurately [32–36]. The speed of atomistic methods also makes them ideal for use in global structural optimisation techniques. All atomistic simulations in this thesis were performed within the General Utility Lattice Package (GULP) [37, 38].

2.3.2 Calculating the Energy

As this thesis concentrates on the structure determination of perovskites, the energy of a system is a highly important property. The stability of a materials structure is determined by its energy, with a lower energy indicating greater stability. In general the energy of a system is calculated from a reference point and so stability is measured as a change in energy. The change in energy of a system is often decomposed into an expansion in terms of interactions between different subsets of the total number of atoms, N [38]:

$$E = \sum_{i=1}^N E_i + \frac{1}{2!} \sum_{i=1}^N \sum_{j=1}^N E_{ij} + \frac{1}{3!} \sum_{i=1}^N \sum_{j=1}^N \sum_{k=1}^N E_{ijk} + \dots \quad (2.10)$$

where the first term E_i represents the change in self energy of the atoms, the second term E_{ij} two-body interactions, the third term E_{ijk} three-body etc. For the atomistic methods used, the self energies of atoms are the result of atomic polarisation due to external potential fields. The two-body terms are due to pairwise interactions between atoms such as the Coulomb interaction, and are dependant upon the distance between the particles. Three-body terms are typically based on bond angles where a penalty, or increase in energy, is due to the size of the deviation from ideal bond angles. For the systems modelled in this thesis the energy contributions from each term generally get smaller the higher the order and so only terms up to two-body have been considered.

Pair Potentials

The Coulomb interaction is a two-body potential that models the electrostatic interaction between two electrically charged particles and is described by Coulombs law:

$$E_{ij}^{Coulomb} = \frac{q_i q_j}{4\pi\epsilon_0 r_{ij}} \quad (2.11)$$

where q is the charge on the ion, r_{ij} is the distance between ions i and j , and the constant ϵ_0 is the permittivity of free space. The Coulomb potential is a long range interaction decaying at a slow rate of $\frac{1}{r}$. The Coulomb energy is generally the most dominant contribution to the total internal energy of the system.

Two other two-body potentials types were used to model the short range interactions. The first is the Lennard-Jones potential [39]:

$$E_{ij}^{LJ} = \frac{B}{r_{ij}^{12}} - \frac{C}{r_{ij}^6} \quad (2.12)$$

The second term is the attractive dispersion force (van der Waals); a result of the interaction between fluctuating dipoles on the two atoms. The first term represents the close range repulsion experienced by atoms due to the Pauli repulsion of overlapping electron orbitals. This term must increase in magnitude more rapidly than the second term with decreasing separation to ensure atoms do not approach too closely. B and C are parameters that are fit to reproduce experimental or ab initio calculated properties. Due to the form of the potential there will exist a distance, r_{ij} , between the atoms at which the energy will be a minimum, thus corresponding to the equilibrium bond distance. Above this value the gradient of the dispersive term will be greater and thus the atom will experience a net attraction. Below this distance the Pauli force is greater and the ions experience a net repulsion. The Lennard-Jones potentials have been shown to successfully model the interaction between neutral noble gases [39].

The second short range interatomic potential is the Buckingham model:

$$E_{ij}^{Buck} = Ae^{\left(\frac{-r_{ij}}{\rho}\right)} - \frac{C}{r_{ij}^6} \quad (2.13)$$

The second term is the same dispersive term used in the Lennard-Jones potential (2.12). The Buckingham potential differs in how it models the Pauli repulsion. Instead of the $\frac{1}{r^{12}}$ decay used in the Lennard-Jones potential, an exponential decay is employed. This is used because the radial decay of electron orbitals is found to be exponential. Additionally, two fitting parameters, A and ρ , are used in the first term. This gives more control over the shape of the potential curves. As $r \rightarrow 0$ the exponential term converges to a constant where as the r^{-6} term diverges. This results in the Buckingham potential becoming increasingly attractive which is unrealistic (we are not modelling gravity!). One method for overcoming this is to additionally include the r^{-12} term.

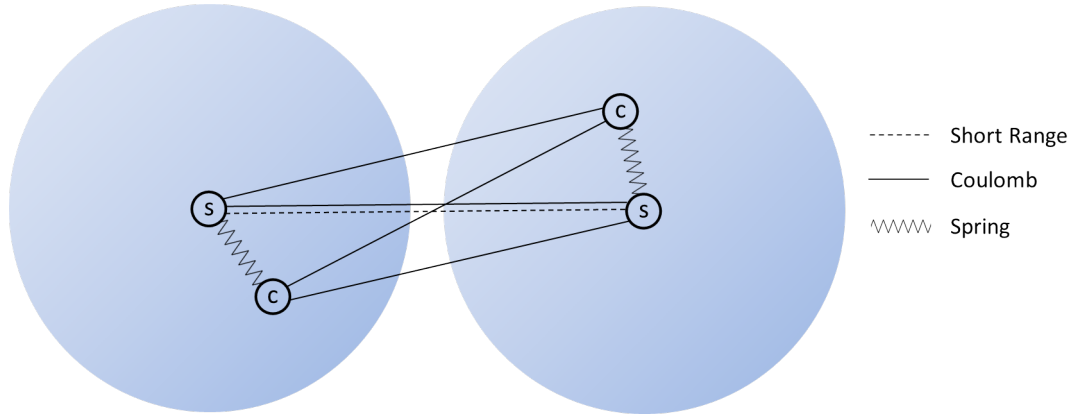


Figure 2.2: The interactions experienced by each particle in the Shell Model. The circles labelled “s” represents a shell and the circles labelled “c” are cores. The core and shell of an individual ion are coupled solely by a spring. Both the core and shell experience Coulomb potentials from both cores and shells of other ions. Only the shell of an ion experiences the short range potentials.

Both the Lennard-Jones (2.12) and Buckingham (2.13) potentials are short range, with the energy of interaction tending to zero rapidly with increasing r . Thus, computational costs can be reduced by applying appropriate radial cut-offs to these potentials without having a significant impact upon the accuracy of the calculation.

Shell Model

In this thesis the incipient ferroelectric material KTaO_3 is modelled. The polarisability of this material is likely to play a significant role in the structure, so the Shell Model was employed [40]. This model separates an individual ion into two point charges labelled core and shell which are linked by a spring. The point charge of the core represents the nucleus and the tightly bound inner electrons. The point charge of the shell represents the centre of the more loosely bound outer electrons of the ion. The sum of the core and shell charges is simply the total charge of the ion. The core and shell of the same ion are electrostatically screened from each other so they do not feel a Coulomb force between each other. Instead, the two components are only coupled to each other by the spring which is generally harmonic although higher order terms may be included. Note that the charges of the core and shell of an ion interact electrostatically with both the core and shell of other ions.

As the shell represents the valence or outer electrons, the short range potentials, which model the Pauli repulsion and van der Waals (dipoles) interaction, are typically only applied to the shells. Figure 2.2 highlights the interactions between two different ions with cores and shells. The energy due to the polarisation of the ion (separation of

core and shell) is simply the energy stored in a spring and is given as:

$$E_{cs}^{spring} = \frac{1}{2!}k_2x_{cs} + \frac{1}{4!}k_4x_{cs} \quad (2.14)$$

where x_{cs} is the core-shell separation on an ion and k_2 and k_4 are spring constants for a given species. Typically, the high frequency dielectric constant, ϵ_∞ , is used for fitting the spring constant, as this property is related to the electronic relaxation time.

2.3.3 Periodic calculations

Perovskites in their bulk phase contain a large number of atoms ($\sim 10^{28} \text{ m}^{-3}$). It is impractical to model a system of this size. Fortunately, the perovskite is an ordered material and so can be modelled as infinitely repeating periodic units as discussed in section 2.2. The energy of an infinite lattice is infinite. Instead, it is more practical to calculate the energy for a single unit cell

The lattice energy of a unit cell is determined as the energy of all interactions within the cell plus half the energy of the interactions between the cell and the rest of the bulk:

$$E^{cell} = E_{ij} + \frac{1}{2}E_{ik} \quad (2.15)$$

where i and j go over all atoms in the unit cell and k goes over all atoms outside the unit cell. The short range potentials are given radial cut-offs and so only ions within the cut-off distance of the unit cell need be considered. The Coulomb potential (2.11) on the other hand, while having a simple form, is much more difficult to calculate in periodic materials. The reason for this is that while the Coulomb potential decays as $\frac{1}{r}$, the number of interacting ions increases with the surface area of the sphere surrounding the ion which is $4\pi r^2$. This means the energy contributions do not diminish with increasing radial cut-off. As a result the energy of the system depends upon the cut-off distance chosen. In this thesis the Ewald Summation [41] technique has been employed to handle this problem.

2.3.4 Fitting

For this thesis new interatomic potentials were developed to model KTaO_3 . Creating potentials that accurately model the behaviour of a system is done by fitting the potential parameters to observables. The observables are typically taken from ab initio calculations or experimental data. The aim is to minimise the Sum of Squares (SS):

$$SS = \sum_{i=1} w_i (f_i^{calc} - f_i^{exp})^2, \quad (2.16)$$

where f^{calc} and f^{exp} are the calculated and observable data, respectively, and w is the weighting factor given to each observable. The sum of squares is an indication of

how closely the potential parameters reproduce the observable values they are being fit against.

Two different techniques were used to perform the fit. The first method follows a typical fitting procedure where the potential parameters are optimised such that the sum of squares relating to the observables is minimized. The second method is the so called relaxed fit. This method optimises the potential parameters such that the sum of squares relating to the observables is minimized for the relaxed geometry. I.e. the potential parameters are modified, the structure is relaxed, and then the sum of squares is calculated. The process is repeated until the sum of squares is minimized. Due to the geometry relaxations performed, the second method is computationally more demanding than the first.

Typically, the first method is used in the initial stages of fitting to obtain a rough set of parameters. These parameters are then refined using the computationally more intensive relaxed fit method. It is often helpful to start with initial parameters that give a reasonable representation of the system. These parameters might come from an existing set in the literature for the material of interest, an existing set for a similar compound, or even just a sensible estimate.

2.4 Electronic Structure Calculations

In this thesis the electronic properties of the perovskites are of great interest. Techniques based at the atomic level are unable to calculate many of these properties and so electronic structure methods must be used. Another advantage of electronic structure methods is that the potentials are generally more transferable. This makes them more reliable than atomistic based approaches when modelling systems that can not be benchmarked against experiment, e.g. small atomic clusters. The drawback of using electronic structure methods is that they are computationally intensive, even when heavily laden with approximations, and are thus limited to smaller systems or smaller data sets.

Electronic structure codes typically run at varying levels of theory, this thesis utilises standard density functional theory (DFT) methods based upon the Kohn-Sham equations described in reference [42]. One of the pitfalls with DFT is that functionals for exchange (quantum requirement of anti-symmetric wave function) and correlation (electron-electron interaction) are unknown. A popular approach to this problem is the generalised gradient approximation (GGA) which uses the density and density gradient to determine the exchange-correlation energy. The GGA functionals used in this thesis are the PBE and PBEsol functionals [43, 44].

The molecular orbitals ψ used within the electronic structure methods are formed

from linear combinations of basis orbitals ϕ :

$$\psi_i = \sum_j^n c_j \phi_j \quad (2.17)$$

where n is the number of orbitals and c_j are the coefficients corresponding to the given basis orbital. The set of basis orbitals used to determine the wave function are defined to be the basis set. The creation of the wave function from the orbitals is analogous to the way a three-dimensional vector is composed of an x, y, and z component. There are two approaches to constructing the basis set: one uses plane waves, the other atom centred orbitals.

Atom Centred Orbitals

Atom centred orbital basis sets use free-atom-like orbitals centred on each of the atoms in the system to create their basis set. Typically, these atomic orbitals themselves are created from a minimal basis set [45, 46].

Plane Wave Orbitals

In some codes where periodic boundary conditions are enforced, the basis set is instead composed of plane waves such that:

$$\psi_i = \sum_G^{G_{max}} c_G e^{iG \cdot r} \quad (2.18)$$

where G is a reciprocal lattice vector and r a point in real space. G_{max} is defined to be the highest energy plane wave that satisfies $\frac{\hbar^2}{2m} G_{max}^2 \leq E_{cut}$. E_{cut} effectively defines the resolution of the basis set, with a higher value giving a more precise basis set but at the cost of computational speed. Generally, E_{cut} is a variable definable within the software package being used. The way in which the plane waves model the electronic wave functions is analogous to the method in which the Fourier series can model a square wave.

Pseudo-Potentials

Close to the nuclei the wave function and gradient may be very large. These regions are difficult to model using plane waves as they require very large values of E_{cut} which would make the calculation very costly. To overcome this problem, many plane based codes utilise pseudo-potentials [47]. Electrons close to the core are tightly bound and not involved in molecular bonding. To this end, the effects of the core electrons and the nucleus can be subsumed into a pseudo-potential. This simplifies the problem so that the plane wave basis set only has to model the valence electrons, reducing computational

cost.

2.5 Local Optimisation

As this thesis deals with structure prediction it is important to find the lowest energy structure, and thus there is a need to perform local minimisations. As the calculated energy depends upon the atomic separation, such algorithms relax the ion positions in small steps which result in a gradual downhill step on the energy landscape until certain criteria are met. The algorithms employed use a combination of functions (energies), gradients (Forces), and second derivatives (Hessian matrix H), and are based on a sequence of one-dimensional line searches.

For example, in the method of steepest descents, the direction of the one-dimensional line search is always in the largest downhill direction. This is repeated until a local minimum is reached with respect to the atomic arrangement. The effect of this zigzagging to the minimum is that a larger distance than necessary is being traversed. A more efficient modification of this method is the conjugate gradients algorithm. This method uses information from the previous step to determine a more optimal route to the minimum.

When determining the direction of the one-dimensional line search the above methods only take into consideration the energy and gradients. For small systems and systems close to the harmonic region algorithms involving the Hessian matrix are more efficient. A quasi-Newtonian method using a BFGS update of an inverse Hessian [48] was employed in this thesis.

On occasion, the stationary point found by one of the optimisation techniques may not be a minimum. For these points, the eigenvectors are used to determine if there are any imaginary modes, and then downhill displacements are made along such directions. In this thesis the RFO [49] method was used in such circumstances. Consequently, this method can be used to locate transition states.

As each method has its advantages and disadvantages, it can be beneficial to switch between optimisation methods when given criteria are reached.

2.6 Global Optimisation

This thesis is concerned with prediction of surface and cluster structures of perovskite materials, i.e. the lowest structure in existence is sought after. As the structure in these phases is currently unknown, or up for debate (no experimentally defined structures), global optimisation techniques must be employed to test a range of possible configurations with the aim of determining the lowest energy structure, the global minimum (GM). Unlike local minimisations, the search for a global minimum may require passing over potential energy barriers, so as to allow the full search space to be covered. As the search space can be very large, success is not guaranteed; there can be a degree of

uncertainty in results. Below are the techniques used within this thesis.

Deterministic Quenching

This method was used for both the cluster and surface searches. Initial structures are created with the atoms in random positions, which are then relaxed using local minimisation techniques. This process is repeated many times in order to fully sample the search space. For large systems the number of possible atomic configurations is going to be extensive, and so the likelihood of finding the global minimum is going to be small. To narrow down the search, book keeping (keeping a record of what has already been tested) might be introduced to prevent duplicate searches. Additionally, constraints based on scientific knowledge can be enforced to exclude arrangements that are known to be undesirable. For example, a restriction on the minimum interatomic separation.

Genetic Algorithm (GA)

Genetic algorithms was used in the structure prediction of clusters. This method

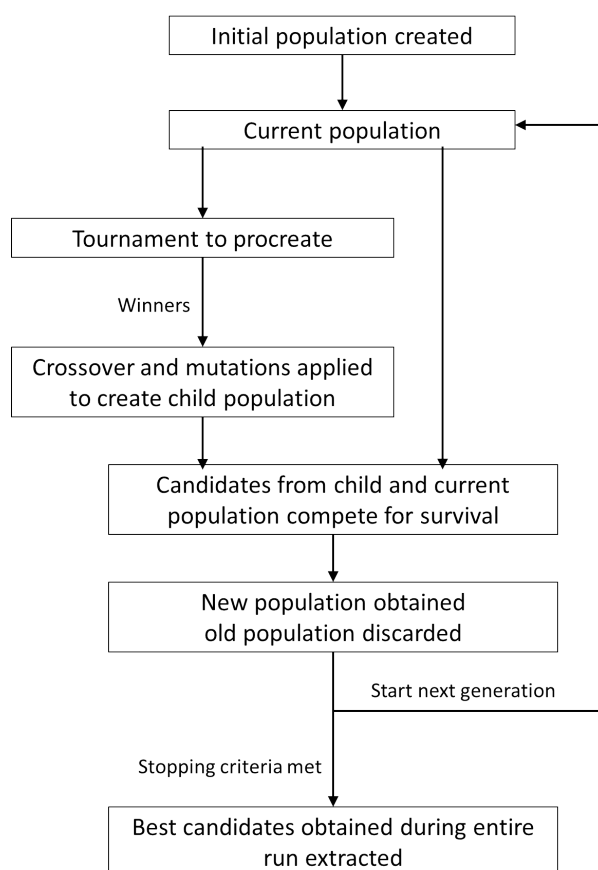


Figure 2.3: Flow chart of a typical GA routine

[50–52] mimics nature's process of evolution. The competitiveness of a candidate structure is determined by its energy (lower energy = better).

Figure 2.3 shows a flow diagram of the steps carried out for a generic GA routine. The GA begins by generating a set of random candidates to become the initial population. Depending on the type of GA employed, the measured energy is either unrelaxed (Darwinian), or relaxed (Lamarckian). The population then undergo a tournament for the right to procreate. A population of child candidate structures are created via either crossover or mutation of the tournament winners. The candidates of the child and current population then compete in a tournament for survival. The winners become the new population from which the next generation begins. This process is repeated until a pre-set number of generations have been completed.

Basin Hopping

The basin hopping technique [53, 54] was also used for cluster generation. This method is essentially a random walk along an energy landscape from one local minimum to the next. The process is initialised by creating a random structure which is relaxed and the energy recorded. The atomic positions of the candidate structure are then either fractionally altered or swapped, and then relaxed again. If the new candidate has a lower energy than its predecessor then it becomes the current structure. Otherwise the predecessor is kept. The process of modifying and relaxing candidates is repeated until a predetermined number of structures have been tested.

2.7 Defects

The formation of defects play a vital role in the properties of a material. Defect engineering, the intentional use of defects, is an important method in which to tailor the properties of a material [55]. The significant effects defects can have on a materials property, combined with the large array of possible defects in just one system, make the computational modelling of defects an attractive prospect not only for the sake of understanding defect properties, but also in the prediction of new materials.

A defect is an imperfection or disorder in an system. In a crystal this could simply be the displacement of an atom off a lattice site, and thus the breaking or reducing of the symmetry of the system. Defects can also change the stoichiometry, e.g. vacancies, add atoms, or the addition of foreign species (impurities). Breaks in the order of a system occurring at a particular lattice site or point in space are usually termed point defects. Point defects may cluster to reduce the energy of the system, producing larger systems of defects such as Frenkel and Schottky, line and planar defects.

The effect a defect has on the energy of a system can be calculated as a difference:

$$\Delta E = E^D - E^{Ideal} \quad (2.19)$$

where E^D is the energy of the system that includes the defect and E^{Ideal} is the energy of the ideal system (no defect). In the computational modelling of defects there are two commonly used approaches. The first is the cluster approach, which is well suited to modelling infinitely dilute defects. Of these methods the Mott-Littleton approach [56] is one of the most popular. The second method is the super cell approach, which is well suited to modelling systems with a sizeable defect concentration. Details of both methods are now discussed.

The Mott-Littleton Method

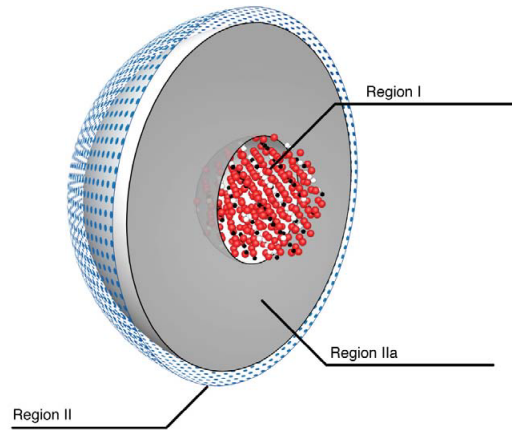


Figure 2.4: The two regions as used in the Mott-Littleton method for defects

The Mott-Littleton approach uses a multi region strategy in which a defect is centred within an inner spherical region (region 1) that is surrounded by point charges extending to infinity (region 2); see Figure 2.4. The atoms in the inner region, close to the defect, are allowed to relax explicitly with respect to their cartesian coordinates. Atoms in the outer region are expected to interact weakly with the defect. For this reason they are instead displaced from their normal lattice position by an amount proportional to the net force experienced. To save on computational effort the outer region is often separated into two slightly different regions. In the outer of these two regions only electrostatic interactions are considered. To ensure the approximations of this method are valid the initial defect free system must be geometry relaxed, and the size of the regions for the defected system must be converged with respect to defect energy.

2.7.1 The Super Cell Method

The defect is modelled in a super cell. The concentration of defects in the system can be controlled by the size of the cell. These calculations are performed in the same manner as any other periodic calculation. For codes in which cluster methods such as the Mott-Littleton approach are unavailable the super cell method must be used to

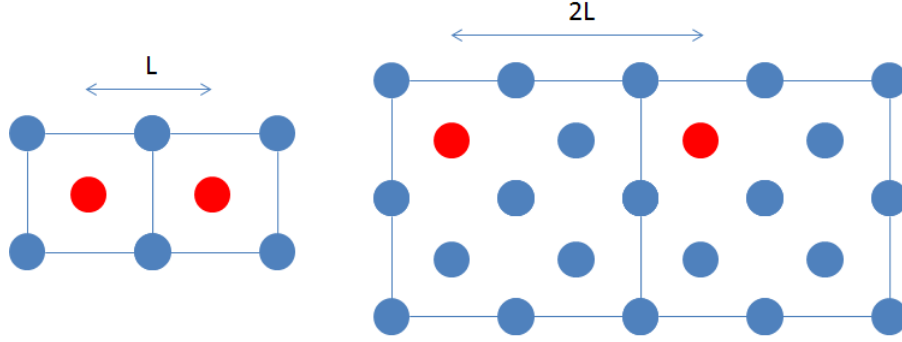


Figure 2.5: A 2-D representation of a defect in a super cell. The image on the left is a simple 1x1 cell, the image on the right is a 2x2. The size of the super cell controls the concentration of the defects and the defect-defect interaction

model infinitely dilute defects. To converge the energy of an isolated defect the distance between the defect and its images is increased by increasing the size of the super cell. Charge neutral defects, e.g. a Ca^{2+} impurity replacing a Mg^{2+} in MgO are relatively quick to converge in comparison to charged defects. This is due to the long range of the electrostatic interaction between the charged images. To improve the convergence of an isolated charged defect in a cubic supercell the following term can be added [57]:

$$\frac{\alpha Q^2}{2\epsilon_0 L} \quad (2.20)$$

the terms α , Q , ϵ_0 , and L are the Madelung constant, the defect charge, the static dielectric constant, and the length of the supercell respectively. This technique can be generalised to non-cubic systems.

2.7.2 Defect formation energy

Equation 2.19 gives the energetic effect a defect has on a system, however, this value does not determine how favourable the formation of the defect is. To ascertain whether a defect is likely to form the formation energy should be computed.

Considering a perovskite system ABO_3 , with arbitrary metals A^{2+} and B^{4+} , the equation for the formation energies of neutral A, B, and O vacancies are [58, 59]:

$$E_{\text{Defect}} = E_{\text{ABO}_3}^D - E_{\text{ABO}_3} + N_A \mu_A + N_B \mu_B + N_O \mu_O \quad (2.21)$$

where $E_{\text{ABO}_3}^D$ is the energy of the system including the defect, E_{ABO_3} the energy of the perfect system, μ_i the chemical potential of the corresponding element, and N_i the number of vacancies of the relevant species. The value for the chemical potentials depends upon the environment, with a higher concentration of a particular species resulting in a

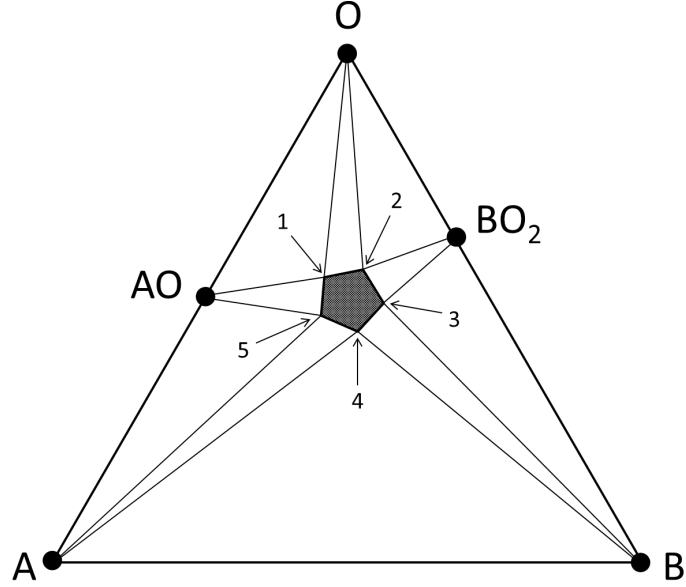


Figure 2.6: Ternary phase diagram for hypothetical material ABO_3 .

larger value. The chemical potentials are constrained to satisfy the condition:

$$\mu_A + \mu_B + 3\mu_O = \mu_{ABO_3} \quad (2.22)$$

Additionally, the chemical potential of each element must not be larger than the potential in its pure phase, i.e.:

$$\begin{aligned} \mu_A &\leq \mu_{A(s)} \\ \mu_B &\leq \mu_{B(s)} \\ \mu_O &\leq \mu_{O(g)} \end{aligned} \quad (2.23)$$

otherwise the precipitation of each of these pure phases will be favourable. Assuming that the binary compounds AO and BO_2 are stable, the additional constraints:

$$\begin{aligned} \mu_A + \mu_O &\leq \mu_{AO} \\ \mu_B + 2\mu_O &\leq \mu_{BO_2} \end{aligned} \quad (2.24)$$

must also be met to prevent the precipitation of these binary compounds. The result of these conditions on the chemical potentials are more easily viewed as a phase diagram as depicted in Figure 2.6. The shaded area represents the region in which the chemical potential conditions are satisfied. The perimeter of the area corresponds to chemical potentials in which the system is in thermodynamic equilibrium with reservoirs of ABO_3 and another of the materials. The vertices correspond to regions in which reservoirs of ABO_3 and two other materials are in thermodynamic equilibrium. Take for example

the point labelled 1 in Figure 2.6. At this point reservoirs of ABO_3 , $\text{O}_2(\text{g})$ and $\text{AO}(\text{s})$ are in equilibrium and the following conditions are satisfied:

$$\begin{aligned}\mu_A + \mu_B + 3\mu_O &= \mu_{\text{ABO}_3} \\ \mu_A + \mu_O &= \mu_{\text{AO}} \\ \mu_O &= \mu_{\text{O}(\text{g})}\end{aligned}\tag{2.25}$$

This can be rearranged to give:

$$\begin{aligned}\mu_O &= \mu_{\text{O}(\text{g})} \\ \mu_A &= \mu_{\text{AO}} - \mu_{\text{O}(\text{g})} \\ \mu_B &= \mu_{\text{ABO}_3} - 2\mu_{\text{O}(\text{g})} - \mu_{\text{AO}}\end{aligned}\tag{2.26}$$

Each of the five points in Figure 2.6 produce a set of chemical potential equations similar to equation (2.26). It is at these vertices in the phase diagram that the defect energies are typically calculated. Thus, for each type of vacancy V_A , V_B , and V_O , in the example ABO_3 system there would be five different defect formation energies depending on the environment. The values used for the chemical potentials μ_{ABO_3} , μ_{AO} , μ_{AO_2} , $\mu_{\text{A}(\text{s})}$, $\mu_{\text{B}(\text{s})}$, and $\mu_{\text{O}(\text{g})}$ are typically the final geometry relaxed energies of each of the systems. Sometimes it is preferable to set the chemical potential of each of the elements in their pure phase to be zero:

$$\begin{aligned}\mu_A &\rightarrow \mu_A - \mu_{\text{A}(\text{s})} \\ \mu_B &\rightarrow \mu_B - \mu_{\text{B}(\text{s})} \\ \mu_O &\rightarrow \mu_O - \mu_{\text{O}(\text{g})}\end{aligned}\tag{2.27}$$

This would then make the values for μ_{ABO_3} , μ_{AO} , and μ_{BO_2} equal to their formation energies, a much more transferable value. For equation (2.21) to consider add atoms or impurities instead of vacancies, the sign of N_i would change to be negative. For the consideration of charged defects, equation (2.21) must be further modified. This is not discussed here, but details can be found in references [60, 61].

The defect energy describe by equation (2.21), while easily calculated within DFT codes, cannot generally be computed in atomistic based simulations in which stoichiometry is not conserved. The potential parameters used to model the atomic interactions of a system are usually non-transferable. For example, potentials used to model an ABO_3 system may not be suitable to model component systems. Thus, the defect energy in atomistic calculations is typically used to analyse stoichiometric defects, or the relative stability of a particular type of defect at different positions.

2.8 Surface Calculations

In this thesis the structural reconstructions of the polar (001) KTaO_3 surface are under investigation. The surface of materials are of great interest as this is the region which interacts with the rest of the world. The surface plays an important role in the fields of catalysis and crystal growth [62]. As the surface represents a break in the periodicity of the material, it can also lead to interesting intrinsic properties such as electronic band bending and surface polarisation [29].

Surface properties are typically hard to characterise experimentally due to interference from the bulk. This makes computational modelling very important as it aids in understanding the surface mechanisms that are giving rise to a particular property.

From a computational perspective, a surface is created by breaking the periodicity of the bulk system in one direction, by removing all atoms from one side of a desired surface plane. The cleaved surface will generally be in an excited state and must undergo a structural relaxation. Typically, during the relaxation of the surface, the inter-planar distances between atomic layers in the direction perpendicular to the surface changes. The periodicity in the two directions normal to the surface often remains unaffected. When simple relaxations do not sufficiently stabilise a surface, a reconstruction is required. This leads to either: the atomic arrangement at the surface differing from the bulk; or a mismatch in the bulk and surface layer stoichiometry. In some cases the reconstruction is not limited to only the surface layer but may include some of the layers beneath.

There are two common methods employed for the computational modelling of surfaces. The first uses a single slab periodic in two dimensions parallel to the surface and surrounded by vacuum. For the work in thesis it was desirable to model a one sided surface. In this case the slab is split into two regions: an upper region containing the surface of interest, where the atoms are relaxed; and a lower region where the atoms are held fixed to simulate a bulk-like environment. The number of atomic layers in the fixed region should be sufficiently large to ensure that the fixed surface does not have an effect on the calculation. Similarly, the number of atomic layers of the relaxed region must also be converged to ensure that the atoms near the interface between the two regions have conformed to their normal bulk arrangement. For a two sided surface calculation, both sides of the slab are allowed to relax. The slab in these calculations are generally symmetric with the same surface on both sides. Typically, there is no need to hold any region fixed, however, if the software being used allows the slab to translate then the central layer of the slab should be held fixed.

The second, alternative approach to modelling a surface is needed when the modelling software being used requires periodic boundary conditions in all directions. This situation arises when using plane wave based DFT packages. This alternative method of surface modelling uses periodically repeating slabs spaced between regions of vacuums.

As with the first approach both one and two sided surfaces can be modelled, with similar convergence requirements on the number of atomic layers to be relaxed. The main difference between this technique and the first is that the slab has periodically repeating images in the direction perpendicular to the surface. As a three dimensional unit cell is used a region of vacuum must be included between the slab and its periodic images. The width of the vacuum region must be sufficiently thick that the repeating slabs do not interact. The thickness of both the slab and vacuum is converged with respect to the surface energy.

Of the two methods discussed, the first, which uses an infinite vacuum, is regarded as the superior as there is no issue regarding slab image interaction. The first method is also faster as it has one less dimension within which to model interactions. GULP, an atomic simulation code, is capable of using either technique. VASP, a plane wave DFT code, requires periodic boundaries and thus can only make use of the periodically repeating slab technique.

2.8.1 Calculating the Surface Energy

The stability of a surface is determined by its surface energy. The surface energy is determined as:

$$E_{surface} = \frac{E_{slab} - nE_{bulk}}{A}, \quad (2.28)$$

where E_{slab} is the relaxed energy of the cleaved system, E_{bulk} is the energy of the bulk unit cell, n the number of equivalent bulk unit cells used in the unit cell for the slab, and A is the surface area exposed within of the unit cell used. In many cases the slab has two sides and thus the area includes both.

$E_{surface}$ can be decomposed into two components. The first is the cleavage energy. This is the energy required to create the surface by breaking the bonds along a plane of the bulk material and separating the two pieces. The second is the relaxation energy after cleaving. For a stable bulk phase, the cleaving energy is always greater than the relaxation energy, otherwise a negative surface energy would be obtained. A negative surface energy would indicate that the surface phase is more stable than the bulk suggesting that the spontaneous dissociation of the bulk should occur.

Equation (2.28) is easy to use when the system under investigation is stoichiometric and contains only one unique surface termination, i.e. a one sided slab or a symmetric two sided slab. The consideration of just one surface of a non-symmetric two sided slab can only be truly achieved in atomistic calculations as a determination of the cleavage energy is required. In electronic structure calculations the cleavage energy cannot be calculated exactly as an electronic relaxation on both surfaces must be carried out. The contribution of the relaxation energy from each surface cannot be separated. In atomistic calculations the electronic relaxation is not required. The methods of calculating the surface energy of either non-stoichiometric or one sided slabs are discussed below.

One Sided Surface (Atomistic)

In the atomistic code GULP a single surface can be modelled using a two region strategy [38]. This approach splits the slab into two sections labelled region 1 and region 2. Region 1 contains the surface of interest and only the atoms in this region are allowed to undergo geometry relaxation during the calculation. Region 1 should also be stoichiometric as the energy of this region will be compared to bulk. Region 2 represents the rest of the bulk material and so the atoms in this region are held fixed during calculations. The size of region 1 must be sufficient that there is minimal strain at the interface, and the size of both regions must be sufficient to converge the surface energy.

The energy of the slab can be decomposed into three parts:

$$E_{slab} = E_{11} + E_{12} + E_{22} \quad (2.29)$$

with E_{11} the interaction energy between all atoms in region 1, E_{22} the interaction energy between all atoms in region 2, and E_{12} the energy of the atoms in region 1 interacting with the atoms in region 2. The energy of region 1 is what is required for the calculation of the surface energy and this is determined as:

$$E_{slab} = E_{11} + \frac{1}{2}E_{12} \quad (2.30)$$

which is similar to the way the bulk energy of a unit cell is calculated. The surface energy can then be calculated using equation (2.28), with E_{slab} the energy of region 1 and n the number of bulk units in region 1.

Non-Stoichiometric Surface (DFT)

As discussed earlier performing DFT calculations on a slab which is not symmetric presents the problem of separating the energy contributions from each surface. Even when the atoms of one side are held fixed there is still the issue of the electronic relaxations. One way to overcome this – in the cases where it is possible – is to sacrifice stoichiometry to produce a symmetric slab. In the case of (001) surfaces of cubic perovskites this is possible.

With the problem of different surfaces removed the issue of non-stoichiometry must be dealt with. One such solution used by Padilla and Vanderbilt [63] is to treat the surface as an initially stoichiometric slab which has been introduced to a layer of defects. Using the hypothetical ABO_3 perovskite this results in a modified version of equation (2.28) to produce:

$$E_{surface} = \frac{E_{slab} - nE_{bulk} + N_A\mu_A + N_B\mu_B + N_O\mu_O}{2A} \quad (2.31)$$

where the conditions on N_i and μ_i are the same as discussed in reference to equation

(2.21). The number of each species considered in the last four terms of the numerator of equation (2.31) must be the same as found in the slab. The factor of two in the denominator is due to there being two surfaces. It should also be noted that another method in which chemical potentials are not considered is proposed by Heifets et al. [64]. However, this method makes the approximation that the electronic relaxation energy of the two different (001) surface terminations (AO and BO₂) are equal.

2.9 Implementation

This section contains brief details on how to run the codes that are used within this body of work. All of the atomistic calculations were performed in General Utility Lattice Program (GULP). GULP requires only a single input file to run. In this file, keywords relating to the type of calculation are specified, for example, defect, phonon, or optimise. The structure of the unit cell is given if using periodic boundaries along with the atom positions in either fractional or cartesian coordinates. The charge of each of the species are specified, as well as the potential parameters and cut-offs for each short range interaction. Any input variables required for the calculation such as k-points, force convergence tolerance, etc. are also included. Finally, the desired output file types can be listed to accompany the standard GULP text output.

The Vienna Ab-initio Simulation Package (VASP) was used for bulk and surface calculations at the electronic level. VASP requires four input files to run: INCAR, POSCAR, KPOINTS, and POTCAR. The INCAR specifies the input parameters such as plane wave cut-off, force tolerances, functional type, optimisation technique etc. The POSCAR lists the unit cell parameters and atomic coordinates for each atom. The KPOINTS file specifies the k-points used. VASP can automatically calculate and weight the k-points given a $n \times n \times n$ grid. The POTCAR lists the potentials used, in the case of this thesis pseudo-potentials were used.

The Fritz Haber Institute ab initio molecular simulations package (FHI-aims) was used in cluster calculations at the electronic level. FHI-aims requires two input files geometry.in and control.in. The geometry.in file is equivalent to the VASP POSCAR file, specifying atomic coordinates and unit cell parameters if required. The control.in file contains similar information as the VASP INCAR, KPOINTS, and POTCAR files.

2.9.1 Knowledge Led Master Controller (KLMC)

To perform a global optimisation of the structure many different atomic configurations will need to be tested. This will require a large number (1,000+) of input files to be created, which will be extremely time consuming. To overcome this problem the in-house code, the Knowledge Led Master Controller (KLMC) [65, 66], was used. KLMC automates many of the labour intensive tasks associated with performing global optimisations. This includes: creating and modifying input files, renaming input and output

files, and extracting information from output files.

KLMC also contains various routines for performing the different global optimisations techniques. For surface calculations the “Solid Solutions” routine was utilised to predict the surface structure. This routine automates the swapping of ions between different predefined lattice sites. The specifics of how this routine was employed are given later in chapter 4. For cluster calculations the “Genetic Algorithms (GA)” and “Basin Hopping (BH)” routines were utilised to predict the atomic structure of nanoclusters. The principles of these methods have already been discussed in this chapter.

Chapter 3

Bulk

3.1 Introduction

In this chapter the structure and properties of the perovskite bulk phase for KTaO_3 , KMgF_3 , and KZnF_3 are reported. Calculations were performed at the atomistic level using interatomic potentials (IP) and at the electronic level using density functional theory (DFT). The calculated properties were compared to experimental data taken from the literature. The IP parameters for KTaO_3 were obtained by fitting to experimental observables at room temperature. The IP parameters for KMgF_3 and KZnF_3 were taken from the literature. Atomistic calculations, including the refinement of IP, were performed using the General Utility Lattice Package (GULP). The electronic structure calculations were performed using the Vienna Ab-initio Simulation Package (VASP) and the Fritz Haber Institute ab initio molecular simulations package (FHI-aims).

While the focus of this thesis is on the structure prediction of nano-clusters and surfaces it is necessary, for a number of reasons, to first model the bulk phase of each compound. When performing surface calculations a slab, periodic in two dimensions, is used. Firstly, the majority of the atoms in the slab will adopt the bulk-like structure, with only atoms on, or near, the surface showing any significant structural deviation from the bulk. Thus, to accurately model a surface, the set of potentials, whether atomistic or electronic, must model the bulk structure well to be reliable. Secondly, to perform a global optimisation, a large number of different structures will need to be tested. Due to the comparatively low computational cost of atomistic calculations compared with electronic structure calculations, it is sensible to use an IP models to siphon through the vast number of candidate structures, producing a “best” set.

Experimental structural determination techniques, such as X-ray and neutron scattering, work best on large periodic structures. For this reason, it is much easier to experimentally determine the structure of the bulk than it is for atomic nanoclusters. In a crystal sample, the majority of the atoms will reside within the bulk and not on the surface. Thus, for most structural measurement techniques, the properties associated

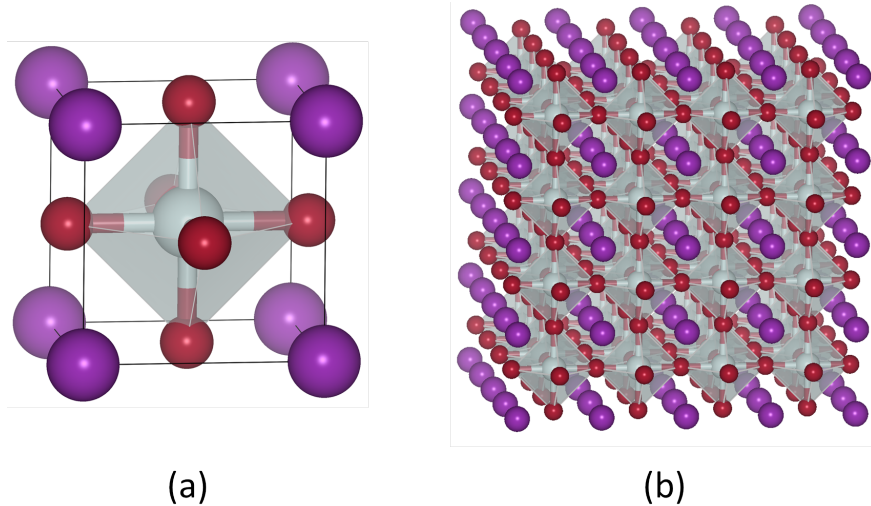


Figure 3.1: (a) ABZ_3 Cubic perovskite unit cell, where A are the purple cations on the corners, B the grey cations at the centre of the octahedra, and Z the red anions on the octahedra corners. (b) Periodic lattice of the ABZ_3 unit cell.

with the bulk will be much larger in amplitude than those associated with the surface. This makes determining surface structure more difficult and leads to the requirement of surface sensitive techniques.

To this end, the vast array of properties, in particular the lattice parameter, associated with the bulk make it the ideal base at which to fit interatomic potentials (IP) against.

3.1.1 $KTaO_3$

$KTaO_3$ adopts the ABZ_3 cubic perovskite structure at all temperatures. The atomic arrangement is shown in Figure 3.1. The structure consists of a regular corner sharing TaO_6 octahedra, with K sitting in the 12-coordinated holes created by the lattice of octahedra. The formal charges attributed to the ions in this material are +1, +5, and -2 for K, Ta, and O respectively, resulting in a closed shell system.

From X-ray diffraction studies, the lattice parameter of the material is determined to be 3.9885 Å by Vousden [67], 3.9883 Å by Zhurova et al [68], and 3.9884 Å by Samara and Morosin [69]. This results in a Ta – O bond length of 2.0 Å and a K – O bond length of 2.82 Å.

Numerous experimental and computational studies on the lattice dynamics have shown that the cubic phase is maintained even at low temperatures [70–77]. The studies also labelled $KTaO_3$ as an incipient or virtual ferroelectric (FE) due to it possessing a transverse optical (TO) FE-like phonon mode. This mode softens (decreases in energy) with decreasing temperature and in a normal FE would become unstable at a low temperature leading to a ferroelectric phase change.

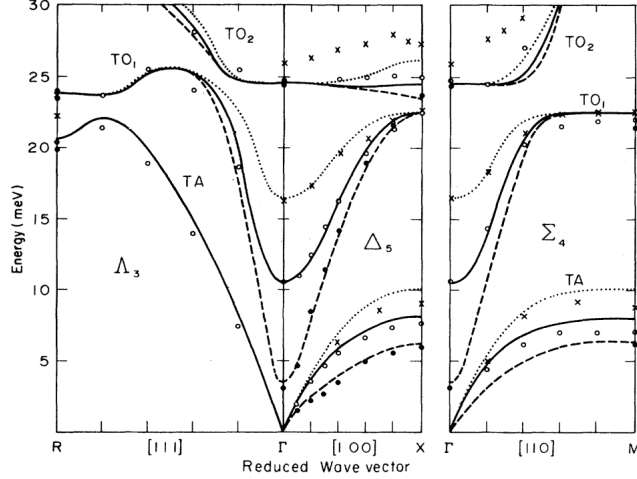


Figure 3.2: Phonon dispersion of low energy modes in KTaO_3 at a range of temperatures from inelastic neutron scattering taken from Ref. [71]. Dashed lines and solid circles are modes at 20 K, the solid lines and empty circles 296 K, and the dotted line and crosses 1220 K. TO_1 is the ferro-electric soft mode.

Figure 3.2 is taken from Ref. [71] and shows the phonon dispersion of KTaO_3 at difference temperatures obtained from inelastic neutron scattering. The dashed lines and solid circles are modes at 20 K, the solid lines and empty circles 296 K, and the dotted line and crosses 1220 K. TO_1 is the soft mode, and it can be seen that in changing the temperature from 1220 K to 20 K the mode has softened by 13 meV (100 cm^{-1}).

KTaO_3 is paraelectric at all temperatures, however, ferro-electricity can be induced by small modifications. While temperature seems to have the most significant effect on the soft mode, it has been shown that stress also has a non-negligible effect on the mode stability [69, 76, 78, 79] and can induce a ferro-electric phase transition. Defects are also seen as a method to promote the phase change. Investigations using Li dopants on the K sites and Nb on the Ta sites have confirmed the induced phase change in KTaO_3 even in very small concentrations [80–84].

The dielectric properties of KTaO_3 are also a source of great interest as they are found to be strongly coupled to the soft mode [77, 78, 85, 86]. Wemple et al. [77] show KTaO_3 to have a large static dielectric constant (ϵ_0) of 243 at room temperature. They also show that ϵ_0 is strongly affected by temperature (like the soft mode), with the constant becoming even larger at low temperatures (see Figure 3.3). They suggest this will have a large effect on transport properties.

In regards to its electronic structure, KTaO_3 possesses a wide indirect (0.5,0.5,0.5) (R) to (0,0,0) (Γ) band gap of $\sim 3.6 \text{ eV}$ [77, 87, 88]. The smallest direct band gap is determined to be $\sim 4.4 \text{ eV}$ and occurs at the Γ point [87, 88]. Many calculations have also been performed in order to ascertain the electronic structure of bulk KTaO_3 [74, 88–92]. Density functional theory appears to greatly underestimate the band gap; many

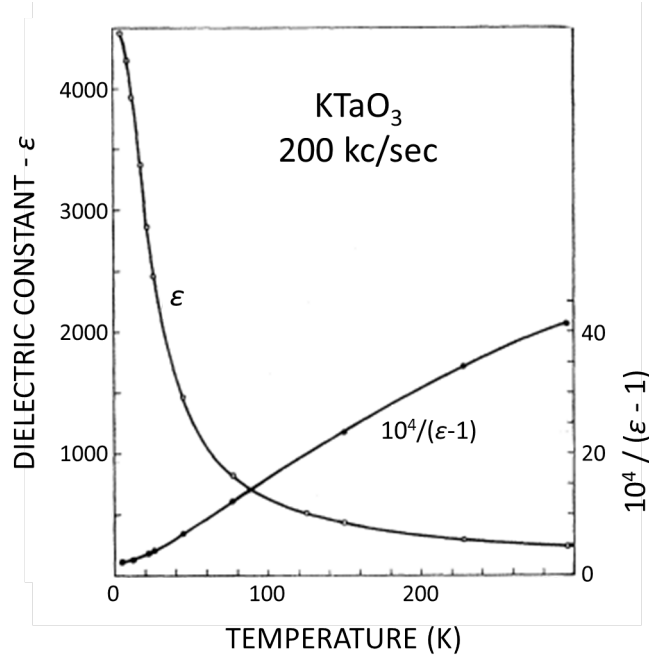


Figure 3.3: KTaO₃ dielectric constant as a function of temperature; adapted from Ref. [77].

GGA calculations report a value of ~ 2.1 eV, almost 1.5 eV below the experimental value (3.6 eV). The GGA calculations do, however, correctly predict an indirect band gap between Γ and R. The direct gap at Γ is also underestimated; most GGA calculations predict this to be ~ 2.7 eV. The hybrid HSE06 functional has fared better, producing a band gap of 3.4 eV. GW calculations have led to the best match with experiment, predicting a value of 3.57 eV.

The properties attributed to KTaO₃ have made it useful in a wide range of applications. These include: electric capacitors for DRAMs, microwave tunable devices, photocatalysts, luminescence capacitor, and fuel cells [93].

3.1.2 KMgF₃

KMgF₃ also adopts the ABZ₃ cubic perovskite structure at all temperatures. Unlike many perovskites in which the Z is usually oxygen and B a transition metal, KMgF₃ is composed of corner sharing MgF₆ octahedra, with fluorine at the corners and magnesium at the centre of the octahedra. Owing to its large band gap of 11.9 eV, KMgF₃ is a promising candidate in: the next generation lithographic devices that require vacuum ultraviolet (UV) transparent lenses [94–97], electro-optic [98, 99], and UV dosimetry [100–102] devices. The cubic structure of the material also removes the issue of birefringence.

KMgF₃ is similar in structure and properties to some of the compounds found in the Earth’s mantle. Due to the stability of the cubic phase over large temperature and

pressure ranges, this material is easier to model under the conditions experienced within the Earth’s mantle as structural phases changes will not need to be considered [103–107].

The lattice parameter for KMgF_3 has been determined to be 3.988 Å at room temperature from both X-ray and neutron diffraction [103, 108, 109]. Wood et al [103] found the cubic phase to be stable at all temperatures between 4 K and 1223 K with the lattice parameter falling to ~ 3.976 Å at 4 K. Computational studies performed using the LDA functional underestimate the lattice parameter (3.91 Å [110] and 3.96 Å [111]) while the GGA functional overestimates (4.03 Å [112] and 4.08 Å [111]). Investigations on the effect of pressure on the system show cubic KMgF_3 to be stable under high pressure [111, 112].

From experimental studies the band gap of the material is found to be ~ 11.9 eV [95, 113]. Computational investigations, however, predict an indirect ($\text{R} - \Gamma$) gap of ~ 7 eV, which significantly underestimates that measured in experiments [110–112]. All calculations agree that the top of the valence band, at the cubic high symmetry point R (0.5,0.5,0.5), is dominated by F 2p states, while the bottom of the conduction band, at the gamma point, is predominantly K 4s states. The lack of hybridisation between the different elements suggest the material is highly ionic. The computational studies also show an increase in band gap with increasing pressure (decreasing volume).

3.1.3 KZnF_3

The structure and behaviour of KZnF_3 is very similar to that already described for KMgF_3 . KZnF_3 also adopts the ABZ_3 cubic structure, with zinc on the B sites (at the centre of the octahedra) in place of magnesium. The ionic radii of zinc and magnesium are very similar, 0.88 Å and 0.86 Å, respectively [114]. The lattice constant for KZnF_3 is found to be 4.055 Å from X-ray diffraction [108, 115], which is 0.067 Å (1.6%) larger than that for KMgF_3 . As with KMgF_3 , calculations performed using GGA functionals typically over estimate this parameter (4.150 Å [116], 4.129 Å [117]), while LDA underestimates (3.981 Å [116], 3.973 Å [117]).

Most of the interest in KZnF_3 is driven by its luminescence properties, which are useful in the application of lasers [118–120]. From experimental studies an indirect band gap of 4.1 eV is observed [115]. As was seen for the other two perovskite compounds, both GGA ($\sim 3.64 - 3.68$ eV) and LDA (3.73 – 3.81 eV) studies underestimate the band gap [116, 117, 121] of KZnF_3 , but all studies concur on a $\text{R} - \Gamma$ indirect band gap. In contrast to the ionic nature of KMgF_3 , the KZnF_3 valence band is comprised of F 2p orbitals hybridised with Zn 3d orbitals, which suggest a degree of covalent bonding between zinc and fluorine. The valence band of KZnF_3 is akin to that of KTaO_3 , which consisted of mixed Ta 5d and O 2p states. The bottom of the conduction band is made up predominantly of Zn 4s and F 2p states, further up the conduction band K 3d contributions become more dominant, with a small mixture of Zn 4p, F 2s, and K 4s being present. The full occupation of the Zn 3d orbital ensures these states are not

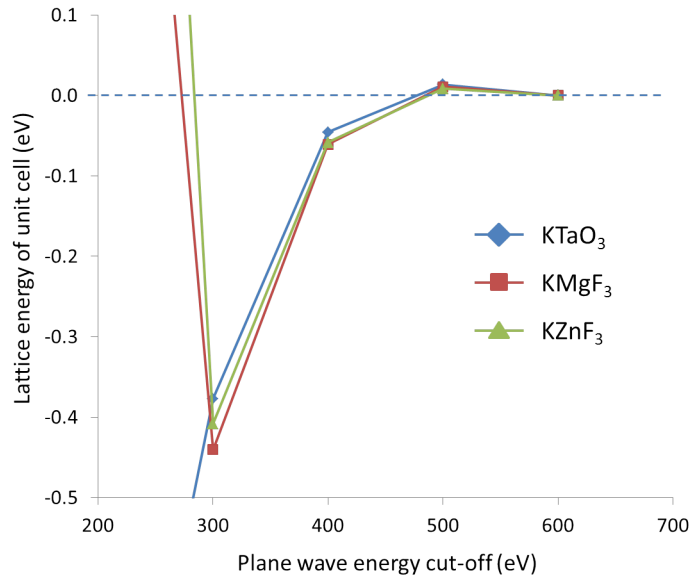


Figure 3.4: Lattice energy convergence of KTaO_3 , KMgF_3 , and KZnF_3 as a function of plane wave energy cut-off; calculated using VASP. The lattice energy shown is relative to the energy obtained using a 600 eV cut-off.

present in the conduction band.

3.2 Electronic Calculations

Electronic structure calculations for the bulk perovskite phase of KTaO_3 , KMgF_3 , and KZnF_3 were performed using two different codes: the Vienna Ab-initio Simulation Package (VASP) and the Fritz Haber Institute ab initio molecular simulations code (FHI-aims).

3.2.1 VASP Settings

VASP is a density functional theory (DFT) code that employs plane waves thereby making it ideal for modelling periodic systems. It is important that the lattice energy is converged with respect to the energy cut-off. The energy cut-off determines the highest frequency plane waves employed in the calculations. As the three perovskites have an experimental lattice parameter close to 4 Å, an initial bulk unit cell with a lattice parameter of 4 Å and a $6 \times 6 \times 6$ gamma centred k-point mesh were used to test the convergence. Calculations were performed using the PBEsol functional [44] and the PAW potentials [47] for the different species.

Figure 3.4 shows the lattice energy of the unit cell as a function of plane wave cut-off energy. Below 300 eV the trends in lattice energy of the different compounds differ. The energy of the fluoride based compounds is larger than their converged energy, while for the oxide based compound it is lower. From 300 eV upwards all three compounds

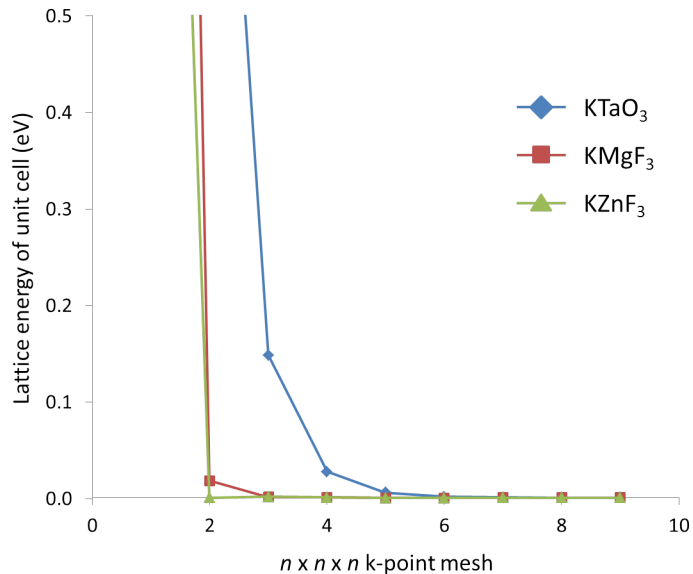


Figure 3.5: Lattice energy convergence of KTaO_3 , KMgF_3 , and KZnF_3 with respect to the number of $n \times n \times n$ k-points sampled; calculated using VASP. The lattice energies are set relative to the energy at $n = 9$.

follow very similar trends and at a cut-off of 500 eV a convergence of less than 0.02 eV (0.004 eV / atom) was achieved for the bulk lattice energy. Henceforth, all further VASP calculations for all three of the materials were performed using a cut-off energy of 500 eV.

It is also important that the lattice energy is converged with respect to the density of k-points. Figure 3.5 plots the lattice energy as a function of k-point density. From the plot, the convergence of the KTaO_3 lattice energy is slower than the convergence of the other two compounds. The initial $6 \times 6 \times 6$ k-point mesh is shown to be highly converged with denser grids resulting in an energy difference of less than 0.001 eV per atom for all three compounds. As 6 is divisible by both 2 and 3, the $6 \times 6 \times 6$ k-point grid is ideal for scaling to larger $2 \times 2 \times 2$ and $3 \times 3 \times 3$ super cells whilst maintaining the same k-point density.

Lastly, the lattice energy must also be converged with respect to the number of electronic bands used in the calculation. With the chosen PAW potentials used, potassium contributes 9 valence electrons to the system, tantalum 5, magnesium 8, zinc 12, oxygen 6, and fluorine 7. This results in a total of 32, 38 and 42 electrons per formula unit for KTaO_3 , KMgF_3 , and KZnF_3 , respectively. This equates to 16, 19, and 21 occupied bands (two electrons per band for collinear calculations). VASP requires at least one unoccupied band and it was found that with this minimum, the lattice energy was suitably converged to within 0.01 meV. It is noted that all three of the materials are wide gap insulators. Thus, for the ideal bulk units the unoccupied states are not going to have any significant impact on the ground state energy of the system. However, as

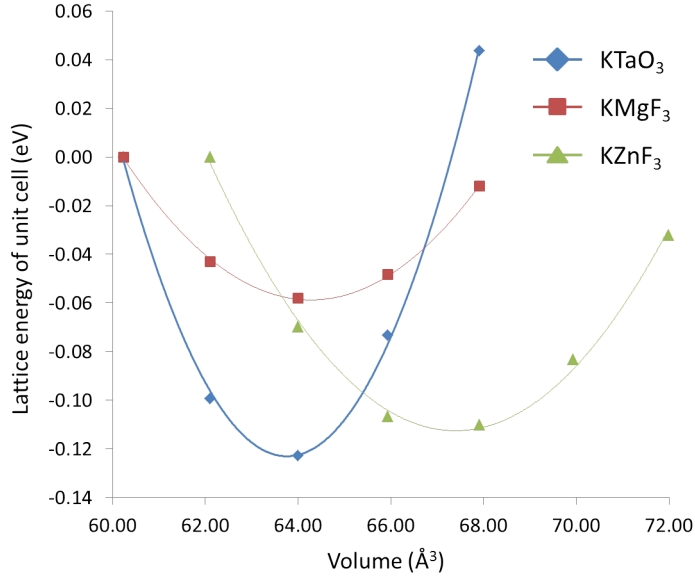


Figure 3.6: Lattice energy as a function of cell volume for KTaO_3 , KMgF_3 , and KMgF_3 ; calculated using VASP. The energy shown is relative to the energy at a volume of 60.24 \AA^3 .

imperfections are added into the system, i.e. from defects or surface cleaving, the unoccupied states may have an impact on the energy and so more than one empty band will be tested. Including more empty bands into the system also allows for more of the conduction band and higher lying states to be analysed in density of states and band structure plots. Thus, further calculations on the bulk are performed using 32 bands for all three perovskites.

To summarize, the settings used for the bulk DFT calculations were:

- PBEsol functional
- Plane wave energy cut-off of 500 eV
- $6 \times 6 \times 6$ gamma centred k-point mesh
- 32 electronic bands

Using these settings, the most stable bulk lattice parameter was determined for each compound. When DFT geometry relaxations were performed, the lattice parameter and shape (and hence volume) of the unit cell were held fixed. The lattice parameter was varied about 4.00 \AA in steps of 0.04 \AA for each calculation. The unit cell lattice energy as a function of its volume is shown in Figure 3.6. The lattice energy of the smallest unit cell tested is set to 0. For KTaO_3 and KMgF_3 this was 60.24 \AA^3 and for KZnF_3 it was 62.10 \AA^3 . Using the Birch-Murnaghan equation of state [122] the lattice parameter at which the energy was a minimum was calculated for each compound. For KTaO_3 , this lead to a lattice parameter of 3.992 \AA (volume of 63.638 \AA^3) resulting in a lattice energy

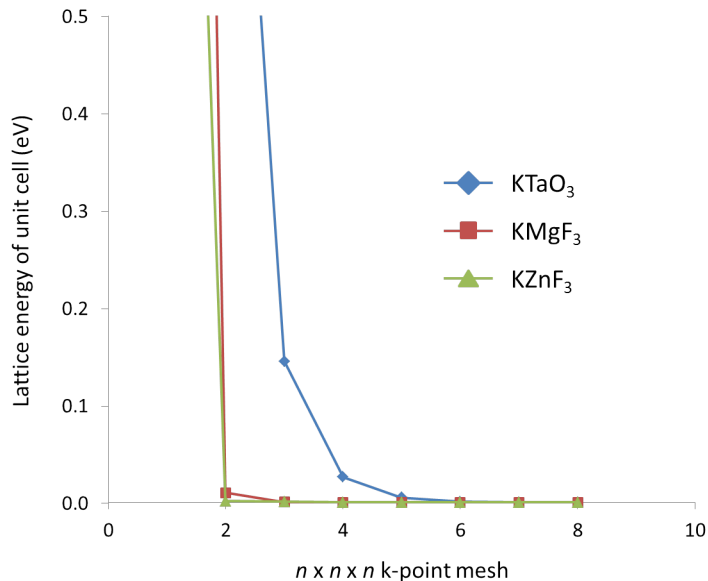


Figure 3.7: Lattice energy convergence of KTaO_3 , KMgF_3 , and KZnF_3 with respect to the number of $n \times n \times n$ k-points sampled; calculated using FHI-aims. The lattice energies are set relative to the energy at $n = 8$.

of -40.659 eV. For KMgF_3 , the lattice parameter was found to be 4.004 Å (volume of 64.186 Å³) which corresponds to a lattice energy of -23.429 eV. While for KZnF_3 , the lattice parameter was found to be 4.065 Å (volume of 67.159 Å³) which corresponds to a lattice energy of -19.547 eV.

3.2.2 FHI-aims Settings

The energy calculated by FHI-aims must also be converged with respect to a number of settings. FHI-aims is an all electron numeric atom-centred basis set code. The basis set is formed of atomic-like orbitals. Thus, the number of empty atomic orbitals included in the calculation in FHI-aims is analogous to the plane wave energy cut-off and number of empty bands. FHI-aims has a series of predefined basis sets labelled: “light”, “tight”, “really_tight” etc. Where the tighter basis sets include more empty orbitals. The FHI-aims calculations in this thesis were performed with the “light” basis set; the difference in relative energies for clusters was found to be less than 0.01 eV/atom between the light and tight basis sets.

Figure 3.7 shows the convergence of the lattice energy as a function of k-point density for KTaO_3 , KMgF_3 , and KZnF_3 using the FHI-aims code. An initial lattice parameter of 4 Å was used for all compounds. The plot is almost identical to the corresponding VASP plot (Figure 3.5). Convergence is slowest for KTaO_3 , however, at $n = 6$ the lattice energy of all compounds have converged to within 0.001 eV per atom.

Figure 3.8 plots the lattice energy as a function of unit cell volume when using the Γ centred $6 \times 6 \times 6$ k-point grid. The volume plots from FHI-aims are very similar to

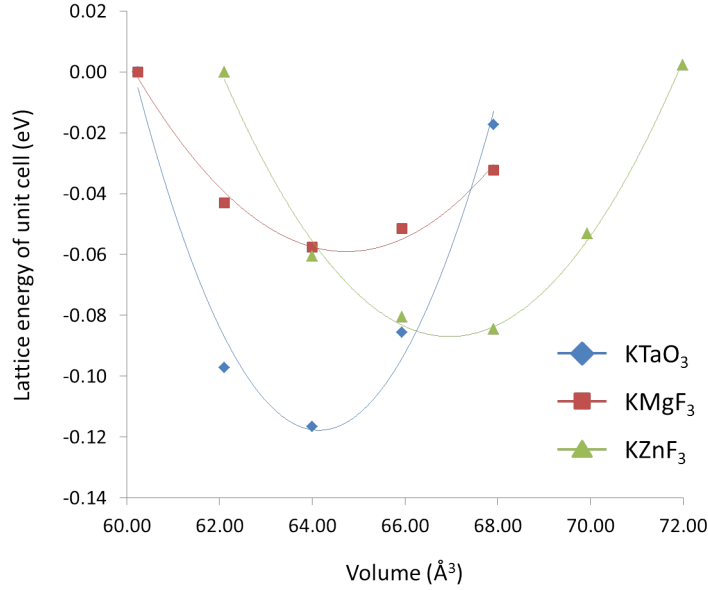


Figure 3.8: Lattice energy as a function of cell volume for KTaO_3 , KMgF_3 , and KMgF_3 ; calculated using FHI-aims. The energy shown is relative to the energy at a volume of 60.24 \AA^3 .

the ones from VASP (Figure 3.6). The Birch-Murnaghan equation was again applied to calculate the lattice parameter at which the energy was a minimum. For KTaO_3 , KMgF_3 , and KZnF_3 the lattice parameters were found to be 3.993 \AA , 4.006 \AA , and 4.056 \AA , respectively.

3.2.3 Formation Energy

The value of the lattice energy for the same system typically varies between codes and is dependant upon the method by which it is calculated. This can be clearly seen in the different lattice energies obtained from VASP and FHI-aims. For KTaO_3 , the lattice energy is calculated to be -40.659 eV by VASP, whereas it is -459625.833 eV in FHI-aims. As energy is computed as a difference, it is often desirable to have a reference point which would allow for comparison between different codes. A commonly used value to measure the energetic stability of a compound is the formation energy. The formation energy is defined as the difference in energy between the compound and the sum of its individual elements. The energy of the individual elements are calculated from their stable bulk or gaseous phases. This energy difference can be computed across many simulation packages.

The formation energy for an ABZ_3 perovskite can be written as:

$$E_f = E_{\text{ABZ}_3} - E_A - E_B - \frac{3}{2}E_{\text{Z}_2} \quad (3.1)$$

E_A and E_B are the lattice energies per atom reported by the simulation package for

the elements A and B in their bulk phase. E_{Z_2} is the reported energy of either the O_2 or F_2 molecule in the gas phase. As VASP required periodic boundaries, the O_2 and F_2 molecule calculations were performed in a large cell of length 16 Å to minimize interactions between periodic images. As FHI-aims does not require periodic boundaries, the calculations of the gas molecules were performed in an infinite vacuum. For the metals a much denser k-point grid ($15 \times 15 \times 15$) was used. The same plane wave cut off, 500 eV, was used for calculating E_{ABZ_3} , E_A , E_B , and E_{Z_2} .

The formation energy was obtained by inserting the energies calculated by the codes for E_{ABZ_3} , E_A , E_B , and E_{Z_2} into equation (3.1). The resulting values are shown in Table 3.1. The formation energies are in very good agreement between the two codes; energy difference less than 0.1 eV. All three compounds are shown to have a negative formation energy, i.e. the perovskite structure is more stable than the individual components. $KMgF_3$ is found to have the highest formation energy of ~ -16.5 eV, whereas for $KTaO_3$ it is ~ -13.7 eV, and $KZnF_3$ has the lowest formation energy of ~ -12.9 eV.

Another check on the stability of the perovskite is to see if any other combination of the elements is more stable. For $KTaO_3$ the stability is compared against the binary compounds K_2O and Ta_2O_5 , $KMgF_3$ is compared against KF and MgF_2 , and $KZnF_3$ against KF and ZnF_2 .

Equations (3.2), (3.3), (3.4) are used to calculate the relative stability of the perovskite phase compared to the binary compounds E_{PV-BC} .

$$E_{PV-BC} = E_{KTaO_3} - \frac{1}{2}E_{K_2O_2} - \frac{1}{2}E_{Ta_2O_5} \quad (3.2)$$

$$E_{PV-BC} = E_{KMgF_3} - \frac{1}{2}E_{KF} - \frac{1}{2}E_{MgF_2} \quad (3.3)$$

$$E_{PV-BC} = E_{KZnF_3} - \frac{1}{2}E_{KF} - \frac{1}{2}E_{ZnF_2} \quad (3.4)$$

Calculations on these component materials were performed in both FHI-aims and VASP with the number of k-points in each direction scaled such that the k-point density was the same or greater than that of the perovskite materials. The relative stability of the perovskites from VASP are: $KTaO_3 = -2.050$ eV; $KMgF_3 = -0.447$ eV; and $KZnF_3 = -0.470$ eV. From FHI-aims the values are: $KTaO_3 = -2.134$ eV; $KMgF_3 = -0.506$ eV; and $KZnF_3 = -0.492$ eV. A negative value indicates the perovskites are more stable than the binary compounds. Of the three materials $KTaO_3$ is by far the most stable relative to the binary compounds (2.1 eV). For the other two perovskites the ranking in relative stability predicted is reversed between the two codes. Results from VASP suggests $KZnF_3$ to have the larger relative stability by 0.23 eV, whereas FHI-aims predicts $KMgF_3$ by 0.14 eV.

Table 3.1 shows: the lattice constant (a), percentage deviation from experimental value, formation energy (E_f), and the time taken to complete one SCF cycle using VASP and FHI-aims. The value of a , for both DFT packages are in very good agreement with experimental values across all three compounds. The agreement between the two codes

Table 3.1: **VASP vs FHI-aims.** The lattice constant (a), percentage deviation from experimental value, formation energy (E_f), and the time taken to complete one SCF cycle using VASP and FHI-aims with the PBEsol functional. Room temperature experimental lattice parameters for KTaO_3 , KMgF_3 , and KZnF_3 are 3.989 Å [67], 3.988 Å [108], and 4.055 Å [115], respectively.

	KTaO_3		KMgF_3		KZnF_3	
	VASP	AIMS	VASP	AIMS	VASP	AIMS
a (Å)	3.992	3.993	4.004	4.006	4.065	4.056
$\Delta a\%$	0.09	0.10	0.40	0.45	0.24	0.02
E_f (eV)	-13.78	-13.70	-16.56	-16.48	-12.86	-12.92
SCF (s)	0.84	2.66	0.85	1.69	0.86	2.57

is also very strong. For KTaO_3 , the difference between the two codes is less than 0.02% and both agree to within 0.10% of the experimental value. Similarly, for KMgF_3 , the agreement between the codes is very strong; less than 0.06%. The difference between DFT and experimental results is, however, slightly larger, but still less than 0.5%. The largest disparity in a between the two codes is found for the compound KZnF_3 ; a difference of 0.22%, however, this is again very small. The value of a generated by FHI-aims is very close to the experimental value, overestimating by only 0.02%, while using VASP it is overestimated by 0.24%. The formation energies, E_f , generated by the two codes correlate very strongly, with the energies never differing by more than 0.08 eV.

To estimate which code is more efficient, the CPU cost for both codes to perform one SCF cycle, when using the same number of cores, was measured. VASP is shown to be faster than FHI-aims by a factor of 2 for KMgF_3 , and a factor of 3 for the other two compounds. This is expected, as plane wave codes are much better suited for periodic calculations compared to atom-centred orbital based codes. To put this in perspective, the VASP calculations of O_2 and F_2 molecules were performed inside a cubic super cell of length 16 Å and took 581 and 348 seconds respectively to complete. In FHI-aims there was no need to use a periodic cell, and for both molecules the calculation was completed in 2.1 seconds. This highlights the respective strengths of the two codes. Thus, further calculations in which periodic boundaries are required (bulk and surface) will be performed using VASP, and molecular / nano-cluster calculations in which periodic boundaries are not required will be run in FHI-aims.

3.2.4 Atomistic Calculations

All atomistic calculations for the perovskites were performed using the General Utility Lattice Package (GULP) [38]. A combination of Buckingham and Lennard-Jones interatomic potentials were used to model the short range interaction, and the Coulomb potential modelled the long range interactions (no radial cut-off) between the ions. In the case of KTaO_3 , the shell model was used to account for the polarisability of the

Table 3.2: **Potential parameters for KMgF₃**. A radial cut-off of 25 Å and 10 Å was used for the Buckingham potentials and Lennard-Jones potentials, respectively.

Charge	K = 0.83	Mg = 1.66	F = -0.83
Buckingham	A (eV)	ρ (Å)	C (eV Å ⁻⁶)
K – K	36831.045	0.26578	0.0000
K – F	6770.553	0.23169	0.0000
F – F	17039.097	0.21500	15.1680
Mg – F	4166.274	0.21500	2.9010
Mg – Mg	905.517	0.21500	0.5557
Lennard – Jones	B (eV Å ⁻¹²)		
Mg – K	10.00		

Table 3.3: **Potential parameters for KZnF₃**. A radial cut-off of 10 Å was used for all potentials.

Charge	K = 1.0	Zn = 2.0	F = -1.0
Buckingham	A (eV)	ρ (Å)	C (eV Å ⁻⁶)
K – K	2189.190	0.1916	0.00
K – F	3521.600	0.2672	0.00
F – F	911.690	0.2707	13.80
Zn – F	1482.300	0.2664	0.00
Lennard – Jones	B (eV Å ⁻¹²)		
Zn – K	5.00		
Zn – Zn	5.00		

system. Details of the potentials and their parameters are given in chapter 2, equations (2.12), (2.13), (2.11), and (2.14).

The potential parameters for KMgF₃ and KZnF₃ were taken from the literature [123, 124] and reported in Tables 3.2 and 3.3. For KTaO₃, the potential parameters were refined from an existing set of potentials published by Exner et al. [125], and are reported in Table 3.4. Although potassium is generally considered purely ionic, shells were included on the K⁺ ions as it has been shown that modelling the polarisability of K⁺ is important near surfaces [126]. Initially, the spring constants were refitted to reproduce the room temperature high frequency dielectric constant with an emphasis on the O²⁻ spring. The other IP parameters were then fitted to reproduce the observed lattice parameter (a), elastic constants (C_{xx}) and dielectric constants (ϵ_x), as listed in Table 3.5, at room temperature. The fit was performed using the “relaxed fit” method implemented in GULP and discussed in chapter 2.

In a second stage, a set of 31 phonon frequency points, measured at room temperature

Table 3.4: **Potential parameters for KTaO_3 .** A radial cut-off of 15 Å was used for all potentials.

Charge	K = 1.0	Ta = 5.0	O = -2.0
Ion	shell charge (e)	k_2 (eV Å ⁻²)	k_4 (eV ² Å ⁻⁴)
K ⁺	-4.723061	356.91688	20000
Ta ⁵⁺	-3.700216	68867.76829	10000
O ²⁻	-2.891878	33.45182	33000
Buckingham	A (eV)	ρ (Å)	C (eV Å ⁻⁶)
K – O	1222.43483	0.346334	39.48
Ta – O	1410.97032	0.369327	10.00
O – O ¹	22700.00000	0.149000	113.26

^aFor the O – O interaction the original Buckingham potential of Catlow [32] was modified so that below 2 Å only the repulsive terms were considered, while above 2.6 Å only the attraction was considered, a polynomial fit was used to smooth the potential between the two cut-offs.

[71], were included in the fit. The dispersion plots from which the phonon data was extracted are shown Figure 3.9.

Preliminary tests revealed that the potentials modelling the O – O interaction allowed the ions to collapse toward each other during global optimisation runs. To remedy this, the Buckingham potential was modified so that: below a radial separation of 2.0 Å the potential was modelled solely by the repulsive $Ae^{(\frac{-r}{\rho})}$ term; at distances greater than 2.5 Å the potential was modelled by the attractive $\frac{C}{r_{ij}^6}$ dispersion term; and in the range 2.0 – 2.5 Å the potential was modelled by a polynomial function that smoothed the potential curve between the other two terms.

Bulk properties of the three perovskite materials, as calculated using the IP within GULP and DFT within VASP, are shown in Table 3.5. The corresponding room temperature (when available) experimental values are also included in Table 3.5 for easy comparison with the calculated values. The IP lattice parameters were determined by constraining the unit cell to be cubic during relaxations of both the atomic positions and the unit cell volume. The IP lattice parameter, a , for KTaO_3 agrees well with experiment lying within 0.02% of the observable. A very good agreement between IP and DFT is also found for the value of a ; a difference of less than 0.09%. Similarly, for KZnF_3 the IP closely reproduce the experimental (0.09%) and DFT (0.15%) values of a . The value of a calculated by the KMgF_3 IP also show good agreement with the experiment (0.92%). The KMgF_3 IP calculations underestimate a compared to experiment, whereas DFT overestimates; this leads to a difference of 1.31% between the two different calculations. With the exception of KMgF_3 simulations, the IP produce lattice parameters closer to experiment than that from DFT.

The DFT bulk modulus, B_0 , was not calculated directly by VASP, but was deter-

Table 3.5: **Observables.** The lattice parameter (a), bulk modulus (B_0), elastic constants (C_{xx}), dielectric constants (ϵ) and lowest energy transverse optical phonon mode (TO_1) as calculated in GULP and VASP, and experimental values, at room temperature when available, from the literature.

Observable		KTaO ₃	KMgF ₃	KZnF ₃
a (Å)	GULP	3.98896	3.9514	4.0586
	VASP	3.99244	4.00388	4.06476
	Exp.	3.98948 [67]	3.988 [109]	4.055 [109]
B (GPa)	GULP	219.1	79.8	76.7
	VASP	203.1	72.6	82.5
	Exp.	230.0 [89]	73.5 [127]	77.6 [127]
C_{11} (GPa)	GULP	433.44	153.1	141.8
	VASP	465.88	142.4	155.7
	Exp.	396.30 [70]	132 [128]	134.5 [128]
C_{12} (GPa)	GULP	111.69	43.1	44.2
	VASP	82.92	36.2	54.6
	Exp.	130.00 [73]	39.6 [128]	52.7 [128]
C_{44} (GPa)	GULP	111.69	43.1	44.2
	VASP	92.44	38.4	34.2
	Exp.	107.10 [70]	48.5 [128]	38.1 [128]
ϵ_0	GULP	243.016	4.055	4.250
	VASP	5.598	2.102	2.400
	Exp.	243.000 [77]	5.98 [129]	7.78 [129]
ϵ_∞	GULP	4.657	N/a	N/a
	VASP			
	Exp.	4.300 [130]	2.04 [129]	2.34 [129]
TO_1 (cm ⁻¹)	GULP	39	130	152
	VASP	88	148	132
	Exp.	85 [71]	168 [129]	141 [129]

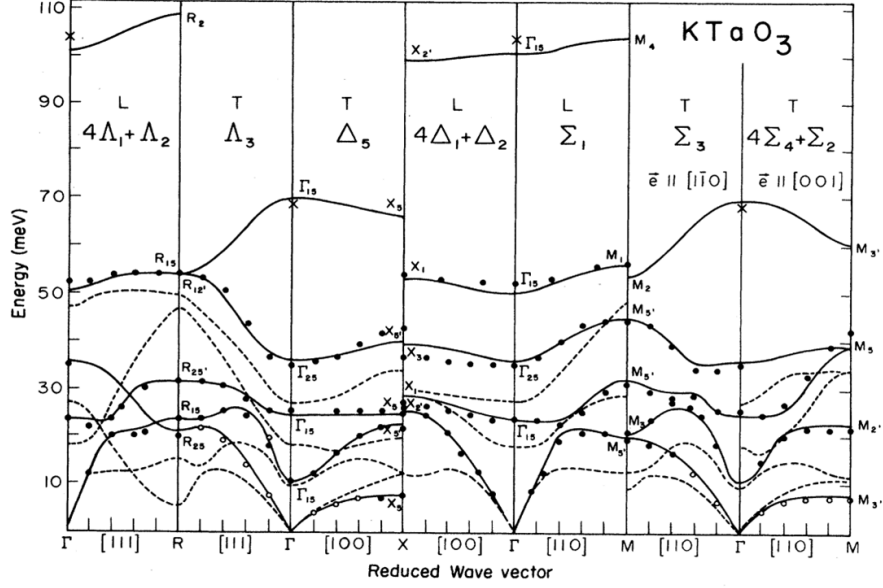


Figure 3.9: Phonon data taken from Ref. [71]. Dots are experimental results and solid lines are calculated from fitted force constants for KTaO_3 . Dashed lines are calculated from force constants for SrTiO_3

mined using the Birch-Murnaghan equation of state during the energy optimisation of the volume. The calculated value of B_0 for KTaO_3 , using the IP model, is in good agreement with the experimental value, underestimating by only 4.7%. The DFT result, however, underestimates by a larger amount of 11.7%. Results for KZnF_3 are similar in this regard, with the IP calculated value of B_0 being closer to experiment, underestimating by only 1.2%, than DFT which overestimates by 6.3%. KMgF_3 differs, in that the DFT value is closer to experiment (1.2%) than the IP value (8.6%).

For KTaO_3 the IP calculated elastic constants show much better agreement to experiment than the DFT. The IP errors for the elastic constants C_{11} , C_{12} , and C_{44} are 9.4%, 14.1%, and 4.3%, respectively, while for DFT they are 17.6%, 36.2%, and 13.7%. For the other two materials there was no clear winner between DFT and IP. All calculated values provided a reasonable estimate with all differences less than 20%.

There is strong agreement between experiment and the IP calculations in regards to the static dielectric constant, ϵ_0 , of KTaO_3 . This is likely a result of KTaO_3 being an incipient ferroelectric. The DFT value was greatly underestimated; smaller by a factor of almost 50. The calculated values of ϵ_0 from the IP models of the other two materials were smaller than the experimental values; 30% for KMgF_3 and 45% for KZnF_3 . The DFT calculated values of ϵ_0 were more severely underestimated, being smaller by a factor of about 3 compare with experiment in both cases.

For the high frequency dielectric constant, ϵ_∞ , the only calculated value presented is that for KTaO_3 . There are no IP values for the other two systems as rigid ion models were employed for the simulations. ϵ_∞ determines how a systems electrons responds to

high frequency electric fields, which is modelled by allowing only the shells to respond to a electric field with a frequency greater than the highest energy vibration.

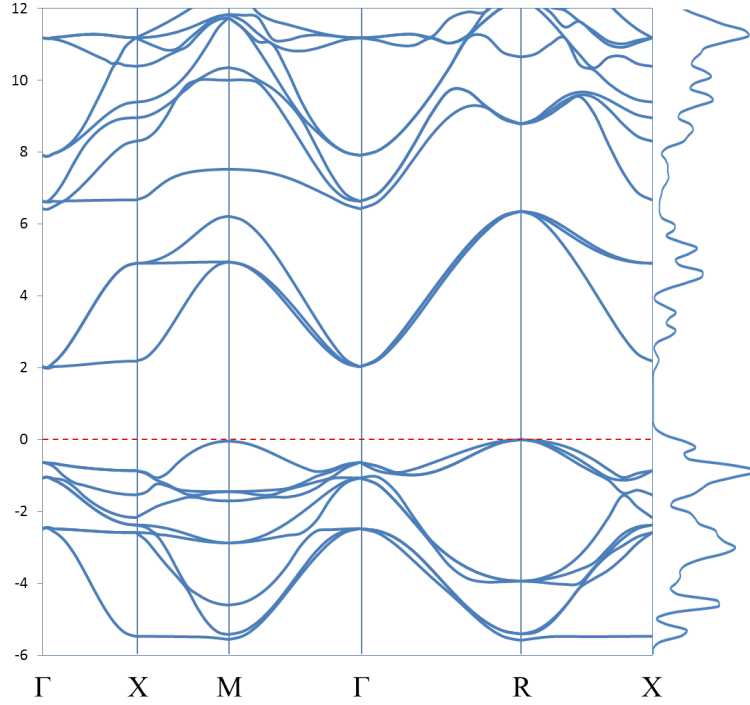


Figure 3.10: Electronic band structure for bulk KTaO_3 , as calculated using VASP. The valence band maximum is set to 0 (red line). The DOS is shown, in line, on the right.

Electronic Density of States and Band Structure

One of the advantages of electronic structure models over atomistic models is that they enable the calculation of the electronic density of states (DOS) and band structure. Figure 3.10 shows the band structure and total DOS (along the right side) close to the Fermi level for the bulk KTaO_3 . The band structure was calculated in VASP using 10 k-points between each of the special cubic symmetry points Γ (0,0,0), X ($\frac{1}{2},0,0$), M ($\frac{1}{2},\frac{1}{2},0$), and R ($\frac{1}{2},\frac{1}{2},\frac{1}{2}$). The electronic bands were shifted so that the valence band maximum (VBM) was at 0 eV. The band structure shows the VBM to be at the R point and a highly disperse conduction band minimum (CBM) at the gamma point. The prediction of the indirect $\Gamma - \text{R}$ band gap is in agreement with other computational studies [74, 88–92]. The width of the band gap is calculated to be 2.03 eV, which is in close agreement with the other computational studies. As with most calculations using the GGA functional, this calculated band gap is a large underestimate (44%) when compared to the experimental value of ~ 3.6 eV [77, 87, 88]. The smallest direct gap is located at the gamma point, and is determined to be 2.66 eV. This is again an underestimate compared to the experimental value of 4.35 eV [88].

Figure 3.11 shows the DOS for KTaO_3 decomposed into its separate elements, as well as an orbital decomposed DOS for each of the species. As with the band diagram, the DOS plot is shifted so that the VBM is at 0 eV. The valence band is seen to be composed of mixed O and Ta states and has a width of just under 6 eV. The top of the

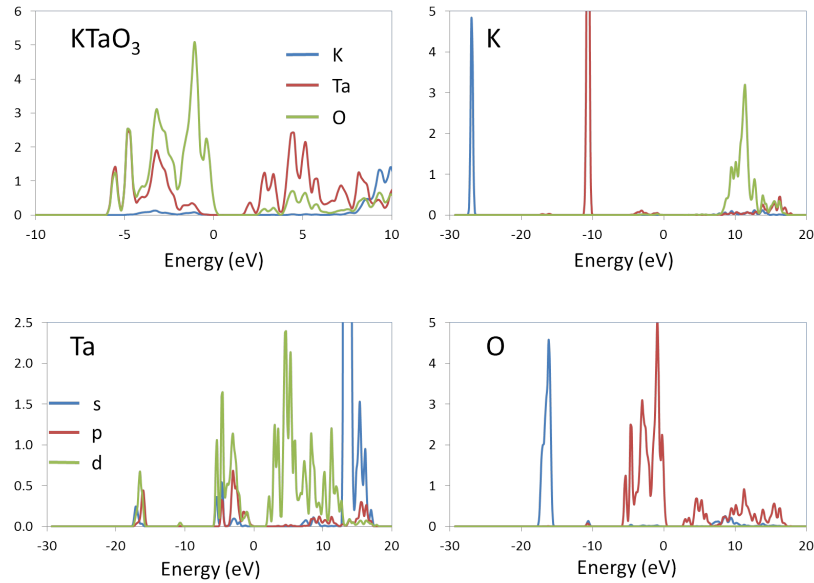


Figure 3.11: Species decomposed DOS for KTaO_3 , and orbital decomposed DOS for each species in KTaO_3 ; calculated using VASP.

valence band is made up solely of O 2p states. Further down the valence band the O 2p states are hybridised with the Ta 5d, 6s, and 6p states.

The conduction band has a width of about 15 eV, extending from 2 eV all the way up to 17 eV. The CBM at 2 eV is composed of Ta 5d states and from ~ 2.5 eV there is a small mixing of O 2p states. Further up the conduction band exists the K 3d orbitals as well as the Ta 6s orbital. The filled K 3s and 3p orbitals result in narrow bands at -27 eV and -11 eV respectively. The filled O 2s band lies at -17 eV and possesses some Ta character. The heavy mixing of the Ta and O states would suggest a large degree of covalency in the Ta – O bonds, while the lack of K mixing may suggest it remains ionic.

Figures 3.12 and 3.13 show the band structure and DOS profile for KMgF_3 . The calculations were performed in the same manner as the KTaO_3 plots, with the VBM again shifted to 0 eV. From the band diagram, KMgF_3 (3.12) is found to also possess an indirect $\Gamma - \text{R}$ band gap but with a much larger width of 7.04 eV. As expected for GGA calculations, the band gap is underestimated (41%); the experimentally determined gap is ~ 11.9 eV [95, 113]. The DOS profile (Figure 3.13) shows the valence band to have a width of ~ 4 eV and almost purely of F 2p character.

The CBM at 7 eV is a low density Mg 3s, 3p, F 2s, and 2p hybridised band almost invisible on the plot. From the band diagram (3.12, this region of low density can be attributed to one or two highly disperse bands. From 10 eV the K 3d states become the dominant feature in the conduction band all the way up to 20 eV. The filled K 4s and 4p orbitals result in bands at -9 eV -26 eV, while the F 2s orbital results in a band at -19 eV. The lack of mixing in the valence band would suggest that KMgF_3 is fairly ionic.

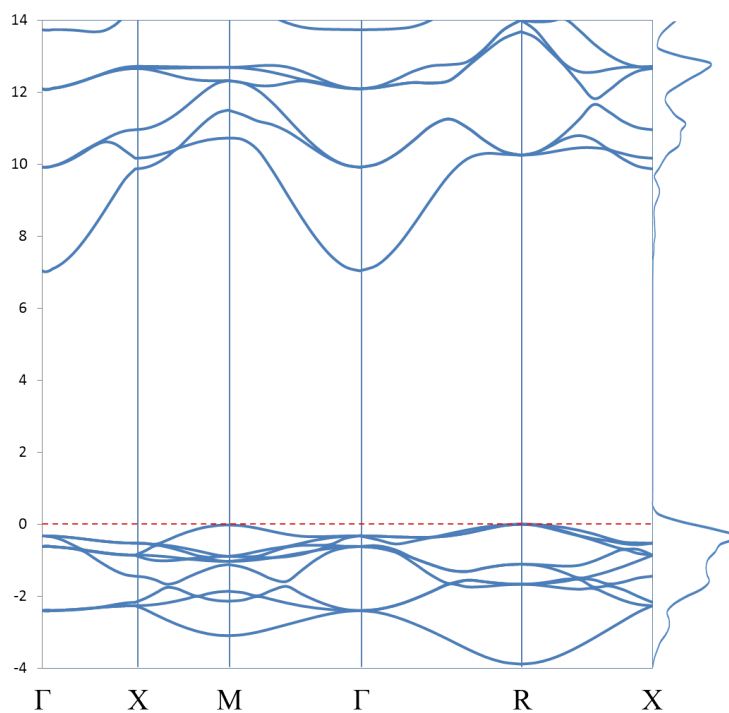


Figure 3.12: Electronic band structure for bulk KMgF_3 , as calculated using VASP. The valence band maximum is set to 0 (red line). The DOS is shown, in line, on the right.

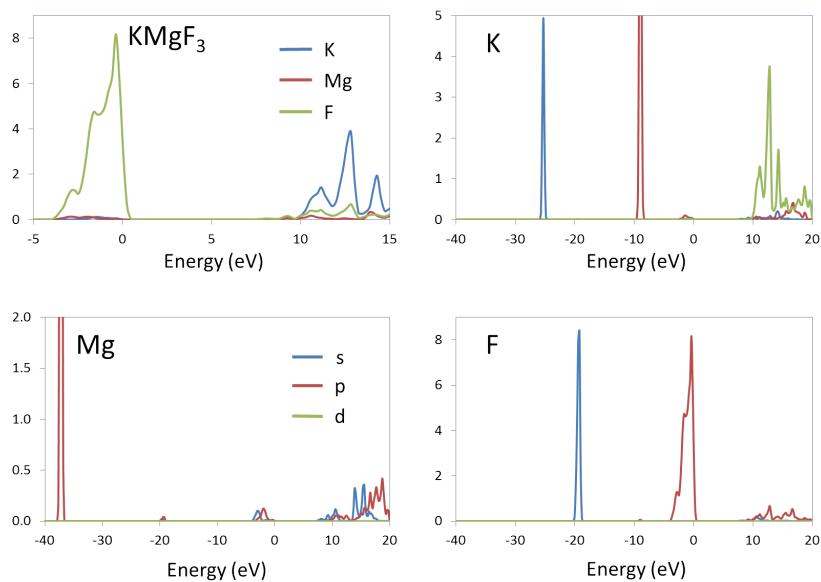


Figure 3.13: Species decomposed DOS for KMgF_3 , and orbital decomposed DOS for each species in KMgF_3 ; calculated using VASP.

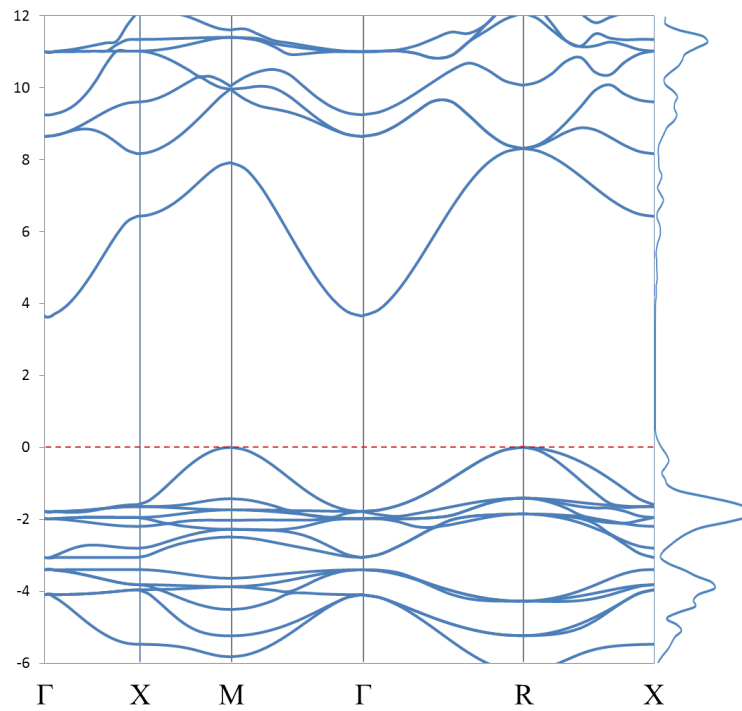


Figure 3.14: Electronic band structure for bulk KZnF_3 , as calculated using VASP. The valence band maximum is set to 0 (red line). The DOS is shown, in line, on the right.

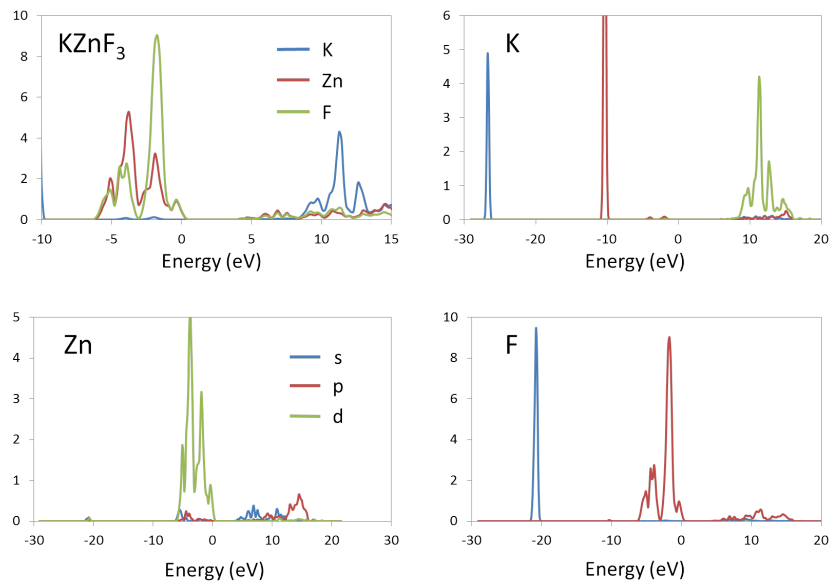


Figure 3.15: Species decomposed DOS for KZnF_3 , and orbital decomposed DOS for each species in KZnF_3 ; calculated using VASP.

Table 3.6: **Atomistic defect energies.** The values presented are the difference in energy between the defected and bulk systems in eV. Mott. indicates the Mott-Littleton method of defect calculation described in chapter 2. The correction used for the super cells is also described in chapter 2.

Vacancy	Mott.	Super cell			Super cell corrected		
		2x2x2	3x3x3	4x4x4	2x2x2	3x3x3	4x4x4
KTaO ₃ : K	5.39	5.25	5.36	5.39	5.26	5.37	5.39
KTaO ₃ : Ta	125.27	119.93	123.52	124.94	120.20	123.70	125.07
KTaO ₃ : O	21.02	21.16	21.20	21.11	21.20	21.23	21.13
KMgF ₃ : K	4.26	3.77	3.96	4.05	4.41	4.39	4.36
KMgF ₃ : Mg	20.36	18.77	19.31	19.55	21.32	21.01	20.83
KMgF ₃ : F	4.62	4.27	4.36	4.42	4.91	4.78	4.74
KZnF ₃ : K	5.80	5.13	5.40	5.52	5.74	5.81	5.82
KZnF ₃ : Zn	26.50	24.66	25.15	25.42	27.09	26.78	26.63
KZnF ₃ : F	6.10	5.60	5.74	5.83	6.21	6.15	6.13

Lastly, the band structure and DOS profile for KZnF₃ can be seen in Figures 3.14 and 3.15. As with the previous two perovskites this material is found to possess an indirect $\Gamma - R$ band gap. The width is calculated to be 3.65 eV, which is 11% smaller than the experimental value of 4.1 eV [115]. This is the best estimate of the band gap calculated for the three ABZ₃ perovskites. Like KTaO₃, and unlike KMgF₃, the KZnF₃ valence band is a mixture of the metal B cation and Z anion states, zinc and fluorine in this case. Unlike KTaO₃, however, the heavily mixed states exist even at the VBM and the zinc character is almost purely d states. The bottom of the conduction band is hybridised Zn 4s and F 2p orbitals with K 3d states becoming the dominant feature from 9 eV. The low lying K 4s and 4p bands are at -27 eV and -11 eV, while the F 2s band resides at -21 eV. As with KTaO₃ there is a significant mixing of the B and Z ions in the valence band and so covalent bonding between zinc and fluorine may be expected.

3.3 Bulk Defects

3.3.1 Atomistic Defects

Single ion vacancy calculations were performed for all three systems at the atomistic level using GULP. The defect energies calculated for these vacancies are shown in Table 3.6.

The values shown represent the difference in energy between the system containing a vacancy and the perfect bulk system, ΔE . Physically, the energy being measured is that required to remove an ion from the system to a distance infinity away. Both the Mott-Littleton and the periodic super cell approach have been utilised, see chapter 2. The Mott-Littleton method models the infinitely dilute defect, whereas the super cell technique models a defect concentration dependant on super cell size. Values in which a

correction has been applied to the super cell approach – with the aim of converging more rapidly to the infinitely dilute defect energy – are also presented. From the table it can clearly be seen that the corrected values do converge more rapidly to the Mott-Littleton values. The correction appears to have less impact on the KTaO_3 vacancies than it does for the other two perovskites. This is likely a result of the KTaO_3 IP employing a shell model which screens the charge, whereas the IP for the other two compounds use rigid ions (no shells). The ratio ΔE between the different vacancy types in a compound are approximately proportional to the square of the charge, suggesting the Coulomb contribution to the defect energy is large (as one would expect). Thus, for all three compounds the K ion has the lowest defect energy, followed by the anion (O, F), and lastly the cation at the octahedral centre. Counter intuitively, the defect energy (uncorrected) is seen to increase with increasing super cell size (decreasing concentration). This result is likely an effect of the uniform background charge applied for modelling charged cells.

3.3.2 DFT defects

To calculate how a defect affects the stability of a system the defect formation energy must be determined. This can be calculated using the following equation:

$$E_{\text{Defect}} = E_{\text{ABZ}_3}^D - E_{\text{ABZ}_3} + N_A\mu_A + N_B\mu_B + N_Z\mu_Z \quad (3.5)$$

where E_{ABZ_3} is the relaxed energy of the ABZ_3 perovskite system before a defect was introduced and $E_{\text{ABZ}_3}^D$ the energy after. N_i and μ_i are the number of vacancies and the chemical potential respectively of element i . See chapter 2 for more details.

To calculate the formation energy the chemical potential of defect species must be determined. This is usually done for the limiting cases in a phase diagram. Figure 3.16 shows a phase diagram from KTaO_3 (left) and KXF_3 (right), where $X = \text{Mg}$ or Zn . Each of the pentagon vertices represents a limiting case at which the reservoirs of the two connected compounds are in thermal equilibrium with the perovskite under investigation. For example, point 1 on the left diagram is a system in which KTaO_3 , K(s) , and K_2O are all in thermal equilibrium.

The chemical potentials calculated at each point for KTaO_3 are shown in equations (3.6) to (3.20).

$$\textbf{Point 1:} \quad \mu_{\text{K}} = \mu_{\text{K(s)}} \quad (3.6)$$

$$\mu_{\text{Ta}} = \mu_{\text{KTaO}_3} - \mu_{\text{K}} - 3\mu_{\text{O}} \quad (3.7)$$

$$\mu_{\text{O}} = \mu_{\text{K}_2\text{O}} - 2\mu_{\text{K}} \quad (3.8)$$

$$\textbf{Point 2:} \quad \mu_{\text{K}} = (\mu_{\text{K}_2\text{O}} - \mu_{\text{O}})/2 \quad (3.9)$$

$$\mu_{\text{Ta}} = \mu_{\text{KTaO}_3} - \mu_{\text{K}} - 3\mu_{\text{O}} \quad (3.10)$$

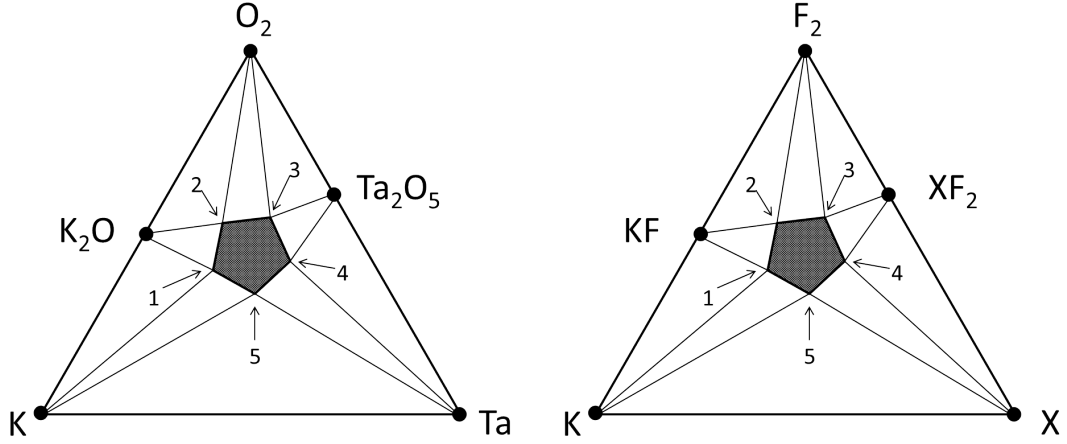


Figure 3.16: Phase diagrams for KTaO_3 (left) and KXF_3 (right), where $X = \text{Mg}$ or Zn .

$$\mu_{\text{O}} = \mu_{\text{O(g)}} \quad (3.11)$$

$$\text{Point 3: } \mu_{\text{K}} = \mu_{\text{KTaO}_3} - \mu_{\text{Ta}} - 3\mu_{\text{O}} \quad (3.12)$$

$$\mu_{\text{Ta}} = (\mu_{\text{Ta}_2\text{O}_5} - 5\mu_{\text{O}})/2 \quad (3.13)$$

$$\mu_{\text{O}} = \mu_{\text{O(g)}} \quad (3.14)$$

$$\text{Point 4: } \mu_{\text{K}} = \mu_{\text{KTaO}_3} - \mu_{\text{Ta}} - 3\mu_{\text{O}} \quad (3.15)$$

$$\mu_{\text{Ta}} = \mu_{\text{Ta(s)}} \quad (3.16)$$

$$\mu_{\text{O}} = (\mu_{\text{Ta}_2\text{O}_5} - 2\mu_{\text{Ta}})/5 \quad (3.17)$$

$$\text{Point 5: } \mu_{\text{K}} = \mu_{\text{K(s)}} \quad (3.18)$$

$$\mu_{\text{Ta}} = \mu_{\text{Ta(s)}} \quad (3.19)$$

$$\mu_{\text{O}} = (\mu_{\text{KTaO}_3} - \mu_{\text{K}} - \mu_{\text{Ta}})/3 \quad (3.20)$$

Similarly, the chemical potentials for KXF_3 ($X = \text{Mg}, \text{Zn}$) are shown in equations (3.21) to (3.35).

$$\text{Point 1: } \mu_{\text{K}} = \mu_{\text{K(s)}} \quad (3.21)$$

$$\mu_{\text{X}} = \mu_{\text{KXF}_3} - \mu_{\text{K}} - 3\mu_{\text{F}} \quad (3.22)$$

$$\mu_{\text{F}} = \mu_{\text{KF}} - \mu_{\text{K}} \quad (3.23)$$

$$\text{Point 2: } \mu_{\text{K}} = \mu_{\text{KF}} - \mu_{\text{F}} \quad (3.24)$$

$$\mu_{\text{X}} = \mu_{\text{KXF}_3} - \mu_{\text{K}} - 3\mu_{\text{F}} \quad (3.25)$$

$$\mu_{\text{F}} = \mu_{\text{F(g)}} \quad (3.26)$$

$$\text{Point 3: } \mu_{\text{K}} = \mu_{\text{KXF}_3} - \mu_{\text{X}} - 3\mu_{\text{F}} \quad (3.27)$$

$$\mu_{\text{X}} = \mu_{\text{XF}_2} - 2\mu_{\text{F}} \quad (3.28)$$

$$\mu_{\text{F}} = \mu_{\text{F(g)}} \quad (3.29)$$

Table 3.7: **Chemical potentials.** The chemical potentials for each species in KTaO_3 , KMgF_3 , and KZnF_3 , calculated at the points shown in the relevant phase diagrams (Figure 3.16).

Element	Chemical potential (eV) at phase diagram point				
	1	2	3	4	5
KTaO_3 : K	-0.90	-2.53	-5.76	-3.98	-0.90
KTaO_3 : Ta	-16.36	-24.51	-21.28	-12.36	-12.36
KTaO_3 : O	-7.80	-4.54	-4.54	-8.11	-9.13
KMgF_3 : K	-0.90	-6.36	-6.80	-1.47	-0.90
KMgF_3 : Mg	-1.81	-12.72	-12.28	-1.62	-1.62
KMgF_3 : F	-6.91	-1.45	-1.45	-6.78	-6.97
KZnF_3 : K	-0.90	-6.36	-6.83	-3.36	-0.90
KZnF_3 : Zn	2.07	-8.84	-8.37	-1.44	-1.44
KZnF_3 : F	-6.91	-1.45	-1.45	-4.92	-5.74

$$\text{Point 4: } \mu_{\text{K}} = \mu_{\text{KXF}_3} - \mu_{\text{X}} - 3\mu_{\text{F}} \quad (3.30)$$

$$\mu_{\text{X}} = \mu_{\text{X(s)}} \quad (3.31)$$

$$\mu_{\text{F}} = (\mu_{\text{XF}_2} - \mu_{\text{X}})/2 \quad (3.32)$$

$$\text{Point 5: } \mu_{\text{K}} = \mu_{\text{K(s)}} \quad (3.33)$$

$$\mu_{\text{X}} = \mu_{\text{X(s)}} \quad (3.34)$$

$$\mu_{\text{F}} = (\mu_{\text{KXF}_3} - \mu_{\text{K}} - \mu_{\text{X}})/3 \quad (3.35)$$

The values of μ used for the metals (K, Ta, Mg, Zn), gas (O_2 , F_2), and binary compounds (K_2O , Ta_2O_5 , KF , MgF_2 , ZnF_2) were the energies of these systems calculated in VASP.

Table 3.7 shows the calculated chemical potentials for each species in KTaO_3 , KMgF_3 , and KZnF_3 at the points shown in the phase diagram (Figure 3.16). Points 2 and 3 on the phase diagram represent oxidising conditions and so at these points μ is largest for the anions. Conversely, μ for the cations at these points are typically at a minimum. Thus, cation vacancies would be most favourable at points 2 and 3, whereas anion vacancies would be least favourable at these points. The other points represent metal rich environments and so lead to reduced μ for the anions and increased μ for the cations.

DFT calculations were performed to investigate neutral vacancies using VASP in $2 \times 2 \times 2$ and $3 \times 3 \times 3$ super cells. The defect energies for KTaO_3 , KMgF_3 and KZnF_3 are given in Table 3.8. The defect formation energy is calculated at each of the points described in the relevant phase diagrams (Figure 3.16). The ordering of ΔE with respect to the different vacancies within each compound agrees with the atomistic calculations. The K vacancy results in the smallest energy change, the B cation at the octahedral centres the largest, and the anions somewhere in the between.

ΔE for K vacancies is smallest in KTaO_3 suggesting that K is more strongly bound in the other two compounds. Decreasing the vacancy concentration from $1/8$ ($2 \times 2 \times 2$) to

Table 3.8: **DFT neutral vacancy energies.** ΔE is the difference in energy between the perfect bulk system and the system containing one vacancy. The defect energies are calculated using chemical potentials at the points shown in the relevant phase diagrams (Figure 3.16).

Vacancy	ΔE	Defect formation energy (eV) at phase diagram point				
		1	2	3	4	5
KTaO ₃ : K 2x2x2	5.34	4.44	2.81	-0.42	1.36	4.44
KTaO ₃ : K 3x3x3	5.27	4.37	2.74	-0.49	1.30	4.37
KTaO ₃ : Ta 2x2x2	31.05	14.69	6.54	9.77	18.69	18.69
KTaO ₃ : Ta 3x3x3	30.71	14.35	6.21	9.44	18.36	18.36
KTaO ₃ : O 2x2x2	10.71	2.91	6.17	6.17	2.60	1.58
KTaO ₃ : O 3x3x3	10.11	2.31	5.57	5.57	2.00	0.97
KMgF ₃ : K 2x2x2	7.44	6.54	1.08	0.63	5.96	6.54
KMgF ₃ : K 3x3x3	7.41	6.51	1.05	0.60	5.93	6.51
KMgF ₃ : Mg 2x2x2	14.49	12.68	1.77	2.21	12.87	12.87
KMgF ₃ : Mg 3x3x3	14.37	12.56	1.64	2.09	12.75	12.75
KMgF ₃ : F 2x2x2	8.51	1.60	7.06	7.06	1.73	1.54
KMgF ₃ : F 3x3x3	8.50	1.59	7.05	7.05	1.72	1.53
KZnF ₃ : K 2x2x2	6.41	5.51	0.05	-0.42	3.05	5.51
KZnF ₃ : K 3x3x3	6.24	5.34	-0.11	-0.58	2.88	5.34
KZnF ₃ : Zn 2x2x2	8.02	10.09	-0.82	-0.35	6.59	6.59
KZnF ₃ : Zn 3x3x3	7.89	9.96	-0.95	-0.48	6.45	6.45
KZnF ₃ : F 2x2x2	7.05	0.15	5.60	5.60	2.13	1.31
KZnF ₃ : F 3x3x3	7.02	0.11	5.57	5.57	2.10	1.28

1/27 (3x3x3) typically changes ΔE by less than 2%. O vacancies in KTaO₃ represent the largest change in Δ with reduced concentration at 6% implying O vacancies have the longest range of effect. For KTaO₃ the formation energy of K vacancies is favourable (negative) at point 3 on the phase diagram implying defects would spontaneously form. The formation energy of Ta vacancies is large at all points on the phase diagram and thus it is not expected Ta vacancies would form. The O vacancy formation energy is lowest at point 5 with values of 1.58 eV (2x2x2) and 0.97 eV (3x3x3) and so O vacancies may form under high temperature.

For KMgF₃ formation energy of K vacancies is again lowest at point 3, however, the formation energy is positive (0.63 eV for 2x2x2 and 0.60 eV for 3x3x3). The Mg vacancy has the largest formation energies although not as high as Ta in KTaO₃ and are higher than the K vacancies at every point. The formation energy of F vacancies are lowest at point 5 on the phase diagram and are of comparable energy to the O vacancies in KTaO₃.

For KZnF₃ the K vacancies are found to be favourable (negative formation energy) at points 3 and 2 with the energies at point 3 similar to those seen for KTaO₃. Interestingly, the Zn vacancies are also shown to be favourable at points 2 and 3. At point 2 the Zn vacancy is more stable, while at point 3 the K vacancy is more stable. The B cation

vacancies were shown to have large formation energies in the previous two compounds. The formation energy of the F vacancies are found to be small (~ 0.1 eV) at point 1 implying anion vacancies are also more easily formed in KZnF_3 than in the other two perovskites.

Structurally, cations moved towards the site of cation vacancies and away from anion vacancies in all three compounds. The opposite was true of anions. These shifts were typically less than 0.1 \AA .

3.4 Summary

In this chapter the bulk properties of three cubic perovskites, KTaO_3 , KMgF_3 , and KZnF_3 have been investigated at both the atomistic and electronic level. The electronic structure calculations were performed using density functional theory with the GGA-PBESol. Implementations within both the VASP and FHI-aims packages were employed. The results obtained showed a very good agreement between the two codes (within 1%) in regards to the lattice parameter, a , and formation energies of the three perovskites. As expected, VASP was found to be the faster code for periodic systems, while FHI-aims proved better for molecular calculations. Thus, VASP was chosen to perform the remaining bulk calculations. The values of a obtained from VASP were within 0.5% of the experimental values, thus a satisfactory structural model for the perovskites was achieved.

In anticipation of the future global optimisations to be performed, which would involve the investigation of a large number structures, a suitable set of interatomic potential parameters was also targeted. Interatomic potential parameters for all three perovskites were found in the literature [123–125]. The set for KTaO_3 were refined in order to achieve a better fit to room temperature experimental data and to include shells on the K ions. It was found that the IP calculations accurately reproduce the experimentally observed lattice parameters. The largest discrepancy in a was found for KMgF_3 , with a difference of only 0.92% from the experimental value.

Both the IP and DFT calculated bulk modulus and three elastic constants (C_{11} , C_{12} , and C_{44}) were found to be within good agreement of experiment. Moreover, for KTaO_3 , the IP results gave a much better match to experiment than that achieved using DFT for all four constants, whereas for the other two compounds the IP and DFT showed similar levels of agreement to experiment.

For the static dielectric constant, only the KTaO_3 IP produced a good estimate, with the DFT and other two IP sets severely underestimating the experimental value.

The band structure and partial density of states (DOS) of the perovskites were calculated. Analysis of the bands showed all three of the compounds to possess an indirect $\Gamma - \text{R}$ band gap. The width of all three band gaps are underestimated, but match closely to previous computational studies using the GGA functional. The DFT calculated band

gap for KZnF_3 gave the best match to experiment, underestimating by only 11%. The calculated gaps for other two compounds underestimated the experimental gap by about 40%. The DOS profile revealed a mixing of the B cation and anion states in the valence band for KTaO_3 and KZnF_3 indicative of possible covalent bonding between the B cation and anions. No such mixing was observed for KMgF_3 suggesting it to be ionic.

Defect calculations revealed K vacancies to be the most easily formed, and are most favourable under oxidising conditions. The B cation vacancies generally had the largest formation energies, Ta in particular which even under oxidising conditions possessed a minimum formation energy of 6.21 eV. An exception was seen with Zn vacancies in KZnF_3 which showed favourable defect formation under oxidising conditions. The anion vacancies were found to have reasonably low formation energy under metal rich conditions and thus may be formed under high temperature.

Chapter 4

The (001) KTaO_3 Surface

4.1 Introduction

In this chapter reconstructions of the polar KTaO_3 (001) surface are investigated. The structure of the reconstructions are initially predicted using global optimisations routines on the interatomic potential (IP) energy landscape. The IP structures are refined using density functional theory (DFT) to ascertain the electronic structure. The formation energy of vacancies in the slab are investigated. Lastly, the reconstructions found for KTaO_3 were applied to other perovskite compounds to see how the energetic ordering of the different structures varied.

4.1.1 The KTaO_3 (001) Surface

With the recent discovery of two-dimensional electron gases (2DEG) on the cleaved (001) surfaces of the wide gap insulators KTaO_3 [131, 132] and SrTiO_3 [133, 134], perovskite surfaces are now the focus of much increased attention. Previously, similar 2DEG had been observed at the interface between strontium titanate (SrTiO_3) and lanthanum aluminate (LaAlO_3) [135–137]. In contrast to the SrTiO_3 surface 2DEG, the KTaO_3 2DEG existed immediately after cleaving before the irradiation (although irradiation did allow for a tuning of the 2DEG). The difference in the formability of the 2DEG was hypothesised to be due to the polar nature of the (001) KTaO_3 surface.

As discussed in previous chapters, KTaO_3 is a typical ABX_3 perovskite material, possessing corner sharing TaO_6 octahedra with K ions situated in the holes. The formal charges of the ions in this material are K^+ , Ta^{5+} , and O^{2-} . This leads to alternating charged planes of KO^- and TaO_2^+ in the (001) direction, which results in Tasker type 3 surfaces [30] when bulk terminated. As mentioned in chapter 2, these surfaces are unstable due a dipole moment perpendicular to the surface that diverges with increasing slab thickness. In order for these surfaces to become stable they must undergo reconstruction such that the dipole is removed. This is usually achieved by the removal and/or addition of atoms at the surface.

While the surfaces of SrTiO₃ have been thoroughly investigated [64, 138–147], there is relatively little data on the KTaO₃ surface and, in particular, its structure.

Fritsch and Schroder [148] performed a computational study on the KTaO₃ (001) surface at the density functional theory level. They investigated (2 × 1) reconstructions of the KO terminated surface. The reconstruction was performed by removing every other row of KO resulting in a dipole free, stepped surface. A relaxation of this initial reconstruction proved to be the most stable surface configuration they found.

Li et al. [149, 150] performed elastic and inelastic helium atom scattering experiments on the KTaO₃ (001) vacuum cleaved surface. Their investigation revealed the presence of metastable periodic features immediately after cleaving. These metastable states were found to decay to a stable (1 × 1) surface over a few hours. Upon thermal cycling of the sample it was found that (2 × 1) and (1 × 2) surface domains were formed. These structures could be removed by heating to above 330 K. The surface was found to be KO dominant. A migration of potassium from the bulk to the surface was the suggested cause of the KO dominance. This result supported previous findings by Szot et al. [151] in which the (001) surface was subject to thermal treatment under oxidising conditions between 700°C and 1100°C. They also found cation segregation at the near surface region.

So, while there is a consensus on the KTaO₃ surface being KO rich, there is only one study in which an attempt has been made to characterise the exact atomic arrangement, and even then only limited arrangements were sampled. The surface is polar and so could reconstruct in many different ways. This chapter focuses on determining the atomic structure of the reconstructed KTaO₃ surface by means of global optimisation.

4.2 Interatomic Potentials (IP)

To successfully perform a surface structure global optimisation a vast number of structural arrangements will need to be considered. To ensure a sufficient number of configurations can be investigated within reasonable time and computational costs a fast, effective method of computation is required. Interatomic potential (IP) based calculations are faster than equivalent electronic structure calculations by orders of magnitude. Over the years IP have been shown to successfully model surface structures [126, 152–161]. This makes IP models ideal for surface structure global optimisation.

In chapter 3 potential parameters for KTaO₃ were fit against bulk properties. The K – O and Ta – O Buckingham interactions both possess non-zero values for the attractive $-C/r^6$ terms. As discussed in chapter 2, the potential energy of a Buckingham potential with a non-zero C term tends to $-\infty$ as $r \rightarrow 0$. Generally, this problem is not realised as sensible interatomic distances are chosen for calculations, and so r is sufficiently large that the energy of the system resides within a potential well. However, when performing global optimisations, atomic configurations may be produced where atoms

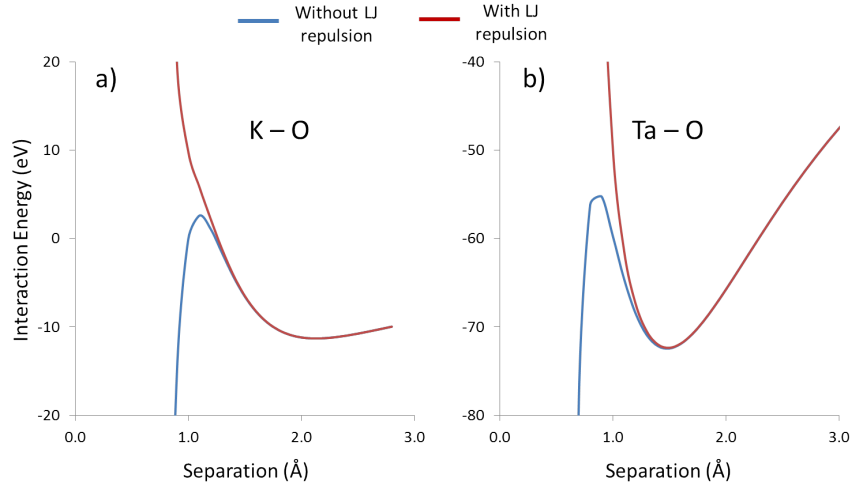


Figure 4.1: Interatomic pair potentials used in GULP calculations. a) is the K–O interaction, b) the Ta–O interaction.

do not lie within a potential well, but instead reside close to a neighbouring atom where the potential energy decreases infinitely with decreasing separation. In these cases, the dispersion term will cause atoms to collapse on top of each other. To compensate for this, repulsive LJ B/r^{12} terms were introduced, where $B = 10 \text{ eV } \text{\AA}^{-12}$ for both the K–O and Ta–O interactions.

Figure 4.1 highlights the change the LJ term had on the IP energy as a function of separation distance r . At distances greater than the equilibrium r_0 (bottom of energy basin) the LJ term has no effect. As r gets smaller than r_0 , the LJ term acts to put in place a new potential barrier that tends to $+\infty$ as $r \rightarrow 0$ thus preventing atoms getting too close.

4.3 A Polar Surface

As previously mentioned, the KTaO_3 (001) surface is a Tasker type 3 surface. These surfaces are considered unstable due the intrinsic dipole they possess perpendicular to the surface when bulk terminated. To stabilise these surfaces a reconstruction must occur such that the dipole is removed.

To highlight the surface instability the visual interface package GDIS was used to create (001) bulk terminated KTaO_3 slabs suitable for GULP two-region surface calculations. There are two different (001) terminations, the KO^- layer, and the TaO_2^+ layer. For the atomistic surface calculations a region 2 (fixed region) with a thickness of six unit cell layers was used. This led to convergence better than 0.0001 Jm^{-2} . Slab relaxations were performed for different sizes of region 1 while the size of region 2 was held fixed. For each termination two calculations were performed: one in which only ion cores were considered, and another in which shells were included. To calculate the

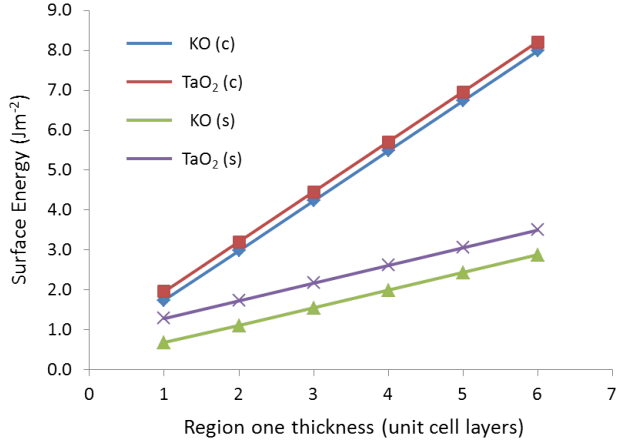


Figure 4.2: Surface energies of bulk terminated surfaces. (c) indicates core only calculations. (s) indicates shells were included in the calculations.

surface energies ($E_{surface}$) equation (4.1) was used:

$$E_{surface} = \frac{E_{region1} - nE_{Bulk}}{A} \quad (4.1)$$

where: $E_{region1}$ is the energy of region 1, E_{Bulk} the lattice energy of one unit cell, n the number of bulk units contained in region 1, and A the surface area of the slab cell being modelled; see chapter 2 for more details.

Figure 4.2 shows the relaxed surface energy of the surface models as a function of region 1 thickness. In all of the calculations the surface energy appears to diverge with increasing thickness. The KO termination is seen to be slightly more stable than the TaO₂ termination both in the core only calculation and the shell calculation. Incorporating shells results in a polarisation effect that opposes the dipole and slows down the surface energy divergence. The inclusion of the shells also opens the gap in surface energy between the KO and TaO₂ terminations. The gap is likely due to the greater polarisability of the surface K ions compared to the Ta ions. In all cases, however, the surfaces are unstable, as indicated by the diverging surface energy.

4.3.1 Reconstructed Surface

To overcome the problem of the dipole a 2 x 2 surface slab is created and then reconstructed by removing half of the top layer x below the bottom layer. Figure 4.3 highlights this reconstruction for a model 2 x 2 two-region KO terminated slab. The green shaded region represents region 2 in which the atoms are fixed during any geometry relaxations. This region must also be reconstructed to ensure charge neutrality within both regions. The same process is applied to the TaO₂ terminated slab. These reconstructions result in surfaces that are free of any dipole moment perpendicular to the surfaces due to a symmetric charge distribution about the slab centre.

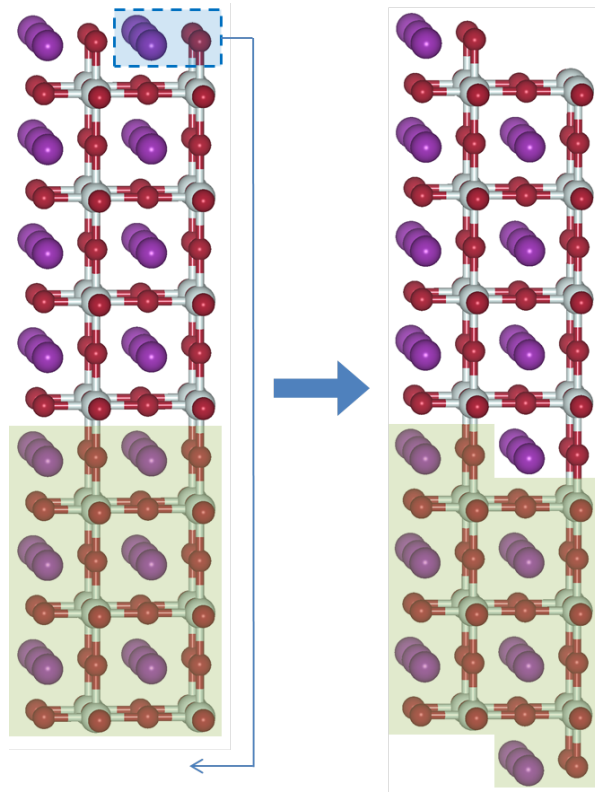


Figure 4.3: Initial reconstruction of the 2 x 2 slab

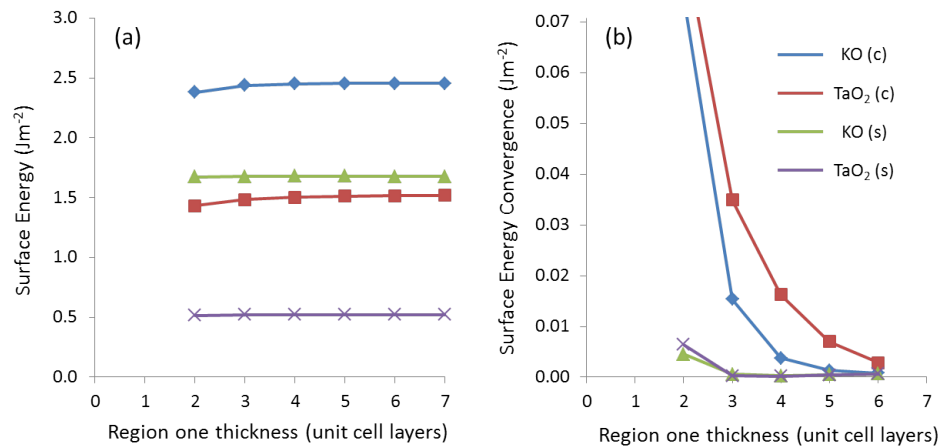


Figure 4.4: (a) Surface energies of the 2 x 2 reconstructed slab. (b) Surface energy convergence of the 2 x 2 reconstructed slab. The surface energy convergence is calculated as $|S_n - S_{n+1}|$ where S_n is the surface energy for n layers thickness

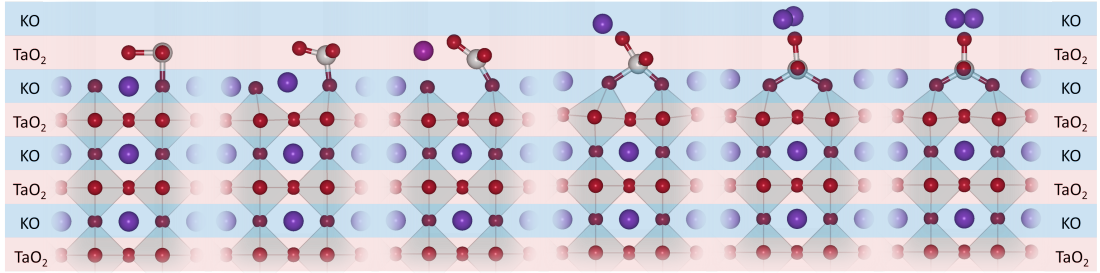


Figure 4.5: An interlayer reconstruction process that occurs during the geometry relaxation of the KTaO_3 (001) half TaO_2 terminated surface. Goes from left to right.

As with the 1×1 surface, the 2×2 surfaces were relaxed using both the core only and core-shell models on a number of slabs where the thickness of region 1 was varied. Figure 4.4 shows the surface energies for the different models (a) and the surface energy convergence (b) as a function of region 1 thickness. It is found that the energy of the reconstructed TaO_2 surface converges faster than the KO surface. The TaO_2 surface has a energy convergence of less than 0.01 Jm^{-2} at a region 1 thickness of two unit cells for both core only and core-shell models, whereas the KO surface requires a thickness of four unit cells to achieve a similar convergence.

Interestingly, the TaO_2 surface has become more stable than the KO termination after the reconstructions. This is the result of an interlayer reconstruction that has occurred during the geometry relaxation procedure within GULP. Figure 4.5 are snapshots taken at different steps of the relaxation which highlight the interlayer reconstruction process. From the initial half TaO_2 terminated surface the two K ions positioned in the sub surface layer below the occupied surface O row push up towards the surface. The oxygen in the row above rise in response. As the rising potassiums get closer to the top of the surface, the surface tantalums fall into the vacated row below, but are located half a (1×1) unit cell (2 \AA) further along the row than the K ions were. This results in a mixed sub-layer (layer directly beneath the outer most surface layer) which can be perceived as alternating unit cell rows of KO and TaO_2 . At the top layer oxygen resides directly above the sub-layer tantalums with K ions taking up positions slightly above the O ions and on either side of the row. The resulting surface structure is a KO zig-zag pattern in which K resides at the zig-zag corners. Thus, this structure is labelled the K-cornered zig-zag surface and is discussed in more detail later on.

4.4 Global Optimisation and KLMC

The Knowledge Led Master Controller (KLMC) [65, 66], an the in-house code, was employed to perform the global optimisation. Many of the features of KLMC have been discussed in chapter 2.

In the global optimisation of the KTaO_3 surface the solid solutions routine of KLMC

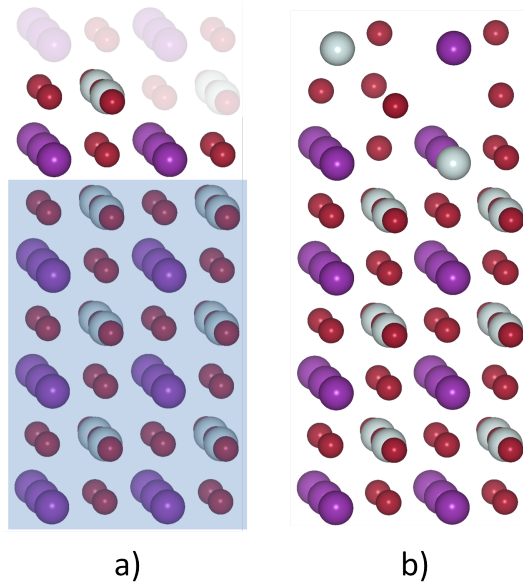


Figure 4.6: A KLMC reconstruction process of the half TO_2 terminated surface. (a) represents the initial configuration in a typical KLMC solid solution surface run. The faded atoms represent unoccupied lattice sites which are available for occupation during the KLMC reordering. Atoms positioned within the blue region will not be involved in the KLMC reordering process. (b) shows an example structure created by the KLMC re-ordering process

was employed. This method works by redistributing the ions over a given set of lattice points under imposed restrictions. An initial configuration of the system may include unoccupied lattice sites. KLMC will then redistribute the ions in a Monte-Carlo (MC) fashion. Restrictions can be imposed on the redistribution by labelling each lattice site. A lattice site can be labelled so that it does not take part in the MC step or to ensure that ions can only switch with like-labelled lattice sites. The cost function used in the global optimisation is the energy of a two-region surface model implemented in the GULP code.

Figure 4.6 shows: (a) an example of an initial atomic set up of region 1 within KLMC, and (b) an example atomic arrangement after a single KLMC MC step. The main difference between the KLMC and GULP input is that the lattice sites in region 1 were divided into 3 types. The first type of lattice site contains atoms that are to be held fixed during each KLMC MC step. These are shown in the region shaded blue. The second type of site contains atoms to be involved with the MC process. The last site are unoccupied sites and are shown as faded atoms. These sites can become occupied during the MC process by atoms moving from the second type of site. The site the atom moved from will then become an unoccupied site.

To ensure a thorough search of energy landscape was completed, the number of layers involved in the KLMC process varied between runs. The reason behind this is that when

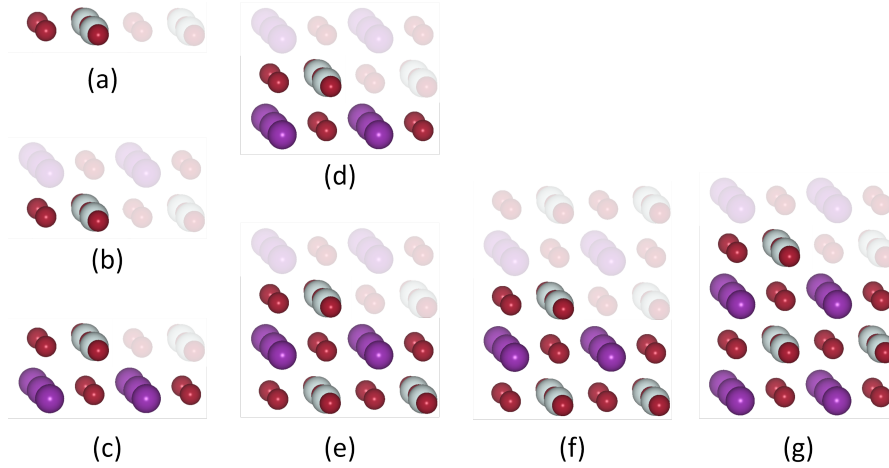


Figure 4.7: The seven different initial KLMC set ups showing only the lattice sites involved in the KLMC Monte-Carlo process of the half TaO_2 terminated surface. Below each of the images shown would exist the rest of the slab

the search space is smaller, the likelihood of exploring the entirety of it is more likely, i.e. there are fewer combinations to test. However, the smaller search space may not include the global minimum. Thus, by performing the separate searches the smaller landscapes can be entirely covered, while the larger ones are at the very least sampled. Figure 4.7 shows the seven different KLMC set ups for the half TaO_2 terminated surface, where only atoms involved in the ion redistribution are included: (a) only the half terminated surface layer and its corresponding empty lattice sites; (b) the surface layer and one empty layer above; (c) the surface layer and one occupied layer below; (d) the surface layer, one layer below, and one layer above; (e) the surface layer, two layers below, and one layer above; (f) the surface layer, two layers below, and two layers above; (g) the surface layer, three layers below, and one layer above. The same seven KLMC set ups are also applied to the half KO terminated surface. For each of these set ups two different type of runs were performed. The first type allows any of the different species to occupy any of the lattice sites. The second type enforces a restriction such that only the cations (K and Ta) can occupy the standard cation lattice sites, while the oxygen can only occupy oxygen lattice sites.

4.5 Stable Atomistic Reconstructions

After the global optimisation runs were completed the lowest energy surfaces from both terminations were inspected. A summary of the findings is given in section 4.5.3 including surface energies and key interatomic distances and angles presented in Table 4.1. The z-position (height perpendicular to surface) of the layer planes is taken to be an average of all the atoms associated with that plane.

4.5.1 IP KO Terminated Reconstructions

The lowest energy half KO terminated surfaces found from the global optimisation are discussed first. These reconstructions are less interesting than the TaO₂ terminated reconstructions as well as higher in energy. However, they are presented so the TaO₂ reconstructions can be compared against them. The TaO₂ reconstructions are discussed in section 4.5.2.

KO Termination: K-cornered Zig-zag Surface (1.52 Jm^{-2})

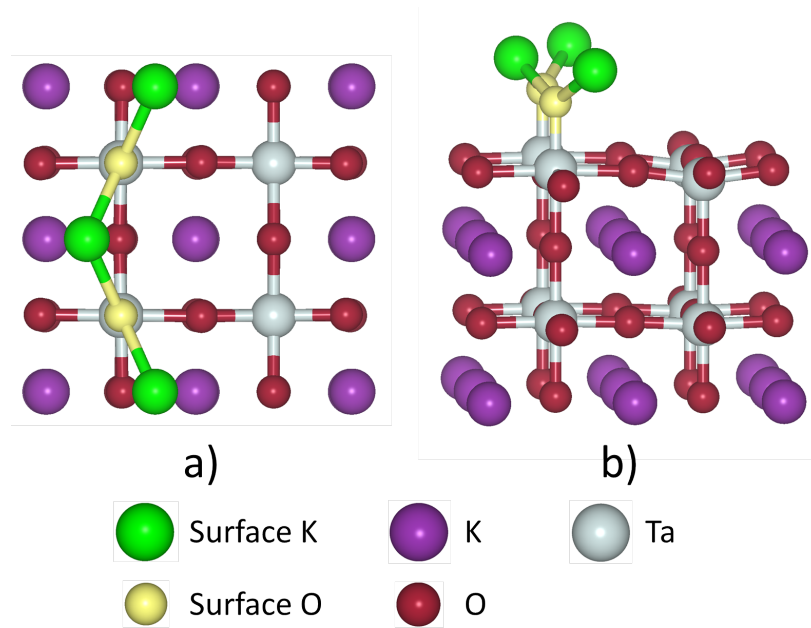


Figure 4.8: KO terminated reconstruction: K-cornered zig-zag surface arrangement. a) top view. b) side view.

The most stable reconstruction of the half KO termination was the K-cornered zig-zag surface. This is illustrated in Figure 4.8. The surface layer consists of KO zig-zag chains with K situated on the corners. The potassium is located 1.02 \AA further above the surface than the oxygen. The O ions in this layer are positioned in rows directly above the sub-layer Ta ions with a bond distance of 1.84 \AA . The K ions are arranged on alternating sides of the O rows at a horizontal separation of 0.89 \AA from the row. This results in a K–O bond distance of 2.41 \AA , much smaller than the bulk separation of 2.82 \AA due to the under-coordination at the surface. The surface O–O separation is 3.99 \AA and the surface K–K separation is 4.37 \AA . The corner O–K–O angle is found to be 111.5° , while the K–O–K angle, arising purely from the difference in z-position of the ions, is 129.7° .

The sub-layer is (001) bulk-like TaO₂ plane having not changed significantly from the initial input geometry. The distance between the sub-layer and the surface plane is

found to be 2.44 Å (1.93 Å to the surface oxygen, 2.95 Å to the potassium), an increase in the separation of the layers compared to the bulk. The sub-layer Ta ions below the surface O are positioned slightly above the plane (0.09 Å), while the sub-layer O lying along the same row between these Ta ions move downwards (0.15 Å) towards the slab centre. The rows in which the Ta ions are exposed to the surface are under-coordinated (5-coordinated) and show the opposite behaviour. The Ta ions move downwards (0.19 Å) and the O move upwards (0.15 Å). The oxygen ions not lying in the Ta rows move closer towards the 5-coordinated Ta ions, forming smaller bonds of length 1.90 Å, and away from the 6-coordinated Ta ions (2.10 Å). This is likely due to two complementary effects, a stronger O–O repulsion at the Ta 6-coordinated ions because of the short bonded surface O, and a reduced repulsion at the 5-coordinated Ta ions as there is no surface O present.

The 3rd layer (layer below sub-layer) has an inter-planar separation of 2.03 Å to the sub-layer and 2.01 Å to the layer below, suggesting the bulk-like separation of 1.99 Å is being more closely adhered to. The greatest shift out of plane is experienced by the O atom directly below the 5-coordinated sub-layer Ta. The downward shift of the tantalum has pushed the oxygen 0.09 Å below the plane. All other vertical shifts are less than 0.04 Å. The K ions on this layer have moved away from the 5-coordinated Ta row in an opposite fashion to the O only rows in the sub-layer. In the next layer below all ionic displacements are less than 0.03 Å.

Subsequent surfaces are discussed in a similar level of detail and the reader is advised to move to section 4.5.2 if the finer details are not of great interest.

KO Termination: KO Island Surface (1.64 Jm⁻²)

The second most stable KO terminated reconstruction is the KO island surface shown in Figure 4.9 As the name suggests the surface layer contains square K–O–K–O islands. As with the K-cornered reconstruction the K ions reside higher above the surface than the O ions with a vertical separation of 0.71 Å. This is 30% smaller than the 1.02 Å found for the K-cornered reconstruction. The difference is a result of the K – K repulsion. If the K–O vertical separation were much larger, the K–K distance would need to be greatly reduced, or the K–O bond length increased to increase the K–K separation. Neither of which appear to be as energetically favourable as reducing the K–K vertical separation above the surface. The surface K–O bond length is very similar to the K-cornered surface at 2.43 Å. The surface K–K separation is 3.31 Å much smaller than seen on the previous surface due to the new position taken up by the K ions. The surface O ions occupy similar positions as in the previous surface but have a reduced separation of 3.25 Å due to the presence of two K ions between them. The surface O–K–O angle is found to be 84.2°, while the K–O–K angle is found to be slightly larger at 86.0°. The bond length between the surface O and sub-layer Ta is 1.82 Å. The distance between the averaged surface layer and sub-layer is 2.25 Å, which is smaller than the equivalent

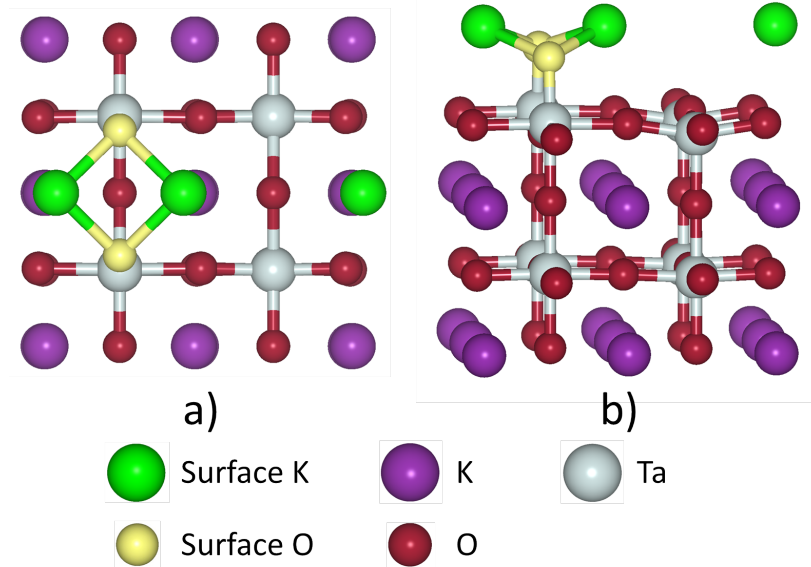


Figure 4.9: KO terminated reconstruction: KO island surface arrangement. a) top view. b) side view.

distance for the K-cornered surface due to the lower lying surface K ions. The relative heights of the ions in the sub layer are very similar to those seen for the previous surface. The sub-layer – 3rd layer separation and 3rd – 4th layer separation is found to be 2.04 Å and 2.01 Å, respectively.

KO Termination: O-cornered Zig-zag Surface (1.67 Jm^{-2})

The third most stable KO terminated reconstruction was the O-cornered zig-zag surface shown in Figure 4.10 The surface layer consists of KO zig-zag chains with K ions positioned in a line and O ions situated on the corners. This surface differs from the previous two in that the oxygen no longer reside on the same row. The surface K–O bond length is 2.61 Å which is almost 10% larger than the previous two surfaces. This is because the surface O ions are held rigidly in place by the sub-layer Ta ions, reducing how far the O ions can move towards the zig-zag centre line compared to the K ions in the previous surfaces. An additional consequence is a much larger O–O separation of 5.08 Å. The K–K separation is found to be 3.99 Å. The vertical separation between the K and O ions is found to be 0.63 Å, the smallest seen so far. The O–K–O angle is the largest seen so far at 152° and the K–O–K angle is 99.5°. The bond length between the surface O and sub-layer Ta is 1.81 Å. The distance between the sub-layer and surface is 2.20 Å reduced compared to the previous surfaces due to the reduced K–O vertical separation. As the surface O ions no longer lie in a row the distortion of the sub-layer is altered. The Ta ions directly below the O ions are located 0.12 Å above the plane while the other under-coordinated Ta ions lie 0.23 Å below the plane. The O ions on the same

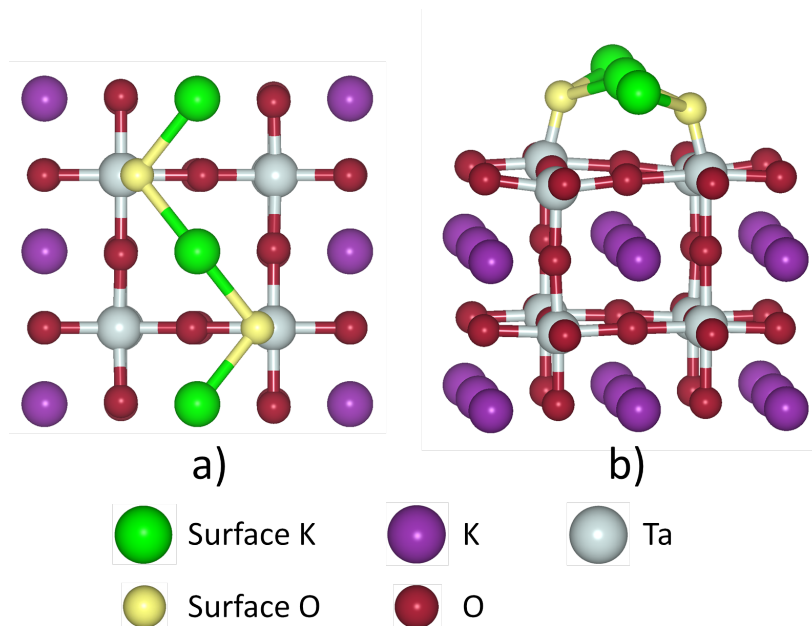


Figure 4.10: KO terminated reconstruction: O-cornered zig-zag surface arrangement. a) top view. b) side view.

row as the Ta ions lie 0.50 \AA above the plane. The O ions situated beneath empty rows lie 0.30 \AA above the plane. The O ions beneath the K ion row are the lowest lying set positioned 0.01 \AA below the plane. The sub-layer – 3rd layer separation and 3rd – 4th layer separation is found to be 2.03 \AA and 2.01 \AA respectively.

KO Termination: KO Diagonal Chain Surface (1.72 Jm^{-2})

Of the four KO terminated reconstructions presented, the KO diagonal chain surface shown in Figure 4.11 was found to be the least stable. The surface layer consists of a linear diagonal KO chain. Unlike the previous reconstructions all the K–O distances at the surface are unique. The K–O bond at the bottom left of Figure 4.11 is found to be 2.41 \AA which is similar to the bond distances seen on the other surfaces. The distance from this O to the K at the centre of the cell, which are not drawn connected, is 3.47 \AA . The distance from the central K ion to the other O ion is 2.38 \AA the smallest KO bond length seen. The distance from this O to the corner K ion is 3.37 \AA . The O ions lie at the same height but the K ions differ in height by 0.02 \AA , the K ion at the centre of the cell being the higher lying. This leads to vertical K–O separations of 0.67 \AA and 0.69 \AA . The oxygen are also seen to be displacing slightly towards the bottom left corner relative to the Ta below them. Due to the diagonal arrangement the O–O and K–K separation are all large varying between 5.55 \AA to 5.70 \AA . The asymmetry of the surface appears to be a result of the K ion positions. The bond distance between the surface O and sub-layer Ta ions is 1.81 \AA , the same as in the O-cornered surface. The distance between the surface and sub-layer planes is 2.26 \AA . The sub-layer plane is arranged similarly to

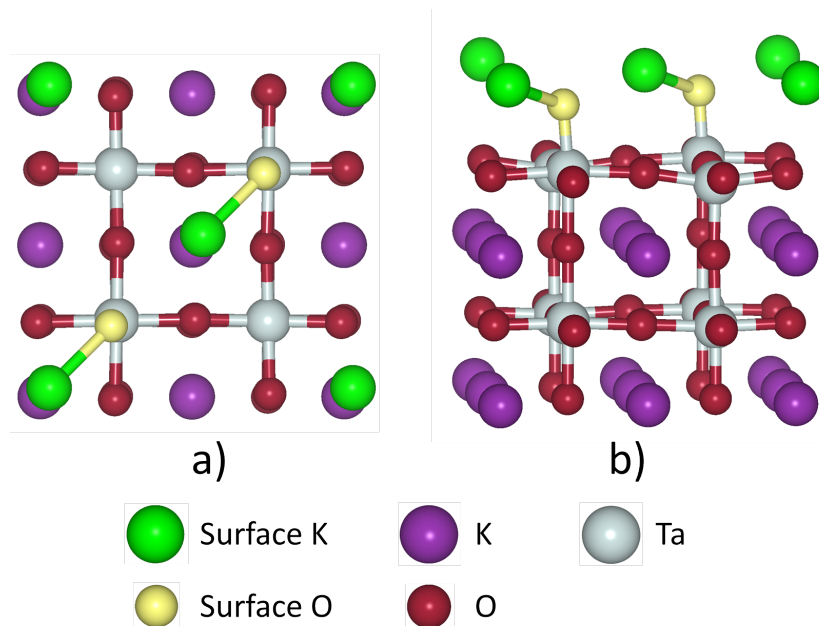


Figure 4.11: KO terminated reconstruction: KO diagonal chain surface arrangement. a) top view. b) side view.

the O-cornered surface. The Ta ions below the surface O ions are located 0.12 \AA above the plane and the other under-coordinated Ta ions lie 0.23 \AA beneath the plane. The sub-layer O ions with the smallest horizontal component of separation to the surface K ions are the lowest lying O ions; there are four of this type. The two O ions closest to the central surface K ion lie 0.02 \AA above the plane and the other two lie exactly on the plane. The remaining four O ions in this layer are positioned 0.05 \AA above the plane. The sub-layer – 3rd layer separation and 3rd – 4th layer separation is found to be 2.03 \AA and 2.01 \AA respectively, exactly the same as in the O-cornered surface.

4.5.2 IP TaO₂ Terminated Reconstructions

For the half TaO₂ termination the reconstructions were much more interesting. The most stable surfaces were produced by not only a re-arrangement of the surface layer but also of the sub-layer. This new reconstruction mechanism was discussed previously and was shown in Figure 4.5. The reconstruction results in a KO surface layer similar to the KO-terminated reconstructions and a mixed sub-layer containing both KO and TaO₂. Figure 4.12 shows this sub-layer, which can be described as alternating rows of bulk-like KO and TaO₂. Below, the two most stable reconstructions are discussed.

TaO₂ Termination: K-cornered Zig-zag Surface (0.52 Jm^{-2})

The most stable half TaO₂ terminated reconstruction is the K-cornered zig-zag surface shown in Figure 4.13. This has a similar surface arrangement to the most stable KO

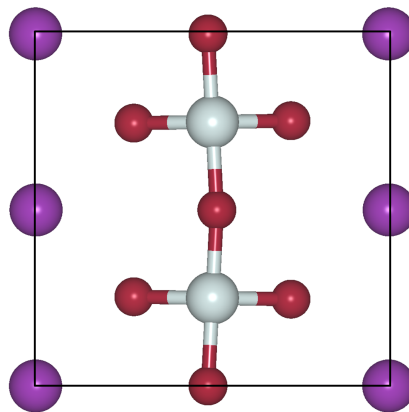


Figure 4.12: The stable mixed sub-layer produced during reconstructions of the half TaO₂ terminated surface.

terminated reconstruction. Both possess K-cornered KO zig-zags across the surface. In the case of the TaO₂ terminated reconstruction, the surface layer K and O ions have a greater vertical separation of 1.15 Å. This allows the K ions to approach much closer to the O ion row making the zig-zag corners appear more obtuse when viewed from above, but more acute when viewed from the side. The O–K–O angle is found to be 117.3° and the K–O–K angle is 121.1°. The effect of the new K position has been to increase the O–K–O angle while reducing the K–O–K angle when compared to the analogous surface layer for the KO reconstructions. The K–O bond distance is also slightly smaller at 2.3 Å. The O–O separation is found to be 3.99 Å and the K–K separation is 4.07 Å. As is the case in all previous reconstructions, the surface O ions are located directly above Ta in the sub-layer. This Ta–O bond distance is 1.86 Å, slightly larger than for all previously discussed reconstructions.

The most interesting feature, and major difference from previous surfaces, is that the sub-layer is split into rows of TaO₂ and KO units. Pre-reconstruction the sub-layer would have been a KO plane while the surface would have been TaO₂. However, during the reconstruction the TaO fell into the sub-layer while K migrated to the surface. The mixed sub-layer is much less planar than for previous reconstructions with the difference between the highest and lowest lying ions being 0.99 Å. The highest positioned atoms on this plane are the Ta and O that lie in the same row. The O resides 0.53 Å and the Ta 0.39 Å above the plane. The K ions are located 0.02 Å below the plane, and the remaining O are situated the lowest, 0.45 Å below. The reason for the low lying O is likely due to the strong attraction felt from the Ta in the plane below directly beneath these O ions and the lack of any countering attraction above.

The separation between the sub-layer and 3rd layer is 2.38 Å, very large compared to the previous reconstructions. The bond between the O ion on third layer and the high lying Ta ion in the sub-layer is stretched to 2.68 Å, a third larger than the typical bulk bond distance. The 3rd – 4th and 4th – 5th layer separations are much more bulk

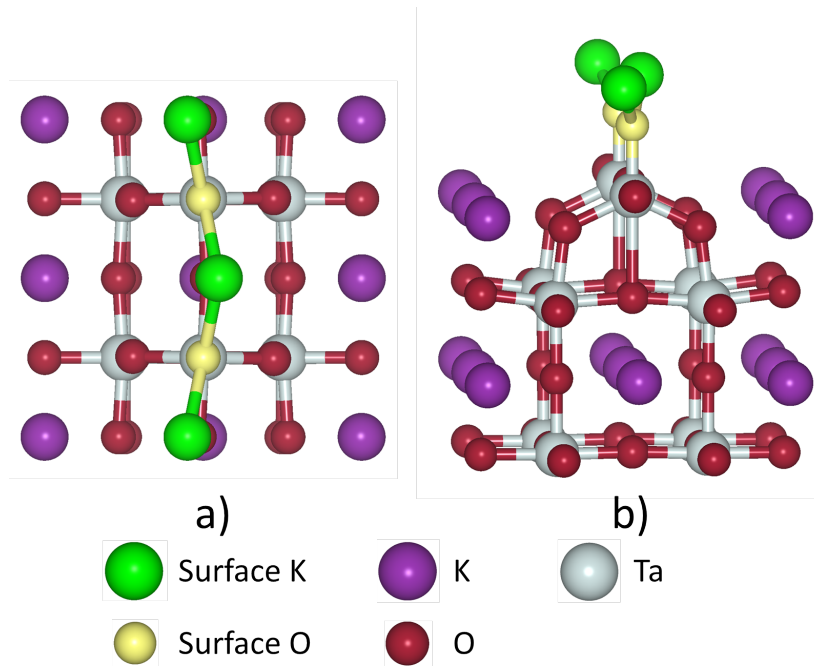


Figure 4.13: KO terminated reconstruction: K-cornered zig-zag surface arrangement. a) top view. b) side view.

like at 2.02 Å and 2.00 Å respectively.

TaO₂ Termination: KO Island Surface (0.84 Jm⁻²)

The next most stable TaO₂ terminated reconstruction is the KO island shown in Figure 4.14. As with the KO terminated KO island reconstruction, this surface has square K–O–K–O islands residing at the top layer. The vertical separation between the K and O in the island is 0.66 Å, slightly smaller than for its KO reconstructed counterpart. This has the effect of increasing the O–K–O angle to 88.5° and reducing the K–O–K angle to 83.0° when compared to the equivalent KO terminated reconstruction. The surface K–O bond length is found to be 2.41 Å, 0.02 Å smaller than its KO terminated counterpart. The O–O separation is found to be 3.36 Å and the K–K separation 3.19 Å. The bond between the surface O and sub-layer Ta is 1.86 Å, and the planar separation between the surface and sub-layer is large at 2.56 Å. The arrangement of the atom in the sub-layer is the same as for the other TaO₂ terminated reconstruction with some minor modifications to the vertical position of the atoms. The Ta and O on the same row are again situated high above the averaged plane. The Ta reside 0.41 Å above. Of the two O ions in this row, the one furthest from the surface K ion is positioned 0.49 Å above the plane, whereas the other surface O ion lies substantially lower, only 0.21 Å above the plane. The sub-layer K ion that forms a horizontal line with the surface K ions is positioned 0.11 Å below the plane. The other sub-layer K ion lies 0.08 Å above the plane. The remaining O ions reside 0.38 Å below the plane strongly attracted to

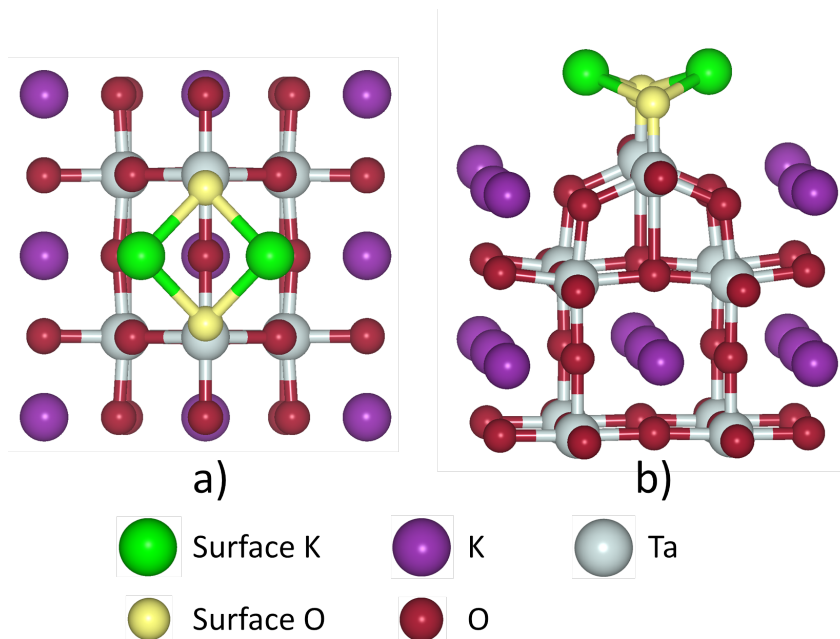


Figure 4.14: KO terminated reconstruction: KO island surface arrangement. a) top view. b) side view.

the Ta in the layer below.

As with the other TaO₂ reconstruction the sub-layer 3rd layer separation is large 2.31 Å, with the sub-layer Ta 3rd layer O bond being stretched to 2.60. The 3rd – 4th and 4th – 5th layer separations are again more bulk like at 2.02 Å and 2.00 Å.

4.5.3 Summary of Atomistic Surfaces

Table 4.1 gives the surface energy and some of the key interatomic distances and angles for the different reconstructions. There is a large difference in the surface energy ($\sim 0.7 \text{ Jm}^{-2}$ / $\sim 0.04 \text{ eV } \text{Å}^{-2}$) between the half TaO₂ terminated and half KO terminated reconstructions. The sub-layer of the TaO₂ terminations undergoes a rearrangement during the reconstruction process going from a standard KO bulk-like plane to a mixed plane consisting of rows of TaO₂ and KO, which is more rumped. The sub-layer of the KO terminations does not undergo any rearrangement and remains a bulk-like TaO₂ plane. The result of the TaO₂ mixed sub-layer is that all Ta ions are six-coordinated, which is not the case in the KO reconstructions where two Ta ions are five-coordinated. The maximising of the Ta coordination is proposed to be energetically favourable and thus why the TaO₂ reconstructions are so low in energy.

For all reconstructions the surface is made up purely of KO units. The lowest energy surface configuration for both terminations was the K-cornered zig-zag (Figures 4.8 and 4.13). This had the largest surface K–O vertical separation, given by Δz K–O in Table 4.1.

Table 4.1: **Surface energy and key inter-atomic distances for the most stable GULP reconstructions.** γ is the surface energy. K–O the bond length between surface K and O ions. O–O and K–K the smallest separation between like-species at the surface. Ta–O the bond length between the surface O and sub-layer Ta ions. O–K–O and K–O–K are the angles between surface ions. Δz K–O is the vertical separation between K and O ions on the surface. Δz L_1 – L_2 the separation between the surface and sub-layer planes. Δz L_2 – L_3 is the separation between the sub-layer and 3rd layer planes. The height of the plane is calculated as the average height of all atoms considered to be in that plane. The surface arrangements are abbreviated as K-c (K-cornered zig-zag), Island (KO island), O-c (O cornered zig-zag), Diagonal (KO diagonal chain).

Termination:	TaO ₂		KO			
	K-c	Island	K-c	Island	O-c	Diagonal
γ (Jm ⁻²)	0.52	0.84	1.52	1.64	1.67	1.72
K–O (Å)	2.34	2.41	2.41	2.43	2.61	2.38/2.41
O–O (Å)	3.99	3.36	3.99	3.25	5.08	5.68
K–K (Å)	4.07	3.19	4.37	3.31	3.99	5.71
Ta–O (Å)	1.86	1.86	1.84	1.82	1.81	1.81
O–K–O (°)	117.3	88.5	111.5	84.2	152.0	151.1
K–O–K (°)	121.1	83.0	129.7	86.0	99.5	151.9
Δz K–O (Å)	1.15	0.66	1.03	0.71	0.63	0.68
Δz L_1 – L_2 (Å)	2.82	2.56	2.44	2.25	2.20	2.26
Δz L_2 – L_3 (Å)	2.38	2.31	2.03	2.04	2.03	2.03

The second most stable surface configuration for both terminations was the KO island (Figures 4.9 and 4.14). The KO island differs from the K-cornered arrangement by the repositioning of one K ion turning the zig-zag chains into square island. The new position of the K ion results in a shorter K–K separation and thus stronger K–K repulsion. A compensatory reduction in Δz K–O and a slightly increased K–O bond length are also observed. The differences between the K-cornered and KO island surface layer structure are more pronounced for the TaO₂ reconstructions. This is reflected in the larger energy gap of 0.32 Jm⁻² between the two different surface layer structures for the TaO₂ reconstructions when compared to a gap of 0.12 Jm⁻² for the KO reconstructions.

For the KO terminated reconstructions, there were two other stable surface arrangements found, the O-cornered zig-zag (c.f. Figure 4.10) and the KO diagonal chain (c.f. Figure 4.11). On these surfaces, O ions do not lie in a row as in the K-cornered and KO island arrangements, but are instead located on alternating rows resulting in a much increased O–O separation. These surface configurations are unable to form during the TaO₂ reconstructions as the mixed sub-layer only has Ta ions in one row and the surface O ions always prefer to be positioned directly above Ta. As the surface O ions are held more rigidly in place by the Ta ions below, they are less able to approach the row of K ions in the O-cornered arrangement than the K ions were able to approach the O row in the K-cornered arrangement. This results in a much longer bond length of 2.61 Å, which is likely the cause of the greater surface energy. The increased O–O separation

compensates for this, but to a smaller degree.

For the KO diagonal case the bond length should be even greater. It appears, however, that rather than having two long K–O bonds, it is more favourable for one of the bonds to shorten at the expense of the other lengthening. This results in one short bond ~ 2.4 Å and one long ~ 3.4 Å. The long bond is not drawn in Figure 4.11 for clarity.

In summary, the half TaO₂ terminated reconstructions are found to be most stable and involves an atomic rearrangement of both the surface layer and sub-layer. The half KO terminated reconstructions only involved an atomic rearrangement on the surface layer. A mixed sub-layer was found for the TaO₂ terminated reconstructions consisting of alternating rows of KO and TaO₂ bulk-like units, which is more heavily ruffled compared to the bulk-like TaO₂ sub-layer seen for the KO terminated reconstructions. The mixed sub-layer is formed by the demotion of TaO from the surface to the sub-layer and the promotion of K to the surface. This results in all Ta being fully coordinated, which is expected to play a major role in the stabilisation of the KTaO₃ surfaces.

4.5.4 The 4 x 4 Surface

The discovery that a mixed sub-layer has a large stabilisation effect upon the polar (001) KTaO₃ surface opens up many avenues to explore in regards to sub-layer reconstruction. The investigation of sub-layers for different surface sizes is another project onto itself and beyond the scope of this thesis.

The 2 x 2 sub-layer contains alternating rows of bulk like KO and TaO₂ units. One question of interest is as to whether the KO and TaO₂ units might favour congregating together on a larger surface rather than alternating. To answer this question a 4 x 4 surface was created that had two KO rows together followed by two TaO₂ rows. Figure 4.15 shows the test reconstruction after a geometry relaxation. The surface K and O

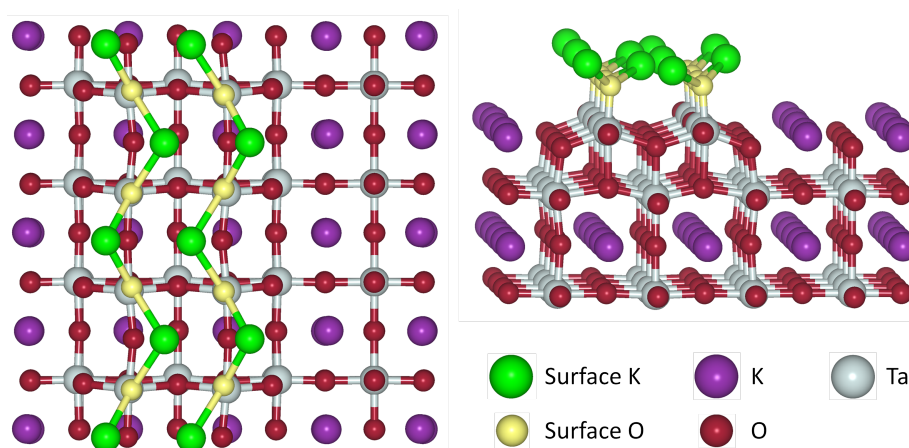


Figure 4.15: A 4x4 TaO₂ terminated reconstruction possessing a mixed sub-layer.

ions are arranged in such a way as to form two parallel K-cornered zig-zag chains. The entire surface layer, as well as the sub-layer Ta ions and the O bonded to them, shift

horizontally in the direction of the row (downwards in the overhead view seen in Figure 4.15). The K-cornered zig-zag chains appear to contract and expand about the K ions. The K ions that bend away from the centre of the two zig-zags have K–O bond lengths of 2.41 Å and 2.38 Å. The shorter of the two bonds is in the same direction that the surface leans. The other K ions that point towards the centre of the zig-zags have longer K–O bond lengths of 2.54 Å and 2.61 Å. The shorter of the two bonds again in the direction of the surface lean. The sub-layer O beneath the inner surface K ions in the Ta row bend towards the inner surface K. The surface energy calculated for this structure was 0.83 Jm^{-2} which is greater in energy than the previously found 2×2 ground state (0.52 Jm^{-2}). Thus, at a first glance the TaO₂ and KO rows in the sub-layer prefer to alternate as can be modelled in the 2×2 surface reconstructions.

4.6 DFT Refined Surfaces

To analyse the electronic structure of the surface, the KTaO₃ reconstructions were refined with DFT using VASP. As VASP requires periodic boundaries in all directions, the two-dimensional, one-sided slabs modelled in GULP must be converted to two sided, symmetric slabs that repeat periodically in the direction perpendicular to the surface, with a vacuum gap separating the slab from its images. As the slab is now two sided, the area, A , considered in equation 4.1 becomes $2A$; see chapter 2 for more details.

The symmetric slab was created by taking half the number of required layers from the top of the GULP 2-D slabs, and then reflecting this in the direction perpendicular to the surface to produce a double sided symmetric slab. The cell size was adjusted to match the DFT optimised bulk lattice parameter as described in chapter 3. The slab used contained 160 atoms which is equivalent to eight 2×2 unit cell layers (combined KO and TaO₂ layer) or 17 individual layers (the two surface layers were only half populated). The difference in surface energy between an 8 unit cell layer slab and a 7 unit cell layer slab was found to be less than 0.005 Jm^{-2} , indicating good convergence. The geometry relaxations were considered converged when the forces on all atoms were less than 0.01 eVÅ^{-1} . The vacuum gap between the periodic slabs was set to be 18 Å, which gave a surface energy convergence of less than 0.01 Jm^{-2} ($< 0.001 \text{ eVÅ}^{-2}$).

In addition to the six reconstructions obtained from GULP three other surfaces were relaxed. The first was the KO terraced surface modelled by Fritsch and Schroder [148] that was also used as the initial configuration for the global optimisations of the half KO terminated surface (Figure 4.3). The second was the same KO surface layer arrangement used by the first additional model, but residing on top of the mixed sub layer, i.e. a TaO₂ terminated reconstruction. The third was a TaO₂ terraced structure used as the initial model for the TaO₂ terminated reconstructions (Figure 4.6). These three surface structures, when tested using the atomistic approach in GULP, reconstructed to one of the other previously presented surface arrangements.

Before performing the DFT calculations on the 2×2 structures, stoichiometric 1×1 surfaces were tested to prove that the reconstructed surfaces were necessary. Four slabs of varying thickness were tested. The thicknesses were 4, 5, 6, and 7 unit cell layers and the surface energies recorded were 0.88, 0.93, 0.98, and 1.02 Jm^{-2} respectively showing a lack of surface energy convergence with respect to slab thickness. Thus, the reconstructions are also proved necessary at the DFT level.

A plane wave cut-off of 500 eV – the same used for the bulk calculations in chapter 3 – was used for all surface calculations. For the 1×1 surface a Γ -centred $6 \times 6 \times 1$ k-point mesh was used. For the 2×2 surface a Γ -centred $3 \times 3 \times 1$ k-point mesh was used. A summary discussion of the surfaces is given in section 4.6.3 accompanied by Table 4.2, which contains some of the key data associated with the surfaces, analogous to Table 4.1 for the GULP surfaces. The KO terminations are again discussed first, skip to 4.6.2 for the TaO_2 reconstructions.

4.6.1 DFT KO Terminated Reconstructions

KO Termination: KO Diagonal Chain Surface 1.04 Jm^{-2})

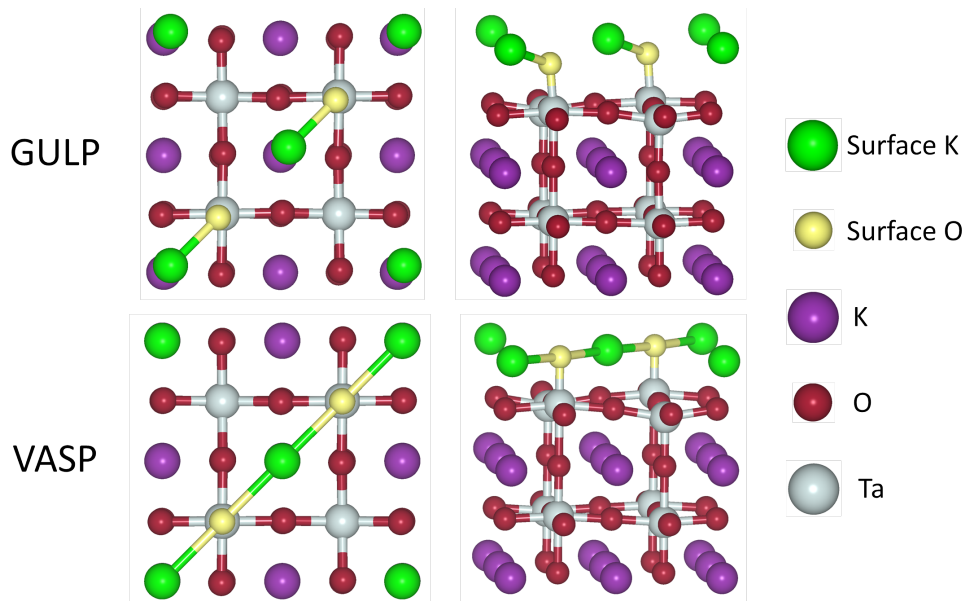


Figure 4.16: KO terminated reconstruction: KO diagonal chain surface arrangement.

Of the half KO terminated reconstructions the most stable according to DFT was the KO diagonal chain structure shown in Figure 4.16. This structure was the least stable of four KO reconstructions presented for the atomistic calculations. During the DFT refinement the surface has undergone some structural adjustments. The most obvious change is the position of the surface K ions. For the GULP structure the surface K ions preferred to be positioned closer to one of the surface O ions. After being run through VASP the surface K ions lie at equal distances from the O ions. The vertical separation

between the surface K and O ions has also decreased significantly from 0.68 Å in GULP to 0.05 Å in VASP meaning the surface plane is much flatter and less rumped. This results in a K–O bond distance of 2.82 Å. Due to the flatness of the plane the K–O–K and O–K–O bond angles are both 177.9° very close to 180° indicating a straight K–O–K–O line across the surface. As the surface K ions are equal distances from the surface O ions, the O do not shift in any direction and are seen to reside directly above a sub-layer Ta ion in contrast to what was seen in the GULP arrangement. The Ta–O bond length between the surface O and sub-layer Ta is reduced slightly from 1.81 Å to 1.79 Å. While the surface layer was found to be much more flatter the sub-layer became slightly more rumped. The Ta ions below the surface O ions were found to lie 0.19 Å above the plane up from 0.12 Å and the under-coordinated Ta sat 0.29 Å below the plane up from 0.23 Å. Due to the symmetry of the O positions they were found to all reside between 0.02 Å and 0.03 Å above the plane. The inter-planar distance between the surface and sub-surface was found to be 2.00 Å noticeably smaller than the 2.26 Å recorded for the GULP structure, this reduction clearly being due to the much flatter surface plane. The inter-planar distance between the sub-surface and the layer below (3rd layer) was found to be 2.10 Å a slightly increase from 2.04 Å. The rumpling on the 3rd layer, and KO layer, was found to be minor with the largest vertical separation found to be 0.06 Å. The rumpling of the 4th layer, a TaO₂ layer, was found to be slightly more substantial with a max vertical separation of 0.22 Å. This suggests the TaO₂ layers are more prone to feel the surface effects likely due to the tight Ta–O bonds between layers.

KO Termination: O-cornered Zig-zag Surface (1.06 Jm⁻²)

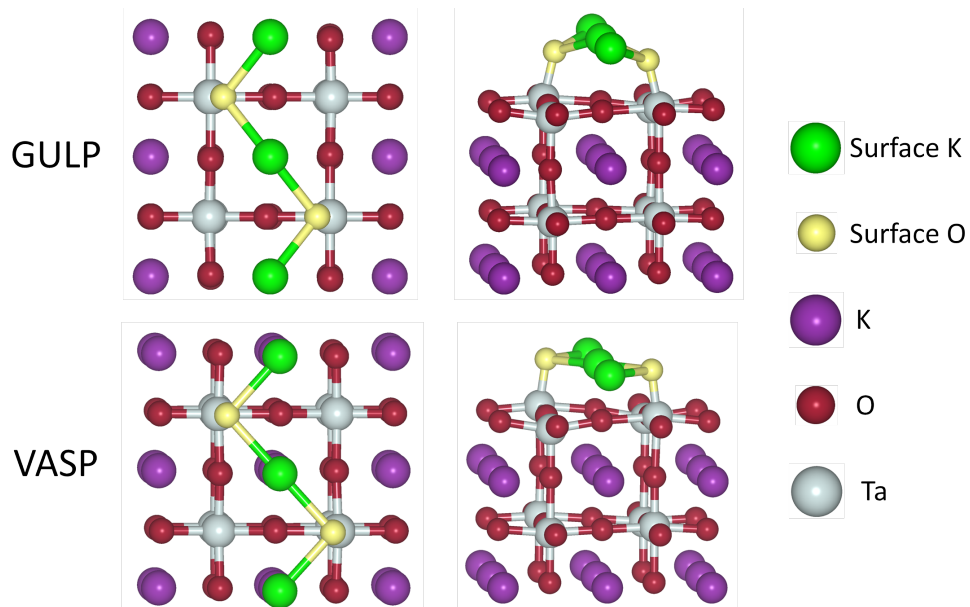


Figure 4.17: KO terminated reconstruction: O-cornered zig-zag surface arrangement.

The second most stable KO terminated reconstruction according to DFT was the O-cornered zig-zag structure shown in Figure 4.17. The relaxation in VASP has again had the effect of flattening the surface layer. The surface K–O vertical separation is 0.01 Å down from 0.68 Å making it the flattest surface layer of all structures analysed. As in the GULP structure, the surface O ion in the VASP arrangement shift towards the central K row although to a slightly lesser extent. The K–O bond distance is found to be 2.69 Å, slightly larger than the GULP equivalent of 2.61 Å. The K–K separation remains unchanged at 3.99 Å but the O–O separation is increased from the 5.08 Å to 5.38 Å due to the less pronounced shift of the O ion. The K–O–K angle is found to be 95.8° while the O–K–O angle is 179.5° indicating a straight line. The Ta–O bond length is 1.79 Å, 0.02 Å smaller than in the GULP structure. The VASP sub-layer is found to be slightly more rumpled than the GULP case. The Ta bonded to the surface O lies 0.20 Å above the plane up from 0.12 Å and the under-coordinated Ta lie 0.29 Å below the plane up from 0.24 Å. The sub-layer O ions positioned beneath the row of surface K ions, lie 0.04 Å above the plane. All other O ions in the sub-layer lie \sim 0.15 Å above the plane. The inter-planar distance between the surface and sub-layer is 1.98 Å and the distance between the sub-layer and the 3rd layer is 2.09 Å. The 3rd and 4th layers mirror the effects seen in KO diagonal chain surface with the 3rd layer (KO layer) having a rumpling of only 0.06 Å and the 4th layer (TaO₂ layer) having a much stronger rumpling of 0.23 Å.

KO Termination: K-cornered Zig-zag Surface (1.08 Jm^{-2})

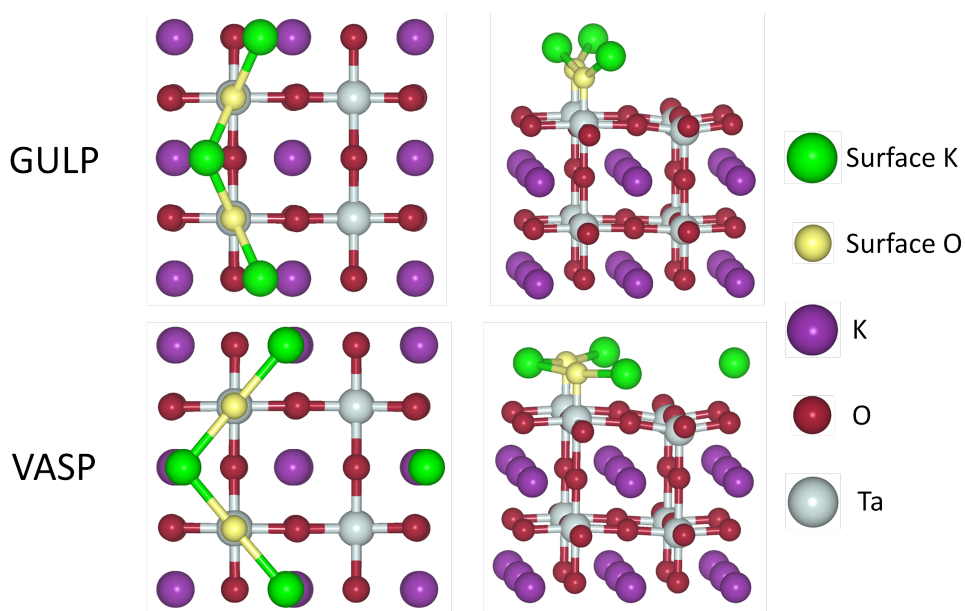


Figure 4.18: KO terminated reconstruction: K-cornered zig-zag surface arrangement.

The K-cornered zig-zag structure shown in Figure 4.18 was found to be the third most

stable KO terminated reconstruction according to DFT. As has been seen previously when going from the GULP structure to the VASP structure, the most prominent change is the position of the surface K ions. In the GULP structure the surface K–O vertical separation was 1.03 Å, the largest of all KO terminated reconstructions. After the DFT relaxation this distance is reduced to 0.20 Å, five times smaller than its GULP counterpart, representing another significant flattening of the surface layer. However, this distance is the largest seen for all DFT relaxed KO terminated reconstructions. The horizontal separation of the surface K ions to the row of surface O ions is in turn increased so that the K ions reside more closely to their ideal lattice sites. The K–O bond distance has thus been increased to 2.62 Å from 2.41 Å. The K–K separation has increased to 5.22 Å from 4.37 Å, while the O–O separation remains unchanged at 4.00 Å. The O–K–O angle is found to be 99.9° and the K–O–K angle is 171.5°, up from 129.7°. The Ta–O bond between the surface O and sub-layer Ta has a length of 1.80 Å, 0.04 Å smaller than seen in the GULP structure. The inter-planar distance between the surface and sub-layer is found to be 2.05 Å, the largest of all the VASP relaxed KO terminated reconstructions. The height of the atoms in the sub-layer has also changed slightly. In the GULP structure the highest lying ions were the O ions that lay in the same row as the under-coordinated Ta ions 0.16 Å above the plane. After the VASP relaxation the highest lying ions are the Ta bonded to the surface O 0.16 Å above the plane. The other lowest positioned ions are the under-coordinated Ta 0.26 Å below the plane up from 0.19 Å. The O in the under-coordinated Ta row lie 0.09 Å above the plane while the O in the other Ta row lie 0.08 Å below the plane. The remaining O reside 0.04 Å above the plane. The size of the rumpling in the 3rd and 4th layers are 0.09 Å and 0.19 Å which is a smaller difference than seen in some of the other VASP relaxed KO terminated reconstructions. The inter-planar distances between the sub-layer and 3rd layer and the 3rd layer and 4th layer are 2.08 Å and 2.03 Å respectively.

KO Termination: KO Terraced Surface (1.10 Jm⁻²)

The KO terraced structure shown in Figure 4.19 was the surface model created during the initial removal of the dipole. The structure proved unstable with the IP and instead reconstructed to the K-cornered arrangement. The structure has again been tested in VASP. This surface was found to be the fourth most stable of the KO terminated reconstructions. The surface atoms shift only fractionally from their bulk lattice points. Both the row of surface K and surface O move towards each other slightly. The K–O vertical separation is found to be 0.11 Å with a K–O bond length of 2.58 Å. The K–K and O–O separation are that of the unit cell length 4.00 Å. The O–K–O and K–O–K bond angles are 101.8° and 101.5° respectively. The bond length between the surface O and sub-layer Ta is recorded to be 1.80 Å. The inter-planar distance between the surface and sub-layer is 2.01 Å. The sub-layer is rumpled in a fashion similar to the other VASP KO terminated reconstructions. The Ta below the surface O are located 0.17 Å above

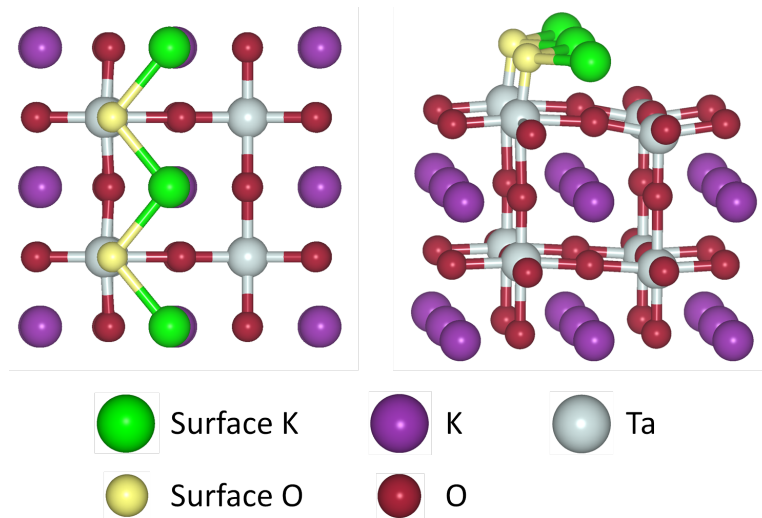


Figure 4.19: KO terminated reconstruction: KO terraced surface arrangement.

the plane and the under-coordinated Ta lie 0.27 \AA below the plane. The high lying O ions reside on the row directly beneath the surface K row 0.08 \AA above the plane. The O in the under-coordinated Ta row are located 0.06 \AA above the plane. The O in the fully coordinated Ta row are situated 0.07 \AA beneath the plane and the remaining O lie 0.02 \AA above the plane. The inter-planar distance between the sub-layer and 3rd layer is 2.08 \AA . The magnitude of the rumpling of the 3rd layer is 0.08 \AA and the 4th layer 0.20 \AA . The inter-planar distance between the 3rd and 4th layer is 2.03 \AA .

KO Termination: KO Island Surface (1.11 Jm^{-2})

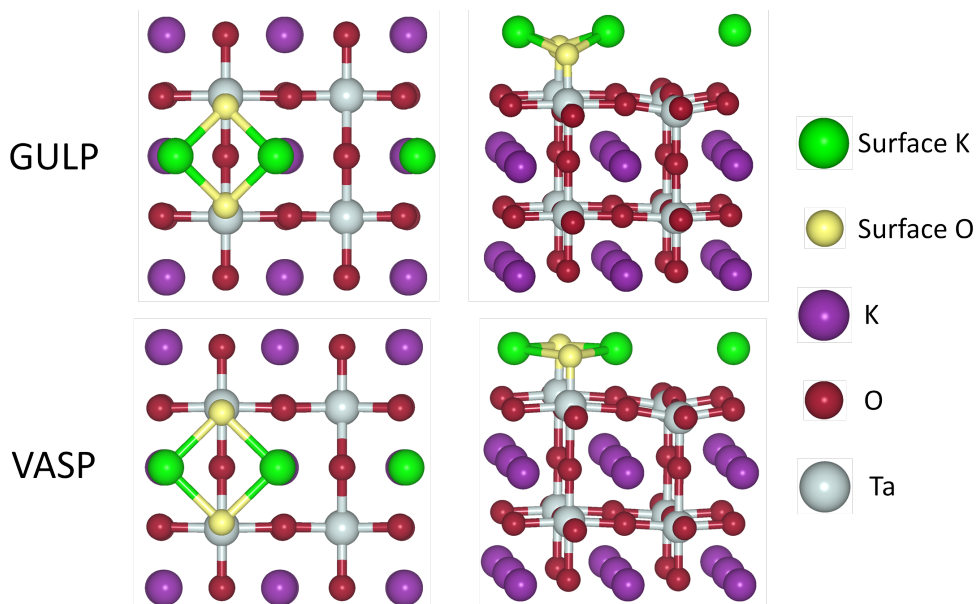


Figure 4.20: KO terminated reconstruction: KO island surface arrangement.

The least stable of the KO terminated reconstructions according to VASP was the KO island surface shown in Figure 4.20. The island structure shows a flattening of the surface layer reducing the K–O vertical separation from 0.71 Å to 0.09 Å. The reduction in vertical separation is accompanied by an increase in the horizontal separation with the overall effect being an increase in the K–O bond length from 2.43 Å to 2.60 Å and an increase in K–K separation from 3.31 Å to 3.70 Å. The degree to which the surface O ions shift towards the surface K ions has decreased slightly resulting in an increase in O–O separation from 3.25 Å to 3.64 Å. The O–K–O and K–O–K bond angles are 88.8 and 90.9, respectively, becoming more square-like than in the GULP structure. The bond length between the surface O and sub-layer Ta is 1.79 Å, and the inter-planar separation between the surface and sub-layer is 2.00 Å. The highest lying ion in the sub-layer is the O in the under-coordinated Ta row that also lies on the same line as the surface K; 0.23 Å above the plane. The Ta beneath the surface O reside 0.17 Å above the plane, and the under-coordinated Ta lie 0.26 Å below the plane. The O directly beneath the centre of the surface KO island is the lowest lying O positioned 0.12 Å below the plane. The other O on the Ta rows reside 0.04 Å below the plane. The remaining O all lie 0.04 Å above the plane. The magnitude of the rumpling in the 3rd and 4th layers are 0.08 Å and 0.20 Å respectively. The inter-planar separations between the sub-layer and 3rd layer and the 3rd layer and 4th layer are 2.08 Å and 2.03 Å respectively.

4.6.2 DFT TaO₂ Terminated Reconstructions

Apart from the TaO₂ terraced structure, all TaO₂ reconstructions feature the mixed sub-layer.

TaO₂ Termination: K-cornered Zig-zag Surface (0.87 Jm⁻²)

Of all the KTaO₃ surfaces investigated the K-cornered zig-zag surface residing on top of the mixed sub-layer obtained from a TaO₂ terminated reconstruction proved to be the most stable both within VASP and GULP. This surface is shown in Figure 4.21. At the surface, the K–O vertical separation has been significantly reduced from 1.15 Å to 0.51 Å. The K–O horizontal separation has in turn increased, resulting in a K–O bond length of 2.43 Å up from 2.34 Å. The K–K separation increased from 4.07 Å to 4.76 Å while the O–O separation remained unchanged at 3.99 Å. The new position of the K ions lead to a decrease in the O–K–O bond angle from 117.3° to 110.0° and an increase in the K–O–K angle from 121.1° to 156.2°. The bond length between the surface O ions and sub-layer Ta is 1.84 Å, which is 0.02 Å smaller than in the GULP structure but the largest of all the VASP structures. The inter-planar separation between the surface and the sub-layer was found to be 2.41 Å, which is 0.41 Å smaller than the GULP structure but about 20% larger than any of the VASP KO terminated reconstructions.

The mixed sub-layer found for the stable TaO₂ terminated reconstructions was dis-

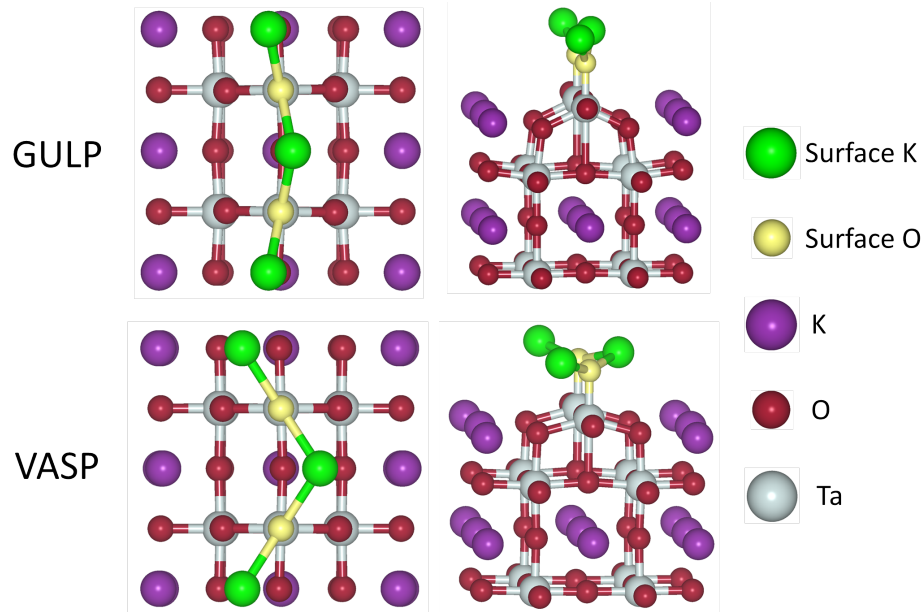


Figure 4.21: TaO₂ terminated reconstruction: K-cornered zig-zag surface arrangement.

cussed earlier and is a combination of TaO₂ and KO rows. The degree of rumpling on the mixed sub-layer has been significantly reduced compared to the GULP structure. The highest lying ions on the sub-layer are the Ta which are 0.32 Å above the averaged plane. The O between the Ta ions lie 0.26 Å above the plane while the other O lie 0.20 Å below the plane. The K ions reside 0.17 Å beneath the plane. The K ions have also been pushed slightly in the horizontal direction away from the nearest surface K ion. The magnitudes of the rumpling in the 3rd (TaO₂ layer) and 4th (KO layer) layers are 0.20 Å and 0.04 Å, respectively. The inter-planar separations between the sub-layer and 3rd layer and the 3rd layer and 4th layer are 2.17 Å and 2.01 Å, respectively.

TaO₂ Termination: KO Terraced Surface (0.89 Jm⁻²)

The KO terraced surface shown in Figure 4.22 was found to be the second most stable reconstruction. The structure was found to be unstable with the IP and instead reconstructed to the K-cornered arrangement discussed above. The surface K ions occupy positions that differ in their vertical separation from the surface O ions. One K ion is vertically separated by 0.54 Å while the other is 0.31 Å. This type of break in symmetry was not observed in the other DFT reconstructions.

The K–O bond length is 2.41 Å for the higher lying K ion and 2.44 Å for the other. The surface O ions shift very slightly away from the higher K ions giving rise to two different O–O separation distances of 4.08 Å and 3.91 Å. The K–K separation is 4.01 Å. The O–K–O bond angle involving the higher positioned K is 115.8° and the other K is 106.7°. The K–O–K bond angle is 111.7°. The bond length between the surface O and sub-layer Ta was found to be 1.84 Å similar to the K-cornered arrangement. The

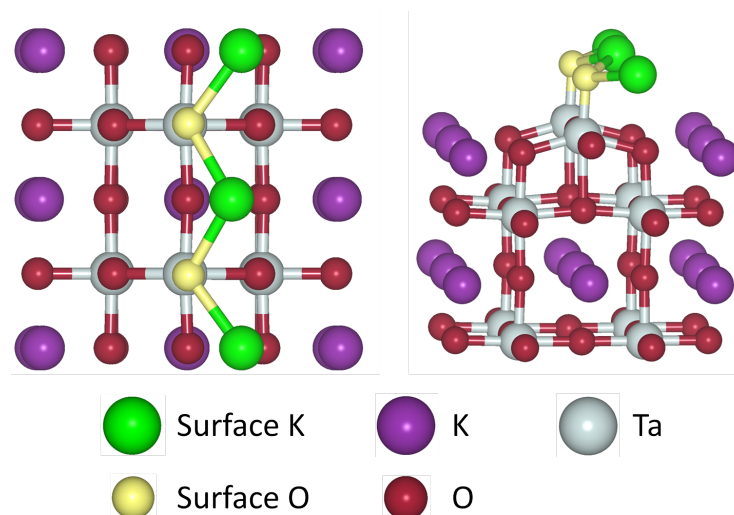


Figure 4.22: TaO₂ terminated reconstruction: KO terraced surface arrangement.

inter-planar separation between the surface and sub-layer is 2.36 Å. As with the TaO₂ terminated K-cornered arrangement the highest lying ion is Ta, 0.31 Å above the plane. The difference in height of the between the two surface K ions leads to a difference in height between the O ions lying in the Ta row. The O ion that lies in this row in line with the surface K ion resides 0.28 Å above the plane, while the other O is only 0.22 Å above. Similarly, the sub-layer K ions differ very slightly in height. The K ion in line with the higher surface K ion is 0.16 Å below the plane, the other K ion is 0.15 Å below. As all the surface K ions lie to one side of the O row, the sub-layer O ions in the same row as the K are 0.18 Å below the plane, while the others sub-layer O ions are 0.22 Å below. The magnitude of the rumpling in the 3rd (TaO₂ layer) and 4th (KO layer) layers are 0.23 Å and 0.05 Å respectively. The inter-planar separations between the sub-layer and 3rd layer and the 3rd layer and 4th layer are 2.17 Å and 2.01 Å, respectively, the same as in the K-cornered arrangement.

TaO₂ Termination: KO Island Surface (0.99 Jm⁻²)

The KO island surface shown in Figure 4.22 was the third most stable reconstruction. As with all VASP relaxed structures this surface shows a flattening of the surface layer compared to the GULP structure. At the surface the K–O vertical separation has been reduced from 0.66 Å to 0.12 Å. This is the smallest seen for the surface reconstructions containing a mixed sub-layer. The K–O bond length has increased to 2.54 Å, up from 2.41 Å. The degree to which the O lean in towards the island centre has decreased, opening up the O–O separation from 3.36 Å to 3.76 Å. The K–K separation has also increased from 3.19 Å to 3.42 Å. The O–K–O bond angle is 95.3° and the K–O–K angle is 84.5°. The bond length between the surface O ion and sub-layer Ta ion is 1.82 Å, 0.02 Å smaller than in the GULP structure. The inter-planar separation between the surface

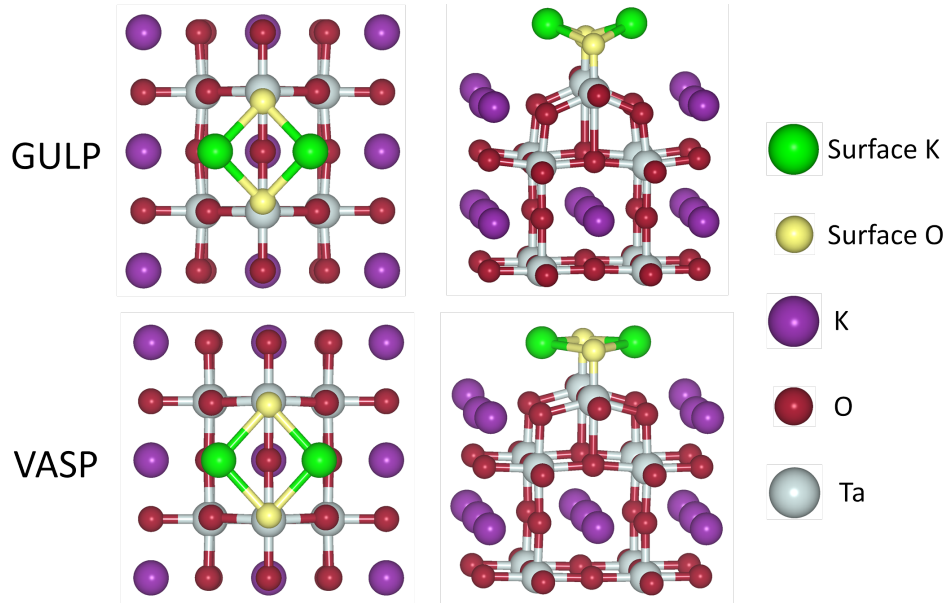


Figure 4.23: TaO₂ terminated reconstruction: KO island surface arrangement.

and the sub-layer is 2.21 Å, down from 2.56 Å. The sub-layer rumpling is similar to that of the other mixed sub-layer structures relaxed by VASP. The highest lying ions on the sub-layer are the Ta, which are 0.34 Å above the averaged plane. The O between the Ta that lie beneath the island centre are 0.22 Å above the plane while the other O lies 0.24 Å above. The remaining O all reside 0.18 Å below the plane. The K ions in line with the surface K reside 0.32 Å beneath the plane and the other K 0.09 Å below. The magnitude of the rumpling in the 3rd (TaO₂ layer) and 4th (KO layer) layers are 0.22 Å and 0.06 Å, respectively. The inter-planar separations between the sub-layer and 3rd layer and the 3rd layer and 4th layer are 2.16 Å and 2.01 Å, respectively.

TaO₂ Termination: TaO₂ Terraced Surface (1.60 Jm⁻²)

The TaO₂ terraced surface shown in Figure 4.24 is the only TaO₂ terminated reconstruction investigated that has Ta in the top surface layer and does not include the mixed sub-layer. The TaO₂ at the surface is arranged in a TaO chain with the remaining O bonded to the Ta on one side of the chain. The chain is slightly zig-zagged so that the O in the chain are angled away from the O protruding off the chain. The surface O ions lie higher on the surface than the Ta. The O ion in the chain coordinated to two Ta ions resides slightly higher than the other O (0.32 Å above the Ta), the singly coordinated O lies 0.27 Å above the Ta. The Ta–O bond distance is 2.07 Å for the two-coordinated O and 1.75 Å singly coordinated O. The O–Ta–O bond angle where both O are two coordinated is 149.1°, and when one of the O are singly coordinated is 101.1°. The Ta–O–Ta bond angle is 149.1°. The Ta–Ta separation distance is 3.99 Å; the same as the lattice constant. A similar separation is found between symmetrically

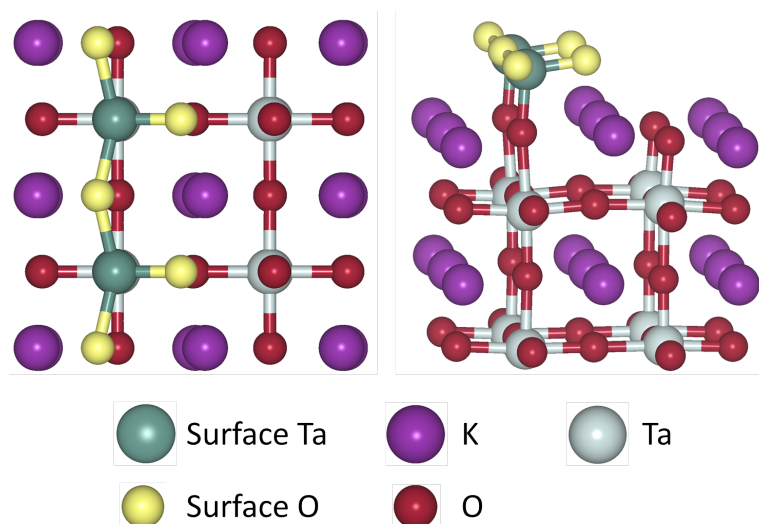


Figure 4.24: TaO₂ terminated reconstruction: TaO₂ terraced surface arrangement.

equivalent surface O. The distance between the two different O types was 2.95 Å.

The sub-layer was a bulk-like KO plane. The bond length between the surface Ta ion and sub-layer O ion is found to be 1.82 Å. This O ion also shifts horizontally away from the singly coordinated surface O, creating a non-180° angle, between the Ta above and below, of 172.9°. The highest lying atoms on sub-layer are the K ions in the same row as the singly coordinated surface O ion; 0.21 Å above the plane. These K ions have also moved 0.32 Å horizontally of this would be bulk lattice site away from the surface Ta row, the position is a result of an attraction to the surface O and a repulsion from the surface Ta. The other K ions lie 0.14 Å below the plane. The sub-layer O ion bonded to the surface Ta ion resides 0.09 Å above the plane and the other O ion lies 0.16 Å below.

The inter-planar distance between the surface and sub-layer is found to be 2.10 Å. The magnitudes of the rumpling in the 3rd (TaO₂ layer) and 4th (KO layer) layers are 0.21 Å and 0.09 Å, respectively. The inter-planar separations between the sub-layer and 3rd layer and the 3rd layer and 4th layer are 2.06 Å and 2.03 Å, respectively.

4.6.3 Summary of DFT Surfaces

Table 4.2 highlights some of the key properties of the VASP relaxed surfaces. The DFT calculations agree with the atomistic calculations in that the TaO₂ terminated reconstructions that feature the mixed sub-layer are the most stable. The TaO₂ terminated reconstruction is the least stable of all the structures investigated, thus, highlighting the importance the reconstruction of the sub-layer has on stabilising the surface. The surface energy from the VASP calculations when compared to the GULP calculations has increased for the TaO₂ reconstructions, whereas it has decreased for the KO reconstructions. This implies the sub-layer reconstruction has a greater stabilising effect in the atomistic calculations than in the DFT calculations.

The stability ordering of the surface layer arrangement (the KO on the top layer) is the same on both types of sub-layer (both KO and TaO₂ reconstructions). However, this order has changed in going from atomistic to DFT calculations. The previous order calculated by GULP was: K-cornered > Island > O-cornered > Diagonal. This has been reordered to: Diagonal > O-cornered > K-cornered > Island, with the K-terraced surface slotting between the K-cornered and Island arrangements. As the Diagonal and O-cornered structures can not reside on the mixed sub-layer, the K-cornered arrangement on the mixed sub-layer remains the ground state. Thus, the same surface structure is predicted as the ground state by both GULP and VASP.

The most general and obvious change in the geometry between the GULP and VASP structures is the flattening of the surface KO layer. In all the structures, the K ion lies higher than the O ion on the surface. On refining the GULP structures within VASP, the vertical separation between the two species reduced by ~ 0.6 Å. The large rumpling at the surface seen in the GULP structures may be a result of using a formal charge model. While the model reproduces the bulk properties well, formal charges might not be entirely suitable at the surface. The reduced surface rumpling seen for the DFT structures is accompanied by an increase in the O–O and K–K separation (when possible). The magnitude of the O–O separation across the different surfaces, anti-correlates with surface energy, with increased O–O separation typically being associated with lower surface energy. This suggests the O–O separation distance plays an important role in surface stability.

In the GULP calculations the rumpling of the mixed sub-layer was almost twice as large as that seen for KO sub-layer. After the structures were refined in VASP the sub-layer rumpling was reduced, more significantly so for the mixed sub-layer. This results in the mixed and KO sub-layers both being flatter with a similar degree of rumpling. The plane height of each layer was defined as the average of all the atoms considered to lie in that layer. The inter-planar separation between the surface and sub-layer has been reduced during the VASP relaxations, an outcome of both the surface and sub-layer planes becoming flatter.

Table 4.2: **Surface energy and key inter-atomic distances for DFT relaxed KTaO₃ surfaces.** The properties listed are the same as in Table 4.1. Bracketed values indicate the difference between the DFT and atomistically optimised surfaces.

		K-c	Terrace	Island	Diagonal	O-c
γ (Jm ⁻²)	TaO ₂	0.87 (0.35)	0.89	0.99 (0.15)	x	x
	KO	1.08 (-0.44)	1.10	1.11 (-0.53)	1.04 (-0.63)	1.06 (-0.66)
K-O (Å)	TaO ₂	2.43 (0.09)	2.41/2.44	2.54 (0.13)	x	x
	KO	2.62 (0.21)	2.58	2.60 (0.17)	2.82 (0.42)	2.69 (0.08)
O-O (Å)	TaO ₂	3.99 (-0.01)	3.91/4.08	3.76 (0.40)	x	x
	KO	4.00 (0.02)	4.00	3.64 (0.39)	5.65 (-0.03)	5.38 (0.30)
K-K (Å)	TaO ₂	4.76 (0.69)	4.01	3.42 (0.23)	x	x
	KO	5.22 (0.85)	3.99	3.70 (0.39)	5.65 (-0.06)	3.99 (0.00)
Ta-O (Å)	TaO ₂	1.84 (-0.02)	1.84	1.82 (-0.04)	x	x
	KO	1.80 (-0.04)	1.80	1.79 (-0.03)	1.79 (-0.02)	1.79 (-0.02)
O-K-O (°)	TaO ₂	110.0 (-7.3)	106.7/115.8	95.3 (6.8)	x	x
	KO	99.9 (-11.6)	101.8	88.8 (4.6)	177.9 (26.8)	179.5 (27.5)
K-O-K (°)	TaO ₂	156.2 (35.1)	111.7	84.5 (1.5)	x	x
	KO	171.5 (41.8)	101.5	90.9 (4.9)	177.9 (26.0)	95.8 (-3.7)
Δz K-O (Å)	TaO ₂	0.51 (-0.64)	0.54/0.31	0.12 (-0.53)	x	x
	KO	0.20 (-0.83)	0.11	0.09 (-0.62)	0.05 (-0.63)	0.01 (-0.61)
Δz L ₁ -L ₂ (Å)	TaO ₂	2.41 (-0.41)	2.36	2.21 (-0.35)	x	x
	KO	2.05 (-0.39)	2.01	2.00 (-0.25)	2.00 (-0.26)	1.98 (-0.22)
Δz L ₂ -L ₃ (Å)	TaO ₂	2.17 (-0.21)	2.17	2.16 (-0.15)	x	x
	KO	2.08 (0.05)	2.08	2.08 (0.04)	2.10 (0.06)	2.09 (0.06)

4.7 Electronic Structure

Table 4.3: **KTaO₃ surface band gaps.** All the gaps are found to be direct at the Γ point. The bulk band gap for KTaO₃ was calculated to be 2.03 eV.

Band Gap (eV)	TaO ₂ terminated reconstructions			KO terminated reconstructions	
	K-c	Terrace	Island	Diagonal	O-c
	1.88	1.88	1.72		
	1.80	1.83	1.72	1.89	1.90

Table 4.3 presents the band gaps for the eight surface slabs investigated as calculated in VASP. All of the band gaps are found to be smaller than the calculated bulk $\Gamma - R$ indirect gap of 2.03 eV. The KO reconstructed diagonal chain structure has the largest band gap of 1.90 eV, 0.13 eV smaller than the bulk. The smallest band gap is found on the KO island structure of both the KO and TaO₂ reconstructions and is calculated to be 1.72 eV. The ground state structure, the TaO₂ reconstructed K-cornered zig-zag surface, is found to have a band gap of 1.88 eV.

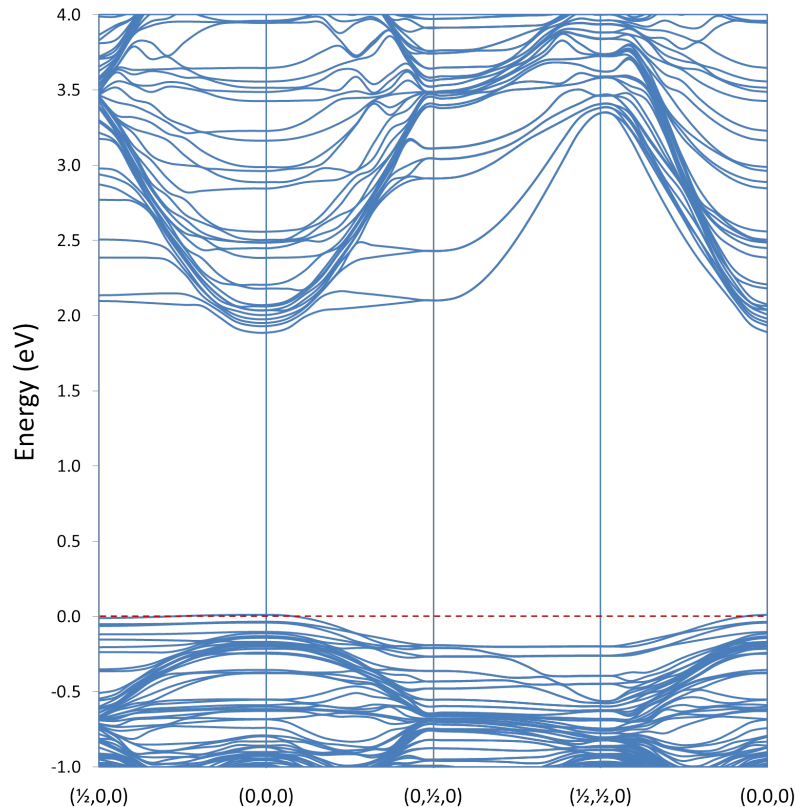


Figure 4.25: Band structure for the TaO₂ terminated K-cornered zig-zag structure. The top of the valence band is shifted to 0 eV.

As slabs with a surface are modelled to be finite in the direction perpendicular to the surface, electronic band dispersion is only measured in two dimensions. The electronic band structure for the ground state surface is shown in Figure 4.25. A direct band gap is measured at the Γ point $(0,0,0)$. The dispersion in the $(\frac{1}{2},0,0)$ and $(0,\frac{1}{2},0)$ direction differ due to the break in symmetry between these two directions at the surface.

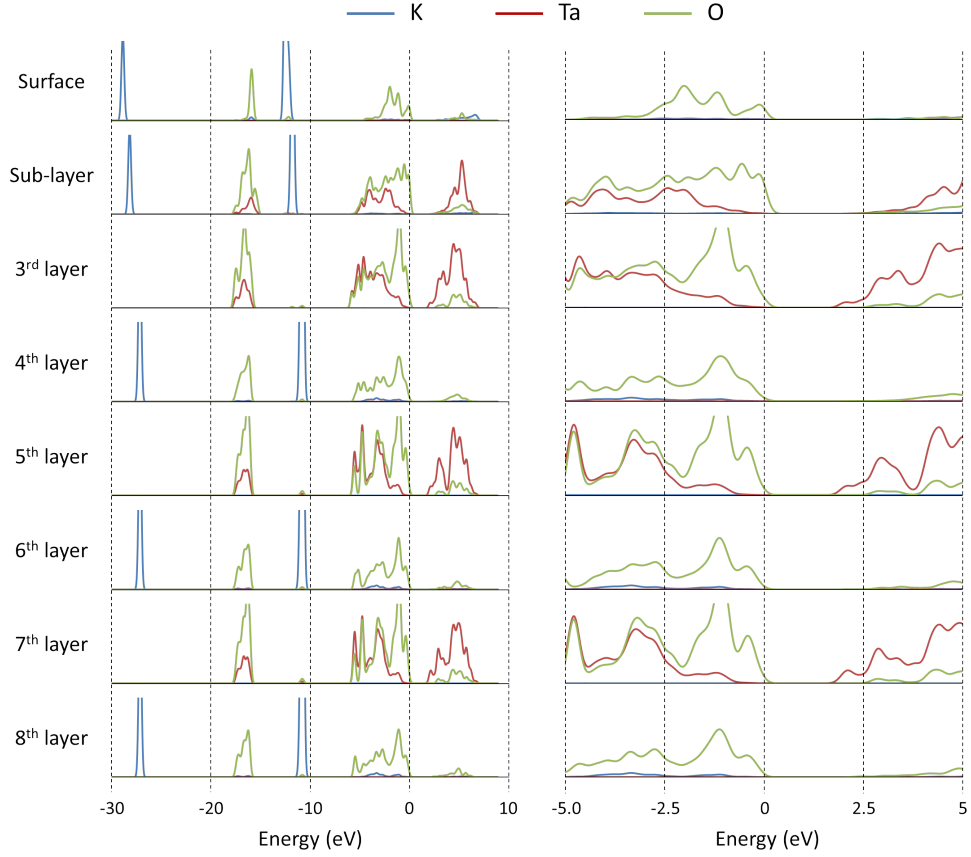


Figure 4.26: The DOS projected onto the different layers in the slab. The DOS is further decomposed into its different species. The left shows the DOS over the range $-30 - 10$ eV. The right magnifies the $-5 - 5$ eV range in which the valence band and conduction band reside.

To get a more detailed impression of the effect the surface has on the electronic structure a decomposed DOS profile was created for the ground state structure. The DOS was decomposed and projected onto each individual atom. For each layer in the slab the atomic DOS were summed together with the result of the top eight layers being shown in Figure 4.26. The deeper layers are expected to be representative of the bulk and so layers 7 and 8 will be referred to as bulk-like.

The DOS profile of the entire slab closely resembles that of the bulk. The filled K 3s and 3p bands are shown as narrow peaks at ~ -27 eV and -11 eV respectively. The O 2s orbital is seen to have undergone some mixing with the Ta orbitals with the band located at ~ -17 eV. The valence band is comprised of mixed O 2p and Ta 5d, 6p and 6s

states, with O 2p being highly predominant close to the valence band maximum (VBM). The conduction band is dominantly Ta 5d with some mixing from O states.

The most obvious difference between the surface and bulk layers are seen in the deeper K 3s, 4p and O 2s bands. The energy levels of the K 3s and 3p bands both decrease towards the surface. The surface bands are the lowest lying with the sub-surface level lying between the surface and bulk levels. The energy levels of the O 2s band behave in an opposite fashion; the energy of the bands increase towards the surface. The shift in these low lying states is likely a result of the under coordination of these ions at the surface. Closer to the band gap, the top of the valence band is found to slightly increase in energy closer to the surface. The bottom of the conduction band is found to significantly increase in energy at the surface layers; upward band bending.

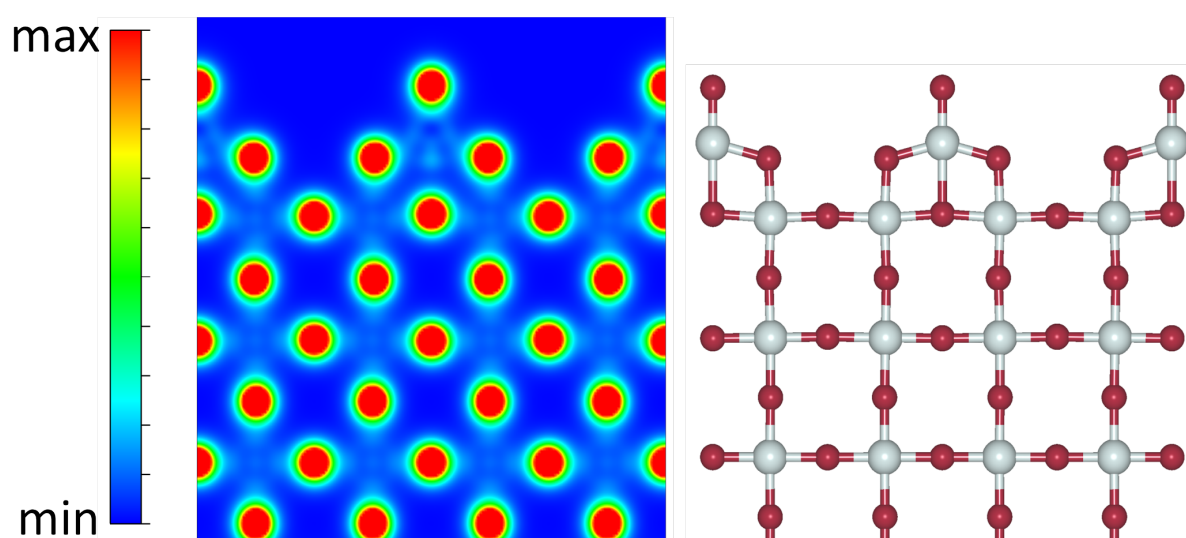


Figure 4.27: Two-dimensional charge density plot of the KTaO_3 ground state surface (TaO_2 terminated K-cornered). The image taken is of a plane in the (010) direction. The blue at the bottom of the spectrum represents low charge density while the red end is high charge density. The image on the right highlights the atom positions. The surface lies at the top of images.

Analysis of the charge density agreed with the DOS. No charge was seen between the K and O ions suggesting highly ionic bonds. Charge is found between the Ta and O suggesting a degree of covalent bonding between the ions. Figure 4.27 shows the charge density on a plane in the (010) direction. Not only is there obvious covalency between the Ta and O, but at the surface the surface O ions and closest sub-layer O ions are seen to share covalent bonding.

Simulated STM images were also created for three of the surfaces and are shown in Figure 4.28. The surfaces simulated were a) the TaO_2 terminated K-cornered zig-zag surface (the ground state), b) the TaO_2 terminated KO terraced surface, c) the KO

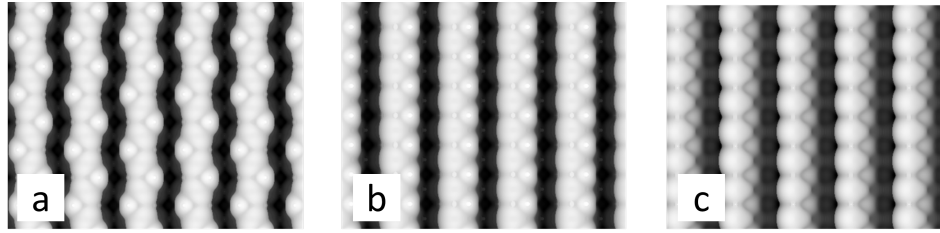


Figure 4.28: Simulated STM images of the KTaO_3 reconstructions. a) the TaO_2 terminated K-cornered zig-zag surface. b) the TaO_2 terminated KO terraced surface. c) the KO terminated KO terraced surface. The images were created by looking at constant charge density levels of bands near the top of the valence band. The brightness indicates the distance from the top of the surface.

terminated KO terraced surface which was the proposed ground state in the limited literature. The difference in surface energy between surfaces a) and b) is small (0.02 Jm^{-2}) suggesting it is likely both surfaces could exist simultaneously. The difference in surface energy between b) and c) is much larger (0.21 Jm^{-2}) making it unlikely surface c) would exist. Both b) and c) structures possess the same surface arrangement of the KO and the STM images show it may be hard to distinguish between the two. Thus, it can be seen that surfaces involving the mixed sub-layer may be mistaken for less stable reconstructions by STM.

4.8 Defects

Defect calculations were performed on the ground state surface (Figure 4.13 for atomistic calculations, Figure 4.21 for DFT) to ascertain where vacancies would be most likely to form. The atoms on the surface have been labelled in Figure 4.29 for clarity.

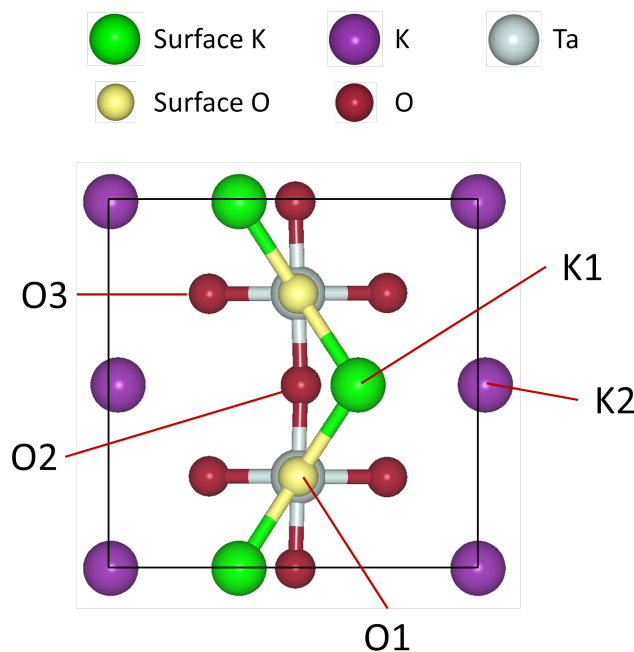


Figure 4.29: Labelling of the unique ions at the surface of the KTaO₃ (001) reconstructed ground state.

4.8.1 Atomistic Defect Models

Oxygen vacancies were modelled at the atomistic level to gauge the agreement between atomistic and DFT calculations on where the vacancies are likely to form. To model the removal of neutral oxygen from the surface (leaving the surface uncharged) the charge on the O ions being removed had to be reallocated, this was done in two ways. The first approach was to delocalise the charge by evenly distributing it over all Ta ions (the shells) in region 1. In the second approach the charge was evenly distributed between the two closest Ta ions. Thus, for an O vacancy in a bulk-like TaO₂ plane the two Ta⁴⁺ would both lie on the same plane as the vacancy. For an O vacancy in the KO plane one Ta⁴⁺ would be in the plane above and the other on the plane below.

The thickness of region 1 was increased to 12 unit cell layers to model the defects (compared with 6 in previous atomistic calculations). After introducing the vacancy and distributing the residual charge the geometry of the slabs were relaxed.

Plots of the defect energy relative to the most stable O vacancy configuration are shown in Figure 4.30 when the charge is delocalised (left) and localised (right). The

energies are plotted as a function of vacancy depth from the surface. Both plots show

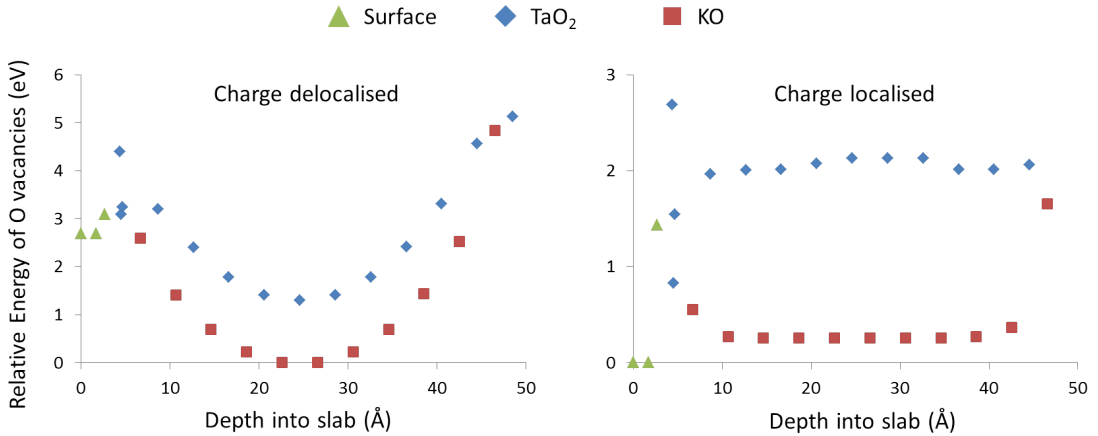


Figure 4.30: Plots of the atomistic defect energy for neutral O vacancies on the KTaO_3 (001) reconstructed ground state surface. On the left the charge associated with the O vacancy has been evenly distributed over all Ta ions. On the right the charge has been evenly distributed to the two Ta ions closest to the O vacancy.

that the formation of O vacancies is more favourable on KO planes than TaO_2 planes. When the charge is delocalised the defect energies form a parabola about the centre of the region 1. This arises due to the creation of a dipole which is minimised when the vacancy is at the centre of region 1. When the charge is localised the most stable vacancies are found at the surface and correspond to the removal of either O1 or O2 from Figure 4.29. The charge is divided among the two sub-layer Ta ions and both vacancy types result in the same final structure. From the perspective of the O1 vacancy the two surface K move into the row directly above the line of sub-layer Ta. They also approach more closely to the remaining surface O ions resulting in a bond length of 2.10 Å. The sub-layer O beneath the surface K rise up out of their plane slightly to approach the surface K. For the removal of O3 the charge is given to the nearest sub-layer Ta and a Ta in the plane below. This results in a different relaxed structure which was higher in energy.

4.8.2 DFT Defects

Neutral O, K, and KO vacancy calculations were performed at the DFT level using VASP. As the DFT surface was symmetric and double sided, vacancies at the surface were introduced on both sides to retain symmetry. To model a bulk-like vacancy in the slab a single oxygen was removed from the central layer of the slab. A slab with a thickness of five unit cell layers was used to model most vacancies. To model the bulk-like O vacancy on a TaO_2 plane a six unit cell layer thick slab was used to maintain symmetry.

The defect formation energies were calculated using:

$$E_{Defect} = E_{ABZ_3}^D - E_{ABZ_3} + N_A\mu_A + N_B\mu_B + N_Z\mu_Z \quad (4.2)$$

where E_{ABZ_3} is the energy of the relaxed ABZ_3 perovskite system before a defect was introduced and $E_{ABZ_3}^D$ the energy after. N_i and μ_i are the number of vacancies and the chemical potential, respectively, of element i . See chapter 2 for more details.

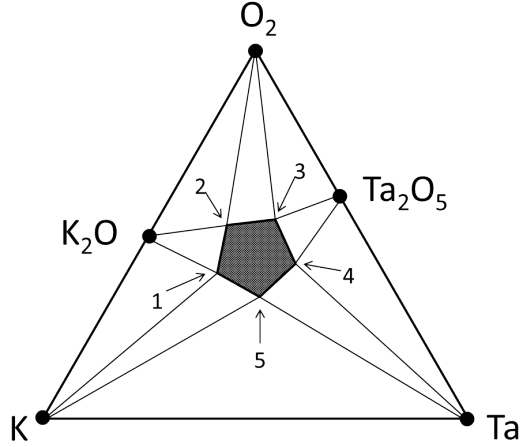


Figure 4.31: Phase diagram for KTaO₃.

The chemical potentials for KTaO₃ have been previously calculated in chapter 2 at the five points on the phase diagram shown in Figure 4.31. The vacancy types investigated include:

- Those labelled in Figure 4.29 from the surface.
- An O vacancy from a KO plane at the centre of the slab.
- An O vacancy from a TaO₂ plane at the centre of the slab.
- A K vacancy from the centre of the slab.
- A double vacancy of two O1 ions.
- A double vacancy of two K1 ions.
- A KO vacancy of O1 and K1.
- A double KO vacancy of two O1 and K1.

The formation energy of these vacancies along with the chemical potentials are given in Table 4.4. μ_O is most negative – and hence the O vacancies most stable – in the metal rich environment describe by point 5 on the phase diagram (Figure 4.31). The order of stability of the DFT oxygen vacancies coincide closely with the atomistic level

Table 4.4: **Defect energies.** The defect energy of vacancies in a KTaO_3 slab calculated at the points shown in Figure 4.31.

Vacancy	Defect formation energy or μ (eV) at phase diagram point				
	1	2	3	4	5
O Vacancies					
μ_O	-7.80	-4.54	-4.54	-8.11	-9.13
O1	2.02	5.28	5.28	1.71	0.69
O2	1.81	5.07	5.07	1.50	0.47
O3	2.40	5.66	5.66	2.09	1.07
O (KO)	2.36	5.62	5.62	2.05	1.02
O (TaO_2)	2.87	6.13	6.13	2.56	1.54
O1 x2	4.65	11.17	11.17	4.03	1.98
K Vacancies					
μ_K	-0.90	-2.53	-5.76	-3.98	-0.90
K1	3.36	1.73	-1.50	0.28	3.36
K2	3.81	2.18	-1.05	0.74	3.81
K (KO)	4.29	2.66	-0.57	1.22	4.29
K1 x2	7.14	3.88	-2.58	0.99	7.14
KO Vacancies					
KO	2.17	3.80	0.57	-1.21	0.84
KO x2	4.76	8.02	1.56	-2.01	2.10

calculations where the charge was split between neighbouring Ta ions. The O2 vacancy (Figure 4.29) is the most stable followed by the O1. The ions in the DFT calculation are much less mobile and so the systems involving the O1 and O2 vacancy do not relax to the same structure as they did for the atomistic model. The removal of oxygen from a KO plane at the centre of the slab is the next most stable followed by the O3 vacancy. The removal of O from a TaO₂ plane at the centre of the slab is the least stable single O vacancy.

The formation of two O1 vacancies proves to be less stable than all single oxygen vacancy models. The order in formation energy implies that O vacancies are more likely to form at the surface than deeper within the material. The surface O vacancies are lower in energy than the defects seen in both the bulk 2x2x2 and 3x3x3 cells investigated in chapter 2. The defect energies from vacancies at the centre of the slab more closely resemble the defect energy seen in the bulk cells. The formation energies for all of these oxygen vacancies are positive which implies the formation of O vacancies is dependant on the temperature of the system.

K vacancies are most stable in the O rich environment described by point 3 on the phase diagram. K1 is the most stable single K vacancy, almost 0.5 eV lower in energy than K2, which in turn is almost 0.5 eV lower in energy than a K vacancy at the centre of the slab. The removal of both K1 ions proves to be even more stable than just the single vacancy at point 3, although less stable at all other points. All formation energies at point 3 are negative and so the vacancies would be expected to spontaneously form, independent of temperature (although this is subject to any migration barriers encountered). As was seen for the O defects, the K vacancies at the surface are lower in formation energy than those seen in the bulk cells. K vacancies from the slab centre have a similar formation energy to the bulk vacancies. The K vacancies in the Ta rich environment described by point 4 on the phase diagram are also seen to have relatively low formation energies, comparable to the energetics seen for the O vacancies at point 5.

The removal of KO units from the surface layer is found to be favourable (negative formation energy) at point 4, and the removal of both KO units even more favourable.

Electronic Structure of Defected Slabs

The appearance of the surface 2DEG in KTaO₃ has been proposed to be a result of oxygen vacancy formation. In this section the electronic structure of the slab containing a surface O vacancy is investigated.

Figure 4.32 compares the density of states (DOS) for a slab containing the O2 vacancy to a stoichiometric slab without any vacancies. The DOS are projected onto individual atomic layers focuses on the top of the valence band and the bottom of the conduction band. The Fermi level for the slab containing the O2 vacancy is located at the bottom of the conduction band and this has been set to 0 eV on the plot. The two

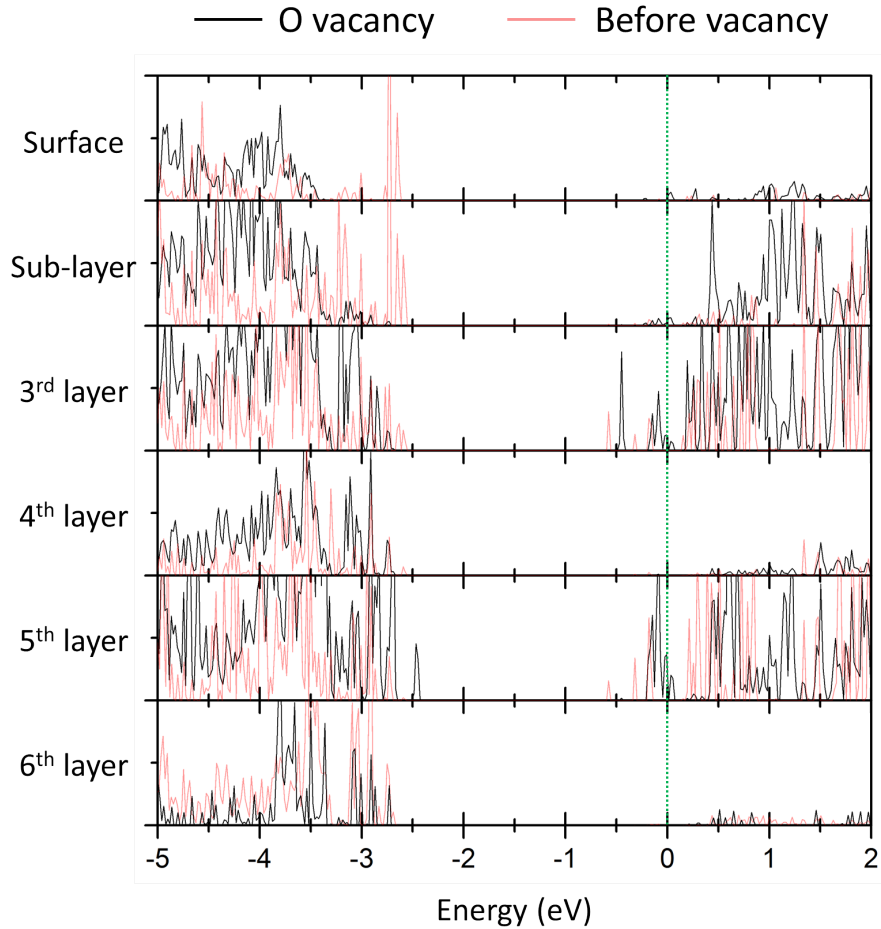


Figure 4.32: The DOS, close to the Fermi level, projected onto layers for a KTaO_3 slab containing a neutral O vacancy (black line) and a stoichiometric slab without vacancies (red line). The Fermi energy is shifted to 0 eV (green line) and sits at the bottom of the conduction band. Even numbered layers are KO, and odd numbers layers are TaO_2 .

different slabs being compared were aligned by their oxygen 1s core levels. The even layers in the DOS plots are KO, and the odd are TaO_2 .

For the slab containing the O vacancy the valence band bends downwards towards the surface, whereas no such bending is seen for the stoichiometric slab. The conduction bands of the two different slabs are quite similar. Both slabs show the lowest lying states to be on the 3rd and 5th layer. The slab with the O vacancy does contain a large peak in the sub-layer significantly lower in energy than any seen for the stoichiometric slab, likely an effect of the defect.

From the DOS profile the slab with the oxygen vacancy appears to be metallic with the charge appearing to be concentrated on layers 3 and 5. Figure 4.33 shows the distribution of charge for the conduction band states in the slab with an O vacancy. a) shows an isosurface of the conduction band charge density. b) shows a contour plot of the conduction band charge density for a plane that bisects the Ta ions.

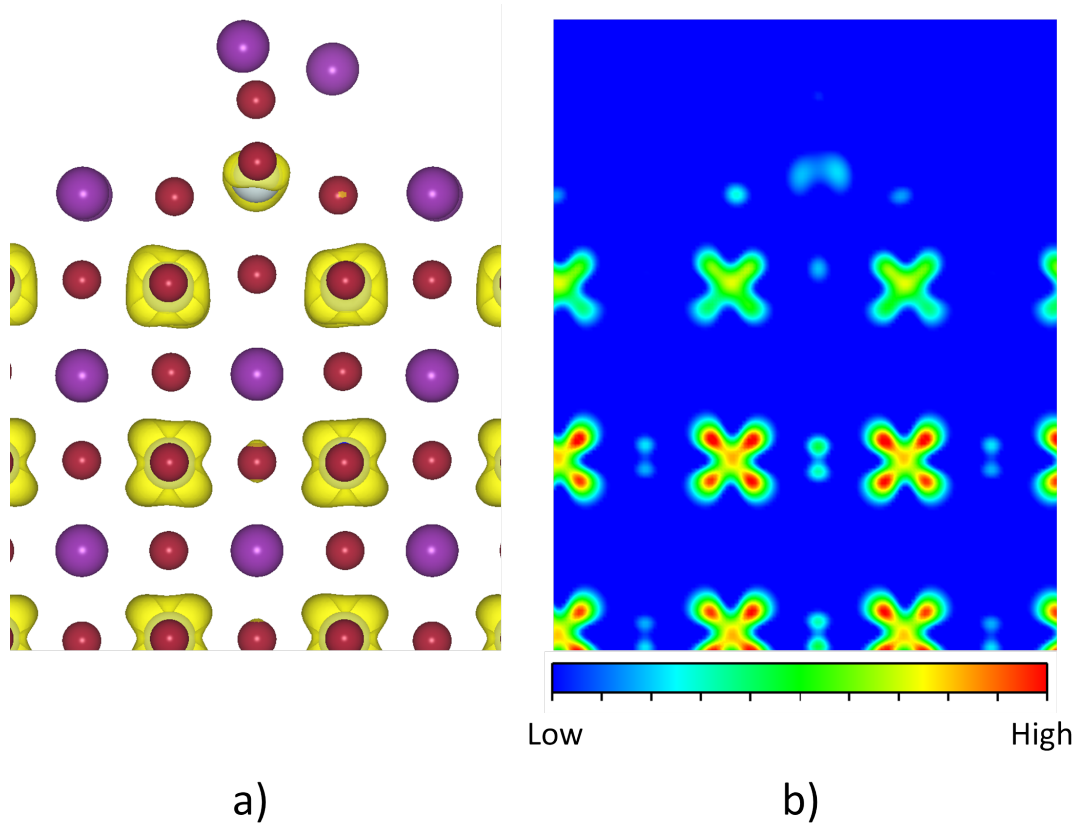


Figure 4.33: Charge density distribution for a KTaO_3 slab containing an oxygen vacancy. a) shows an isosurface of the conduction band charge density. b) shows a contour plot of the conduction band charge density for a plane that bisects the Ta ions. a) and b) are aligned so that the layers are in line with each other, the surface is at the top. The purple, grey, and red spheres are K, Ta, and O, respectively.

The charge is clearly shown to reside on the Ta ions, and is densest on the ions away from the surface in the bulk (5th layer). The massing of negative charge in the bulk is in contrast to what is reported in the literature [131]. However, it should be noted that while the centre of the slab has converged to its bulk like structure, the slab might not be thick enough for electronic surface effects to have become negligible at the slab centre.

To continue the investigation into the cause of the surface 2DEG two avenues may be explored. Firstly, the thickness of the slab may be increased to ensure that the slab centre is devoid of any surface effects. Secondly, the quality level of the calculations can be increased. This would involve including spin-orbit effects [162] and using hybrid functionals [163–165].

Table 4.5: **Data mining of KTaO_3 surface reconstructions.** The surface energies of the KTaO_3 reconstructions applied to the ABZ_3 cubic perovskite phases of KMgF_3 , KZnF_3 , and BaSnO_3 .

Surface Reconstruction	Surface Energy (Jm^{-2})			
	KTaO_3	KMgF_3	KZnF_3	BaSnO_3
BZ ₂ term.: A-cornered	0.87	0.85	0.74	1.38
AZ term.: A-cornered	1.08	0.72	0.58	1.60
BZ ₂ term.: BZ ₂ terraced	1.60	0.99	0.78	1.67

4.9 Data Mining Surfaces

In this last section, the reconstructed surface structures of KTaO_3 are tested (data-mined) for the ABZ_3 cubic perovskite phases of KMgF_3 , KZnF_3 , and BaSnO_3 . For KMgF_3 and KZnF_3 the charges on the A, B, and Z ions are +1, +2, and -1, respectively. For BaSnO_3 the charges on the A, B, and Z ions are +2, +4, and -2, respectively. This results in charge neutral AZ and BZ₂ planes. As the planes are charge neutral the bulk terminated surfaces are going to be stable, with one of the terminations likely being the ground state. However, the relative energies of the reconstructions for different compounds may give insight into what makes these surfaces stable. Three of the KTaO_3 surface reconstruction were applied to the other cubic perovskites. These reconstructions were:

- The TaO_2 terminated: K-cornered zig-zag surface arrangement (cf. Figure 4.21).
- The KO terminated: K-cornered zig-zag surface arrangement (cf. Figure 4.18).
- The TaO_2 terminated: TO_2 terraced surface arrangement (cf. Figure 4.24)

The surface slabs were rescaled to match the lattice parameters of the relevant compound. The lattice parameters for KMgF_3 and KZnF_3 were previously determined in chapter 3. The bulk unit cell lattice parameter (a) for BaSnO_3 was determined in VASP using the approach described in Chapter 3 for KTaO_3 , KMgF_3 , and KZnF_3 . The value of a for BaSnO_3 was calculated to be 4.136 Å, which is within 0.5% of both the experimentally observed value [166], and calculated values from other DFT investigations [60, 167]. All surface calculations employed a 500 eV plane wave cut-off and a Γ -centred 3 x 3 x 1 k-point mesh.

The surface energies obtained from the data mined reconstructions are given in Table 4.5. The energy rankings for the reconstructions of the two fluoride based compounds are in agreement. The AZ terminated: A-cornered arrangement is the lowest in energy. For the BZ₂ terminated reconstructions, the A-cornered surface arrangement – the ground state for KTaO_3 , which involved the migration of A ions to the surface – is the next lowest in energy. The BZ₂ terraced surface is the highest in energy of the three. The two fluoride compounds differ most in the relative energies of the two BZ₂ reconstructions.

For KMgF_3 the K-cornered arrangement was 0.14 Jm^{-2} lower in energy than the BZ_2 terraced structure. For KZnF_3 the difference in energy between the two reconstructions is only 0.04 Jm^{-2} . This indicates that the migration of A ions to the surface for the BZ_2 termination, is less of a stabilising effect for KZnF_3 than it is for KMgF_3 .

Compared to KTaO_3 , the effect of maximising the coordination of the B cation is less stabilising for the fluoride based compounds. This is illustrated by the fact that the AZ terminated: A-cornered surface is lower in energy than the BZ terminated: A-cornered surface.

On the other hand, the energy rankings of the BaSnO_3 surfaces agree with those of KTaO_3 . The BZ_2 terminated: A-cornered surface is the lowest in energy. Suggesting that, like with KTaO_3 , the maximising the coordination of the B cation is a strongly stabilising effect. The formal charges are higher for BaSnO_3 than for the fluoride based perovskites, giving weight to the hypothesis that the cation migration is charge driven.

The Goldschmidt tolerance factors (see chapter 1) for these perovskites are 0.964, 0.935, 0.926, and 0.930 for KTaO_3 , KMgF_3 , KZnF_3 , and BaSnO_3 , respectively. The ionic radii used for the ions were: K = 1.52 \AA , 1.49 \AA , Ta = 0.78 \AA , Mg = 0.86 \AA , Zn = 0.88 \AA , Sn = 0.83 \AA , O = 1.26 \AA , and F = 1.19 \AA , all taken from Ref. [114]. The tolerance factor for BaSnO_3 lies between that of KMgF_3 and KZnF_3 , whereas the surface energy rankings of BaSnO_3 agree with KTaO_3 . This implies that it is unlikely the AZ / BZ_2 size ratio has as strong an effect as the charge, on how stabilising the A ion migration is.

For the non-polar perovskites, the 1×1 bulk terminated surface energies were calculated for comparison. Two types of surface calculations were performed. The first involved stoichiometric slabs possessing two different surface terminations. The second used symmetric non-stoichiometric slabs with the same termination on each side. The non-stoichiometric slabs were created by removing either an AZ or BZ_2 layer from the surface of the stoichiometric slabs. For the stoichiometric slabs the average surface energy of the two different terminations was calculated. For the non-stoichiometric slabs the surface energy was calculated using:

$$E_{\text{surface}} = \frac{E_{\text{slab}} - nE_{\text{bulk}} + N_{\text{AZ}}\mu_{\text{AZ}} + N_{\text{BZ}_2}\mu_{\text{BZ}_2}}{2A} \quad (4.3)$$

where E_{slab} is the energy of the slab, N_i the number of i layers removed, μ_i the chemical potential of i , E_{bulk} the energy of the bulk unit cell, and n the number of equivalent bulk unit cells required to make the stoichiometric slab before the removal of layers.

The surface simulations were performed using slabs that were seven unit cell layers thick separated by a vacuum gap of 10 \AA . The seven layer thick slabs were found to have a surface energy difference of less than 0.001 Jm^{-2} from five layer thick slabs. For the non-stoichiometric slabs, one layer of either AZ or BZ_2 was removed from the seven

Table 4.6: **Perovskite 1 x 1 surface energies.** The surface energies (001) 1 x 1 surfaces of KMgF₃, KZnF₃, and BaSnO₃.

Surface	Surface Energy (Jm ⁻²)		
	KMgF ₃	KZnF ₃	BaSnO ₃
Stoichiometric (averaged)	0.52	0.46	1.10
AZ term. (AZ rich)	0.19	0.15	0.27
AZ term. (BZ ₂ rich)	0.41	0.38	0.79
BZ ₂ term. (AZ rich)	0.86	0.78	1.95
BZ ₂ term. (BZ ₂ rich)	0.64	0.55	1.43

unit cell thick stoichiometric slabs. The chemical potentials were constrained by:

$$\mu_{ABZ_3} = \mu_{AZ} + \mu_{BZ_2} \quad (4.4)$$

where μ_{ABZ_3} is the calculated unit cell lattice energy of the perovskite. Thus, the chemical potential for each binary compound had two different values depending on the limits. In the AZ rich limit:

$$\mu_{AZ} = \mu_{AZ(s)} \quad (4.5)$$

$$\mu_{BZ_2} = \mu_{ABZ_3} - \mu_{AZ} \quad (4.6)$$

and in the BZ₂ rich limit:

$$\mu_{BZ_2} = \mu_{BZ_2(s)} \quad (4.7)$$

$$\mu_{AZ} = \mu_{ABZ_3} - \mu_{BZ_2} \quad (4.8)$$

where $\mu_{X(s)}$ is the lattice energy of compound X.

The surface energies calculated for the 1 x 1 slabs are given in Table 4.6. KZnF₃ is found to have the lowest surface energy of the three perovskites, while BaSnO₃ has the highest. For all three perovskites, under all conditions, the AZ termination is shown to be significantly lower in energy than the BZ₂ termination. The smallest gap in surface energy between the AZ and BZ₂ terminations is found for KZnF₃ under BZ₂ rich conditions; calculated to be 0.17 Jm⁻². As expected, the bulk terminated 1 x 1 surfaces are generally lower in energy than the reconstructed surfaces (cf. Table 4.5). However, there are a few exceptions. For all compounds, the A-cornered reconstructions from either termination are lower in energy than the 1 x 1 BZ₂ surface under AZ rich conditions. All of the reconstructions for the BaSnO₃ are lower in energy than the 1 x 1 BZ₂ surface under AZ rich conditions. The BaSnO₃ A-cornered reconstruction from the BZ₂ termination is lower in energy than the 1 x 1 BZ₂ surface under any conditions. From these results it is clear that surfaces in which the B cations are under-coordinated and exposed to the surface are higher in energy. The stabilising effect of maximising the

B cation coordination is greater for the more highly charged BaSnO_3 , than it is for the fluoride compounds

4.10 Conclusion

In this chapter reconstructions of the KTaO_3 (001) polar surface have been investigated at both the atomistic level using interatomic potentials (IP), and the electronic level using density functional theory (DFT).

The stoichiometric 1×1 bulk terminated surfaces were shown to be unstable by both the IP and DFT calculations; as expected for polar surfaces. Using a 2×2 slab, terraced surfaces were created for both terminations to remove the dipole perpendicular to the surface.

A global optimisation at the IP level was performed using the terraced surfaces as initial configurations. The global optimisation revealed six low energy surface reconstructions. The lowest energy configurations were a result of the TaO_2 terminated terrace structures reconstructing so that Ta moved from the surface into the bulk, and K migrated out towards the surface. These reconstructions resulted in a surface layer of KO, and a mixed sub-surface layer of alternating rows of KO and TaO_2 . The Ta ions in the sub-layer were six coordinated making this type of reconstruction the only one in which all Ta ions were fully coordinated. It is assumed that this cation interlayer exchange is charge driven, with the maximising of the Ta coordination having a stabilising effect.

The IP surface structures were refined using DFT to investigate the electronic structure. The DFT geometry optimisation led to the atomic layers near the surface becoming less rumpled in comparison to the IP structures. As with the IP, the DFT calculations found the reconstructions in which Ta ions had descended from the surface into the bulk, with K ions migrating in the opposite direction, to be the lowest in energy, reinforcing the idea that a maximisation of the Ta coordination was highly stabilising. Six of the DFT surface structures presented in this thesis are lower in energy than the lowest energy structure from the literature [148].

A density of states (DOS) profile for the surface reconstruction with the lowest energy (ground state) revealed the band gap of the stoichiometric KTaO_3 slab similar to the bulk gap; approximately 2 eV.

Defect calculations involving neutral K, O, and KO vacancies were performed on the ground state slab. The formation of K and O vacancies were revealed to be more favourable at the surface than at the centre of the slab. K vacancies were found to be the most favourable, possessing a negative defect formation energy, when in an oxygen rich environment. Surface KO vacancies, under Ta rich conditions, were found to have a negative formation energy. The creation of O vacancies was most favourable under metal rich conditions, with the lowest formation energy calculated to be 0.47 eV.

For the slab with a surface O vacancy the Fermi level was found to reside at the bottom of the conduction band, cause the slab to become metallic. An investigation into the charge density revealed the charge to be concentrated close to the centre of the slab. This charge distribution is in contrast to what is seen in the literature for the (001) KTaO_3 surface [131, 132]. It is suggested that further calculations including spin-orbit coupling and hybrid functionals be carried out, to investigate the formation of the 2DEG at the surface.

Lastly, three of the KTaO_3 surface reconstructions were applied to the ABZ_3 cubic perovskite phases of KMgF_3 , KZnF_3 , and BaSnO_3 . The three reconstructions tested were: (a) an AZ surface layer on top of the AZ-BZ₂ mixed sub-layer. (b) an AZ surface layer on top of a BZ₂ sub-layer. (c) a BZ₂ surface layer on top of a AZ sub layer. (a) and (c) are rearrangements of the same termination. For the fluoride compounds, (b) had the lowest energy of the three reconstructions. For BaSnO_3 , (a) was lowest in energy. In all cases, (c) had the highest energy. The charges on the ions A, B, and Z are twice as large for BaSnO_3 compared with the fluoride perovskites. Thus, the strength of the stabilising effect associated with B cations moving from the surface into the bulk appears to have a correlation with the ion charge.

The perovskites KMgF_3 , KZnF_3 , and BaSnO_3 are all non-polar in (001) direction, and so the 1 x 1 bulk terminated surfaces are expected to be stable, with one of the terminations being the ground state. This was indeed found to be the case, with the AZ termination being the lowest in energy for all three compounds. Thus, the reconstruction mechanism observed for the KTaO_3 (001) surface is expected to be specific to polar surfaces.

A recent study by Druce et al [168] used Low-Energy Ion Scattering (LEIS) to investigate the very outermost surface layers of III-III perovskite materials after high temperature annealing. It was found that the outermost layer of these materials was rich with A cations. Just below the surface layer existed regions rich in B cations. These findings support the atomic rearrangement at the surface shown in this chapter.

Further work investigating the stability of these reconstructions applied to perovskites, in which the formal charge on the A and B cations is the same, would help illuminate how large an effect the charge disparity between the two different cations has on the stabilisation effect of the B cation maximising its coordination.

Chapter 5

KMgF₃ and KZnF₃ Clusters

5.1 Introduction

The emphasis of the thesis now focuses on the atomic structure that results when the number of atoms is such that each atom is part of the surface, i.e. nanoclusters. In this chapter nanoclusters of the perovskite compounds KMgF₃ and KZnF₃ have been investigated. This work is part of an international collaborative effort to determine the efficiencies of a number of global optimisation (GLOp) techniques currently employed by world leading experts within the field of structure prediction. The GLOp techniques used were Genetic Algorithms (GA), Basin Hopping (BH), and Stochastic Quenching (SQ). The techniques were tested on how quickly they found the lowest energy structure, the global minimum (GM), and the 10 lowest energy, local minima (LM) structures. All work presented in this chapter is my own.

The first section of results compares the performance of three different global optimisation techniques in predicting the low energy structures of the nanoclusters. The global optimisations are performed on the interatomic potential (IP) energy landscape for cluster size $n = 1 - 9$, where n is the number of formula units used. The best IP structures were refined through DFT. The optical properties were calculated for the DFT nanoclusters. Lastly, structures with bulk-like features were compared to globally optimised clusters, over the sizes $n = 8 - 12$.

5.1.1 Nanocluster Structure Prediction

Nanoclusters have enjoyed a large influx in research over recent decades owing to their unique catalytic [169–171] and optical [172–174] properties, which are tunable by controlling cluster size [175–177]. Due to the small size of these particles, it is difficult to ascertain their structural properties from conventional X-ray and neutron scattering methods. For this reason, the structure of nanoclusters are often “predicted”. Generally, there are considered to be two styles of approach in predicting these structures [178]: (a) a “top-down” approach, where the bulk material is scaled down to the nano-scale. (b) a

“bottom-up” approach, where nanoclusters built up from individual atoms.

The “top-down” method is typically more useful for larger clusters containing 1,000s of atoms. This method often makes use of molecular dynamics (MD) and Wulff constructions [179]. The “bottom-up” approach is generally more useful for smaller clusters, such as those investigated in this thesis (5 – 100 atoms). Various global optimisation techniques have been developed and employed to predict the structure of these small nanoclusters. Popular techniques that have been employed include: Genetic Algorithms (GA) [52, 180–184], Basin Hopping (BH) [53, 66, 185, 186], MD [187, 188], and Simulated Annealing (SA) [189, 190]. While there has been extensive research into predicting the structure of small nanoclusters for single elements and binary compounds [187, 191–196], there is relatively little on ternary compounds such as perovskites [182].

5.2 Global Optimisation: Performance

Three of Global Optimisation (GLOp) techniques tested were Stochastic Quenching (SQ), Basin Hopping (BH), and Genetic Algorithms (GA). The SQ method randomly places ions into a box and then performs a geometry relaxation. BH starts with one such relaxed random structure, thereafter, each new trial structure is based upon small atomic displacements and ion interchange of the last successful structure. The GA approach starts with a population of relaxed random structures. The structures then compete to “breed” (to produce a new “child” population) or survive in “tournaments”. The aim of these GLOp techniques is to find local minima energy structures with the lowest energy structure efficiently. The global minimum (GM), generally being the favoured prize. The effectiveness of the GLOp technique is determined by how quickly the GM structure is located and how many of the lowest energy local minima (LM) are found.

These three techniques were tested using KLMC, with the atomistic relaxations being performed in the General Utility Lattice Program (GULP). For the BH technique, the maximum atomic displacement allowed during the cluster modifications was capped at 1.5 Å per atom. A temperature of 0 K was employed for the metropolis criterion, $P = e^{\frac{\Delta E}{kT}}$, where P is the probability of the modified cluster being chosen, ΔE the difference in energy between the previous and current structures, k the Boltzmann constant, and T the temperature. Thus, the current cluster could only be replaced by a lower energy cluster. For the GA, a population size of 32 was chosen. It was found that smaller populations were more efficient on smaller energy landscapes, while the larger populations excelled on the larger landscapes. Each of the methods were run four times and the results averaged.

5.2.1 Efficiency Locating Global Minimum

The first test is how quickly each of the GLOp techniques locate the GM. Figures 5.1 and 5.2 show the statistics relating to finding the GM for the KMgF_3 and KZnF_3

clusters when employing the three GLOp techniques. More precisely, the figures report

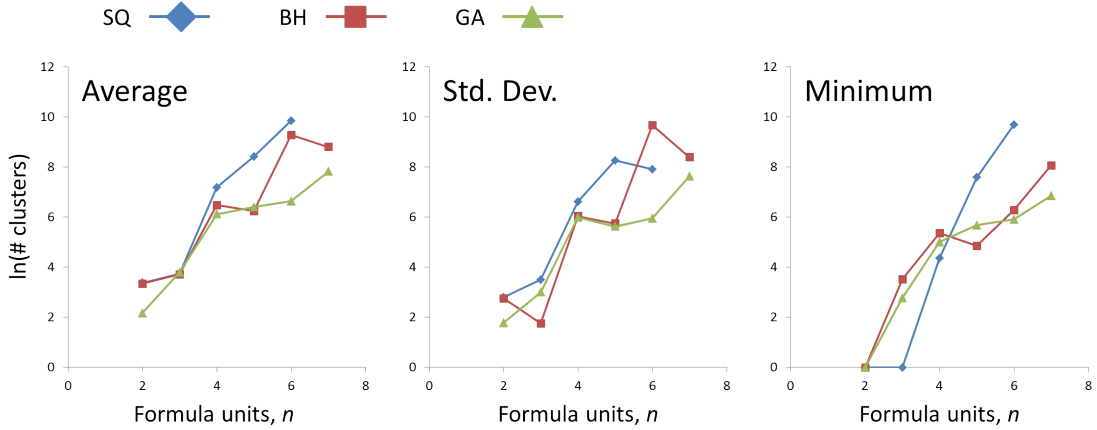


Figure 5.1: Comparison of the efficiency at finding the $(\text{KMgF}_3)_n$ GM cluster for three different global optimisation techniques: Stochastic Quenching (SQ), Basin Hopping (BH), and Genetic Algorithms (GA). The computational cost is measured as the number of cluster optimisations performed before the GM structure is found, as a function of cluster size (formula units). The first graph reports the average obtained across four different runs; the second reports the standard deviation associated with this average; and the third reports the best (lowest cost) of the four runs.

the average computational cost, over four independent runs, in locating the GM as a function of cluster size in formula units, n , for $(\text{KMgF}_3)_n$ and $(\text{KZnF}_3)_n$, as well as the standard deviation and the cost of the best run. The cost is measured as the number of cluster optimisations (CO) performed in each run before the GM structure was located and is displayed on a log scale in the figures.

The number of possible configurations a cluster can form is expected to increase exponentially with the number of atoms the cluster contains. Thus, a linear trend would be expected in Figures 5.1 and 5.2.

For KMgF_3 , it can be seen that at small cluster sizes, up to $n = 4$ (20 atoms), the average cost of finding the GM for all three techniques are roughly equal and therefore of similar efficiency. Above four formula units, the relative performance of the SQ method rapidly drops and becomes the least efficient approach. Moreover, the SQ method was not employed above $n = 6$ as it became ineffective.

Of the other two methods, the GA is found to be the better at locating the GM of the larger clusters. At $n = 6$, the BH technique struggles to locate the GM; becoming almost as inefficient as the SQ method.. The spike in the cost of the BH method is accompanied by a spike in the standard deviation at this point. In fact the large average in this cost is due to one of the runs taking exceptionally long to locate the GM, requiring just under 40,000 (CO) to locate the GM, while the other runs all required less than 3,000 (CO) to locate the GM. This highlights the possible benefit of performing multiple runs over just one long run. For $n = 8$ and 9, neither the BH or the GA techniques were able to

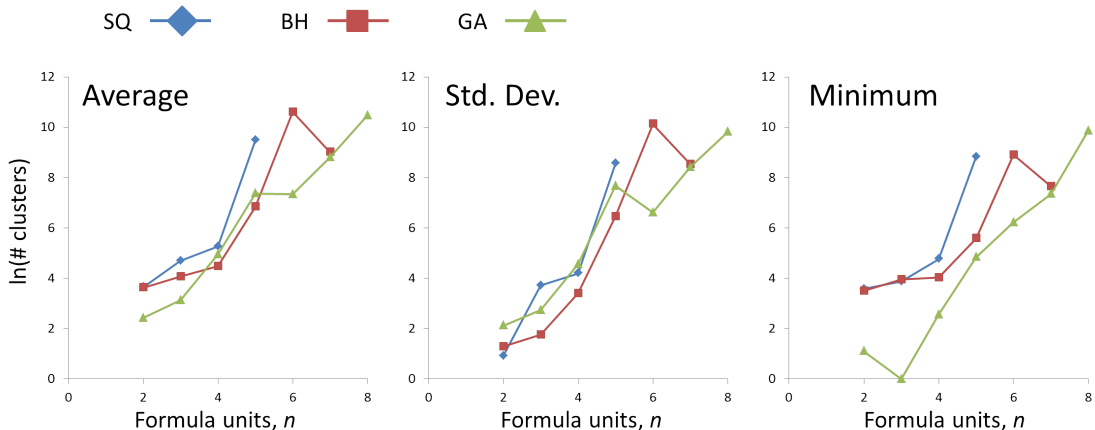


Figure 5.2: Comparison of the efficiency at finding the $(\text{KZnF}_3)_n$ GM cluster for three different global optimisation techniques: Stochastic Quenching (SQ), Basin Hopping (BH), and Genetic Algorithms (GA). The computational cost is measured as the number of cluster optimisations performed before the GM structure is found, as a function of cluster size (formula units). The first graph reports the average obtained across four different runs; the second reports the standard deviation associated with this average; and the third reports the best (lowest cost) of the four runs.

locate the GM on all four runs within 100,000 (CO).

For KZnF_3 , a similar trend of results is seen. At small cluster sizes there is not a large difference in efficiency, however, as cluster size grows the SQ technique rapidly becomes the least efficient. At $n = 6$ the SQ method fails to locate the GM on all four runs within 100,000 CO. For the larger cluster sizes, the GA and BH method are competitive, with the GA being slightly more efficient. A spike is again seen in the BH technique at $n = 6$, accompanied by a spike in the standard deviation. This time, however, the result is not as skewed, with the four runs finding the GM after 7,000, 25,000, 61,000, and 67,000 CO. The difficulty the BH approach has in finding the GM at $n = 6$ may be a feature of the IP energy landscape. At $n = 8$ the BH technique was only able to find the GM in two of the four runs within 100,000 CO; the GA found the GM in all four runs. At $n = 9$ neither method found the GM in all four runs.

5.2.2 Efficiency Locating Top Ten Local Minima

While locating the GM is often a high priority, finding other low energy local minima (LM) structures can be just as important. This is especially true for larger sized clusters as the energy difference between different structures can be very small. The significance of having small energy differences between GM and lowest energy LM is that a range of the clusters would exist at finite temperature. Furthermore, when the energy difference between similarly ranked clusters becomes small, the accuracy of the energy function may begin to affect the ranking of the structures. The shift in relative energy between different structures due to alterations of the potentials or functional used will have a

more pronounced effect on the energetic ordering (ranking). Statistics with respect to how quickly the top ten LM were found for each GLOp technique are discussed. Figures 5.3 and 5.4 show the speed or cost at which the top ten most stable structures are located during the GLOp runs of the KMgF_3 and KZnF_3 clusters respectively. For the

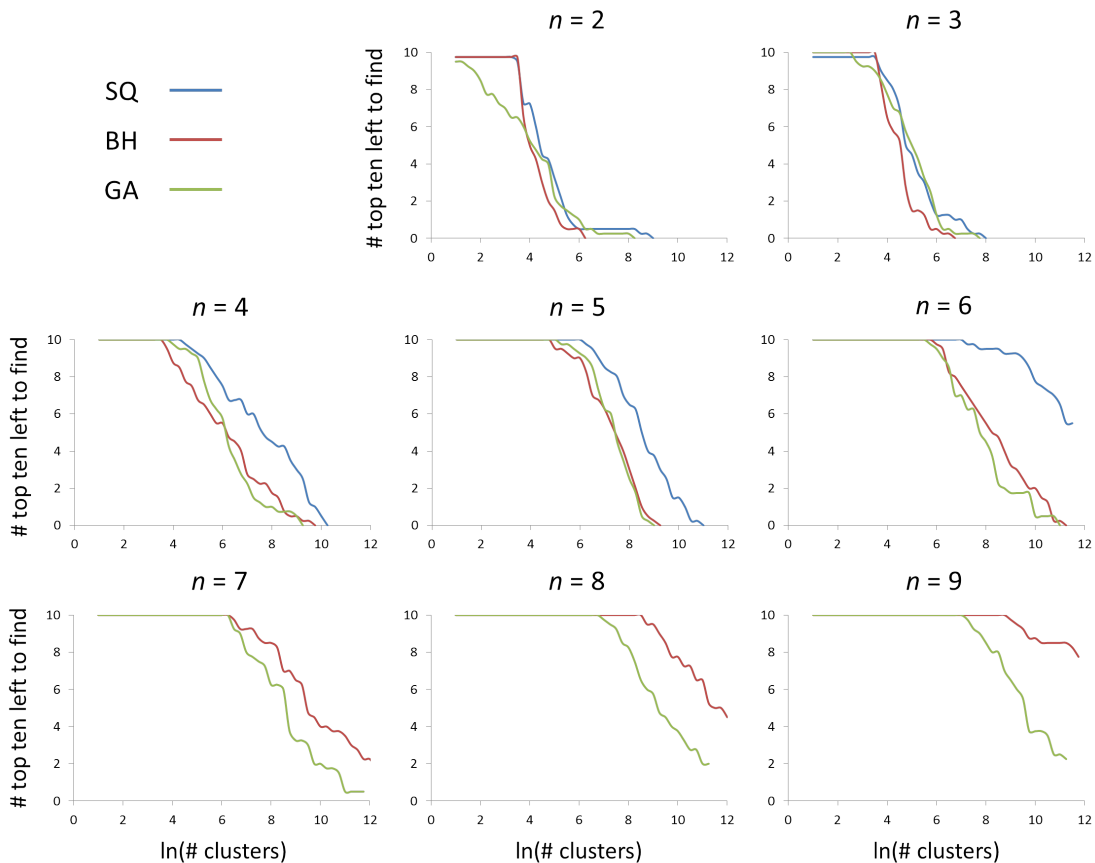


Figure 5.3: Comparison of the efficiency at which the three different GLOp techniques, SQ, BH, and GA found the ten most stable clusters for different sized $(\text{KMgF}_3)_n$ clusters.

KMgF_3 clusters, the three techniques are competitive at generating the top ten LC for smaller sizes. At $n = 4$ the SQ method can be seen to be lagging behind the other two methods, moreover, at $n = 6$ the SQ method fails to find all top ten LM structures. The GA and BH method remain equally effective up until $n = 7$, at which point the GA becomes the more proficient of the two. $n = 7$ is also the cluster size at which the GA and BH techniques begin to struggle locating all top ten LM structure within 100,000 cluster optimisations. As the cluster size gets bigger the gap in the efficiency of the two methods also appears to increase. For the KZnF_3 clusters, the results are similar, except that the GA techniques proves to outperform the others at a much earlier stage (at $n = 5$). The GA approach proved to be better at searching the landscape of KZnF_3 than KMgF_3 in that it finds all ten clusters for KZnF_3 at $n = 7$; whereas the BH misses one cluster in one of its four runs at $n = 6$. Overall, it can be seen that when it comes

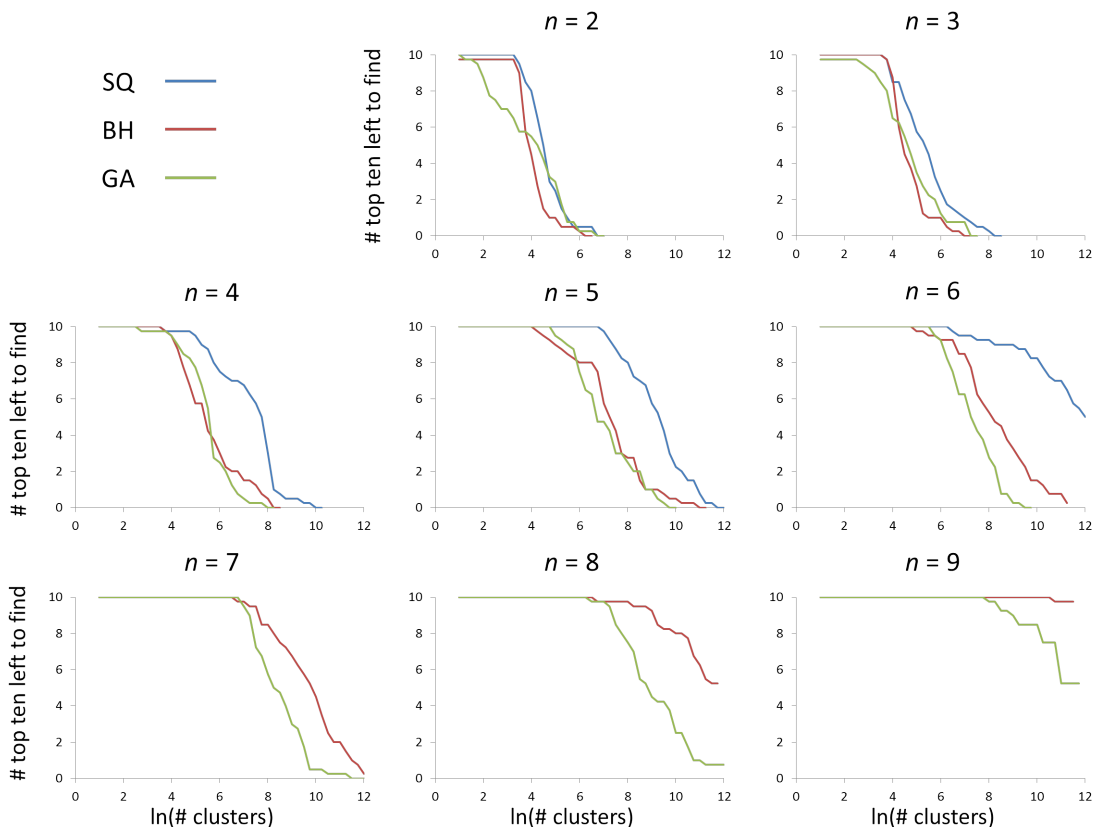


Figure 5.4: Comparison of the efficiency at which the three different GLOP techniques, SQ, BH, and GA found the ten most stable clusters for different sized $(\text{KZnF}_3)_n$ clusters.

to predicting the top ten LM structures, the GA method again appears to be the most effective, followed by BH, with SQ proving to be much less efficient than the other two techniques when n is greater than 3.

5.2.3 Cluster Geometry Optimisation Cost

The cost at which the efficiency of the techniques has been measured is simply the number of cluster optimisations performed. However, not all GLOP techniques chosen by our collaborators perform cluster geometry optimisations. Additionally, the cost of optimising can vary greatly with cluster geometry. To make a fairer comparison between a wider range of techniques, the cost was converted into units that are more widely applicable. The cluster optimisation unit is broken into the number of individual energy, first derivative, and second derivative calculations performed. The breakdown is shown for each GLOP technique at each cluster size in Figures 5.5 and 5.6 for KMgF_3 and KZnF_3 , respectively. The figures show that the average computational cost of performing a cluster geometry optimisation varies between the different GLOP techniques! The SQ method requires the most effort when performing a geometry optimisation. This is a result of these cluster being created in a highly random way and so the structure re-

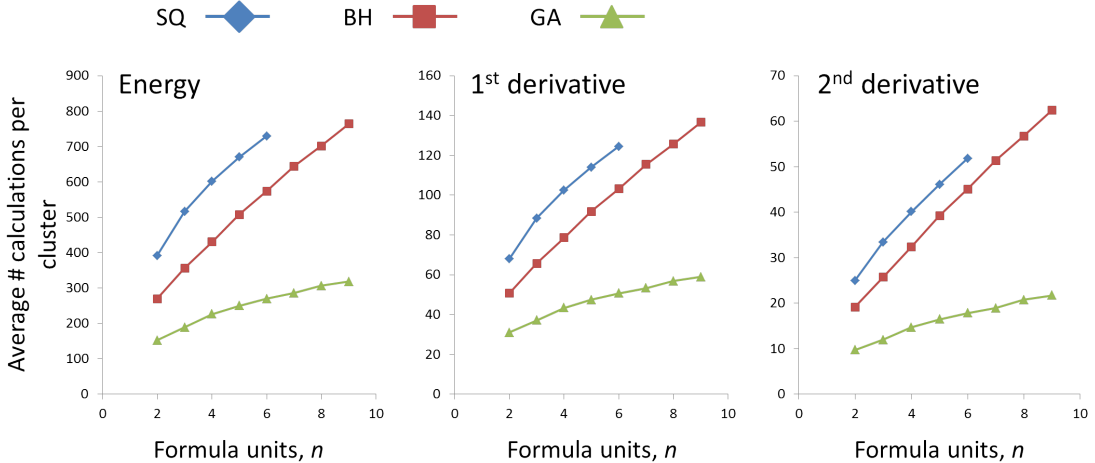


Figure 5.5: Average number of calculations performed for each $(\text{KMgF}_3)_n$ cluster optimisation during the three GLOp techniques: Stochastic Quenching (SQ), Basin Hopping (BH), Genetic Algorithms (GA).

quires a lot of rearranging to find a local minima. The BH method results in the second most expensive geometry optimisations. The reduced cost compared to the SQ technique is due to the BH structures (except the first configuration tested on a particular run) being modifications of previously relaxed structure. As the BH process does not totally randomise the structure, stable fragments of the cluster may exist at the start of the geometry relaxation process and so less effort is required. The GA clusters are the cheapest to relax. Many of the cluster being optimised with this technique are the result of two different relaxed cluster being halved and merged together. This suggests many of the atoms are already sitting in relatively stable positions with the atoms at the interface of the two halves being where most of the effort must be applied. Thus, the relaxation process starts from a partially relaxed position.

The major difference in going from the KMgF_3 clusters to the KZnF_3 is the increase in cost of the BH clusters relative to the GA and SQ clusters. This suggests that the KZnF_3 compound is more sensitive to the modifications performed in the BH method than the KMgF_3 clusters.

Table 5.1 shows the cost of first and second derivative calculations as a ratio against the cost of a single energy calculation. This data is employed to compute a standardised cost for each of the three GLOp techniques used, allowing for a fairer comparison between these methods and those used by our collaborators. From the table it appears, counter-intuitively, that calculating the derivative is cheaper than calculating the energy. However, determining the derivatives requires computing the energy. The cost of calculating the energy is the most expensive part in determining the derivative. This cost is not attributed to the derivative, but recorded as an energy calculation. Thus, the derivative cost is simply the additional cost on top of these energy calculations, hence the small expense. Similarly so for the second derivative.

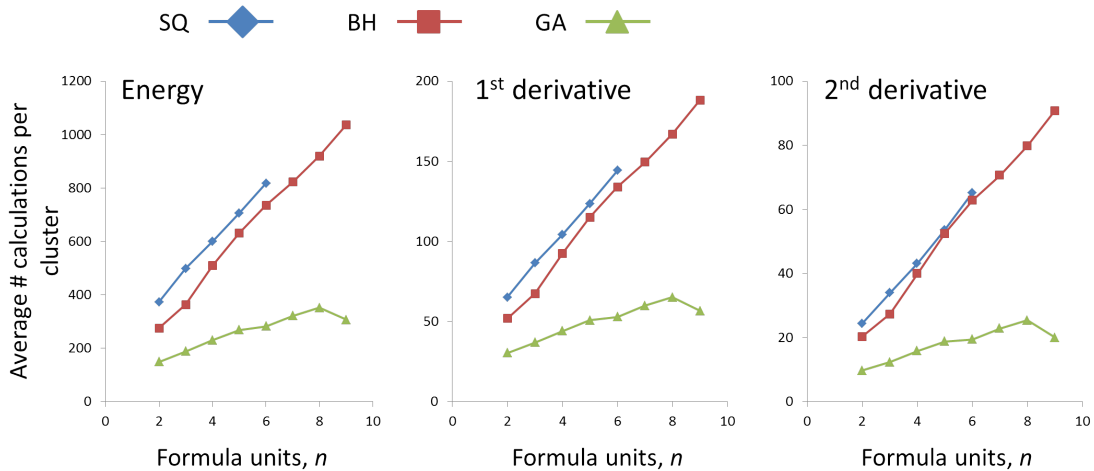


Figure 5.6: Average number of calculations performed for each $(\text{KZnF}_3)_n$ cluster optimisation during the three GOp techniques: Stochastic Quenching (SQ), Basin Hopping (BH), Genetic Algorithms (GA).

Table 5.1: **Calculation ratios.** The relative cost of first (E') and second (E'') derivative calculations as a ratio against the cost of an energy calculation (E'/E , E''/E). Bear in mind the calculation of a derivative requires the calculation of the energy, the cost of these energy calculations are not included in the derivative cost.

n	2	3	4	5	6	7	8	9
E'	0.70	0.47	0.37	0.34	0.29	0.30	0.31	0.32
E''	5.96	7.63	9.29	10.95	12.61	14.27	15.94	17.60

Lastly, it should be noted that the settings used for each of the GOp techniques will have an impact on how quickly the cluster relaxations are performed. For example, performing the SQ method using an extremely large box will undoubtedly increase the cluster relaxation cost as the atoms will have further to travel before residing in a local minima. Similarly, having a very small step size in the BH method will decrease relaxation cost as the previously relaxed structure will have undergone a much smaller alteration, but these parameters will also affect the GOp ability to span the space of possible configurations, and therefore the success of finding the desired LM.

5.2.4 Summary

Analysis of the GOp performance in relation to the structure prediction of KMgF_3 and KZnF_3 clusters has shown the GA technique to be the most superior of the three methods tested. When attempting to locate the GM structures it was found that all three techniques were competitive for the smaller clusters (≤ 20 atoms). For larger cluster sizes the SQ technique became ineffective. The GA method was found to outperform the BH at the finding the GM for the larger sized clusters with the difference in efficiency

becoming more pronounced as cluster size increased. The efficiency at which the clusters predict the top ten lowest energy structures was also investigated. The results match closely to those seen in the locating of the GM. The SQ falls behind as soon as the clusters have more than 20 atoms. The GA method outperforms the BH above $n \approx 7$. Lastly, the average cost required to relax the geometry of each cluster was determined for each GOp approach, so as to make the cost function fairer when comparing with other GOp techniques. The cost was measured as the number of energy, first derivative, and second derivatives performed to relax the cluster geometry. It was found that the GA method, on top of being the most efficient with respect to the number of cluster optimisations, also had the smallest cost for each cluster optimisation. The SQ approach had the most expensive cluster optimisations.

5.3 The Global Optimisation Cluster Results

5.3.1 Cluster Energies

Table 5.2: **KMgF₃ IP Cluster Energies $n = 1 - 5$** . The IP energies of the ten lowest energy (KMgF₃)_n LM clusters for $n = 1 - 5$. The clusters were found using the global optimisation routines and match those found by our collaborators.

Rank	$n = 1$	$n = 2$	$n = 3$	$n = 4$	$n = 5$
1	-24.336	-51.499	-78.318	-105.581	-132.884
2	-23.945	-51.477	-78.233	-105.558	-132.847
3	-22.201	-50.915	-78.158	-105.557	-132.775
4		-50.885	-78.134	-105.484	-132.774
5		-50.876	-78.132	-105.479	-132.773
6		-50.803	-78.128	-105.449	-132.761
7		-50.767	-78.105	-105.424	-132.743
8		-50.760	-78.094	-105.418	-132.738
9		-50.670	-78.089	-105.410	-132.717
10		-50.667	-78.088	-105.394	-132.714

Tables 5.2 – 5.5 report the interatomic potential energies of the ten lowest energy unique LM for clusters of (KMgF₃)_n and (KZnF₃)_n, for sizes $n = 1$ to 9. These clusters were found using the global optimisation techniques discussed previously in section 5.2. The energies in the tables show a trend that the difference in energy between 1st and 10th ranked clusters decreased as cluster size increases. This means that as the cluster size grows there is likely to be a higher density of unique clusters within the thermal energy range from the GM. The reason for this is due to the difference at which the energy and number of possible configurations evolve as cluster size is increased. The change in energy of adding a formula unit to the cluster is linear while the number of possible configurations follows a factorial trend.

Figure 5.7 plots the energy per atom of the top ten clusters for each size relative to

Table 5.3: **KZnF₃ IP Cluster Energies $n = 1 - 5$** . The IP energies of the ten lowest energy (KZnF₃)_{*n*} LM clusters for $n = 1 - 5$. The clusters were found using the global optimisation routines and match those found by our collaborators.

Rank	$n = 1$	$n = 2$	$n = 3$	$n = 4$	$n = 5$
1	-33.802	-71.197	-107.967	-145.957	-183.449
2	-33.224	-71.155	-107.868	-145.945	-183.304
3	-31.025	-70.438	-107.858	-145.850	-183.252
4		-70.420	-107.849	-145.708	-183.173
5		-70.405	-107.846	-145.497	-183.157
6		-70.377	-107.834	-145.443	-183.123
7		-70.351	-107.815	-145.423	-183.089
8		-70.303	-107.794	-145.410	-183.086
9		-70.280	-107.778	-145.397	-183.070
10		-70.235	-107.776	-145.394	-183.033

Table 5.4: **KMgF₃ IP Cluster Energies $n = 6 - 9$** . The IP energies of the ten lowest energy (KMgF₃)_{*n*} LM clusters for $n = 6 - 9$. The clusters were found using the global optimisation routines and match those found by our collaborators.

Rank	$n = 6$	$n = 7$	$n = 8$	$n = 9$
1	-160.252	-187.816	-215.292	-242.822
2	-160.207	-187.809	-215.287	-242.791
3	-160.187	-187.739	-215.254	-242.743
4	-160.178	-187.735	-215.228	-242.734
5	-160.174	-187.731	-215.220	-242.729
6	-160.170	-187.730	-215.175	-242.718
7	-160.167	-187.717	-215.163	-242.714
8	-160.166	-187.714	-215.158	-242.698
9	-160.161	-187.680	-215.152	-242.682
10	-160.151	-187.660	-215.141	-242.662

the bulk:

$$E_{relative} = \frac{E_{cluster}}{(5n)} - \frac{E_{bulk}}{5} \quad (5.1)$$

where $E_{cluster}$ and E_{bulk} are the absolute energies obtained for the cluster and bulk, n is the number of formula units the cluster contains, and a factor of 5 is used as one formula unit contains 5 atoms. The bulk energies for KMgF₃ and KZnF₃ are -28.329 and -38.715 eV per formula unit. For KMgF₃, the three relative energies of the $n = 1$ clusters are 0.799, 0.877, and 1.226 eV per atom. For KZnF₃, the three relative energies of the $n = 1$ clusters are 0.983, 1.098, and 1.538 eV per atom. These are omitted from Figure 5.7 to increase the clarity of the remaining data in the plots. The gap in energy between the GM cluster and LM9 can be seen to decrease with increasing cluster size for both KMgF₃ and KZnF₃. The only notable exception occurs at $n = 3$ for KZnF₃ which shows a energy range narrower than expected. The energy ranges of the KZnF₃ clusters

Table 5.5: **KZnF₃ IP Cluster Energies $n = 6 - 9$** . The IP energies of the ten lowest energy (KZnF₃)_n LM clusters for $n = 6 - 9$. The clusters were found using the global optimisation routines and match those found by our collaborators.

Rank	$n = 6$	$n = 7$	$n = 8$	$n = 9$
1	-220.971	-258.759	-296.454	-334.139
2	-220.965	-258.662	-296.435	-334.104
3	-220.962	-258.642	-296.433	-334.098
4	-220.865	-258.607	-296.431	-334.097
5	-220.856	-258.597	-296.367	-334.092
6	-220.845	-258.573	-296.360	-334.072
7	-220.813	-258.561	-296.350	-334.065
8	-220.780	-258.554	-296.334	-334.063
9	-220.776	-258.542	-296.329	-334.055
10	-220.760	-258.530	-296.329	-334.039

appear to be slightly larger than for KMgF₃. This is a result of the overall tighter binding of the bonds in KZnF₃ which can be seen in the difference in the bulk energies of the two compounds. The graphs show a downward trend of the relative energies with increasing cluster size, implying that larger clusters are thermodynamically more stable. It is expected that the energies will tend to 0 with increasing size where the bulk phase will precipitate due to being the most stable phase.

5.3.2 Atomic Structure of IP Clusters

$n = 1$

Figure 5.8 shows the three clusters found when $n = 1$ for both (KMgF₃)_n and (KZnF₃)_n. The same colour scheme for atoms is employed in this and all other figures that follow. Only three LM configurations are found for $n = 1$; the same three are found for both compounds. As these clusters involve so few atoms, they are less complex and so it is easier to understand their structure. The global minimum (GM) structure adopts a planar arrangement with the X²⁺ cation (X = Mg²⁺ or Zn²⁺) bonded to all three F ions and the K ion bonded to two. The X – F bond length to the isolated F is 1.756 Å and 1.763 Å for X = Mg and Zn respectively, a difference of less than 0.5% between the compounds. The other X – F bond has length 1.825 Å for X = Mg and 1.848 Å for X = Zn, showing the Zn – F bond to be larger than the Mg – F bond by 1.3%. The K – F bonds are also found to be longer in the KZnF₃ compound by 2.6 % with the bonds being 2.424 Å and 2.486 Å in length for KMgF₃ and KZnF₃, respectively. The F – X – F bond angle between the two identical F ions are 92.2° for X = Mg and 89.9° for X = Zn. The F – K – F angle is 65.8° for KMgF₃ and 63.4° for KZnF₃. The F – F separation between symmetrically equivalent F ions is 2.632 Å for KMgF₃ and 2.611 Å for KZnF₃, a difference of 0.8%. Thus, the differences in bond lengths and angles

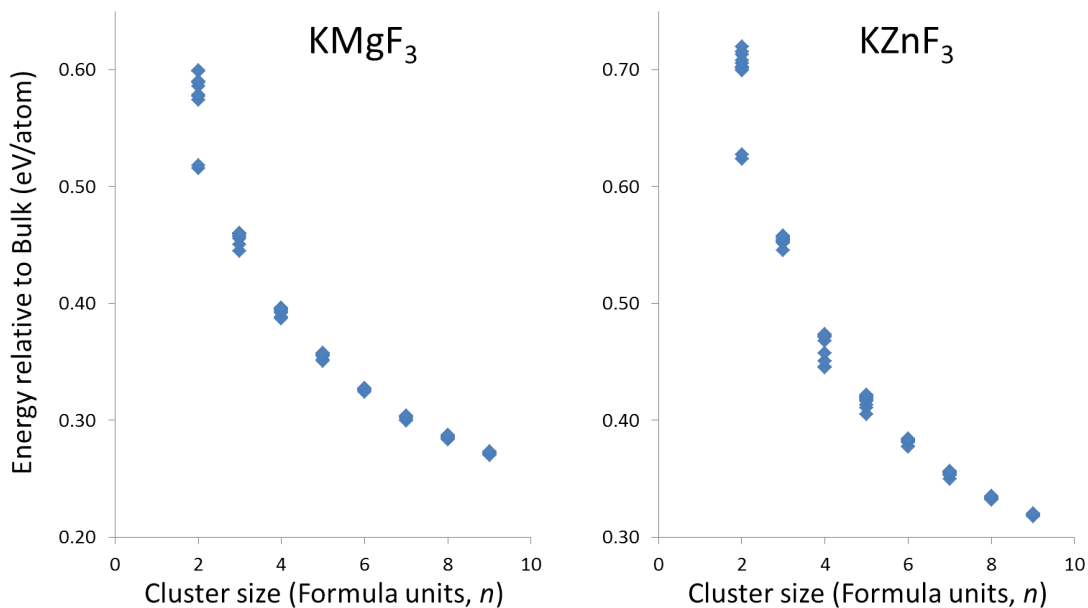


Figure 5.7: IP energies for top ten structures for each cluster size relative to the bulk.

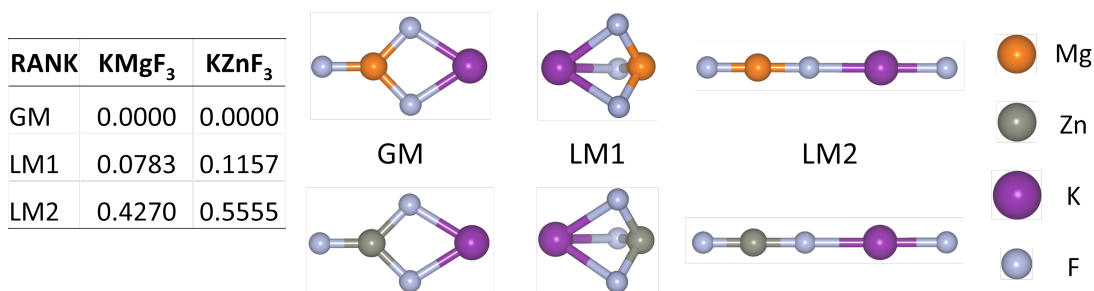


Figure 5.8: The three stable LM IP clusters found for $n = 1$. The table shows the energy for each cluster relative to the GM in eV/atom

between the compounds have not significantly affected the anion separation. The X – K separation on the other hand has been more strongly affected with the K – Mg distance being 3.302 Å while the K – Zn distance is 3.7% larger at 3.424 Å. A formal charge model was used for KZnF₃ and a partial charge model for KMgF₃ and so it is expected that the cation – cation repulsion will be stronger for the formal charge model. Additionally, K – F bonds are longer for KZnF₃ while the X – F bonds are fairly similar between compounds suggesting the K ion may be modelled as larger in the KZnF₃ compound. Thus, it appears that the differences between the two compounds can be ascribed to the stronger cation – cation repulsion and the larger K ion modelled by the KZnF₃ potentials.

The second ranked structure, local minimum 1 (LM1), is a more compact, three-dimensional structure. The three fluorine atoms form an equilateral triangle and the two cations are positioned in line with the triangle centre either side of the triangular

plane. The Mg – F bond distance is 1.798 Å and the Zn – F bond only 0.8% larger at 1.812 Å. The K_{Mg} – F bond distance is 2.589 Å and the K_{Zn} – F is 2.679 Å which is 3.5% longer. The K – Mg bond distance is found to be 2.812 Å and the K – Zn distance is 3.7% larger at 2.916 Å. This again shows the K – F bond and cation separation to be the most sensitive to the change in the divalent cation.

The third ranked cluster, LM2, is a linear stick structure and is by far the least thermodynamically stable of all $n = 1$ clusters investigated. The cations reside either side of a central F ion with the other two F ions at the ends of the stick. This structure exhibits the same behaviour as the other two structures where the bond lengths and cation separation are both greater in $KZnF_3$. There is one notable difference: the Mg – F bond to the outer F ion is 0.2% longer than for Zn – F, which is the first time a longer bond has been seen in the $KMgF_3$ compound. This is likely to be due to the reduced number of next nearest neighbour anions, which has the effect of reducing the anion – anion repulsion experienced by this edge F ion. As the $KZnF_3$ model uses formal charges, the reduction is more significant for this compound.

$n = 2$

The $n = 2$ clusters are composed of 10 atoms and introduce like cation – cation interactions which are absent in $n = 1$. The top ten most thermodynamically stable structures (the GM and LM1–9) are shown in Figure 5.9. The same best three structures are found

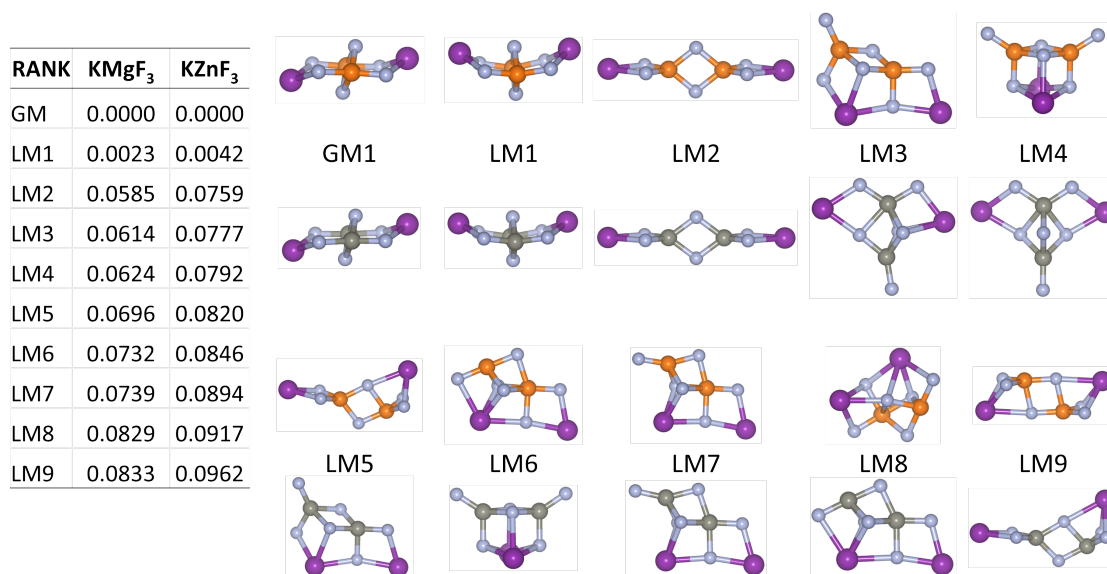


Figure 5.9: Ten most thermodynamically stable LM IP clusters for $n = 2$. The table shows the energy for each cluster relative to the GM in eV/atom

for both compounds. The first two are particularly close in energy, have identical connectivity, and are significantly more thermodynamically stable than the other clusters. The GM is an almost planar $K_2X_2F_4$ ring with cations and anions alternating around

the ring and like cations sitting on opposite sides. The K ions sit slightly off plane in opposite directions, whereas for LM1 they are both positioned on the same side of the plane. The X cations have distorted the ring by moving inwards towards the centre and are linked by two F ions sitting above and below the ring centre. These F ions bonded to two X cations lean towards the closest K ions, i.e. the K ion that is shifted of the plane in the same direction as the F ion. The result is that the X ions are much closer together and closer to the cluster centre than the K ions are. The Mg – Mg separation is 2.994 Å and the Zn – Zn distance is 3.114 Å. This difference of 5.0% is the largest seen so far for near-neighbours between the two compounds and emphasises the effect of the difference in coulomb repulsion. The F ion coordinated to two Mg ions has a Mg – F bond length of 1.936 Å, while the equivalent bond in the Zn based structure has a length of 1.971 Å; a difference of only 1.8%. On the other hand, the F – Mg – F angle involving the two F ions that are coordinated to both Mg ions is 6.1% larger than the equivalent F – Zn – F angle; the angles calculated to be 78.7° and 74.2°, respectively. This results in the central F – F separation for KMgF₃ being 3.3% larger than in the KZnF₃ structure. The F – F separation, as opposed to the Zn – F bond distance, has been sacrificed in the KZnF₃ cluster to accommodate the increased Zn – Zn separation. The rest of the clusters follow a pattern similar to the $n = 1$ clusters with the bonds being slightly longer in the KZnF₃ compound, the K – F bond in particular.

The LM1 structure differs only slightly from the GM. The K ions are now both positioned on the same side above the plane of the ring as already described. Additionally, the F ions coordinated to both Mg ions no longer lean in any preferential direction and so the structure has a vertical plane of symmetry passing through both X ions. The remaining F ions are also seen to move slightly upwards following the K ions which reduces the symmetry of the X – F bonds to the central F ions. As with the GM, the Zn – Zn separation is 5.0% larger than the Mg – Mg separation, so again showing the prevalent difference in cation – cation repulsion. The K – F bond length is about 1% smaller in LM1 compared to the GM for both compounds. The slight increase in energy of this structure with respect to the GM is likely a result of the increased compactness, which reduces the cation–cation and anion–anion separation resulting in stronger Coulomb repulsion.

The third ranked cluster, LM2, has a structure in which the coordination numbers are the same as those seen for the GM and LM1, however, the local environment around the X cations is different. LM2 adopts a linear chain arrangement with the cations separated by two interlinking F ions. Each subsequent link in the chain is rotated about the axis to minimize repulsion between the F ions. The X ions reside at the centre of the chain with the K ions at either end. The X – X separation is 5.2% larger in the KZnF₃ structure while the X – K separation is only 3.8% larger. As in the case of LM1 and the GM, the F – F separation is sacrificed to accommodate this change.

Beyond the first three structures the ordering differs and there are different structures

in the top ten for the two different compounds. A general feature of the structures is that the divalent ions have a higher coordination and are closer to the centre of the structure than the K ions. This is a result of the divalent ions having a higher charge and so are more dominant in maximizing their coordination which is achievable at the centre of the cluster. This has been seen in previous studies involving cluster structure prediction [182]. Of note are LM3 and LM4 for KZnF_3 : these structures are not in the top ten for the KMgF_3 compound. These structures succeed in centralising the Zn ions, making Zn less exposed to the cluster surface. They are also fairly open which would help reduce the ionic repulsions and more easily accommodate the larger K ions, features which are more exaggerated in the KZnF_3 potentials. Another example are LM6 and LM7 for KMgF_3 , which have become LM8 and LM7, respectively, when going to KZnF_3 . These two structures are very similar, the only change being the coordination of the F ion at the top left of the image. For KZnF_3 , it is favourable to have this F ion coordinated to just the Mg ion. In this case the Zn – K separation is increased by over 10% leading to a more energetically favourable arrangement than the K – F bond would give. For KMgF_3 , the partial charge model, the additional K – F bond appears to be the more energetically favourable and hence the difference in order between the two compounds. The KMgF_3 LM5 structure has also undergone a large shift in rank when going to KZnF_3 to become LM9. This structure is similar to LM2 except one of the K ions has folded over to become triply bonded. In doing so the K ion has approached closely to the X ion, 2.905 Å for Mg and 3.007 Å for Zn. This is a particularly small separation for these ions, and has a more prominent effect on the KZnF_3 compound, hence the large fall in rank.

$n = 3$

The $n = 3$ clusters are shown in Figure 5.10. They have 15 atoms and so are much more complex. This makes characterising the subtle differences that make one cluster lower in energy than another much more difficult. In addition, due to the larger number of possible structures, the difference in stability between the clusters in the top ten is small. This makes it harder to isolate what are the more energetically significant features, for example, the shortening of one or two bonds by 0.1 Å may be enough to switch ordering. Instead, it is probably more useful to identify some of the main structural features present in the better LM clusters, which would indicate low energy characteristics. The structures ranked first and second for both compounds are the same. These two clusters resemble a fragment of the $n = 2$ LM1 cluster. This is easier to see in LM1. The GM for $n = 3$ looks to be the $n = 2$ LM1 combined with the $n = 1$ LM1. LM1 appears as the $n = 2$ LM1 combined with the $n = 1$ GM. In both cases the X ion of the $n = 1$ cluster is positioned towards the centre of the $n = 2$ cluster, while the K ion points away. The combining of smaller stable pieces to create a large stable cluster is the mechanism employed by the GA technique and so may be a hint as

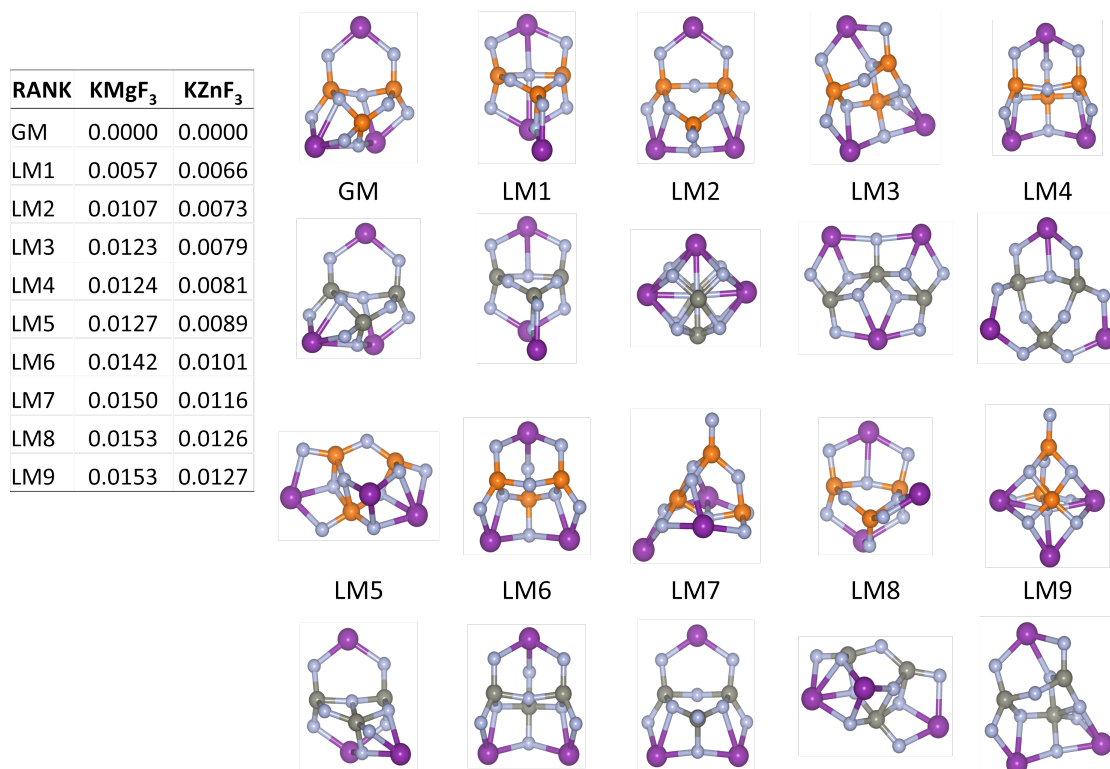


Figure 5.10: Ten most thermodynamically stable LM IP clusters for $n = 3$. The table shows the energy for each cluster relative to the GM in eV/atom

to why the GA technique was so effective. The X ions are again found to be positioned closer to the centre of the cluster than the K ions. This theme is prevalent throughout all the $n = 3$ clusters. This shows that it is energetically favourable for the more highly charged cations to fill their coordination by being near the centre of the cluster despite the larger Coulomb repulsion that would exist between cations. The bonds of the $n = 3$ structures follow the pattern of the smaller clusters with the KZnF₃ bonds being longer than the KMgF₃ bonds, 1-2% for the X – F bonds and 3% for K – F.

$n = 4$

The top ten clusters for $n = 4$ are shown in Figure 5.11. This is the first size at which the GM differ between compounds. The GM for KMgF₃ is a highly ordered symmetrical structure. The Mg ions are all 5-coordinated and sit in equivalent positions forming a square about the centre of the cluster. Two of the K ions sit off plane in line with the centre of this square completing a hollow cage like structure at the centre. The other two form ‘wings’ with two F ions on opposite sides of the cage. The GM for KZnF₃ is a different structure. There are two unique Zn sites, which reside close to the centre of the cluster, and are both 5-coordinated. Two of the K ions sit below the Zn ions forming a K – F – K – F island which also completes a hollow cage region. The other two K ions form ‘wings’, not too dissimilar to those seen in the KMgF₃ GM, that point

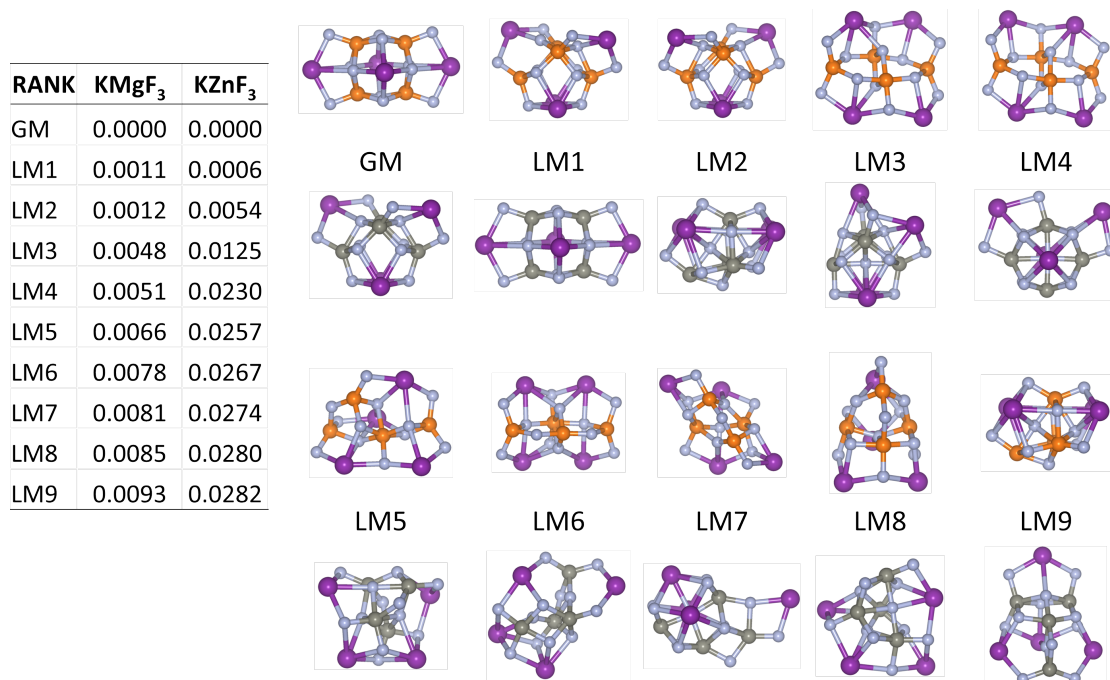


Figure 5.11: Ten most thermodynamically stable LM IP clusters for $n = 4$. The table shows the energy for each cluster relative to the GM in eV/atom

in opposite directions. The GM structure for KMgF₃ is LM1 for KZnF₃, and the GM structure for KZnF₃ is LM2 for KMgF₃. Typically, it is found that many of the highly stable structures for one compound are also seen to be highly stable for the other, i.e. small changes in rank. That being said, there are marked differences between the two potential sets. The difference in energy between the first and tenth ranked potentials is three times greater for KZnF₃ $n = 4$, (c.f. Figure 5.11). This is much greater than the scale between their bulk energies of 1.37 and so cannot be attributed to the average energy scale between the two sets of IP. Instead, the shrinking of the energy gap between first and tenth ranked clusters for KMgF₃ is due to the existence of many very similar structures. For example, the structure of LM1 is very similar to that of LM2, and the structure of LM3 closely resembles that of LM4 and LM6. For KZnF₃, the generation of many similar structures is not seen. This suggests the KZnF₃ potential energy landscape is smoother than the KMgF₃ landscape with fewer potential barriers. The $n = 4$ clusters follow the trend of the smaller sets with the X ions being closer to the centre than the K ions. The KZnF₃ bonds are also longer with the X – X cation separation in particular being larger for Zn.

$n = 5$

A brief look at the $n = 5$ structures shown in Figure 5.12 shows the main features of the $n = 4$ clusters are again prevalent. The Mg and Zn ions continue to dominate the centre of the clusters. Similar low-energy structures exist for the two compounds;

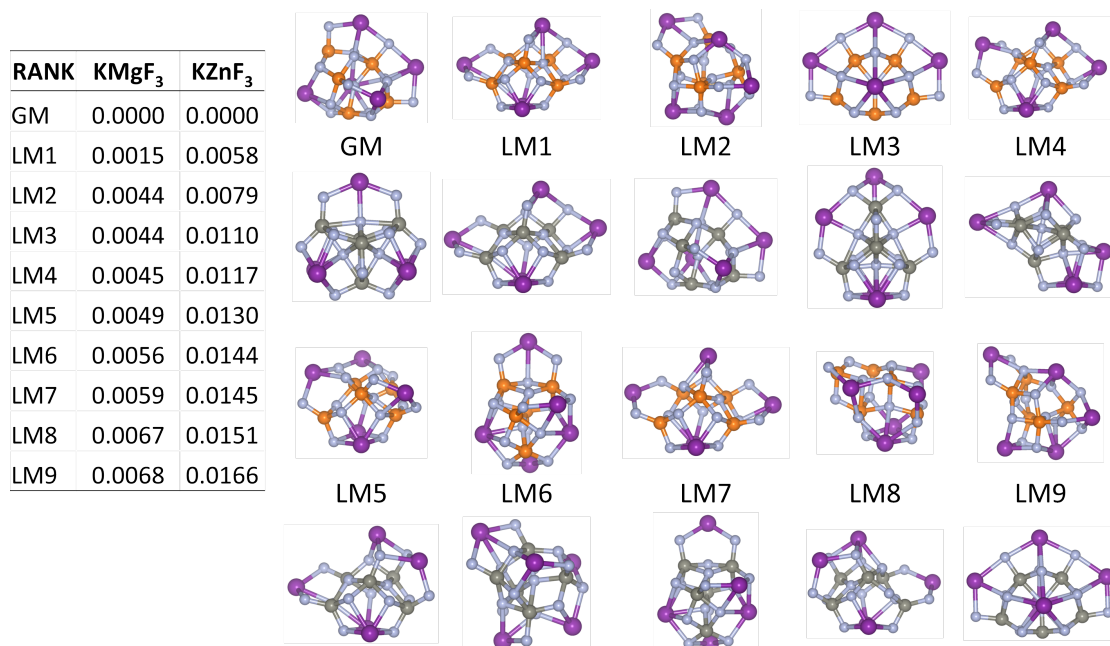


Figure 5.12: Ten most thermodynamically stable LM IP clusters for $n = 5$. The table shows the energy for each cluster relative to the GM in eV/atom

for example, the KMgF₃ GM is the KZnF₃ LM2, whereas LM1 is the same in both compounds. Additionally, the highly ordered KMgF₃ LM3 structure is LM9 for KZnF₃. Differences in structures between the two compounds are also present; for example, the highly ordered KZnF₃ GM does not exist in the KMgF₃ top ten, and neither does the highly ordered LM3. The emergence of repeated features from the smaller clusters also becomes more apparent. The K₂F₂ square island that is seen attached at the bottom of the KZnF₃ $n = 4$ GM (c.f. Figure 5.11) appears in many clusters, i.e. LM1. The KF ‘wings’ seen in the KMgF₃ $n = 4$ GM are used in a repeating fashion along the edges of many of the clusters; this can be seen particularly clearly in KMgF₃ LM3.

$n = 6 - 9$

As the cluster size becomes larger the differences and similarities become more difficult to distinguish. This is highlighted in Figure 5.13, which shows the GM structures found for $n = 6 - 9$. As with the previous sets of low energy LM clusters, the GM for $n = 6 - 9$ all show the X ions to reside at the centre of the cluster while the K ions are pushed out to the surface. The KZnF₃ $n = 6$ and KMgF₃ $n = 8$ GM structures have higher symmetry, whilst the rest appear amorphous. Thus, it is undetermined whether high symmetry is favoured.

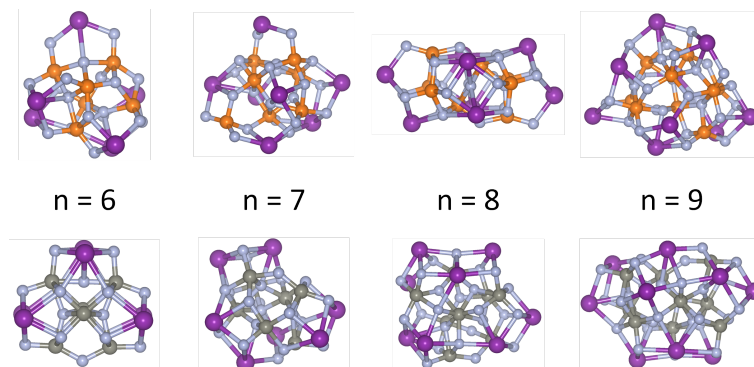


Figure 5.13: The IP GM structures for $n = 6 - 9$

5.4 IP vs DFT Energies

This section discusses the change in ranking, with respect to energy, of the LM clusters when going from IP to DFT. The majority of DFT calculations are performed in FHI-AIMS using the PBEsol functional to stay consistent with previous chapters. However, for the smaller clusters a comparison between the PBEsol and PBE functionals is investigated. At $n = 1$ there were only three IP clusters found for both KMgF_3 and KZnF_3 (cf. Figure 5.8). For $(\text{KMgF}_3)_1$, the IP energies relative to the ground state were 0.078 (LM1) and 0.427 (LM2) eV/atom. Relaxing the IP structures through DFT using the PBEsol functional gave relative energies of 0.091 (LM1) and 0.499 (LM2) eV/atom. Using the PBE functional the relative energy of LM1 was 0.095. The LM2 structure proved to be unstable when using the PBE functional and reconstructed to the GM structure. For $(\text{KZnF}_3)_1$, the IP energies relative to the ground state were 0.116 (LM1) and 0.555 (LM2). With the PBEsol functional the energies became 0.118 (LM1), 0.375 (LM2) eV/atom. Switching to PBE the energies were 0.118 (LM1) and 0.354 (LM2). There were no structural changes observed when refining these structures for KZnF_3 . The relative energies of the IP clusters and DFT clusters are of the same magnitude suggesting the binding energy between the atoms modelled by the IP is of the right scale. Both the IP and DFT clusters agree that the energy gap between the GM and LM1 is bigger for KZnF_3 . There is disagreement for the gap between GM and LM2 with the IP showing it to be bigger for KZnF_3 whereas the DFT have it bigger for KMgF_3 . Where there is a one-to-one match between structures the DFT functionals show very good agreement, with the difference in energies less than 6% in all cases.

Above $n = 1$ the number of IP clusters obtained from global optimisation becomes much larger and so it is more sensible to employ statistics and relate these energies graphically. For $n = 2$, all IP clusters were included in analysis. Above $n = 2$, only the top 100 clusters were considered. For $n = 2$, the IP global optimisation found 39 KMgF_3 unique clusters. Figure 5.14 compares the relative energies of the $n = 2$ LM structures between the different methods of calculations. The first column of plots

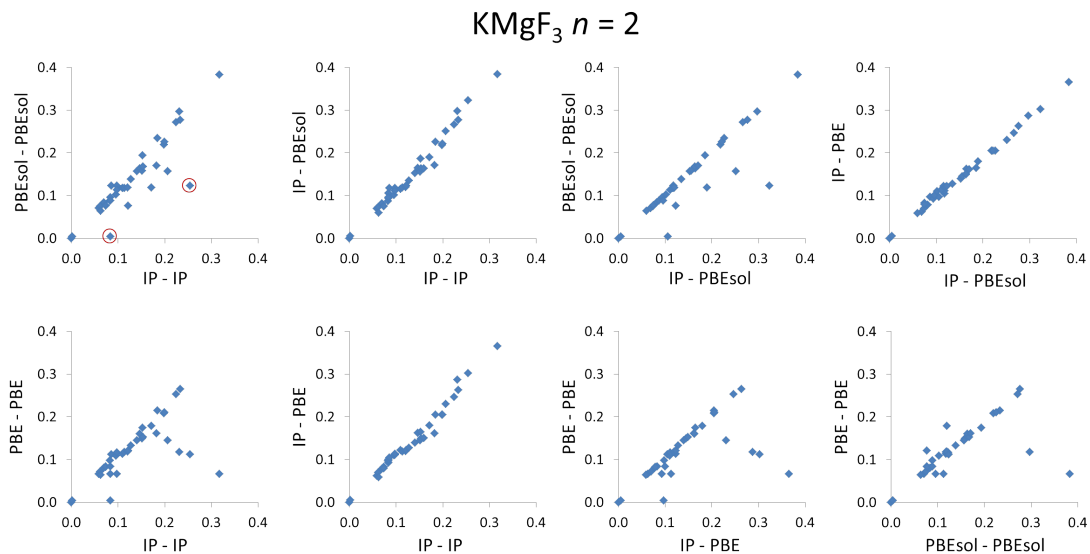


Figure 5.14: Plots comparing the energy of LM clusters calculated using different theoretical models for $(\text{KMgF}_3)_n$, $n = 2$. The axis are labelled $\langle \text{structure method} \rangle - \langle \text{energy method} \rangle$, where the structure method is the theoretical model used to relax the LM structure, and energy method is the model by which the energy was calculated (no additional relaxation). For Example, IP - PBEsol is the energy of a structure which has been relaxed using the IP model, but had the energy of that structure calculated using DFT with the PBEsol functional. All energies are relative to the GM and given in eV/atom.

compare the relative IP relaxed energies to the DFT relaxed energies using PBEsol (top) and PBE (bottom). In the ideal scenario, all points would lie along a linear line. This would indicate a perfect linear relationship between the IP and DFT energies where the energy ranking of each structure would also be the same in both sets of calculations. The two plots do appear to show a strong correlation between the IP and DFT calculations, however, there are a few points that sit far away from the linear relationship; to understand why, additional plots were created.

Column two show the relationship between the IP and DFT single point (unrelaxed) calculated energies. This determines how well the IP and DFT energy agree when the structures are exactly the same. The plot in this case shows strong agreement between the IP and DFT regardless of the functional. The third column plots the relationship between the DFT single point and DFT relaxed energies. A strong correlation would indicate that the relaxation energy was constant for the difference clusters. This would most likely occur when the DFT relaxed structures closely resembled the IP structures. In this case only small structural changes would occur during the DFT refinement and thus the relaxation would typically be small and constant. Points that are a significant distances from the linear relationship are likely the result of noticeable structural changes. It can be seen from column three that there are a few outliers. These points

also closely match the outliers in column one, thus, it is expected that these points are due to structural changes. Figure 5.15 shows the structures of the two points circled red in the first column of Figure 5.14 before and after DFT relaxation. The left image

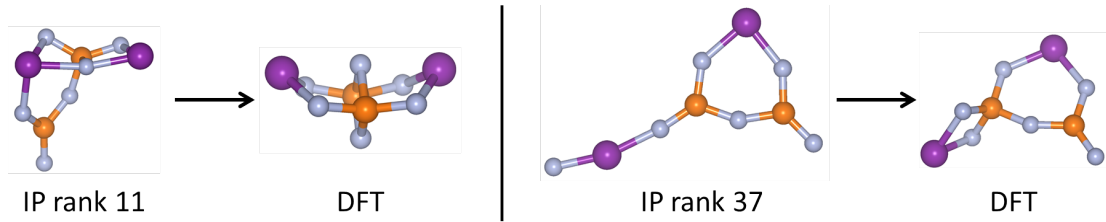


Figure 5.15: The structural changes that occur for the two points circled in red in Figure 5.14. On the left the IP rank 11 cluster when refined through DFT collapses to the IP rank 2 structure. On the right the IP rank 37 when refined through DFT collapses to the IP rank 13 structure.

shows the 11th ranked IP cluster, which is 0.0834 eV/atom higher in energy than the GM, undergoes a significant structural change during the DFT relaxation. The final DFT structure is the same as the 2nd ranked IP cluster. The DFT relative energy of the resulting structure is 0.0038 eV/atom, the IP equivalent of this structure has an energy of 0.0023 eV/atom. The right image shows the 37th ranked IP cluster, which is 0.2541 eV/atom higher in energy than the GM, also undergoes a significant structural change during the DFT relaxation. The final DFT structure is the same as the 13th ranked IP cluster. The DFT energy of the resulting structure is 0.1235 eV/atom, the IP equivalent of this structure has an energy of 0.0852 eV/atom. If the IP energy of the circled points in Figure 5.14 was amended to that of the post-DFT refined structure these points would fit much closer to the visible linear trend. Thus, the large deviations from the trend can be attributed to change in the atomic configuration. Lastly, the energies obtained using the PBEsol and PBE functionals are compared directly in the fourth column of Figure 5.14. The top plot shows a comparison of the single point energies while the bottom compares the relaxed energies. The single point energies show a very strong correlation between the two functionals with no points deviating from the linear relationship. The relaxed energies also show a strong correlation; however, there are a few points that deviate from the general trend. The points above the linear distribution would indicate the PBEsol energy has decreased significantly, suggesting a greater structural change of the PBEsol cluster relative to the PBE. The points below would indicate a greater structural change. Having checked the low or high lying cluster this is found to be true.

Figures 5.16 and 5.17 show similar plots for $n = 3$ and $n = 4$ to those just discussed for $n = 2$. At a first glance the energies of the IP vs DFT relaxed clusters (column one) have a much weaker correlation than was seen for $n = 2$. The IP vs DFT single point calculations (column two) also appears to have a more smeared relationship. The correlation is stronger for the DFT single point vs relaxed energies plots (column three)

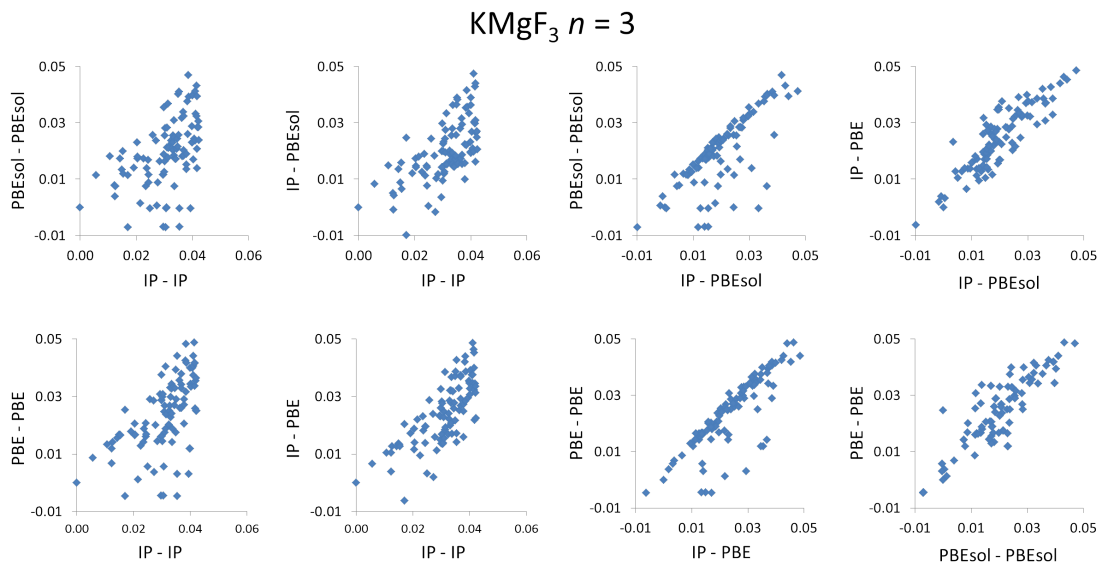


Figure 5.16: Plots comparing the energy of LM clusters calculated using different theoretical models for $(\text{KMgF}_3)_n$, $n = 3$. All energies are relative to the GM and given in eV/atom. Refer to Figure 5.14 for details about axis labels.

than the two previous columns of plots suggesting the problem is less to do with structures obtained by the IP model and more to do with their energies calculated by the IP. However, the correlation is still not as good as those seen for $n = 2$ as there appear to be a much greater spread, although this is partly due to there being more points plotted. The PBEsol vs PBE plots (column four) also show a stronger correlation than columns one and two. Further increasing cluster size resulted in the correlation between IP and DFT energies of the LM clusters becoming worse.

Figure 5.18 compares the energies of the LM clusters between the different methods of calculation for KZnF_3 when $n = 2$. Straight away it can be seen that the KZnF_3 IP energies do not match as closely to DFT as the KMgF_3 IP energies did for $n = 2$. The first column of plots does not show the almost straight line of points indicative of a strong linear relationship of the energies as was seen for KMgF_3 . Looking at column two it can be seen that the correlation between the IP and DFT energies when the structures are exactly the same is much weaker than those seen for KMgF_3 . Thus, the increased mismatch in KZnF_3 cannot be attributed solely to structural changes. Column three, which compares the relaxed and unrelaxed DFT energies, is also seen to be less correlated than its KMgF_3 counterpart. This indicates the KZnF_3 IP and DFT clusters have a greater structural mismatch than for KMgF_3 . The fourth column shows a good agreement between the PBEsol and PBE functionals. Figure 5.19 shows the plots for $n = 3$. It is clear that with the increased cluster size, there is even less agreement between the IP and DFT. The correlation was found to get worse with clusters sized $n = 5 - 9$, which were refined using the PBEsol functional only. The lack of correlation for the

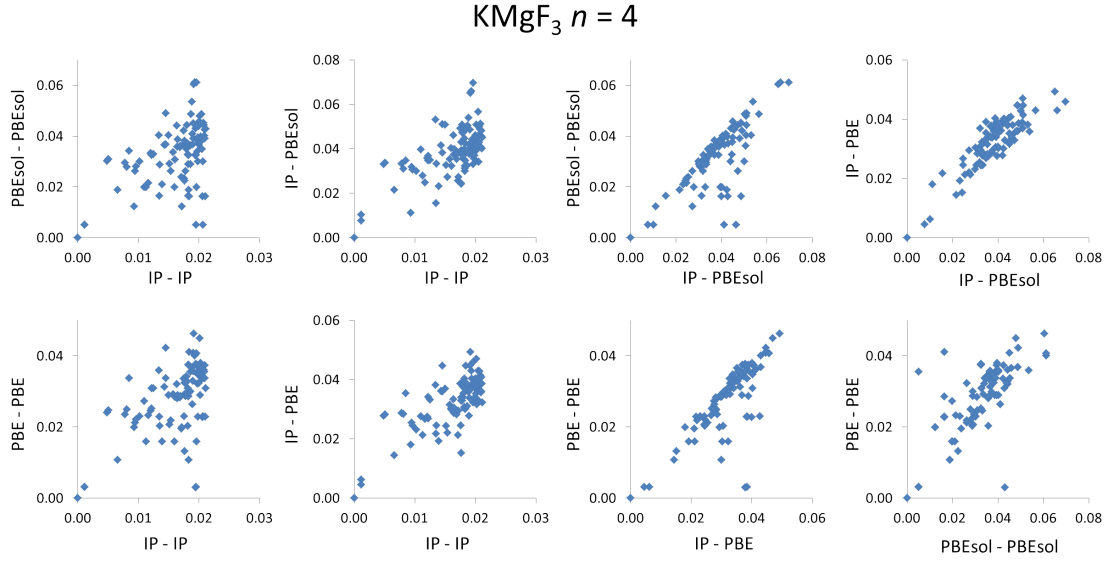


Figure 5.17: Plots comparing the energy of LM clusters calculated using different theoretical models for $(\text{KMgF}_3)_n$, $n = 4$. All energies are relative to the GM and given in eV/atom. Refer to Figure 5.14 for details about axis labels.

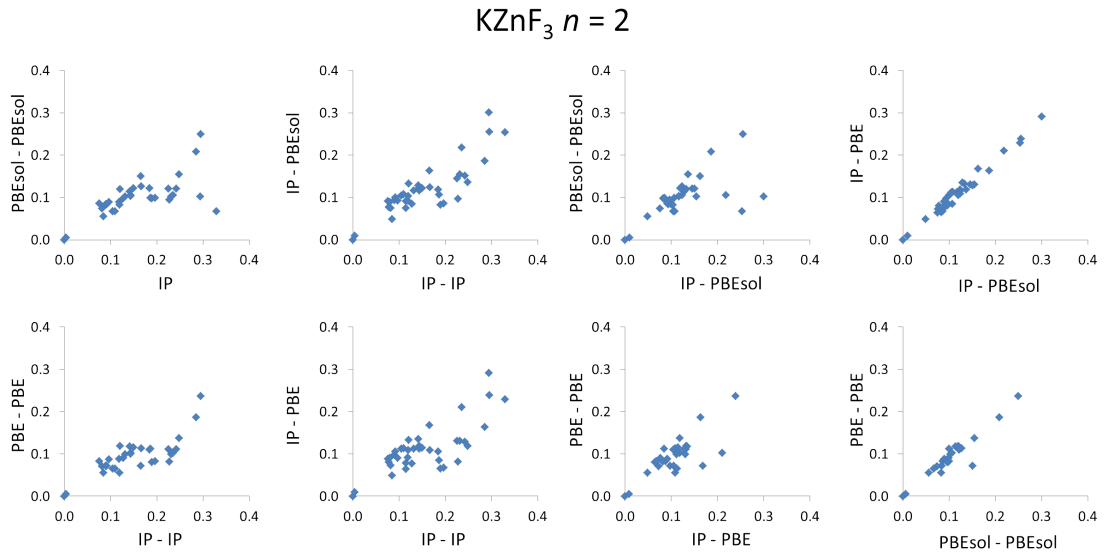


Figure 5.18: Plots comparing the energy of LM clusters calculated using different theoretical models for $(\text{KZnF}_3)_n$, $n = 2$. All energies are relative to the GM and given in eV/atom. Refer to Figure 5.14 for details about axis labels.

larger clusters is attributed to both: the discrepancy in energies between the IP the DFT models; and discrepancies in LM structure between IP and DFT models. A good agreement is again shown between the two DFT functionals for the KZnF_3 structures. The plots for $n = 4$ are not shown here; however, as with $n = 3$ there was poor agreement between the IP and DFT results.

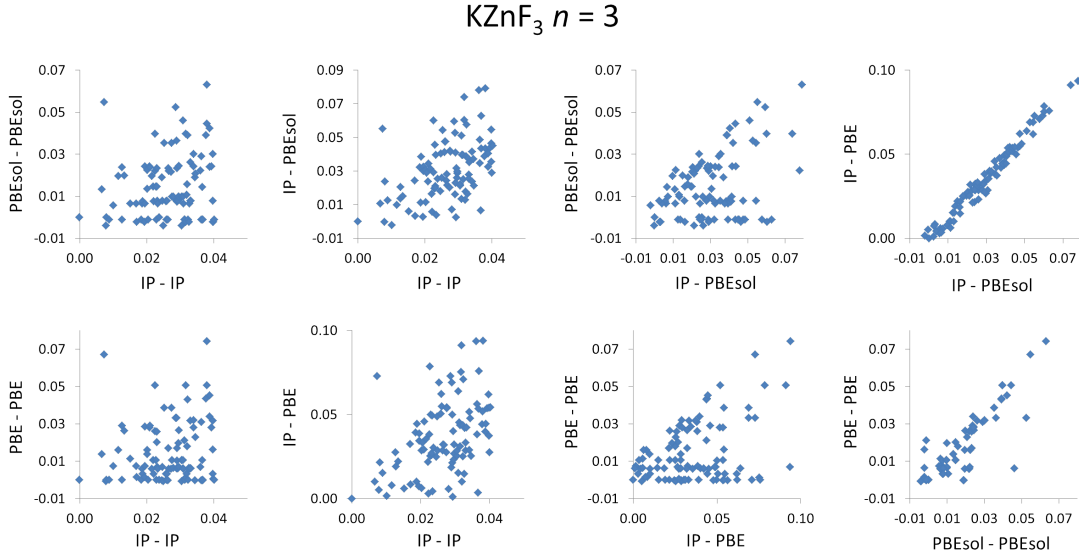


Figure 5.19: Plots comparing the energy of LM clusters calculated using different theoretical models for $(\text{KZnF}_3)_n$, $n = 3$. All energies are relative to the GM and given in eV/atom. Refer to Figure 5.14 for details about axis labels.

One way to help judge the agreement between sets of calculations without a visual aid is to calculate the correlation coefficient. The Pearson product-moment correlation coefficient, r is defined as [197]:

$$r_{x,y} = \frac{\sum_{i=1}^n (x_i - \bar{x})(y_i - \bar{y})}{\sqrt{\sum_{i=1}^n (x_i - \bar{x})^2} \sqrt{\sum_{i=1}^n (y_i - \bar{y})^2}} \quad (5.2)$$

A value of $r = 1$ indicates a strong positive linear relationship, whereas $r = -1$ indicates a strong negative linear relationship, and $r = 0$ indicates no linear correlation. The coefficients for the plots shown in Figures 5.14 – 5.19 as well as KZnF_3 $n = 4$ are shown in Table 5.6. The statistics shown in the table agree with what was determined from the plots. The values of r between the IP and DFT relaxed energies are much higher for KMgF_3 than for KZnF_3 . This indicates that the KMgF_3 IP cluster energies match more closely to DFT values. The value of r decreases with cluster size, with a relatively large decrease from $n = 2$ to 3 compared with $n = 3$ to 4. With the exception of $n = 2$ the coefficients between the DFT relaxed and single point energies is stronger than between the IP and DFT single point energies for KMgF_3 . This suggests that as the clusters get larger the differences in the ranking of the structures is more influenced by the relative energy discrepancies between IP and DFT of like structures than it is by structural mismatch. In relation to the large jumps in correlation from $n = 2$ to 3, a large reason for this may be due to the energy range of the IP cluster selected. For $(\text{KMgF}_3)_n$ $n = 2$ (Figure 5.14), it can be seen that the IP energy range of clusters was approximately 0.4 eV/atom, whereas for $n = 3$ (Figure 5.16) it was 0.04 eV/atom, and

Table 5.6: **Correlation between IP and DFT energies.** The Pearson product-moment correlation coefficient between energies calculated from various computational methods. IP – represents interatomic potentials; PS – DFT calculation in FHI-AIMS using PBEsol functional; and P – DFT calculation in FHI-AIMS using PBE functional. The superscript denotes which computational method was used to obtain the LM structure. For example, PS^{IP} describes the PBEsol energy of the LM found by relaxing with IP.

	KMgF ₃			KZnF ₃		
	$n = 2$	$n = 3$	$n = 4$	$n = 2$	$n = 3$	$n = 4$
IP ^{IP} v PS ^{PS}	0.840	0.500	0.474	0.669	0.179	0.155
IP ^{IP} v PS ^{IP}	0.987	0.635	0.647	0.851	0.484	0.188
PS ^{IP} v PS ^{PS}	0.844	0.745	0.758	0.611	0.388	0.618
IP ^{IP} v P ^P	0.611	0.574	0.545	0.575	0.164	0.038
IP ^{IP} v P ^{IP}	0.986	0.746	0.728	0.771	0.435	0.038
P ^{IP} v P ^P	0.567	0.822	0.767	0.530	0.390	0.395
PS ^{IP} v P ^{IP}	0.997	0.879	0.869	0.988	0.987	0.972
PS ^{PS} v P ^P	0.708	0.880	0.720	0.948	0.874	0.650

for $n = 4$ (0.0) it was 0.02 eV/atom. When the DFT structures are kept identical to the IP structures (column 2 in the Figures), the variation of the DFT cluster energies about a given IP energy is ~ 0.02 eV/atom. This means the deviations in DFT energy are of the same order as the total IP energy range, which makes it harder to see the correlation. To check if this was a major contributing factor a random sample of 100 IP clusters were generated using the SQ technique for $n = 4$ and 5. It was expected that this would create a much larger spectrum of clusters energies that was obtained by only looking at the 100 most stable from a full global optimisation run. These clusters were relaxed using the PBEsol functional only. The plots for these samples are shown in Figure 5.20. The IP vs DFT relaxed for $n = 4$ of this broader spectrum of cluster energies shows a stronger and more obvious correlation than was seen in Figure 5.17. For $n = 5$, the correlation is also very obvious. The IP vs DFT single point energies (column 2) in particular show a very strong relationship. This suggests that structural rearrangement is the dominant cause for differences in the IP and DFT energies. The correlation coefficient between the IP and DFT relaxed energies was 0.746 and 0.660 for $n = 4$ and 5, respectively. Both of these values are greater than what was recorded for $n = 3$ (0.500). The coefficient between the IP vs DFT single point energies was particularly high at 0.974 and 0.975 for $n = 4$ and 5, respectively, which is as good as the $n = 2$ coefficient of 0.987. This agrees with what was deduced from the plots: the significant deviations from the linear relationship between IP and DFT energies are a result of structural change. Looking at the structure of the outliers confirms this. Also of note is that in all of the cases inspected, the rearranged DFT cluster has the same, or similar, structure to an IP cluster of lower energy. This indicates that the DFT refinement is not rearranging the atoms into structures that are unique to the

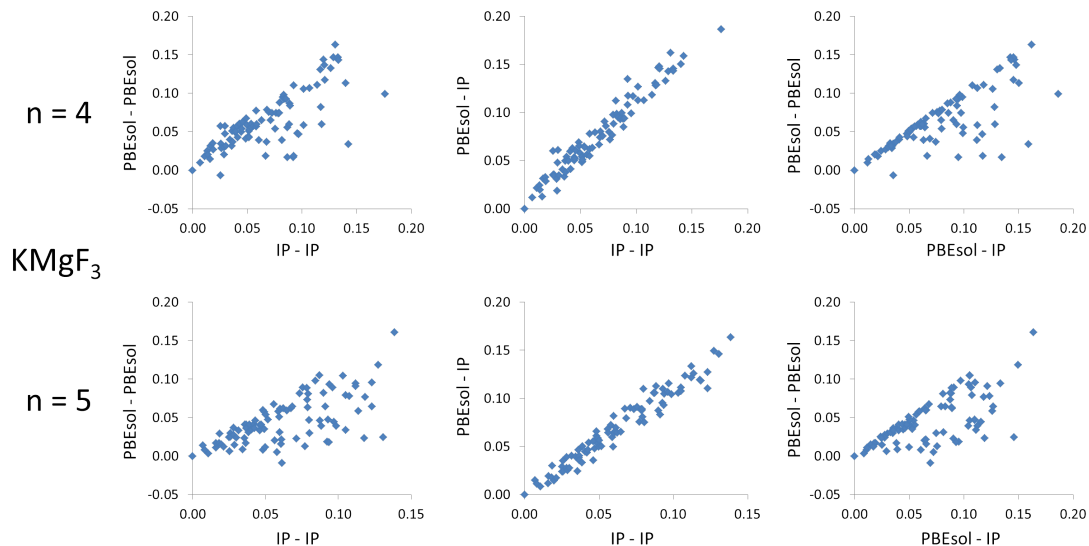


Figure 5.20: Plots comparing the energy of LM clusters calculated using different theoretical models for a 100 random cluster sample created using the SQ technique for $(\text{KMgF}_3)_n$, $n = 4$ and 5 . All energies are relative to the GM and given in eV/atom. Refer to Figure 5.14 for details about axis labels.

DFT landscape. To see if there are structures unique to the DFT energy landscape, i.e. structures with metal-metal bonding, would require a DFT global optimisation. It was also found that many of the IP structures that underwent significant atomic relaxation during the DFT refinement were very open, diffuse structures. The DFT relaxation collapsed these structures to form denser clusters, suggesting that many of the potential barriers on the IP energy landscape do not exist on the DFT landscape.

In summary, it has been shown that the KMgF_3 IP are better at generating and ranking suitable atomic structures to be modelled on the DFT landscape than the KZnF_3 IP. This may be a consequence of the KZnF_3 IP using a formal charge model whereas the KMgF_3 IP employ a partial charge model. As the cluster size grows, the ordering of the clusters change more significantly between IP and DFT. This is a result of the higher density of possible cluster structures that exist within a given energy range rather than a deterioration in the agreement between IP and DFT. To be confident that all the top structures are accounted for (if that is the goal) a suitable energy range of clusters to be refined must be chosen. Lastly, the majority of clusters that underwent significant structural change during the DFT refinement resolved into structures that had already been found on the IP energy landscape at a lower energy.

5.5 DFT Data Mining

Another approach to identify the DFT local minima of a material, is to “data mine”. Data mining, in this context, is the process of using the DFT structures of one compound

as candidate structures for another compound. This method is particularly useful when there are no good IP for the material of interest but a list of structures are available for another similar material. The procedure of data mining has been applied to the $(\text{KMgF}_3)_n$ and $(\text{KZnF}_3)_n$ clusters. The DFT LM clusters for KMgF_3 and KZnF_3 , that were obtained by refining IP clusters using the PBEsol functional, were cross-data-mined between the two compounds. This means that the KMgF_3 DFT LM structures were used as candidate configurations for KZnF_3 by replacing Mg with Zn. The new KZnF_3 candidate was then relaxed at the DFT level using the PBEsol functional. The same process was applied to generate new KMgF_3 structures.

For $n = 1$, the results were unsurprising as the same three structures existed for both compounds. Plots similar to those presented in the previous section were created to show the relationship between the energies of the KMgF_3 and KZnF_3 structures obtained from data mining. Figure 5.21 shows the results for $n = 2$. The first column

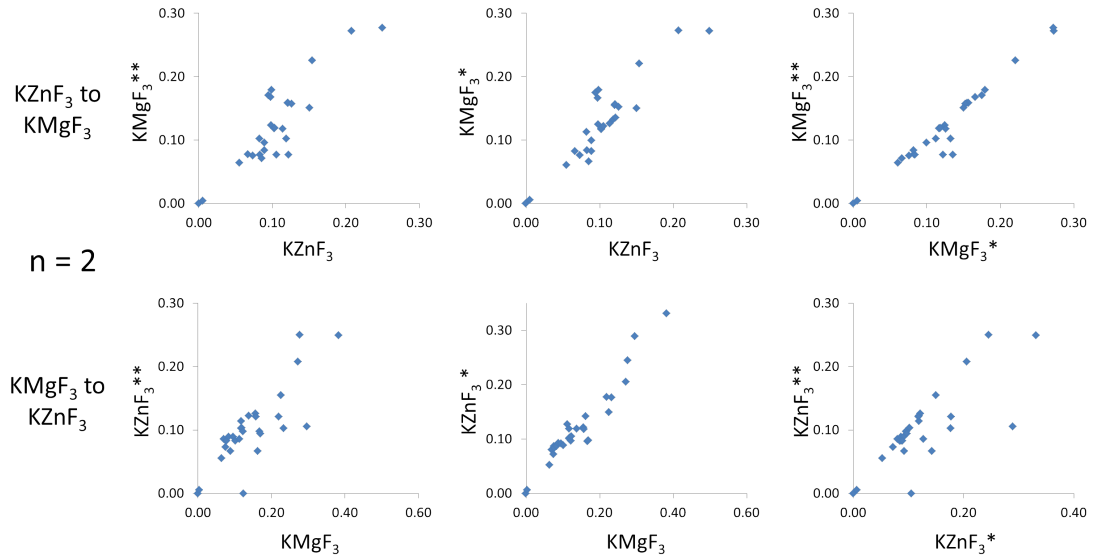


Figure 5.21: Plots showing the relative energy of $(\text{KMgF}_3)_n$ and $(\text{KZnF}_3)_n$ clusters when cross data mined for $n = 2$. * indicates the structure was created by performing a Mg-Zn swap on a previously found cluster, but the structure was not relaxed before calculating the energy. ** indicates the structure was created by performing a Mg-Zn swap on a previously found cluster, and the energy was calculated after performing a relaxation.

shows the relative relaxed cluster energies of the material of interest against the energies of the material the structures were data mined from. The second column shows the single point energies instead of relaxed energies for the material of interest. The third column makes a comparison of the relaxed and single point energies of the material of interest. From column one it can be seen that there is a good agreement between the relaxed cluster energies of KZnF_3 and KMgF_3 . Column two also shows a strong correlation indicating that the relative energies of clusters with identical structures are

consistent across both compounds. Column three shows a strong correlation between the single point and relaxed energies indicating that the two compounds are structurally very similar. The agreement is found to be stronger when data mining from KZnF_3 to KMgF_3 . This suggests that KMgF_3 more easily adopts the KZnF_3 structures while the KZnF_3 compound is more “fussy” opting to change structure more readily to a lower energy cluster. Figure 5.22 shows similar plots for $n = 4$. It can immediately be seen

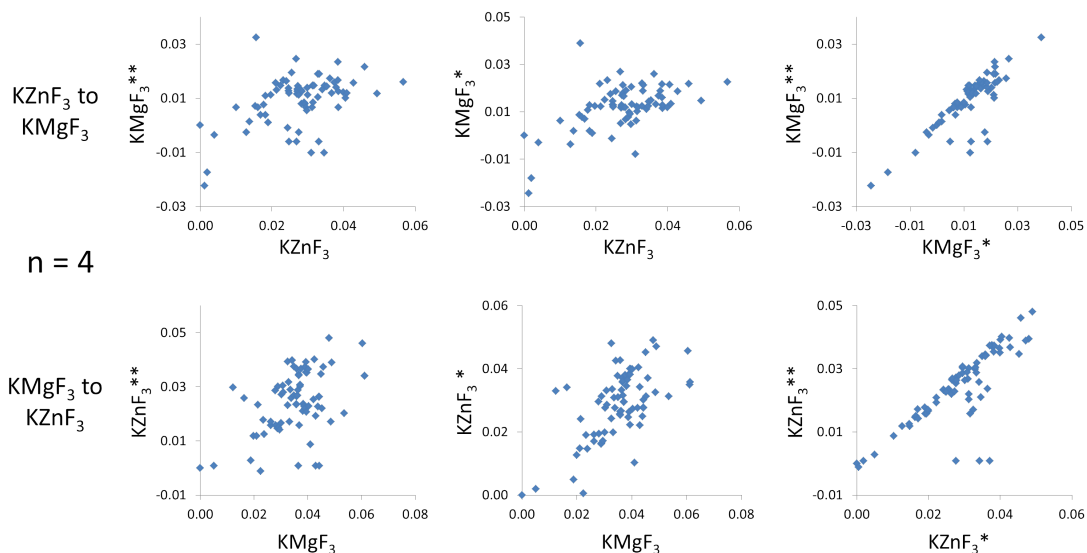


Figure 5.22: Plots showing the relative energy of $(\text{KMgF}_3)_n$ and $(\text{KZnF}_3)_n$ clusters when cross data mined for $n = 4$. * indicates the structure was created by performing a Mg-Zn swap on a previously found cluster, but the structure was not relaxed before calculating the energy. ** indicates the structure was created by performing a Mg-Zn swap on a previously found cluster, and the energy was calculated after performing a relaxation.

that the agreement in energies is not as strong at this size. A strong correlation is observed in column three, however, indicating that structurally the clusters are very similar. Increasing the cluster size even further to $n = 8$ revealed an unexpected result. Figure 5.23 shows the plots for $n = 8$. Surprisingly, the correlation is much stronger for $n = 8$ than it was for $n = 4$ despite the energy range being smaller. The relaxed vs single point energies (column 3) show a particularly strong correlation indicating the two compounds form very similar structures. Table 5.7 shows the correlation coefficients between these data mined structures for $n = 2 - 9$. The table agrees with the plots showing a high correlation coefficient in all three categories for $n = 2$. For $n = 3 - 7$, the coefficient is found to be much lower, but at $n = 8$ and 9 becomes much higher again. The relaxed vs single point coefficients (column 3) are consistently high for each calculation. This suggests that the two compounds form clusters that are structurally very similar. Thus, the discrepancy between the relaxed energies of the two different compounds arises due to the structures having slightly different levels of stability for

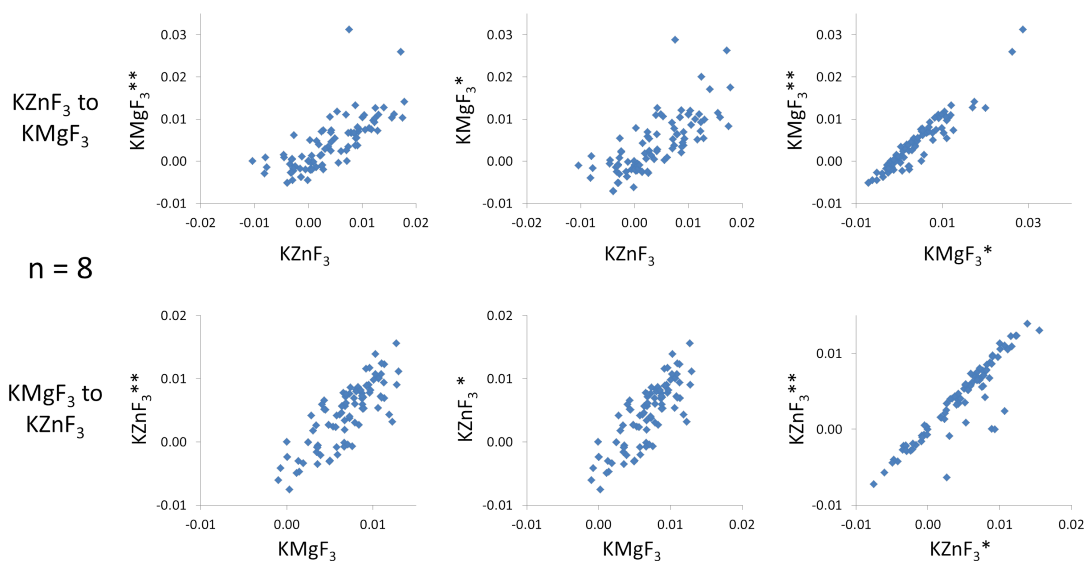


Figure 5.23: Plots showing the relative energy of $(\text{KMgF}_3)_n$ and $(\text{KZnF}_3)_n$ clusters when cross data mined for $n = 8$. * indicates the structure was created by performing a Mg-Zn swap on a previously found cluster, but the structure was not relaxed before calculating the energy. ** indicates the structure was created by performing a Mg-Zn swap on a previously found cluster, and the energy was calculated after performing a relaxation.

each material. That the largest clusters boast higher correlation coefficients between the different compounds compared to the mid sized clusters agrees with what was seen in the plots. This unexpected result suggests that it is in clusters with 15 – 35 atoms where the differences between the Zn and Mg ions affect the cluster the most; it is likely that this is a result of the cation coordination at these sizes. Lastly, the list of correlation coefficients suggests that the DFT data mining is more effective than the IP to DFT method. This is particularly true for KZnF_3 where both the IP energies and structures were found to transfer poorly to DFT. The drawback to the data mining method is that the structures must exist already for a similar compound having been found by refining IP cluster through DFT or performing a computationally expensive DFT global optimisation. As the pool of data gets larger, however, this method will become increasingly more valuable and reliable.

5.6 Structures of the Clusters Optimised by DFT

This section looks at the structure and properties of the lowest DFT energy LM clusters found. The DFT clusters were obtained by a DFT refinement of the top 100 IP structures (when 100 were available) found using global optimisation, and from data mining these DFT structures from the other compound. Figure 5.24 plots the energy of the top ten most stable structures relative to the bulk in eV/atom as a function of cluster size.

Table 5.7: **Data mining correlation.** The Pearson product-moment correlation coefficient between relative energies of data mined structures. The three columns correspond to the respective columns of plots in Figures 5.21 – 5.23.

	Relaxed		Single Point		Relaxed vs SP	
	KMgF ₃	KZnF ₃	KMgF ₃	KZnF ₃	KMgF ₃	KZnF ₃
$n = 2$	0.888	0.815	0.922	0.959	0.974	0.792
$n = 3$	0.655	0.579	0.563	0.777	0.829	0.654
$n = 4$	0.457	0.475	0.550	0.624	0.825	0.813
$n = 5$	0.675	0.701	0.606	0.726	0.807	0.877
$n = 6$	0.626	0.484	0.492	0.646	0.886	0.816
$n = 7$	0.725	0.645	0.576	0.645	0.877	0.949
$n = 8$	0.813	0.687	0.792	0.727	0.950	0.929
$n = 9$	0.750	0.730	0.744	0.812	0.950	0.919

Overall, the range of the relative energies is very similar to what was obtained using the

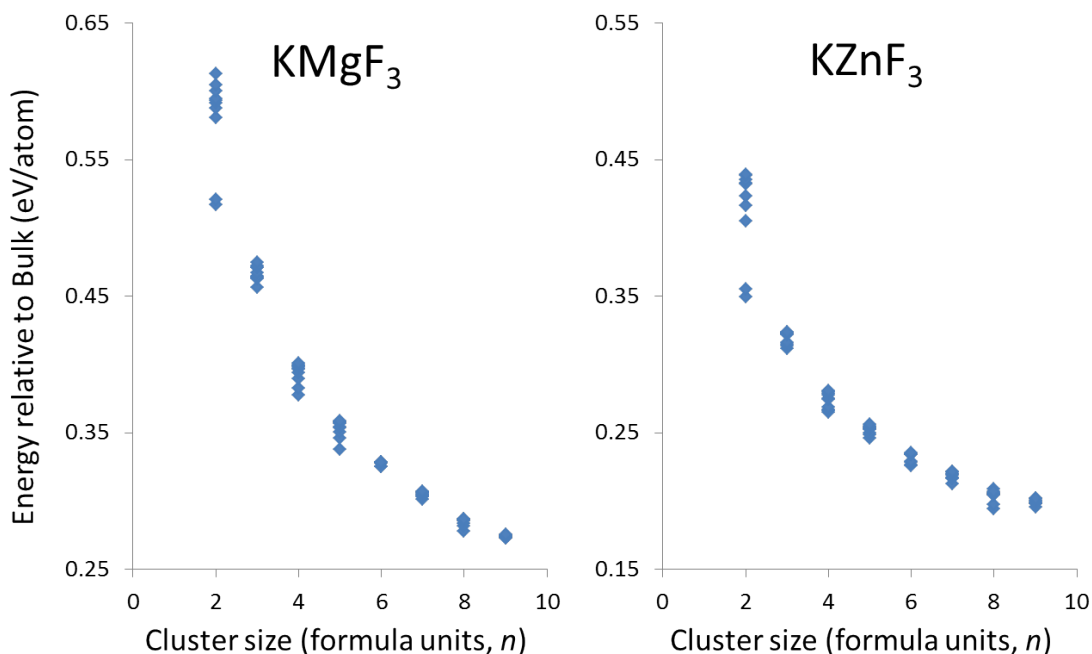


Figure 5.24: DFT energies relative to the bulk for top ten LM structures for each cluster size.

IP: i.e. between the top ten for each size, and between the different sizes. In contrast to what was seen for the IP energies, the KZnF₃ DFT cluster energies are closer to the bulk value than those for the KMgF₃ clusters. The $n = 8$ GM structure for KZnF₃ is lower in energy than the $n = 9$ GM. This is the only time the GM for a particular size is seen to be more stable than a GM of a larger size, which suggests that the $n = 8$ GM is a particularly stable configuration. As was seen with the IP clusters, the energy range of the top ten DFT structures gets smaller with increasing cluster size; an exception at

$n = 8$ is observed and this is due to the exceptional stability of the GM.

$n = 1$

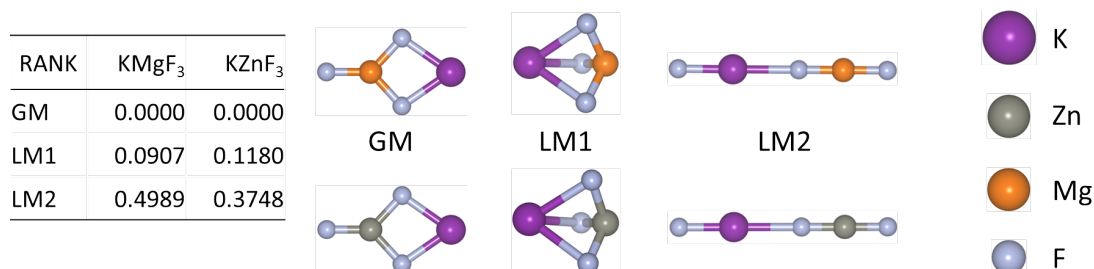


Figure 5.25: The three stable $(\text{KMgF}_3)_n$ and $(\text{KZnF}_3)_n$ DFT clusters for $n = 1$. The table shows the energy for each cluster relative to the GM in eV/atom.

The atomic structures of the DFT LM clusters for $n = 1$ are shown in Figure 5.25, and possess the same configurations predicted earlier by the IP clusters. The DFT energetic ordering of these structures is also the same as it was for the IP. The GM is the planar structure with the X (Mg or Zn) cation triply bonded and the K cation doubly bonded. The X – F bond distance to the isolated F is 1.794 Å and 1.766 Å for X = Mg and Zn respectively, a difference of 1.5%. This is a larger difference than what was seen between the IP bond lengths (0.5%). For the IP, the Zn – F bond was longer than the Mg – F bond; however, this order has changed upon DFT refinement. Both sets of bonds are found to be larger than their IP counterparts. The other X – F bond length was 1.872 Å for Mg and 1.875 Å for Zn (a difference of less than 0.2%). Again the DFT bonds are longer than their IP equivalents. The K – F bond length was measured to be 2.418 Å for KMgF_3 and 2.412 Å for KZnF_3 ; a difference of less than 0.3%. These bond lengths are smaller than what was seen for the IP structures. The K – X separation differ by less than 0.2% and are found to be 3.263 Å and 3.258 Å for X = Mg and Zn, respectively. The DFT K – X separation is only 1.2% smaller than what was predicted by the KMgF_3 partial charge IP model, but 5.0% smaller than what was predicted by the KZnF_3 formal charge model. The F – F separation between the symmetrically equivalent F atoms are 2.747 Å (KMgF_3) and 2.749 Å (KZnF_3). This is almost 5% larger than what was predicted by the IP models.

For the $n = 1$ GM cluster, it had been shown that the differences in atomic separation between the two compounds are much smaller for the DFT structures, often by a factor of 10, than the differences between the IP structures. The cation – cation and anion – anion separations of the DFT structures are more closely modelled by the KMgF_3 partial charge model, although the KMgF_3 IP still over estimate the cation separation by over 4%.

From a Mulliken analysis of the cluster, the charge on the K ion is $0.88e$ (KMgF_3) and $0.84e$ (KZnF_3), and the charge of X is $1.17e$ (Mg) and $0.89e$ (Zn). The isolated

F ion has Mulliken charges $-0.67e$ (KMgF_3) and $-0.52e$ (KZnF_3), and the other F ions $-0.69e$ (KMgF_3) and $-0.60e$ (KZnF_3). This suggests that KMgF_3 represents a more ionic system than KZnF_3 whereas the opposite was used in the IP models. Additionally, the charges of the F ions indicate that the less coordinated anions have less charge; this difference is more pronounced for KZnF_3 and reflects the change in F – X bond lengths between IP and DFT models. The charges shown here are much smaller than those used in either IP model and might explain why the cation – cation separation is overestimated by the IP. Analysis of the charges also suggest that the under-coordination that exists in clusters may make a partial charge model favourable to a formal charge model.

The second most stable structure, local minimum 1 (LM1), has both the K and the X (Mg or Zn) cation triply bonded. The X – F bonds are found to be 1.837 \AA (Mg) and 1.839 \AA (Zn), within 0.2% of each other. The K – F bonds are found to be 2.646 \AA (KMgF_3) and 2.697 \AA (KZnF_3), showing a much larger difference between the two compounds of 2.6%. The ordering of the K – F bond length has reversed compared to the GM, as it is now larger in KZnF_3 . Despite the longer K – F bond in KZnF_3 the cation – cation separation is smaller at 2.754 \AA compared to 2.800 \AA for KMgF_3 , a 2.2% difference. This is due to an increased K – F – X angle of 74.8° (X = Zn); up from 71.9° (X = Mg) (4.0% difference). This also causes an increase in anion – anion separation by 1.2%.

The Mulliken charges on LM1 are K = $0.92e$ (KMgF_3) and $0.85e$ (KZnF_3), X = $1.07e$ (Mg) and $0.87e$ (Zn), and F = $-0.66e$ (KMgF_3) and $-0.57e$ (KZnF_3). As with the GM structure, LM1 is found to be more ionic for KMgF_3 than for KZnF_3 ; this is the suspected cause of the larger cation – cation separation in KMgF_3 . As with the GM cluster, the LM1 cation – cation separation calculated by DFT is smaller than that calculated by the IP model. The charge on the K ion increases for both materials following the increase in the K ion coordination. Conversely, the charge on the X ions have reduced. While their coordination number has not changed the arrangement of the bonded F ions have. The F ions no longer symmetrically surround the cation but all sit on one side of the ion.

The third structure, LM2, is a linear stick cluster which is much less stable than the other clusters. The most notable difference between the two materials for this structure is that both Mg – F bond lengths are $\sim 3.0\%$ larger than the Zn – F bond lengths. This is likely a feature of the different ionic radii of the two divalent cations. The K – F bonds do not show as great a variation in length between the two compounds. The K – F bond involving the F ion at the end of the structure is about 2.2 \AA . The K – F bond involving the other F ion is about 2.7 \AA ; the increased distance is likely a result of cation – cation repulsion.

The charges on the ions are K = $0.76e$ (both), X = $1.32e$ (Mg) and 0.887 (Zn), and F = $-0.78e$, $-0.68e$, $-0.62e$ (KMgF_3) and $-0.76e$, $-0.46e$, $-0.42e$ (KZnF_3). The most highly charged F ion is the one located on the edge bonded to K. The F ion with smallest

charge is found on the other edge bonded to the X ion. The charge on the K ion and its closest bonded F are very similar; this suggests that the charge transferred from the K ion lies purely on this F. The bond distance between these two is much smaller than the other K – F bond, suggesting there is a strong ionic bond between these two ions. The other ions appear to form a F–Mg–F dumbbell structure, with one end loosely attached to the K ion. The dumbbell segment is more ionic for KMgF_3 than KZnF_3 .

In summary, the $n = 1$ clusters show the DFT structures between the two compounds to be much more alike than those found for the IP structures. KMgF_3 is found to be more ionic than KZnF_3 in contrast to what was found when the IP model was employed. The Mulliken charges of the DFT structures suggest that even the partial charge IP model overestimates the charges on the structures. The consequence of this is that the cation – cation separation is much smaller in the DFT structures.

$n = 2$

RANK	KMgF_3	KZnF_3
GM	0.0000	0.0000
LM1	0.0038	0.0055
LM2	0.0638	0.0555
LM3	0.0709	0.0669
LM4	0.0750	0.0735
LM5	0.0766	0.0829
LM6	0.0776	0.0833
LM7	0.0835	0.0856
LM8	¹ 0.0882	0.0891
LM9	0.0960	0.0896

Figure 5.26: The five lowest energy $(\text{KMgF}_3)_n$ and $(\text{KZnF}_3)_n$ LM DFT clusters for $n = 2$. The table shows the energy for the top ten clusters relative to the GM in eV/atom. In the table a superscript “1” indicates the structure was only found by IP to DFT refinement. A lack of superscript means the structure was found from both methods.

The top five DFT structures for $n = 2$ are shown in Figure 5.26. The top three (lowest energy) clusters are the same in structure and rank for both compounds. The top two structures are in agreement with those predicted by the IP model. The third ranked structure, LM2, is the cube-like cluster that was actually ranked 5th for KMgF_3 and 7th for KZnF_3 when using IP. The chain like structure that was ranked third with the IP is now ranked 4th for KMgF_3 and 7th for KZnF_3 (not shown). Thus, the denser structure of LM2 is lower in energy, when refined by DFT, than the more diffuse structure $((\text{KMgF}_3)_2 \text{ LM3})$. The difference in energy between the GM and LM9 is ~ 0.1 eV/atom for both compounds, which is similar to the difference calculated by the IP models. As was found for the IP clusters, the top two DFT structures are significantly lower in energy than the other LM.

The GM has the same ring-like structure as was seen for the IP. The charges on the cations are $K = 0.91e$ (KMgF_3) and $0.84e$ (KZnF_3), $X = 1.07e$ (Mg) and $0.92e$ (Zn). For the F ion, there were two unique positions. The F ions between the two X cations have charges $-0.68e$ (KMgF_3) and $-0.59e$ (KZnF_3), the other F $-0.62e$ (KMgF_3) and $-0.58e$ (KZnF_3). As with the $n = 1$ clusters, KMgF_3 is more ionic. There are two types of X – F bonds. The X – F bond between the two X ions has length 1.963 \AA ($X = \text{Mg}$) and 2.022 \AA ($X = \text{Zn}$). These have a large difference of 3.5%. The other X – F bond reverses the size order between the two materials; 1.853 \AA (Mg) and 1.834 \AA (Zn). The DFT X – F bonds, are in general, larger than their IP equivalents. The K – F bonds have very similar lengths at 2.485 \AA (KMgF_3) and 2.494 \AA (KZnF_3). Surprisingly, the X – X separation is almost 3% greater for Zn than Mg despite Mg having the larger charge. Unsurprisingly these distances are smaller than their IP equivalents. The Mg – K distance is larger than the Zn – K by 1.1%, and both DFT distances are smaller than the IP distance.

The second cluster, LM1, is the same structure predicted by the IP model, and closely resembles the GM. The bond lengths of LM1 are similar to those seen for the GM structure. The only significant change is that the degeneracy of the X – F bond distances to the central F ions between the two X ions has been lifted. This is due to a change in symmetry of LM1 with respect to the GM. The Mg – F bond lengths changed by $\pm 0.03 \text{ \AA}$ while the Zn – F bond distances changed by $\pm 0.06 \text{ \AA}$. The charge on most of the cations remain unchanged from the GM structure; only the charge on the central F ions have changed. The central F ion with the reduced bond length to the X cations, decreased in charge by $\sim 0.02e$ for KMgF_3 and $\sim 0.06e$ for KZnF_3 . The other central F ion increased in charge by $\sim 0.02e$ for KMgF_3 and $\sim 0.06e$ for KZnF_3 . The bond distance appears to have a correlation with the charge in this case.

The third ranked cluster, LM3, has a cube-like structure that differs significantly from the GM and LM1. The charge has increased by $0.05e$ on the Mg and $0.02e$ on the Zn. This is likely a result of the F anions more fully occupying the space around these cations. The F ions that are bonded to two X ions have the largest charge of the anions. The isolated F ions have the smallest charge. This conforms to the running theme of the more coordinated and tightly bound ions exhibiting a higher charge. The Zn – Zn separation is again larger than the Mg – Mg separation, this time by 1.3%. The X – F separation is within 0.3% between the two compounds.

For the remaining clusters, including those not shown, some general themes were discovered. The Zn – F bond distance was marginally larger than the one of the equivalent Mg – F bonds except in the case when the F ion was isolated or singly bonded. The Zn – Zn separation was marginally larger than the Mg – Mg distance, this is likely a result of the larger Zn – F bond length rather than any cation – cation interaction. In all cases, the KMgF_3 clusters were found to be more ionic than KZnF_3 .

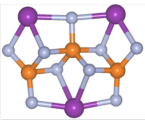
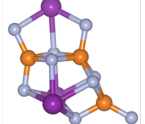
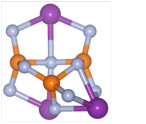
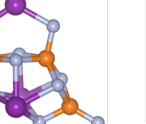
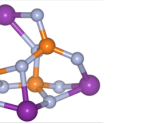

RANK	KMgF ₃	KZnF ₃						
GM	0.0000	0.0000						
LM1	0.0067	0.0019						
LM2	0.0070	0.0029						
LM3	¹ 0.0075	0.0040						
LM4	¹ 0.0084	0.0097						
LM5	0.0109	0.0106						
LM6	0.0145	0.0107						
LM7	¹ 0.0149	0.0114						
LM8	0.0158	0.0117						
LM9	0.0184	0.0119						

Figure 5.27: The five lowest energy (KMgF₃)_n and (KZnF₃)_n DFT clusters for $n = 3$. The table shows the energy for the top ten clusters relative to the GM in eV/atom. In the table a superscript “1” indicates the structure was only found by IP to DFT refinement, a “2” means the structure was only found through cross data mining. A lack of superscript means the structure was found from both methods.

$n = 3$

The top five DFT clusters for $n = 3$ are shown in Figure 5.27. Three out of the top five structures are seen in both compounds. These three clusters have the same relative energy ranking for both compounds. However, the top five DFT structures differ greatly in ranking from the top IP structures.

The GM DFT cluster is almost flat in shape with two four-coordinated X ions and one five-coordinated X ion. This cluster has improved significantly in ranking upon DFT refinement; it was ranked 4th for KZnF₃, and 11th for KMgF₃ on the IP energy landscape. There is greater variation for the Zn – F bond lengths (1.824 Å to 2.025 Å) than there is for the Mg – F bond (1.848 Å to 1.985 Å). For $n = 3$, the KMgF₃ IP, while less accurate in ranking the cluster energy, reproduce the DFT structure more accurately than the KZnF₃ potentials. The X – X separation was found to be larger for Zn (3.020 Å) than Mg (2.949 Å) by 2.4%. As with the smaller clusters, the KMgF₃ structure is more ionic than KZnF₃. Interestingly, the five-coordinated Mg ion has a lower charge (0.99e) than the less coordinated Mg ions (1.08e), where as the five-coordinated Zn ion has a higher charge (0.94e) than the other two Zn ions (0.93e).

The second ranked cluster, LM1, has a structure which combines the GM for $n = 1$ with LM1 for $n = 2$. This structure was not seen in the top ten for either compound with IP. The DFT LM1 was ranked 14th for the KZnF₃ IP and 24th for KMgF₃ IP with the structure altered slightly breaking symmetry. The large difference in stability is likely a result of the isolated F ion. As with the DFT GM the Zn – F bonds have a greater variation in length compared to the Mg – F bonds. The Zn – Zn separation is again larger than the Mg – Mg separation. KMgF₃ is again seen to be more ionic. The Mg with the highest charge (1.10e) is connected to the isolated F ion, while the Zn with the highest charge (0.98e) is the most coordinated (five) ion closest to the centre of the

RANK	KMgF ₃	KZnF ₃
GM	0.0000	0.0000
LM1	0.0051	0.0011
LM2	0.0123	0.0019
LM3	0.0164	0.0040
LM4	0.0188	² 0.0098
LM5	0.0199	¹ 0.0100
LM6	¹ 0.0210	0.0129
LM7	0.0214	0.0137
LM8	0.0224	0.0153
LM9	0.0234	0.0156

Figure 5.28: The five lowest energy $(\text{KMgF}_3)_n$ and $(\text{KZnF}_3)_n$ DFT clusters for $n = 4$. The table shows the energy for the top ten clusters relative to the GM in eV/atom. In the table a superscript “1” indicates the structure was only found by IP to DFT refinement, a “2” means the structure was only found through cross data mining. A lack of superscript means the structure was found from both methods.

cluster.

LM2 for KMgF_3 has the same structure as LM3 for KZnF_3 . As with the previous two structures KZnF_3 is found to be less ionic, to possess a greater variation in its Zn – F bond length, and to have a larger X – X cation separation than KMgF_3 . The remaining clusters for $n = 3$ also followed the trend of KMgF_3 being more ionic than KZnF_3 .

$n = 4$

The top five clusters for $n = 4$ are shown in Figure 5.28. Three out of the top five structures are present for both compounds and, when exclusively considered, agree in energy ranking. Thus, the DFT show a better agreement across compounds than the IP did, where only three out of ten structures were paired and the energy order different.

The DFT GM for KZnF_3 is a moderately flat structure and was ranked 57th with the KZnF_3 IP. The cluster consists of a central six-coordinated Zn ion and three four-coordinated Zn ions around the edge of the cluster. Three of the K ions adopt positions around the edge of the cluster and are four-coordinated, the other K ion is located behind the central Zn (into the page) and is coordinated to three F ions. The central Zn ion has a relatively high charge of $1.00e$, the other Zn ions have a charge of $0.93e$.

The KMgF_3 GM and KZnF_3 LM1 have the same structure resembling a cage with wings. This cluster was also highly stable with the IP. The structure is high degree of symmetry, with four identical X ions all five-coordinated. Mulliken analysis of the charges again prove KMgF_3 to be more ionic, however, the average charge of $0.97e$ on the Zn ions is larger than seen in previous clusters. The evidence of the clusters charges so far indicate that the larger the coordination number on the Zn ion the higher the charge.

RANK	KMgF ₃	KZnF ₃
GM	0.0000	0.0000
LM1	0.0087	0.0023
LM2	0.0126	¹ 0.0037
LM3	0.0162	¹ 0.0059
LM4	¹ 0.0169	0.0065
LM5	0.0193	0.0069
LM6	² 0.0197	0.0070
LM7	0.0204	¹ 0.0078
LM8	0.0205	¹ 0.0085
LM9	0.0209	0.0100

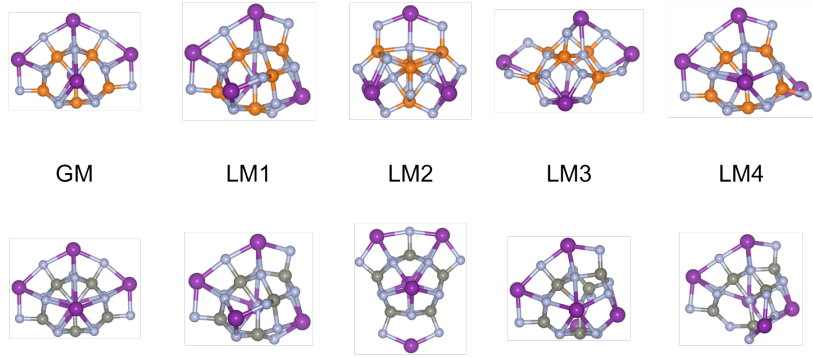


Figure 5.29: The five lowest energy DFT clusters for $n = 5$. The table shows the energy for the top ten clusters relative to the GM in eV/atom. In the table a superscript “1” indicates the structure was only found by IP to DFT refinement, a “2” means the structure was only found through cross data mining. A lack of superscript means the structure was found from both methods.

$n = 5$

The top five clusters for $n = 5$ are shown in Figure 5.29. The GM and LM1 are found to be the same for both compounds. The DFT GM, as has been seen at all smaller sizes, is a highly ordered structure. Two of the X ions are six-coordinated and one is five-coordinated. The other two are five/six-coordinated depending on the choice of cut-off, and the F ion at the centre of the cluster lies 2.8 Å away from these X ions. KMgF₃ is still found to be more ionic than KZnF₃. The Mg with the smallest charge are the six-coordinated ions (0.91e) and the largest charge is seen on the five/six-coordinated ions (1.06e). For Zn, the five/six-coordinated ions have the largest charge (0.99e) and the smallest is seen on the five-coordinated ion (0.91e).

The remaining $n = 5$ clusters all continue to show KMgF₃ to be the more ionic compound. The average charge on Zn ion is larger at this size than for smaller clusters.

$n = 6 - 9$

The top three clusters for $n = 6 - 9$ are shown in Figure 5.30. The clusters show the same trend seen for the IP. The divalent ions take up positions close to the centre of the cluster, thus maximising their coordination. Typically, similar structures are found within the top three LM clusters at each size for both compounds. The average charge on the Zn ions increases as cluster size grows. There is no obvious relationship between the charge of the Mg ion and cluster size. Similarly, no trend is seen for the charge of the K ion in either compound. The absence of any charge/cluster size relationship for the K ion may be due to a lack of any coordination/cluster size relationship, as K ions are found to be residing at the surface of the structure for all cluster sizes.

The $n = 8$ GM and LM1 for KZnF₃ are particularly noteworthy. These two structures are significantly lower in energy than the other clusters in the top ten. The gap in energy

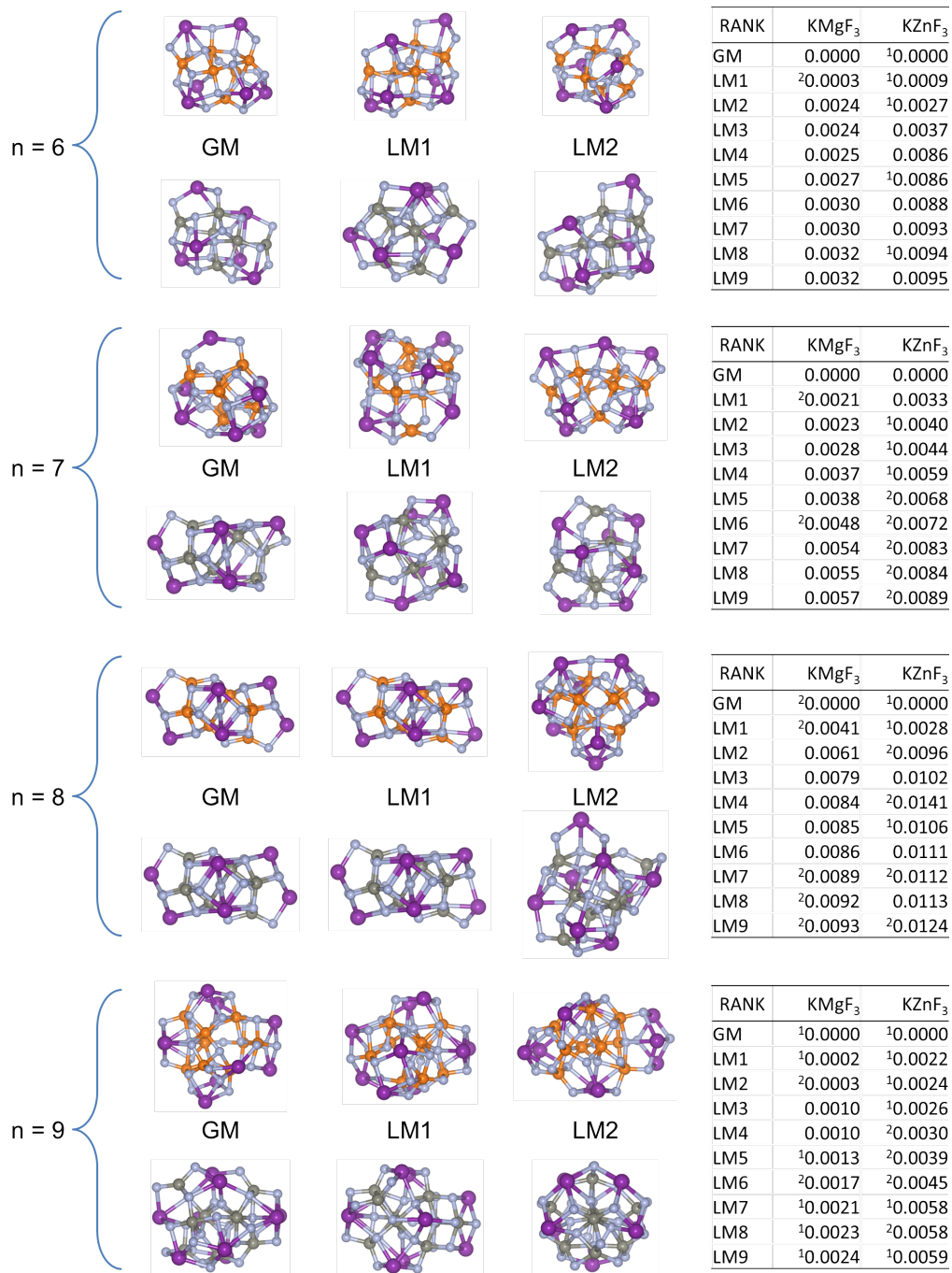


Figure 5.30: The three lowest energy $(\text{KMgF}_3)_n$ and $(\text{KZnF}_3)_n$ DFT clusters for $n = 6 - 9$. The tables shows the energy for the top ten clusters relative to the GM in eV/atom. In the table a superscript "1" indicates the structure was only found by IP to DFT refinement, a "2" means the structure was only found through cross data mining. A lack of superscript means the structure was found from both methods.

from the GM to LM2 is 0.0096 eV/atom, whereas the gap in energy from LM2 to LM9 is less than a third of that, at 0.0028 eV/atom. The highly symmetric $n = 8$ GM structure is also lower in energy per atom than the $n = 9$ GM structure. This is the only occurrence where a GM at a particular cluster size is more stable a larger sized GM. This suggests that either the $n = 8$ KZnF₃ GM is a “magic cluster” ?? (a cluster of exceptionally low energy), or the DFT $n = 9$ KZnF₃ GM has not yet been found.

For the larger cluster sizes, it is difficult to pinpoint any specific structural features, for a number of reasons, that increase stability: (a) they are visually more complex, and (b) a greater number of different structures will exist within a small energy range. Thus, it may be more useful to apply statistics to the top clusters. To better understand the average local environment of the different cations – as well as to give data for comparison with experimental radial distribution functions – density distribution plots were created. The density distribution was calculated for each cluster size by determining the radial distance (r_{ij}) between the ion species of interest, i , and all other ions in the cluster, j . Each radial distance calculated between a pair of ions is smeared using a Gaussian function to aid in visualisation. The amplitude of each Gaussian was scaled by r_{ij}^{-2} to get a density distribution rather than a number distribution. The amplitude of each Gaussian was then scaled again by the Boltzmann factor, $e^{-\Delta E_i/kT}$, where ΔE_i is the difference in energy per atom between the GM at that size and the i th cluster, k is the Boltzmann constant, and T the temperature. A temperature of 300 K was used. The Gaussians from each cluster for a given size were summed together into a plot, with the total amplitudes in the final plot being divided by the total weight, i.e. the sum of the Boltzmann factors.

Figure 5.31 shows the distribution for the two cations in each material at cluster sizes $n = 2, 4$, and 9 as well as the bulk. For the bulk distribution, the ion responsible for each peak has been labelled. From the Mg ion centred plot it can be seen that the nearest neighbour distance is approximately 2 Å and is shortest for $n = 2$, as would be expected due to the under coordination of the Mg ions in small clusters. As the clusters get larger the peak tends towards the bulk like value. At approximately 3 Å there is the presence of density in the clusters not seen in the bulk. This arises from Mg – Mg next-nearest neighbours absent in the bulk. Due to all the K ions being pushed out to the edges of the clusters the Mg ions are allowed to get closer to each other. The Zn distribution shows an almost identical behaviour, the only noticeable difference being the shorter, wider peaks of nearest neighbour Zn – F distances, which suggest that the Zn – F bond is more flexible in regards to its length which was seen explicitly in the large variation of bond length for the smaller clusters.

The K centred distributions show the same behaviour in both compounds. The first peak for the clusters show a significant difference from that of the bulk suggesting an average K – F bond up to 0.3 Å shorter in the clusters than the bulk. Even as the cluster size goes from $n = 2$ to 9, the peaks do not appear to be converging as rapidly

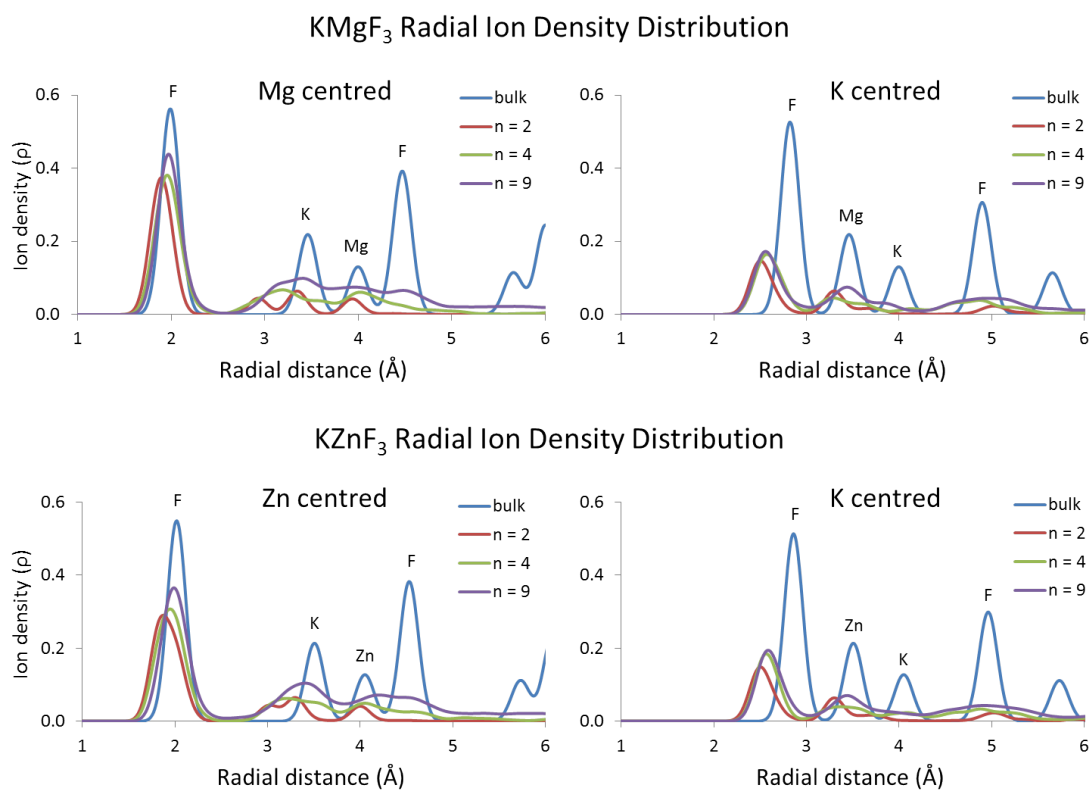


Figure 5.31:

towards the bulk peak. As with the X ions the shorter bond distances hint at the under-coordination except it is a much more extreme case for the K ions. The under-coordination is further implied by the smaller area under the cluster peaks compared to the bulk peak. Unlike in the case of the X ion distributions the second and third peaks remain in the bulk order. The second peak representing the K – X separation is shorter than the bulk value but does appear to approach the bulk value as cluster size grows. Again the much smaller area under the cluster peak compared to the bulk confirms the K ions are positioned towards the edge of the cluster.

5.7 Electronic Structure and Optical Properties

Density of States (DOS) plots for the GM clusters of both materials for $n = 1, 2$ and 9 as well as the bulk are shown in Figure 5.32. The plots are shifted such that the highest occupied molecular orbital (HOMO) is located at 0 eV. The DOS plots show that increasing the size of the cluster, increases the density of energy levels close to the HOMO and LUMO (lowest unoccupied molecular orbital) as would be expected due to there being more atoms, and hence a greater number of energy levels. For the KMgF_3 clusters, the HOMO region is dominated by F states and the LUMO region contains mainly K states with some mixing from Mg. For KZnF_3 , the HOMO is mainly

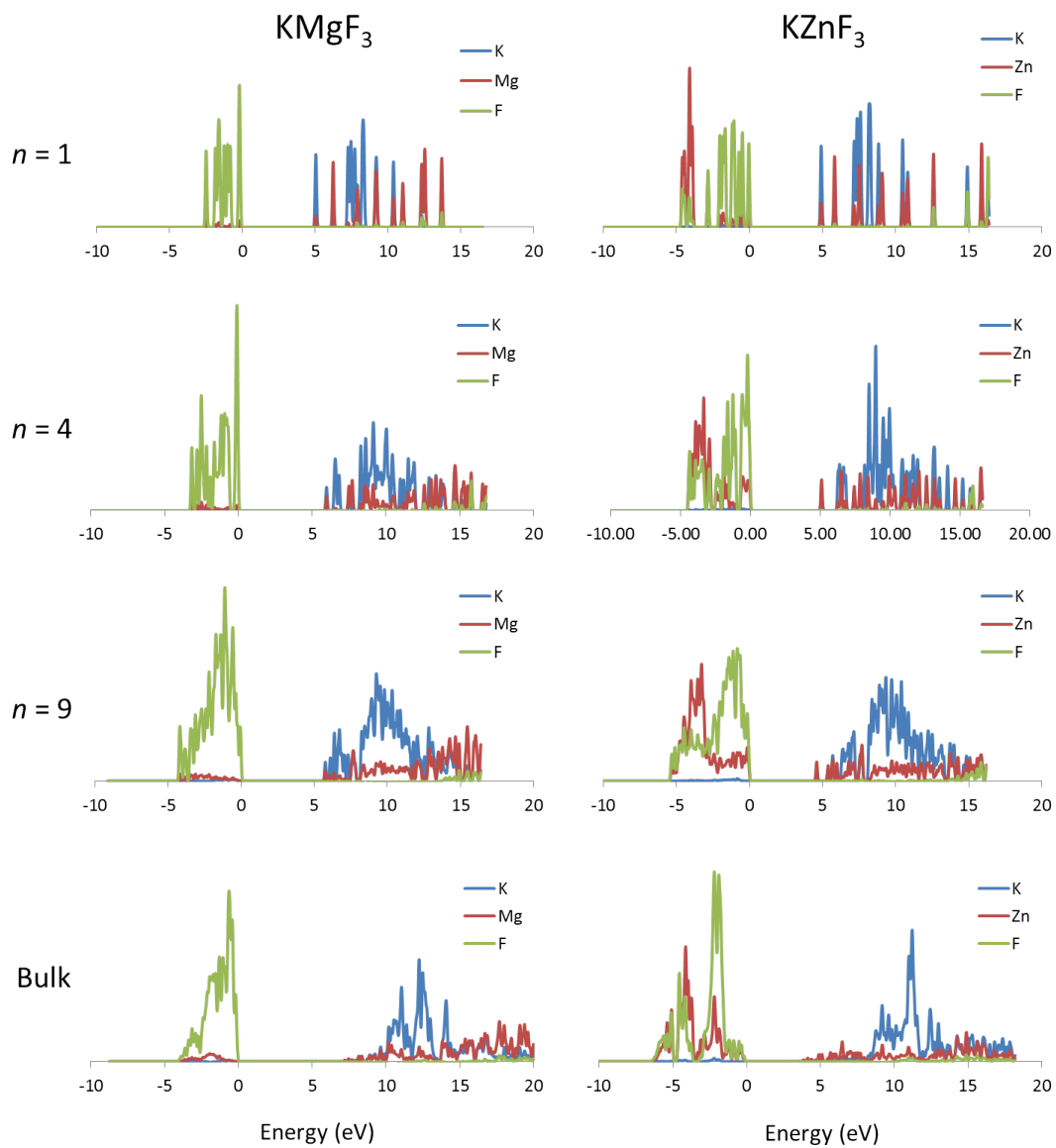


Figure 5.32: DOS for KMgF_3 (left) and KZnF_3 (right), clusters and bulk. The clusters sizes shown are for $n = 1, 4,$ and 9 , where n is the number of formula units.

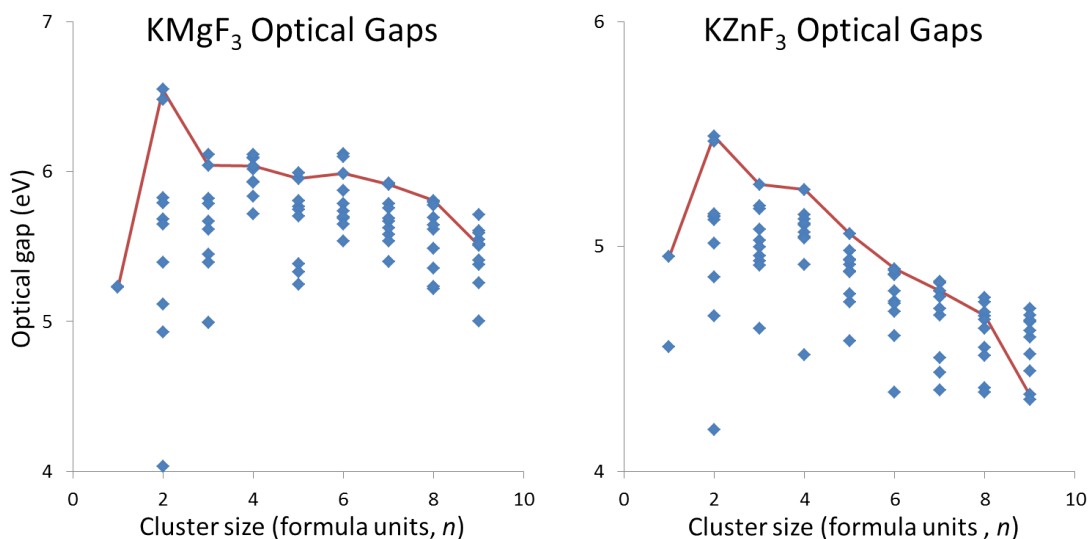


Figure 5.33: The HOMO-LUMO gap for the top ten structures at each size for KMgF_3 and KZnF_3 clusters. The red line tracks the gap for the GM structure at each size. The calculated values for the bulk band gap of KMgF_3 and KZnF_3 , are 7.02 eV and 3.72 eV, respectively.

F states with mixture from Zn with the Zn mixing becoming more prominent at lower orbital energy for all clusters. The LUMO is a mixture of Zn and K states with the Zn component becoming more dominant as cluster size increases.

The DOS profile for the KZnF_3 clusters are similar to that of the bulk DOS. On the other hand, the DOS profile for the KMgF_3 clusters disagree at the LUMO, with the dominance of K states seen in the clusters not present in the bulk. The K dominance does not appear to be diminishing as cluster size increases either.

Figure 5.33 shows the HOMO-LUMO gaps of the top ten structures at each size for KMgF_3 and KZnF_3 clusters. The figure highlights the gap for the GM with a red line. For $n = 1$, the gap calculated for the linear stick (LM2) is 0.85 eV for KMgF_3 , and 0.86 eV for KZnF_3 . The clusters for both materials show the same qualitative trend, a gradual decrease in gap as the cluster size increases with kinks at $n = 3$ and 5 for KMgF_3 and $n = 3$ for KZnF_3 . The downward trend is much more obvious for KZnF_3 . The spread in the calculated gap of the top ten structures is found to be greater for KMgF_3 than KZnF_3 at each size. With the exception of $n = 9$ for KZnF_3 , the GM gap is always one of the largest gaps calculated for the top ten clusters. The main difference between the two compounds, is that the KMgF_3 gap for clusters is smaller than the calculated bulk gap (7.02 eV), while the KZnF_3 gap for clusters is larger than the bulk (3.72 eV). This means the calculated gaps for the KZnF_3 clusters are tending towards the bulk value. However, the gap for the KMgF_3 clusters are tending away from the bulk value at the cluster sizes investigated. The DOS profiles (cf. 5.33) for the KMgF_3 clusters showed the LUMO to be dominated by K states. Thus, it is suggested here,

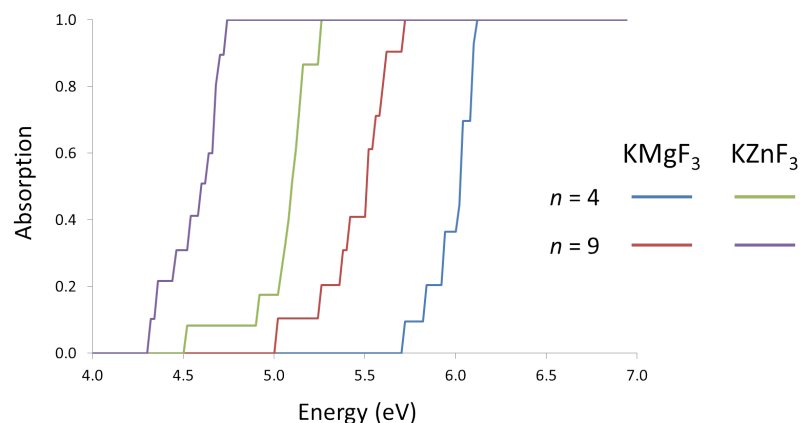


Figure 5.34:

that the differing local environment of the K ions in the clusters, compared to the bulk, leads to the discrepancy in the optical gap.

The KZnF_3 cluster DOS profiles show the LUMO to be made up of Zn states. The Zn ions in the clusters achieve a coordination much more comparable to that seen in the bulk, than that achieved by the K ions. Thus, this may be the reason the KZnF_3 optical gaps more closely resemble the bulk values.

The way in which the LUMO states are constructed, may also explain the greater variation in calculated gap found for the top ten structures of KMgF_3 compared with KZnF_3 . The K ions generally experience a more variable local environment, and the LUMO of the KMgF_3 clusters are heavily influenced by the K ion. Thus, leading to a more variable gap. It is expected that as the size of the clusters increases, the value KMgF_3 HOMO-LUMO gap will eventually stop decreasing and begin to tend upwards towards the value of the bulk gap. However, the cluster sizes considered up to now are still far away from this range. This is consistent with the fact that for the two systems considered, the cluster sizes have not been large enough for the perovskite unit cell (which is correlated with the size of the band gap, of course) to be present in the global minimum structure.

For comparison with future experiments, crude absorption spectra for $(\text{KMgF}_3)_n$ and $(\text{KZnF}_3)_n$ have been created for $n = 4$ and 9 ; see Figure 5.34. The figure shows the cumulative absorption for the top ten clusters, with the amplitude each cluster contributed scaled by the Boltzmann factor using a temperature of 300 K. It is assumed that a constant absorption is contributed from each cluster for all energies larger than the HOMO-LUMO gap. There is a clear difference in absorption spectra (very little overlap) between the two compounds, regardless for cluster size, with KMgF_3 absorbing at a higher energy. Similarly, for both compounds there is a clear difference in absorption spectra between the $n = 4$ and $n = 9$ clusters. The $n = 4$ clusters absorb at a higher energy than the $n = 9$ clusters. The sharp differences in the spectra suggest absorption

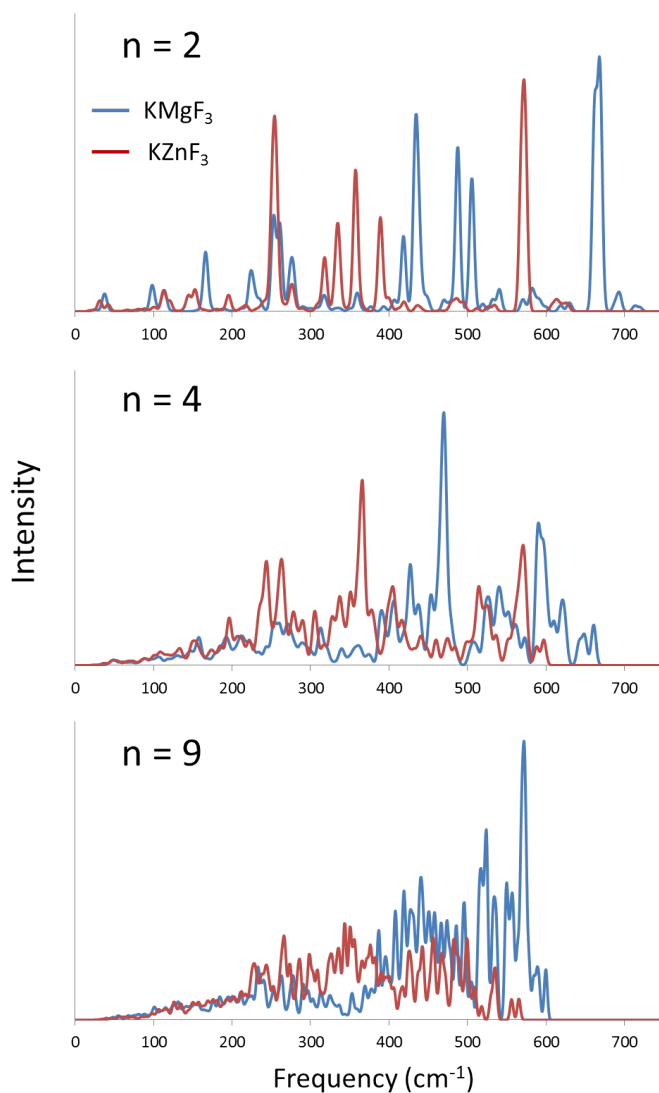


Figure 5.35: Calculated infrared spectra for $(\text{KMgF}_3)_n$ and $(\text{KZnF}_3)_n$ clusters, where $n = 2, 4$ and 9 .

spectroscopy may be a possible method to distinguish between these clusters.

Finally, infrared data is presented in Figure 5.35 for comparison with future experiments. The infrared frequencies and their corresponding intensities were calculated for the top ten clusters at each size using FHI-aims. The calculated vibrational frequencies were smeared using a Gaussian function to aid visualisation. The Gaussians for each cluster at a particular size were scaled according to the Boltzmann factor, and then summed together. The highest frequencies are found to be slightly higher in KMgF_3 than KZnF_3 , with these frequencies decreasing as cluster size increases.

5.8 Bulk-like Clusters

So far the structure of all low energy clusters have the Mg and Zn ions residing closer to the cluster centre, while the K cations are positioned along the outer edges of the cluster. The structure of a cluster containing even one K ion near the cluster centre remains to be seen. In this brief section, $(\text{KMgF}_3)_n$ clusters with a structure more similar to the perovskite bulk phase are investigated. These bulk-like clusters are compared with low energy structure found through global optimisation in an attempt to determine at what size do bulk-like clusters begin to emerge.

The cluster size sampled was $n = 8 - 20$. Three types of structure generation were employed:

Type 1 Type 1 created structures by performing a global optimisation using Genetic Algorithms (GA) on the IP landscape. The lowest energy candidates were then refined through DFT. This techniques has already been used in this chapter to generate cluster structures.

Type 2 Type 2 used the solid solutions routine of KLMC discussed in chapter 4. A cubic structure containing a K ion at the centre, with all ions on lattice sites was created; see Figure 5.36. The cube contained 1 K ion, 8 Mg ions, and 12 F ions. The remaining atoms were randomly distributed on lattice sites around the cube, with F ion restricted to F lattice sites, while the cations could occupied either cation site. The available lattice sites were chosen within a radial cut-off from the central K ion. The radial cut-off was chosen so that there was not more than one empty shell of lattice sites when all ions were made to occupy positions as close to the centre as possible. The ions of the cube were held fixed, while the ions around the cube were allowed to relax with respect to geometry using the IP. The relaxed structure was refined through DFT.

Type 3 Type 3 involved taking stoichiometric cuts from the bulk, and relaxing them using IP. The IP relaxed structures were then refined through DFT.

For Type 1, structures were generated for $n = 10, 12, 15,$ and 20 ($n = 8$ and 9 had previously been done). At least 15,000 structures were sampled at each size, with the top 50 being refined through DFT. It is assumed a sample size of 15,000 candidates will not lead to all, or even most, of the top structure being found. However, it is expected that the search will be large enough to yield at least a few of the top structures. For Type 2, structures were generated for $n = 8 - 20$. 10,000 structures were sampled at each size, with the top 50 being refined through DFT. For Type 3, structures were generated for $n = 8$ ($2 \times 2 \times 2$ cut), 12 ($2 \times 2 \times 3$ cut), 16 ($2 \times 2 \times 4$ cut), 18 ($2 \times 3 \times 3$ cut), and 20 ($2 \times 2 \times 5$ cut).

Figure 5.37 plots energy of the global minima (GM) found for each method at each size. The values plotted are relative to the energy of the Type 1 GM at $n = 20$. The

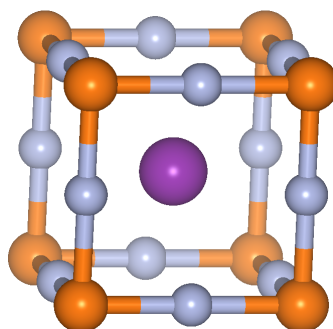


Figure 5.36: The central section of clusters created using Type 2. K, Mg, and F ions are purple, orange, and grey spheres, respectively.

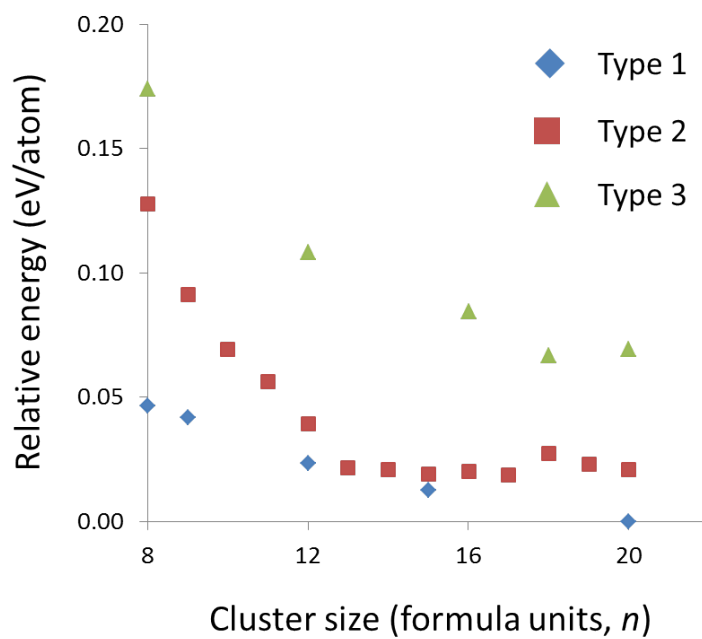


Figure 5.37: The central section of clusters created using Type 2. K, Mg, and F ions are purple, orange, and grey spheres, respectively.

energy of the Type 1 GM are found to be the lowest, which is expected as there are no constraints on the global optimisation. The Type 2 clusters are found to be the second lowest in energy, while the Type 3 clusters are highest. From the plot, it is clear the difference in energy between Type 1 and the other types has decreased with increasing n . The energies of Type 2 fall almost linearly from $n = 8$ to 13, after which the energy difference between clusters sizes varies less. From $n = 13$ the difference in energy between the GMs of Type 1 and 2 is small. The difference calculated at $n = 15$ is 0.007 eV/atom. Compare this to the value of kT at 300 K: 0.026 eV. Thus, it can be expected that cluster in which K ions are seen towards the centre may exist at around this size. At $n = 18 - 20$ the Type 2 clusters increase in energy compare to $n = 17$. This may be: a feature of the constraints imposed on the global optimisation technique; a result of an insufficient number of structure candidates being tested; or the point at which the IP and DFT disagree more. Additional calculations will need to be performed to ascertain the cause of the hike in energy.

The Type 3 clusters, which represents bulk cuts, are much higher in energy than the other two form of clusters. The difference in energy between Type 1 and Type 2 clusters has been reduced with increased cluster size, from 0.127 eV/atom at $n = 8$, to 0.069 eV/atom at $n = 20$. However, the difference in energy at $n = 20$ does not suggest bulk cuts will be found yet. The Type 3 cluster at $n = 18$ appears to off trend compared to the other clusters. The $n = 18$ cluster is a $2 \times 3 \times 3$ cut, where as the other clusters follow a $2 \times 2 \times X$ pattern of cut. Thus, it can be deduced that the more cubic bulk cuts, which have a higher volume to surface ratio are likely to be lower in energy. This is correlates with what was seen for the GM cluster found from the GA global optimisations, where the low energy structures for the larger sized cluster are quite dense, conforming to spherical shapes.

Lastly, it should be noted that at $n = 15$, none of the top 50 structures found using Type 1 had a K ion near the centre of the cluster. The DFT energy difference between the Type 1 and Type 2 GM was 0.007 eV/atom at this size. However, the IP energy difference was found to be 0.034 eV/atom, almost five times larger. This cannot be attributed to energy differences between clusters being larger for the IP structures than the DFT structure. It was shown earlier in the chapter that the energy range of the top 10 clusters was similar for DFT and IP calculations. This indicates the IP find K ions at the centre of clusters energetically more unfavourable than DFT does. The cause is likely a result of the IP modelling the K ions to be slightly larger, and possessing a higher charge, than that seen for DFT. As a consequence, global optimisations performed using IP are more likely to rule out bulk-like clusters, or clusters with K ions near the centre, than the DFT would have. This highlights why using another method like “data mining” complimentary to the IP global optimisations could be useful.

5.9 Conclusion

In this chapter $(\text{KMgF}_3)_n$ and $(\text{KZnF}_3)_n$ nanoclusters have been investigated. The structure of the nanoclusters were unknown, and so global optimisations using interatomic potentials (IP) were performed to predict the structure. Three global optimisation techniques were tested: Genetic Algorithms (GA), Basin Hopping (BH), and stochastic Quenching (SQ). The tests were performed on clusters sized $n = 1 - 9$. The GA technique was found to be the best, performing slightly better than BH on the larger clusters ($n = 7 - 9$). SQ was found to be ineffective above $n = 5$.

Using the results from the GA the lowest energy structures, at each size from $n = 1$ to 9, were inspected. It was found that the two compounds, KMgF_3 and KZnF_3 , shared many of the same low energy structures. The structure of the clusters revealed that it was energetically favourable for the more highly charged X cation (Mg or Zn) to sit closer to the centre of the cluster, while the K cation was pushed to the edges. This allowed the X cation to achieve a higher coordination.

For both compounds, the top 100 structures (when available) at each cluster size were refined (relaxed w.r.t geometry) through DFT. It was found that the correlation between the IP and DFT energetic ordering of the structures was better for KMgF_3 than KZnF_3 . It is suggested this was due to the KMgF_3 IP using partial charges, while the KZnF_3 IP used formal charges. This was deduced from the cation separation observed for the KMgF_3 IP structures matching more closely to the DFT ones, where as the cation separation in the KZnF_3 IP structures significantly overestimated those seen for DFT.

The DFT structures were “data mined” across the two compounds. I.e. a DFT structure for KMgF_3 was refined for KZnF_3 (Mg replaced with Zn). The process revealed the IP search had missed some of the low energy DFT structures. The energetic ordering of the clusters, and the structures themselves, was more similar between the two compounds for DFT than was seen for the IP. Like the lowest energy IP structures, the DFT structures had the X ion residing closer to the centre of the cluster, while the K ions were positioned towards the edges.

The HOMO-LUMO gaps for each DFT cluster were calculated. It was found that the gaps for the KMgF_3 clusters were smaller than the bulk perovskite band gap. The gap for KZnF_3 clusters was larger than the bulk perovskite band gap. Both compounds showed a trend of decreasing band gap with increased cluster size, indicating that optical measurements may be useful in determining cluster size. Infrared vibrational frequencies were also calculated for clusters. KMgF_3 was found to have the higher frequencies, with the top frequencies for both compounds decreasing with increasing cluster size.

Lastly, clusters with a structure more similar to the perovskite bulk phase were compared against the globally optimised clusters. These clusters were tested over the size range $n = 8 - 20$. The global optimisation searches for the larger clusters were

less extensive than those performed earlier in the chapter, as only rough estimates of the energy and structure were required. Two different types of clusters were compared against the globally optimised structures. One type created structures in which a K ion was forced to be near the cluster centre. The other type used bulk cuts. It was found that at around $n = 13$ the clusters with K ions in the centre became energetically competitive with the structures found from global optimisation. The bulk cuts reduced the energy gap from the best structures from 0.127 eV/atom at $n = 8$, to 0.069 eV/atom at $n = 20$. However, this gap does not make the bulk cuts competitive, and so the cluster size will need to become much larger before bulk-like structures begin to form.

Chapter 6

Conclusion

In this chapter the results and conclusions of the thesis are summarised, along with suggestions for future work.

The structure of ABZ_3 perovskite materials in their non-bulk phases has been the focus of this thesis. The atomic arrangement of perovskite polar surfaces and nanoclusters are relatively unknown. This is largely due to conventional structure determination techniques, such as X-ray and neutron scattering, proving ineffective on these phases. To determine the non-bulk phase structures, global optimisation techniques have been employed. Such techniques require sampling a number of possible atomic configurations. The size of the sample required typically increasing with system size. Interatomic potentials (IP) can offer a fast and reliable approach to screen for suitable atomic configurations. Thus, IP are ideal for global structural optimisation searches.

In the first section of results, IP parameters for $KTaO_3$ were refined by fitting to bulk properties, while IP parameters for $KMgF_3$ and $KZnF_3$ were taken from the literature. Both IP and density functional theory (DFT) calculations were employed independently to model the bulk phase and a comparison made to the properties calculated by the two different levels of theory. To test the suitability of our chosen modelling parameters, the calculated properties were compared with experimentally observed properties. A strong agreement between the two levels of theory was found, with the calculations also matching closely to experiment. The properties calculated using the $KTaO_3$ IP showed a particularly strong match to experiment. From the DFT calculations, it was also possible to analyse the electronic structure. A hybridisation of the B and Z ion states was found for $KTaO_3$ (Ta–O) and $KZnF_3$ (Zn–F), indicative of covalent bonding. No such mixing of the states was seen for $KMgF_3$, suggesting a more ionic structure.

Defects, in the form of neutral vacancies, were modelled in super cells of the bulk. For $KTaO_3$, K vacancies under oxidising conditions were the most thermodynamically stable. O vacancies were found to have a low energy of formation under metal-rich conditions. Ta vacancies were the most unstable. For the two fluoride perovskites, vacancies of both cations were found to be favourable under oxidising conditions. F vacancies had higher

formation energies, but relatively low in any non-oxidising environment.

A global optimisation was performed on the polar (001) surface for KTaO_3 to determine the lowest energy 2×2 reconstructions.

Interestingly, the most stable reconstructions required cation interlayer exchange at the surface. Ta ions moved from the originally TaO_2 terminated surface into the sub-surface layer below, while K ions moved from the sub-surface onto the surface layer. This enables the Ta ion to achieve a higher coordination which appears to be a stabilising mechanism for this material. It is proposed the preferential filling of the tantalum coordination is charge driven, as tantalum is the higher charged cation. The reconstructions did not appear to have any significant effect on the electronic structure of the material. Note that ABZ_3 type perovskites contain alternating layers of AZ and BZ_2 (A-B-A-B) along the (001) direction. Typically, the AZ terminated surface is found to be the most stable. Thus, computational models are generally set up with an A terminated, A-B-A-B type slab. Here it is shown, that starting with a B terminated, B-A-B-A-B type slab, and then exchanging the B cation on the surface layer with the A cation in the sub-surface layer produces a surface of lower energy. This reconstruction results in an A-AB-B-A-... layered structure, with a A cations on the topmost surface layer and an mixed sub-layer containing both A and B cations.

Defects, in the form of K and O vacancies, were introduced to the surface slabs. It was shown that the vacancies were more stable at the surface than in the bulk, thus suggesting thus suggesting vacancies will migrate to the surface. As with the bulk calculations, K vacancies, under oxidising conditions, were found to be the most stable. The creation of O vacancies was most favourable under metal rich conditions, with the lowest formation energy calculated to be 0.47 eV; 0.52 eV lower than in the bulk. An upward band bending towards the surface was seen for both K and O vacancies. This suggests an accumulation of holes at the surface in the presence of K vacancies, and an accumulation of electrons in the bulk for O vacancies. In the case of the O vacancies, this is in direct contrast to what is proposed in the literature. Experimentally, a two-dimensional electron gas (2DEG) is observed on the (001) cleaved surface of KTaO_3 . It is suggested that the 2DEG is in part due to oxygen vacancy formation. To further investigate this phenomenon, it is proposed that additional calculations be performed. Firstly, to ensure the electronic effects of the surface are distinguished from the bulk, a slab of larger thickness should be used to model the KTaO_3 surface. Secondly, spin-orbit coupling should be introduced in to the model in order to test whether the 2DEG is a result of orbital splitting due to spin. Finally, should neither of these modifications reveal the 2DEG, hybrid calculations which are considered more reliable, but equally more expensive should be attempted to confirm predictions.

The low energy surface reconstructions discovered for KTaO_3 were exploited to investigate surface of the perovskites: KMgF_3 , KZnF_3 , and BaSnO_3 . The ground state structure for KTaO_3 , also proved to be the lowest energy reconstruction for BaSnO_3

when compared against all the surface structures found for KTaO_3 . Of the surface structures tested for BaSnO_3 , the ranking of the reconstructions, with respect to energy, proved identical to the rankings seen for KTaO_3 . The change in ranking of the surfaces, with respect to energy, was greatest for KZnF_3 . Of the three compounds tested, BaSnO_3 has the ions with the highest oxidation states. This suggests the strength of the stabilising effect of the reconstruction mechanisms are coupled to the charges of the system. To verify this, additional calculations should be performed in which the KTaO_3 surface reconstructions are applied to a wider range of perovskite materials. In particular, III-III perovskites would be a good next step, as I-V and II-IV have already been investigated. This will allow for the contribution of different effects such as cation size, bonding covalency, open vs closed shell systems, and orbital effects to be investigated alongside cation charge. Moreover, charge and relative ion size can be changed continuously in the IP model to investigate the effect they have on the surface energy. In addition, the surface periodicity should also be varied to reduce the symmetry being imposed upon the structure. This could include investigating 2×4 , 4×4 , 5×5 , and greater surfaces.

Further investigation of the surfaces may also include molecular dynamics at the surface, to simulate the effect of surface melting. This additional technique may result in new structures being discovered that may have been screened out by the Basin Hopping approach.

As well as surfaces, stoichiometric nanoclusters of the fluoride perovskites KMgF_3 and KZnF_3 were also investigated, as part of an international collaborative effort to determine the most effective global optimisation techniques. The size of the nanoclusters ranged from 5 to 100 atoms. The structures were determined by performing a global optimisation on the IP energy landscape for each composition. The performance of three different global optimisation techniques were tested: Genetic Algorithms (GA), Basin Hopping (BH), and stochastic Quenching (SQ). The GA were more successful and more efficient at finding the GM and other low energy LM, although only slightly outperforming the BH technique. SQ was found to be severely less effective than the other two methods for systems containing more than 25 atoms.

The 100 lowest energy LM clusters were refined using DFT. The structure of the low energy clusters showed the B cations (Mg or Zn) to sit close to the cluster centre, while the K ions resided at the surface of the LM clusters. The agreement in the energetic ordering, or ranking, of structures between IP and DFT was found to be strong for KMgF_3 . The KMgF_3 IP were based charge model, whereas the KZnF_3 IP used formal charges. This led to KZnF_3 IP structures overestimating the cation-cation separation compared to the DFT structure. The ranking of DFT structures were also shown to correlate strongly across the two compounds. Low energy structures for KMgF_3 generally proved to be low energy structures for KZnF_3 , and vice-versa. Thus, the process of “data mining”, employing the LM structures of one compound as initial

models to be refined for another compound, is a very useful approach in the structure prediction of nanoclusters. As such, the atomic structures of the DFT LM nanoclusters reported here, once published, will be uploaded into the WASP@N database [198] for others to exploit.

The optical gap of the clusters was found to decrease with increasing cluster size, and therefore, along with other nanocluster properties may be tuned by controlling particle size.

None of the $n = 1$ nor the larger low energy LM nanoclusters found from global optimisation contained K ions near the centre. However, the bulk structure of these compounds are made up of perovskite cells in which K ions are 12-coordinated. Therefore, there must be a transition at a larger size than that considered here, where it is energetically favourable for K ions to reside inside the cluster. In an attempt to find this transition, two additional constrained searches were conducted for nanoclusters containing 40 – 100 atoms. In one set of runs, one K ion was fixed at the centre of the cluster. In the second set, nanoclusters were created from cuts of bulk perovskite. It was found that at around 60 atoms the clusters with K ions in the centre became energetically competitive (within 0.02 eV/atom of the GM) with the structures found from global optimisation. The bulk cuts reduced the energy gap to the GA GM from 0.127 eV/atom at $n = 8$, to 0.069 eV/atom at $n = 20$. However, these relaxed bulk-cuts are still higher in energy than those found by the global optimisation techniques; the cluster size will need to become much larger before bulk-like structures begin to form.

In summary, the structure of surface and nanocluster phases of ABZ_3 perovskite compounds has been investigated. Using global optimisation routines, unsurprisingly it was found that structures in which the B cation was able to maximise its coordination were energetically more favourable as this cation has the higher charge. For nanoclusters, this led to a segregation of cations species, with B ions at the cluster centre, and A cations at the surface. For the (001) polar surface, it was previously predicted that the surface would also be K terminated. However, my results suggest a more complex picture: a sub-layer composed of both A and B cations. It should also be noted that there are many similarities in the structures and their respective rankings based on energy of formation when comparing different compounds that adopt the perovskite phase. Thus, the method of “data mining” has proved extremely useful.

Further work into the nanoclusters would include looking at non-stoichiometric particles in case these structures proved to be more stable than their stoichiometric counterparts. This would greatly increase the number of possible candidate structures. The natural follow on from this would be to then look at charged clusters. To investigate the size at which the bulk structure begins to form, larger clusters will need to be tested. Performing global optimisations on clusters containing many hundreds, if not thousands, of atoms will be very computationally expensive. A suitable alternative may be to perform molecular dynamics on bulk cuts, to more effectively determine at what size the

bulk structure precipitates.

To conclude, this thesis has shed light on the atomic structure of perovskite polar surfaces and nanoclusters. Although the size of the nanoclusters modelled were not large enough to contain fragments/features of the bulk and surface structures, the work has highlighted the usefulness of global optimisations and data mining.

Bibliography

- [1] Huan Zhang et al. “Structural stability and formability of ABO₃-type perovskite compounds”. In: *Acta Crystallographica Section B Structural Science* 63.6 (Nov. 9, 2007), pp. 812–818.
- [2] Chonghe Li, Kitty Chi Kwan Soh, and Ping Wu. “Formability of ABO₃ perovskites”. In: *Journal of Alloys and Compounds* 372.1 (June 9, 2004), pp. 40–48.
- [3] A. S. Bhalla, R. Guo, and R. Roy. “The perovskite structure – a review of its role in ceramic science and technology”. In: *Material Research Innovations* 4.1 (Nov. 1, 2000), pp. 3–26.
- [4] Yu.F. Zhukovskii et al. “A comparative ab initio study of bulk and surface oxygen vacancies in PbTiO₃, PbZrO₃ and SrTiO₃ perovskites”. In: *Solid State Communications* 149.33 (Sept. 2009), pp. 1359–1362.
- [5] Keqin Huang, Robin S. Tichy, and John B. Goodenough. “Superior Perovskite Oxide-Ion Conductor; Strontium- and Magnesium-Doped LaGaO₃: I, Phase Relationships and Electrical Properties”. In: *Journal of the American Ceramic Society* 81.10 (Oct. 1, 1998), pp. 2565–2575.
- [6] Maria Alfredsson et al. “Dopant control over the crystal morphology of ceramic materials”. In: *Surface Science* 601.21 (Nov. 1, 2007), pp. 4793–4800.
- [7] M. V. Raymond and D. M. Smyth. “Defects and charge transport in perovskite ferroelectrics”. In: *Journal of Physics and Chemistry of Solids*. Proceeding of the 3rd Williamsburg Workshop on Fundamental Experiments on Ferroelectrics 57.10 (Oct. 1996), pp. 1507–1511.
- [8] Tatsumi Ishihara, Hideaki Matsuda, and Yusaku Takita. “Doped LaGaO₃ Perovskite Type Oxide as a New Oxide Ionic Conductor”. In: *Journal of the American Chemical Society* 116.9 (May 1, 1994), pp. 3801–3803.
- [9] M. Saiful Islam. “Computer modelling of defects and transport in perovskite oxides”. In: *Solid State Ionics* 154–155 (Dec. 2, 2002), pp. 75–85.
- [10] K. S. Aleksandrov and V. V. Beznosikov. “Hierarchies of perovskite-like crystals (Review)”. In: *Physics of the Solid State* 39.5 (May 1, 1997), pp. 695–715.

- [11] S. N. Ruddlesden and P. Popper. “New compounds of the K_2NiF_4 type”. In: *Acta Crystallographica* 10.8 (Aug. 1, 1957), pp. 538–539.
- [12] S. N. Ruddlesden and P. Popper. “The compound $Sr_3Ti_2O_7$ and its structure”. In: *Acta Crystallographica* 11.1 (Jan. 1, 1958), pp. 54–55.
- [13] B. V. Beznosikov and K. S. Aleksandrov. “Perovskite-like crystals of the Ruddlesden-Popper series”. In: *Crystallography Reports* 45.5 (Sept. 1, 2000), pp. 792–798.
- [14] A.M. Glazer. “Simple ways of determining perovskite structures”. In: *Acta Crystallographica* 1.31 (May 1975), pp. 756–762.
- [15] V. M. Goldschmidt. “Die Gesetze der Krystallochemie”. In: *Naturwissenschaften* 14.21 (May 1, 1926), pp. 477–485.
- [16] Mats Johansson and Peter Lemmens. “Crystallography and Chemistry of Perovskites”. In: *Handbook of Magnetism and Advanced Magnetic Materials*. John Wiley & Sons, Ltd, 2007.
- [17] H. A. Jahn and E. Teller. “Stability of Polyatomic Molecules in Degenerate Electronic States. I. Orbital Degeneracy”. In: *Proceedings of the Royal Society of London A: Mathematical, Physical and Engineering Sciences* 161.905 (July 15, 1937), pp. 220–235.
- [18] Michael W. Lufaso and Patrick M. Woodward. “Jahn–Teller distortions, cation ordering and octahedral tilting in perovskites”. In: *Acta Crystallographica Section B Structural Science* 60.1 (Feb. 1, 2004), pp. 10–20.
- [19] Roman V. Shpanchenko et al. “Synthesis, Structure, and Properties of New Perovskite $PbVO_3$ ”. In: *Chemistry of Materials* 16.17 (Aug. 1, 2004), pp. 3267–3273.
- [20] Koji Yamakawa et al. “Novel $Pb(Ti, Zr)O_3$ (PZT) Crystallization Technique Using Flash Lamp for Ferroelectric RAM (FeRAM) Embedded LSIs and One Transistor Type FeRAM Devices”. In: *Japanese Journal of Applied Physics* 41.4 (Apr. 1, 2002), p. 2630.
- [21] F. London and H. London. “The electromagnetic equations of the superconductor”. In: *Proceedings of the Royal Society of London Series a-Mathematical and Physical Sciences* 149 (A866 Mar. 1935), pp. 0071–0088.
- [22] D. W. Murphy et al. “New superconducting cuprate perovskites”. In: *Physical Review Letters* 58.18 (May 4, 1987), pp. 1888–1890.
- [23] M. Hamalainen et al. “Magnetoencephalography - Theory, Instrumentation, and Applications to Noninvasive Studies of the Working Human Brain”. In: *Reviews of Modern Physics* 65.2 (Apr. 1993), pp. 413–497.
- [24] S. Mitani et al. “Tunnel-MR and spin electronics in metal-nonmetal granular systems”. In: *Journal of Magnetism and Magnetic Materials* 198-99 (June 1999), pp. 179–184.

- [25] John Druce et al. “Oxygen exchange and transport in dual phase ceramic composite electrodes”. In: *Faraday Discussions* 182 (Nov. 3, 2015), pp. 271–288.
- [26] Stephen J. Skinner. “Recent advances in Perovskite-type materials for solid oxide fuel cell cathodes”. In: *International Journal of Inorganic Materials* 3.2 (Mar. 2001), pp. 113–121.
- [27] Arthur P. Ramirez. “Oxide Electronics Emerge”. In: *Science* 315.5817 (Mar. 9, 2007), pp. 1377–1378.
- [28] Cheng Cen et al. “Oxide Nanoelectronics on Demand”. In: *Science* 323.5917 (Feb. 20, 2009), pp. 1026–1030.
- [29] J. Mannhart and D. G. Schlom. “Oxide Interfaces – An Opportunity for Electronics”. In: *Science* 327.5973 (Mar. 26, 2010), pp. 1607–1611.
- [30] P. W. Tasker. “The stability of ionic crystal surfaces”. In: *Journal of Physics C: Solid State Physics* 12.22 (Nov. 28, 1979), p. 4977.
- [31] Neil W. Ashcroft and N. David Mermin. *Solid State Physics*. New York: Brooks/Cole, Jan. 2, 1976. 848 pp.
- [32] C. R. A. Catlow. “Point Defect and Electronic Properties of Uranium Dioxide”. In: *Proceedings of the Royal Society of London. A. Mathematical and Physical Sciences* 353.1675 (Apr. 21, 1977), pp. 533–561.
- [33] G. V. Lewis and C. R. A. Catlow. “Potential models for ionic oxides”. In: *Journal of Physics C: Solid State Physics* 18.6 (Feb. 28, 1985), p. 1149.
- [34] Scott M. Woodley et al. “Development of a New Interatomic Potential for the Modeling of Ligand Field Effects”. In: *The Journal of Physical Chemistry B* 105.29 (July 1, 2001), pp. 6824–6830.
- [35] E Flikkema and S. T Bromley. “A new interatomic potential for nanoscale silica”. In: *Chemical Physics Letters* 378.5 (Sept. 12, 2003), pp. 622–629.
- [36] Aron Walsh et al. “Potential energy landscapes for anion Frenkel-pair formation in ceria and india”. In: *Solid State Ionics. Exploring Chemical and Structural Complexity of Novel Ion Conductors* 184.1 (Mar. 3, 2011), pp. 52–56.
- [37] J. D. Gale. “GULP: A computer program for the symmetry-adapted simulation of solids”. In: *Journal of the Chemical Society-Faraday Transactions* 93.4 (Feb. 21, 1997), pp. 629–637.
- [38] Julian D. Gale and Andrew L. Rohl. “The General Utility Lattice Program (GULP)”. In: *Molecular Simulation* 29.5 (2003), pp. 291–341.
- [39] J. E. Jones. “On the Determination of Molecular Fields. II. From the Equation of State of a Gas”. In: *Proceedings of the Royal Society of London. Series A, Containing Papers of a Mathematical and Physical Character* 106.738 (Oct. 1, 1924), pp. 463–477.

- [40] B. G. Dick and A. W. Overhauser. “Theory of the Dielectric Constants of Alkali Halide Crystals”. In: *Physical Review* 112.1 (Oct. 1, 1958), pp. 90–103.
- [41] P. P. Ewald. “Die Berechnung optischer und elektrostatischer Gitterpotentiale”. In: *Annalen der Physik* 369.3 (1921), pp. 253–287.
- [42] W. Kohn and L. Sham. “Self-Consistent Equations Including Exchange and Correlation Effects”. In: *Physical Review* 140.4 (Nov. 15, 1965), A1133–A1138.
- [43] John P. Perdew, Kieron Burke, and Matthias Ernzerhof. “Generalized Gradient Approximation Made Simple”. In: *Physical Review Letters* 77.18 (Oct. 28, 1996), pp. 3865–3868.
- [44] John P. Perdew et al. “Restoring the Density-Gradient Expansion for Exchange in Solids and Surfaces”. In: *Physical Review Letters* 100.13 (Apr. 4, 2008), p. 136406.
- [45] W. J. Hehre, R. F. Stewart, and J. A. Pople. “Self-Consistent Molecular-Orbital Methods. I. Use of Gaussian Expansions of Slater-Type Atomic Orbitals”. In: *The Journal of Chemical Physics* 51.6 (Sept. 15, 1969), pp. 2657–2664.
- [46] J. Slater. “Atomic Shielding Constants”. In: *Physical Review* 36.1 (July 1, 1930), pp. 57–64.
- [47] Peter Schwerdtfeger. “The Pseudopotential Approximation in Electronic Structure Theory”. In: *ChemPhysChem* 12.17 (2011), pp. 3143–3155.
- [48] D. F. Shanno. “Conditioning of Quasi-Newton Methods for Function Minimization”. In: *Mathematics of Computation* 24.111 (July 1970), p. 647.
- [49] Ajit Banerjee et al. “Search for stationary points on surfaces”. In: *The Journal of Physical Chemistry* 89.1 (Jan. 1985), pp. 52–57.
- [50] S. M. Woodley et al. “The prediction of inorganic crystal structures using a genetic algorithm and energy minimisation”. In: *Physical Chemistry Chemical Physics* 1.10 (May 15, 1999), pp. 2535–2542.
- [51] Jh Holland. “Genetic Algorithms”. In: *Scientific American* 267.1 (July 1992), pp. 66–72.
- [52] Roy L. Johnston. “Evolving better nanoparticles: Genetic algorithms for optimising cluster geometries”. In: *Dalton Transactions* 22 (Nov. 4, 2003), pp. 4193–4207.
- [53] David J. Wales and Jonathan P. K. Doye. “Global Optimization by Basin-Hopping and the Lowest Energy Structures of Lennard-Jones Clusters Containing up to 110 Atoms”. In: *The Journal of Physical Chemistry A* 101.28 (July 1, 1997), pp. 5111–5116.
- [54] Stefan Goedecker. “Minima hopping: An efficient search method for the global minimum of the potential energy surface of complex molecular systems”. In: *The Journal of Chemical Physics* 120.21 (June 1, 2004), pp. 9911–9917.

- [55] Harry L. Tuller and Sean R. Bishop. “Point Defects in Oxides: Tailoring Materials Through Defect Engineering”. In: *Annual Review of Materials Research* 41.1 (2011), pp. 369–398.
- [56] N. F. Mott and M. J. Littleton. “Conduction in polar crystals. I. Electrolytic conduction in solid salts”. In: *Transactions of the Faraday Society* 34 (Jan. 1, 1938), pp. 485–499.
- [57] M. Leslie and N. J. Gillan. “The energy and elastic dipole tensor of defects in ionic crystals calculated by the supercell method”. In: *Journal of Physics C: Solid State Physics* 18.5 (Feb. 20, 1985), p. 973.
- [58] Akio Shigemi and Takahiro Wada. “Enthalpy of Formation of Various Phases and Formation Energy of Point Defects in Perovskite-Type NaNbO_3 by First-Principles Calculation”. In: *Japanese Journal of Applied Physics* 43.9 (Sept. 1, 2004), p. 6793.
- [59] Guo-Xin Qian, Richard Martin, and D. Chadi. “First-principles study of the atomic reconstructions and energies of Ga- and As-stabilized GaAs(100) surfaces”. In: *Physical Review B* 38.11 (Oct. 15, 1988), pp. 7649–7663.
- [60] David O. Scanlon. “Defect engineering of BaSnO_3 for high-performance transparent conducting oxide applications”. In: *Physical Review B* 87.16 (Apr. 22, 2013), p. 161201.
- [61] S. Zhang and John Northrup. “Chemical potential dependence of defect formation energies in GaAs: Application to Ga self-diffusion”. In: *Physical Review Letters* 67.17 (Oct. 21, 1991), pp. 2339–2342.
- [62] Junjiang Zhu et al. “Perovskite Oxides: Preparation, Characterizations, and Applications in Heterogeneous Catalysis”. In: *ACS Catalysis* 4.9 (Sept. 5, 2014), pp. 2917–2940.
- [63] J. Padilla and David Vanderbilt. “Ab initio study of BaTiO_3 surfaces”. In: *Physical Review B* 56.3 (July 15, 1997), pp. 1625–1631.
- [64] E. Heifets et al. “Ab initio calculations of the SrTiO_3 (110) polar surface”. In: *Physical Review B* 69.3 (Jan. 21, 2004), p. 035408.
- [65] M. R. Farrow, Y. Chow, and S. M. Woodley. “Structure prediction of nanoclusters; a direct or a pre-screened search on the DFT energy landscape?” In: *Physical Chemistry Chemical Physics* 16.39 (Sept. 17, 2014), pp. 21119–21134.
- [66] Scott M. Woodley. “Knowledge Led Master Code Search for Atomic and Electronic Structures of LaF_3 Nanoclusters on Hybrid Rigid Ion–Shell Model–DFT Landscapes”. In: *The Journal of Physical Chemistry C* 117.45 (2013), pp. 24003–24014.

- [67] P. Vousden. “A study of the unit-cell dimensions and symmetry of certain ferroelectric compounds of niobium and tantalum at room temperature”. In: *Acta Crystallographica* 4.4 (July 1, 1951), pp. 373–376.
- [68] E A Zhurova et al. “Electron density and atomic displacements in KTaO_3 ”. In: *Acta crystallographica. Section B, Structural science* 56 (Pt 4 Aug. 2000), pp. 594–600.
- [69] G. A. Samara and B. Morosin. “Anharmonic Effects in KTaO_3 : Ferroelectric Mode, Thermal Expansion, and Compressibility”. In: *Physical Review B* 8.3 (Aug. 1, 1973), pp. 1256–1264.
- [70] H.H Barrett. “Ultrasonic propagation velocity in KTaO_3 ”. In: *Physics Letters A* 26.6 (Feb. 12, 1968), pp. 217–218.
- [71] C. H. Perry et al. “Phonon dispersion and lattice dynamics of KTaO_3 from 4 to 1220 K”. In: *Physical Review B* 39.12 (Apr. 15, 1989), pp. 8666–8676.
- [72] David J. Singh. “Stability and phonons of KTaO_3 ”. In: *Physical Review B* 53.1 (Jan. 1, 1996), pp. 176–180.
- [73] R. Comès and G. Shirane. “Neutron-Scattering Analysis of the Linear-Displacement Correlations in KTaO_3 ”. In: *Physical Review B* 5.5 (Mar. 1, 1972), pp. 1886–1891.
- [74] Suleyman Cabuk. “Ab initio volume-dependent elastic and lattice dynamics properties of KTaO_3 ”. In: *physica status solidi (b)* 247.1 (2010), pp. 93–97.
- [75] A. V. Postnikov, T. Neumann, and G. Borstel. “Phonon properties of KNbO_3 and KTaO_3 from first-principles calculations”. In: *Physical Review B* 50.2 (July 1, 1994), pp. 758–763.
- [76] L. Zhang et al. “On the Possible Curie Temperature and Ferroelectricity for SrTiO_3 and KTaO_3 ”. In: *physica status solidi (a)* 168.1 (1998), pp. 325–329.
- [77] S. H. Wemple. “Some Transport Properties of Oxygen-Deficient Single-Crystal Potassium Tantalate (KTaO_3)”. In: *Physical Review* 137.5 (Mar. 1, 1965), A1575–A1582.
- [78] H. Uwe et al. “Stress induced ferroelectricity in KTaO_3 ”. In: *Solid State Communications* 13.7 (Oct. 1, 1973), pp. 737–739.
- [79] Hiromoto Uwe and Tunetaro Sakudo. “Raman-scattering study of stress-induced ferroelectricity in KTaO_3 ”. In: *Physical Review B* 15.1 (Jan. 1, 1977), pp. 337–345.
- [80] H. Uwe et al. “Ferroelectric microregions and Raman scattering in KTaO_3 ”. In: *Physical Review B* 33.9 (May 1, 1986), pp. 6436–6440.
- [81] P. DiAntonio et al. “Polar fluctuations and first-order Raman scattering in highly polarizable KTaO_3 crystals with off-center Li and Nb ions”. In: *Physical Review B* 47.10 (Mar. 1, 1993), pp. 5629–5637.

- [82] U. T. Höchli, H. E. Weibel, and L. A. Boatner. “Extrinsic Peak in the Susceptibility of Incipient Ferroelectric $\text{KTaO}_3\text{:Li}$ ”. In: *Physical Review Letters* 41.20 (Nov. 13, 1978), pp. 1410–1413.
- [83] O. Hanske-Petitpierre et al. “Off-center displacement of the Nb ions below and above the ferroelectric phase transition of $\text{KTa}_{0.91}\text{Nb}_{0.09}\text{O}_3$ ”. In: *Physical Review B* 44.13 (Oct. 1, 1991), pp. 6700–6707.
- [84] S. R. Andrews. “X-ray scattering study of the random electric dipole system $\text{KTaO}_2\text{:Li}$ ”. In: *Journal of Physics C: Solid State Physics* 18.7 (Mar. 10, 1985), p. 1357.
- [85] R.G. Geyer et al. “Microwave dielectric properties of single-crystal quantum paraelectrics KTaO_3 and SrTiO_3 at cryogenic temperatures”. In: *Journal of Applied Physics* 97.10 (May 2005), pp. 104111–104116.
- [86] K. F. Pai, T. J. Parker, and R. P. Lowndes. “The temperature dependence of the dielectric response of KTaO_3 by dispersive Fourier transform spectroscopy”. In: *Journal of the Optical Society of America* 68.10 (Oct. 1, 1978), pp. 1322–1325.
- [87] A. Frova. “The absorption edge of KTaO_3 and its dependence on electric fields”. In: *Il Nuovo Cimento B Series 10* 55.1 (May 1, 1968), pp. 1–14.
- [88] G. E. Jellison et al. “Optical functions of KTaO_3 as determined by spectroscopic ellipsometry and comparison with band structure calculations”. In: *Physical Review B* 74.15 (Oct. 31, 2006), p. 155130.
- [89] T. Neumann et al. “Electronic structure of KNbO_3 and KTaO_3 ”. In: *Physical Review B* 46.17 (Nov. 1, 1992), pp. 10623–10628.
- [90] A.R. Benrekia et al. “Structural, electronic and optical properties of cubic SrTiO_3 and KTaO_3 : Ab initio and GW calculations”. In: *Physica B: Condensed Matter* 407.13 (July 2012), pp. 2632–2636.
- [91] Minseok Choi, Fumiyasu Oba, and Isao Tanaka. “Hybrid density functional study of oxygen vacancies in KTaO_3 and NaTaO_3 ”. In: *Physical Review B* 83.21 (June 10, 2011), p. 214107.
- [92] Huihui Wang, Feng Wu, and Hong Jiang. “Electronic Band Structures of ATaO_3 (A = Li, Na, and K) from First-Principles Many-Body Perturbation Theory”. In: *J. Phys. Chem. C* 115.32 (2011), pp. 16180–16186.
- [93] H. Bouafia et al. “Structural, elastic, electronic and thermodynamic properties of KTaO_3 and NaTaO_3 : Ab initio investigations”. In: *Computational Materials Science* 75 (July 2013), pp. 1–8.
- [94] Takeshi Nishimatsu et al. “Band Structures of Perovskite-Like Fluorides for Vacuum-Ultraviolet-Transparent Lens Materials”. In: *Japanese Journal of Applied Physics* 41 (Part 2, No. 4A 2002), pp. L365–L367.

- [95] Haruo Takahashi and Ryumyo Onaka. “The XUV Spectra of KMgF_3 and NaMgF_3 ”. In: *Journal of the Physical Society of Japan* 43.6 (Dec. 15, 1977), pp. 2021–2029.
- [96] Kohei Yamanoi et al. “Perovskite fluoride crystals as light emitting materials in vacuum ultraviolet region”. In: *Optical Materials* 36.4 (Feb. 2014), pp. 769–772.
- [97] Kiyoshi Shimamura et al. “Growth and Characterization of KMgF_3 Single Crystals by the Czochralski Technique under CF_3 Atmosphere”. In: *Japanese Journal of Applied Physics* 39.12 (Dec. 1, 2000), p. 6807.
- [98] Tsuguo Fukuda et al. “Crystal growth of new functional materials for electro-optical applications”. In: vol. 4412. 2001, pp. 18–25.
- [99] K. Shimamura et al. “Crystal Growth of Fluorides for Optical Applications”. In: *Crystal Research and Technology* 36.8 (2001), pp. 801–813.
- [100] A.V. Gektin, I.M. Krasovitskaya, and N.V. Shiran. “High-temperature thermoluminescence of KMgF_3 -based crystals”. In: *Journal of Luminescence* 72–74 (June 1997), pp. 664–666.
- [101] A. V. Gektin, I. M. Krasovitskaya, and N. V. Shiran. “UV-dosimetric material based on KMgF_3 perovskite”. In: *Radiation Measurements* 29.3 (May 1998), pp. 337–340.
- [102] G. Kitis et al. “ $\text{KMgF}_3\text{:Ce}$, An Ultra-High Sensitivity Thermoluminescent Material - (Letter to the Editor)”. In: *Radiation Protection Dosimetry* 82.2 (Mar. 1, 1999), pp. 151–152.
- [103] I. G. Wood et al. “Thermal expansion and atomic displacement parameters of cubic KMgF_3 perovskite determined by high-resolution neutron powder diffraction”. In: *Journal of Applied Crystallography* 35.3 (June 1, 2002), pp. 291–295.
- [104] Francesco Demartin et al. “Parascandolaite, KMgF_3 , a new perovskite-type fluoride from Vesuvius”. In: *Physics and Chemistry of Minerals* 41.6 (June 1, 2014), pp. 403–407.
- [105] J. P. Poirier et al. “Viscosity and conductivity of the lower mantle; an experimental study on a MgSiO_3 perovskite analogue, KZnF_3 ”. In: *Physics of the Earth and Planetary Interiors* 32.3 (June 1983), pp. 273–287.
- [106] A. E. Ringwood. “Mineralogical constitution of the deep mantle”. In: *Journal of Geophysical Research* 67.10 (Sept. 1, 1962), pp. 4005–4010.
- [107] A. R. Chakhmouradian et al. “The crystal chemistry of synthetic potassium-bearing neighborite, $(\text{Na}_{1-x}\text{K}_x)\text{MgF}_3$ ”. In: *Physics and Chemistry of Minerals* 28.4 (May 1, 2001), pp. 277–284.
- [108] Purnendu Parhi and V. Manivannan. “Novel microwave assisted solid state metathesis synthesis of KMF_3 ($\text{M}=\text{Zn}, \text{Mn}, \text{Mg}, \text{and Co}$)”. In: *Materials Letters* 62.19 (July 15, 2008), pp. 3468–3470.

- [109] V. Manivannan, P. Parhi, and Jonathan W. Kramer. “Metathesis synthesis and characterization of complex metal fluoride, KMgF_3 ($M = \text{Mg, Zn, Mn, Ni, Cu}$ and Co) using mechanochemical activation”. In: *Bulletin of Materials Science* 31.7 (Dec. 1, 2008), pp. 987–993.
- [110] M. Sahnoun et al. “Full potential calculation of structural, electronic and optical properties of KMgF_3 ”. In: *Materials Chemistry and Physics* 91.1 (May 15, 2005), pp. 185–191.
- [111] G. Vaitheeswaran et al. “High-pressure structural, elastic, and electronic properties of the scintillator host material KMgF_3 ”. In: *Physical Review B* 76.1 (July 13, 2007), p. 014107.
- [112] Shouxin Cui et al. “High-pressure structural, electronic and optical properties of KMgF_3 : A first-principles study”. In: *Journal of Alloys and Compounds* 484.1 (Sept. 18, 2009), pp. 597–600.
- [113] J. H. Beaumont, A. J. Bourdillon, and J. Bordas. “Reflection spectra of perovskites from 8 eV to 60 eV”. In: *Journal of Physics C: Solid State Physics* 10.2 (Jan. 28, 1977), p. 333.
- [114] R. D. Shannon. “Revised effective ionic radii and systematic studies of interatomic distances in halides and chalcogenides”. In: *Acta Crystallographica Section A* 32.5 (Sept. 1, 1976), pp. 751–767.
- [115] Neetu Tyagi, P. Senthil Kumar, and R. Nagarajan. “Room temperature optical absorption and intrinsic photoluminescence in KZnF_3 ”. In: *Chemical Physics Letters* 494.4 (July 19, 2010), pp. 284–286.
- [116] M.G. Brik, G.A. Kumar, and D.K. Sardar. “Ab initio, crystal field and experimental spectroscopic studies of pure and Ni^{2+} -doped KZnF_3 crystals”. In: *Materials Chemistry and Physics* 136.1 (Sept. 14, 2012), pp. 90–102.
- [117] A. Meziani, D. Heciri, and H. Belkhir. “Structural, electronic, elastic and optical properties of fluoro-perovskite KZnF_3 ”. In: *Physica B: Condensed Matter* 406.19 (Oct. 1, 2011), pp. 3646–3652.
- [118] En-Hai Song et al. “Temperature-tunable upconversion luminescence of perovskite nanocrystals $\text{KZnF}_3:\text{Yb}^{3+}, \text{Mn}^{2+}$ ”. In: *Journal of Materials Chemistry C* 1.27 (June 20, 2013), pp. 4209–4215.
- [119] K. R. German, U. Dürr, and W. Künzel. “Tunable single-frequency continuous-wave laser action in $\text{Co}^{2+}:\text{KZnF}_3$ ”. In: *Optics Letters* 11.1 (Jan. 1, 1986), pp. 12–14.
- [120] W. Künzel, W. Knierim, and U. Dürr. “CW infrared laser action of optically pumped $\text{Co}^{2+}:\text{KZnF}_3$ ”. In: *Optics Communications* 36.5 (Mar. 1, 1981), pp. 383–386.

- [121] T. Seddik et al. “Elastic, electronic and thermodynamic properties of fluoroperovskite KZnF_3 via first-principles calculations”. In: *Applied Physics A* 106.3 (Mar. 1, 2012), pp. 645–653.
- [122] F. D. Murnaghan. “The Compressibility of Media under Extreme Pressures”. In: *Proceedings of the National Academy of Sciences* 30.9 (Sept. 15, 1944), pp. 244–247.
- [123] David Jason Binks. *Computation modelling of zinc oxide and related oxide ceramics*. University of Surrey, 1994.
- [124] S. Neelamraju et al. “Ab initio and empirical energy landscapes of $(\text{MgF}_2)_n$ clusters ($n = 3, 4$)”. In: *Physical Chemistry Chemical Physics* 14.3 (2012), p. 1223.
- [125] M. Exner et al. “Computer simulation of defects in KTaO_3 ”. In: *Physical Review B* 52.6 (Aug. 1, 1995), pp. 3930–3940.
- [126] E. Heifets, E. Kotomin, and P.W.M. Jacobs. “Calculations of the atomic structure of the KNbO_3 (110) surface”. In: *Thin Solid Films* 374.1 (Oct. 3, 2000), pp. 64–69.
- [127] Anne M. Hofmeister. “Calculation of bulk modulus and its pressure derivatives from vibrational frequencies and mode Grüneisen Parameters: Solids with cubic symmetry or one nearest-neighbor distance”. In: *Journal of Geophysical Research: Solid Earth* 96 (B10 1991), pp. 16181–16203.
- [128] M. Rousseau, J. Nouet, and A. Zarembowitch. “Interatomic force constants studies of AMF_3 perovskite-type crystals ($A = \text{K, Rb}$; $M = \text{Mg, Ni, Co, Zn, Mn}$)”. In: *Journal of Physics and Chemistry of Solids* 35.8 (1974), pp. 921–926.
- [129] C. H. Perry and E. F. Young. “Infrared Studies of Some Perovskite Fluorides. I. Fundamental Lattice Vibrations”. In: *Journal of Applied Physics* 38.12 (Nov. 1, 1967), pp. 4616–4624.
- [130] A. S. Barker and J. J. Hopfield. “Coupled-Optical-Phonon-Mode Theory of the Infrared Dispersion in BaTiO_3 , SrTiO_3 , and KTaO_3 ”. In: *Physical Review* 135.6 (Sept. 14, 1964), A1732–A1737.
- [131] P. D. C. King et al. “Subband Structure of a Two-Dimensional Electron Gas Formed at the Polar Surface of the Strong Spin-Orbit Perovskite KTaO_3 ”. In: *Physical Review Letters* 108.11 (Mar. 14, 2012), p. 117602.
- [132] A. F. Santander-Syro et al. “Orbital symmetry reconstruction and strong mass renormalization in the two-dimensional electron gas at the surface of KTaO_3 ”. In: *Physical Review B* 86.12 (Sept. 19, 2012), p. 121107.
- [133] W. Meevasana et al. “Creation and control of a two-dimensional electron liquid at the bare SrTiO_3 surface”. In: *Nature Materials* 10.2 (Jan. 16, 2011), pp. 114–118.

- [134] A. F. Santander-Syro et al. “Two-dimensional electron gas with universal subbands at the surface of SrTiO₃”. In: *Nature* 469.7329 (Jan. 13, 2011), pp. 189–193.
- [135] A. Ohtomo and H. Y. Hwang. “A high-mobility electron gas at the LaAlO₃/SrTiO₃ heterointerface”. In: *Nature* 427.6973 (Jan. 29, 2004), pp. 423–426.
- [136] Mark Huijben et al. “Electronically coupled complementary interfaces between perovskite band insulators”. In: *Nature Materials* 5.7 (July 2006), pp. 556–560.
- [137] Jaekwang Lee and Alexander A. Demkov. “Charge origin and localization at the n-type SrTiO₃/LaAlO₃ interface”. In: *Physical Review B* 78.19 (Nov. 17, 2008), p. 193104.
- [138] H. Bando et al. “Structure and electronic states on reduced SrTiO₃(110) surface observed by scanning tunneling microscopy and spectroscopy”. In: *Journal of Vacuum Science & Technology B* 13.3 (May 1, 1995), pp. 1150–1154.
- [139] Johannes Brunen and Jörg Zegenhagen. “Investigation of the SrTiO₃ (110) surface by means of LEED, scanning tunneling microscopy and Auger spectroscopy”. In: *Surface Science* 389.1 (Nov. 6, 1997), pp. 349–365.
- [140] Ariana Pojani, Fabio Finocchi, and Claudine Noguera. “Polarity on the SrTiO₃ (111) and (110) surfaces”. In: *Surface Science* 442.2 (Nov. 20, 1999), pp. 179–198.
- [141] E. Heifets et al. “Ab initio modeling of surface structure for SrTiO₃ perovskite crystals”. In: *Physical Review B* 64.23 (Nov. 28, 2001), p. 235417.
- [142] Natasha Erdman et al. “The structure and chemistry of the TiO₂-rich surface of SrTiO₃ (001)”. In: *Nature* 419.6902 (Sept. 5, 2002), pp. 55–58.
- [143] François Bottin, Fabio Finocchi, and Claudine Noguera. “Facetting and (n x 1) reconstructions of SrTiO₃(1 1 0) surfaces”. In: *Surface Science* 574.1 (Jan. 1, 2005), pp. 65–76.
- [144] D. S. Deak. “Strontium titanate surfaces”. In: *Materials Science and Technology* 23.2 (2007), pp. 127–136.
- [145] R. I. Eglitis and David Vanderbilt. “First-principles calculations of atomic and electronic structure of SrTiO₃ (001) and (011) surfaces”. In: *Physical Review B* 77.19 (May 6, 2008), p. 195408.
- [146] Bruce Russell and Martin Castell. “Reconstructions on the polar SrTiO₃ (110) surface: Analysis using STM, LEED, and AES”. In: *Physical Review B* 77.24 (June 10, 2008), p. 245414.
- [147] James A. Enterkin et al. “A homologous series of structures on the surface of SrTiO₃(110)”. In: *Nature Materials* 9.3 (Mar. 2010), pp. 245–248.

- [148] J. Fritsch and U. Schroder. “Reconstruction of the (001) surface of potassium tantalate”. In: *Physica Status Solidi B-Basic Research* 215.1 (Sept. 1999), pp. 827–831.
- [149] Jaime A. Li et al. “Observation of a Metastable Periodic Structure for the (001) Surface of KTaO_3 after Cleaving In Situ”. In: *Physical Review Letters* 86.21 (May 21, 2001), pp. 4867–4870.
- [150] Jaime A. Li et al. “Surface structure and dynamics of $\text{KTaO}_3(001)$ ”. In: *Physical Review B* 68.4 (July 1, 2003), p. 045402.
- [151] K. Szot et al. “Chemical inhomogeneity in the near-surface region of KTaO_3 evolving at elevated temperatures”. In: *Journal of Physics: Condensed Matter* 12.22 (June 5, 2000), p. 4687.
- [152] E. A. Kotomin et al. “Atomistic simulations of the $\text{LaMnO}_3(110)$ polar surface”. In: *Physical Chemistry Chemical Physics* 5.19 (Sept. 17, 2003), pp. 4180–4184.
- [153] E. A. Kotomin et al. “Comparative study of polar perovskite surfaces”. In: *Surface Science*. Proceedings of the 22nd European Conference on Surface Science 566–568, Part 1 (Sept. 20, 2004), pp. 231–235.
- [154] N. H. de Leeuw, G. W. Watson, and S. C. Parker. “Atomistic Simulation of the Effect of Dissociative Adsorption of Water on the Surface Structure and Stability of Calcium and Magnesium Oxide”. In: *The Journal of Physical Chemistry* 99.47 (Nov. 1, 1995), pp. 17219–17225.
- [155] Nora H. de Leeuw and Stephen C. Parker. “Atomistic simulation of the effect of molecular adsorption of water on the surface structure and energies of calcite surfaces”. In: *Journal of the Chemical Society, Faraday Transactions* 93.3 (Jan. 1, 1997), pp. 467–475.
- [156] Nora H. de Leeuw and Stephen C. Parker. “Surface Structure and Morphology of Calcium Carbonate Polymorphs Calcite, Aragonite, and Vaterite: An Atomistic Approach”. In: *The Journal of Physical Chemistry B* 102.16 (Apr. 1, 1998), pp. 2914–2922.
- [157] N. H. de Leeuw et al. “Modelling the effect of water on the surface structure and stability of forsterite”. In: *Physics and Chemistry of Minerals* 27.5 (May 1, 2000), pp. 332–341.
- [158] Zhimei Du and Nora H. de Leeuw. “A combined density functional theory and interatomic potential-based simulation study of the hydration of nano-particulate silicate surfaces”. In: *Surface Science* 554.2 (Apr. 10, 2004), pp. 193–210.
- [159] S. C. Parker, N. H. de Leeuw, and S. E. Redfern. “Atomistic simulation of oxide surfaces and their reactivity with water”. In: *Faraday Discussions* 114 (Jan. 1, 1999), pp. 381–393.

- [160] David J. Cooke, Arnaud Marmier, and Stephen C. Parker. “Surface Structure of (10 $\bar{1}$ 0) and (11 $\bar{2}$ 0) Surfaces of ZnO with Density Functional Theory and Atomistic Simulation”. In: *The Journal of Physical Chemistry B* 110.15 (Apr. 1, 2006), pp. 7985–7991.
- [161] Ben Slater et al. “Study of Surface Segregation of Antimony on SnO₃ Surfaces by Computer Simulation Techniques”. In: *The Journal of Physical Chemistry B* 103.48 (Dec. 1, 1999), pp. 10644–10650.
- [162] Alastair I. M. Rae. *Quantum Mechanics, Fifth Edition*. 5 edition. New York: CRC Press, Sept. 19, 2007. 352 pp.
- [163] Axel D. Becke. “A new mixing of Hartree–Fock and local density-functional theories”. In: *The Journal of Chemical Physics* 98.2 (Jan. 15, 1993), pp. 1372–1377.
- [164] Jochen Heyd, Gustavo E. Scuseria, and Matthias Ernzerhof. “Hybrid functionals based on a screened Coulomb potential”. In: *The Journal of Chemical Physics* 118.18 (May 8, 2003), pp. 8207–8215.
- [165] John P. Perdew, Matthias Ernzerhof, and Kieron Burke. “Rationale for mixing exact exchange with density functional approximations”. In: *The Journal of Chemical Physics* 105.22 (Dec. 8, 1996), pp. 9982–9985.
- [166] Takuji Maekawa, Ken Kurosaki, and Shinsuke Yamanaka. “Thermal and mechanical properties of polycrystalline BaSnO₃”. In: *Journal of Alloys and Compounds* 416.1 (June 8, 2006), pp. 214–217.
- [167] J. Cuervo Farfán et al. “Structural properties, electric response and electronic feature of perovskite”. In: *Physica B: Condensed Matter*. Proceedings of the Workshop ”At the Frontiers of Condensed Matter IV” - Current Trends and Novel Materials 404.18 (Oct. 1, 2009), pp. 2720–2722.
- [168] J. Druce et al. “Surface termination and subsurface restructuring of perovskite-based solid oxide electrode materials”. In: *Energy & Environmental Science* 7.11 (Oct. 15, 2014), pp. 3593–3599.
- [169] John D. Aiken III and Richard G. Finke. “A review of modern transition-metal nanoclusters: their synthesis, characterization, and applications in catalysis”. In: *Journal of Molecular Catalysis A: Chemical* 145.1 (Sept. 8, 1999), pp. 1–44.
- [170] Kohsuke Mori et al. “Hydroxyapatite-Supported Palladium Nanoclusters: A Highly Active Heterogeneous Catalyst for Selective Oxidation of Alcohols by Use of Molecular Oxygen”. In: *Journal of the American Chemical Society* 126.34 (Sept. 1, 2004), pp. 10657–10666.
- [171] Jairton Dupont et al. “Transition-Metal Nanoparticles in Imidazolium Ionic Liquids: Recyclable Catalysts for Biphasic Hydrogenation Reactions”. In: *Journal of the American Chemical Society* 124.16 (Apr. 1, 2002), pp. 4228–4229.

- [172] Kelly Sooklal et al. “Photophysical Properties of ZnS Nanoclusters with Spatially Localized Mn^{2+} ”. In: *The Journal of Physical Chemistry* 100.11 (Jan. 1, 1996), pp. 4551–4555.
- [173] Günter Schmid et al. “Current and future applications of nanoclusters”. In: *Chemical Society Reviews* 28.3 (1999), pp. 179–185.
- [174] Isabel Díez and Robin H. A. Ras. “Fluorescent silver nanoclusters”. In: *Nanoscale* 3.5 (2011), p. 1963.
- [175] T. Vossmeier et al. “CdS Nanoclusters: Synthesis, Characterization, Size Dependent Oscillator Strength, Temperature Shift of the Excitonic Transition Energy, and Reversible Absorbance Shift”. In: *The Journal of Physical Chemistry* 98.31 (Aug. 1, 1994), pp. 7665–7673.
- [176] K. S. Hong, Tae-Keun Hong, and Ho-Soon Yang. “Thermal conductivity of Fe nanofluids depending on the cluster size of nanoparticles”. In: *Applied Physics Letters* 88.3 (Jan. 16, 2006), p. 031901.
- [177] Jie Zheng, Caiwei Zhang, and Robert M. Dickson. “Highly Fluorescent, Water-Soluble, Size-Tunable Gold Quantum Dots”. In: *Physical Review Letters* 93.7 (Aug. 13, 2004), p. 077402.
- [178] Stefan T. Bromley et al. “Approaching nanoscale oxides: models and theoretical methods”. In: *Chemical Society Reviews* 38.9 (Aug. 19, 2009), pp. 2657–2670.
- [179] G. Wulff. “XXV. Zur Frage der Geschwindigkeit des Wachstums und der Auflösung der Krystallflächen : Zeitschrift für Kristallographie - Crystalline Materials”. In: *Zeitschrift für Kristallographie - Crystalline Materials* 34 (1901), pp. 449–530.
- [180] Aron Walsh and Scott M. Woodley. “Evolutionary structure prediction and electronic properties of indium oxide nanoclusters”. In: *Physical Chemistry Chemical Physics* 12.30 (July 22, 2010), pp. 8446–8453.
- [181] Scott M. Woodley, Alexey A. Sokol, and C. Richard A. Catlow. “Structure Prediction of Inorganic Nanoparticles with Predefined Architecture using a Genetic Algorithm”. In: *Zeitschrift für anorganische und allgemeine Chemie* 630.13 (2004), pp. 2343–2353.
- [182] S.M. Woodley. “Structure Prediction of Ternary Oxide Sub-Nanoparticles”. In: *Materials and Manufacturing Processes* 24.3 (2009), pp. 255–264.
- [183] A. Rapallo et al. “Global optimization of bimetallic cluster structures. I. Size-mismatched Ag-Cu, Ag-Ni, and Au-Cu systems”. In: *Journal of Chemical Physics* 122.19 (May 15, 2005), p. 194308.
- [184] Sarah Darby et al. “Theoretical study of Cu–Au nanoalloy clusters using a genetic algorithm”. In: *The Journal of Chemical Physics* 116.4 (Jan. 22, 2002), pp. 1536–1550.

- [185] E. Flikkema and S. T. Bromley. “Dedicated Global Optimization Search for Ground State Silica Nanoclusters: $(\text{SiO}_2)_N$ ($N = 6 - 12$)”. In: *The Journal of Physical Chemistry B* 108.28 (July 1, 2004), pp. 9638–9645.
- [186] Stefan T. Bromley and Edwin Flikkema. “New materials from fully coordinated SiO_2 nanoclusters”. In: *Computational Materials Science*. Proceedings of the 4th International Conference on the Theory of Atomic and Molecular Clusters (TAMC-IV) The 4th International Conference on the Theory of Atomic and Molecular Clusters 35.3 (Mar. 2006), pp. 382–386.
- [187] S. Hamad et al. “Structure and Stability of Small TiO_2 Nanoparticles”. In: *The Journal of Physical Chemistry B* 109.33 (Aug. 1, 2005), pp. 15741–15748.
- [188] Andrei Burnin and Joseph J BelBruno. “ Zn_nSm^+ cluster production by laser ablation”. In: *Chemical Physics Letters* 362.3 (Aug. 19, 2002), pp. 341–348.
- [189] J. Christian Schön and Martin Jansen. “First Step Towards Planning of Syntheses in Solid-State Chemistry: Determination of Promising Structure Candidates by Global Optimization”. In: *Angewandte Chemie International Edition in English* 35.12 (July 9, 1996), pp. 1286–1304.
- [190] K. Doll, J. C. Schoen, and M. Jansen. “Ab initio energy landscape of LiF clusters”. In: *The Journal of Chemical Physics* 133.2 (2010), p. 024107.
- [191] Andrew Logsdail, Lauro Oliver Paz-Borbün, and Roy L. Johnston. “Structures and Stabilities of Platinum–Gold Nanoclusters”. In: *Journal of Computational and Theoretical Nanoscience* 6.4 (Apr. 1, 2009), pp. 857–866.
- [192] Huifeng Qian et al. “Total Structure Determination of Thiolate-Protected Au_{38} Nanoparticles”. In: *Journal of the American Chemical Society* 132.24 (June 23, 2010), pp. 8280–8281.
- [193] Riccardo Ferrando, Julius Jellinek, and Roy L. Johnston. “Nanoalloys: from theory to applications of alloy clusters and nanoparticles”. In: *Chemical Reviews* 108.3 (2008), pp. 845–910.
- [194] T. P. M. Goumans and Stefan T. Bromley. “Stardust silicate nucleation kick-started by $\text{SiO} + \text{TiO}_2$ ”. In: *Philosophical Transactions of the Royal Society of London A: Mathematical, Physical and Engineering Sciences* 371.1994 (July 13, 2013), p. 20110580.
- [195] Faye Pittaway et al. “Theoretical Studies of Palladium–Gold Nanoclusters: Pd–Au Clusters with up to 50 Atoms”. In: *The Journal of Physical Chemistry C* 113.21 (May 28, 2009), pp. 9141–9152.
- [196] Dora J. Borbün-González et al. “Structural Insights into 19-Atom Pd/Pt Nanoparticles: A Computational Perspective”. In: *The Journal of Physical Chemistry C* 113.36 (Sept. 10, 2009), pp. 15904–15908.

- [197] Karl Pearson. “Contributions to the Mathematical Theory of Evolution. II. Skew Variation in Homogeneous Material”. In: *Philosophical Transactions of the Royal Society of London. A* 186 (Jan. 1, 1895), pp. 343–414.
- [198] S. M. Woodley. *Web Assisted Structure Prediction at the Nanoscale*. 2015. URL: <http://hive.chem.ucl.ac.uk:8080/WASP/index.html>.